materials

Special Issue Reprint

Wood-Based Materials in Building

Edited by
Radosław Mirski and Dorota Dukarska

www.mdpi.com/journal/materials

MDPI

Wood-Based Materials in Building

Wood-Based Materials in Building

Editors

Radosław Mirski
Dorota Dukarska

MDPI • Basel • Beijing • Wuhan • Barcelona • Belgrade • Manchester • Tokyo • Cluj • Tianjin

Editors

Radosław Mirski
Poznań University of
Life Sciences,
Poznań, Poland

Dorota Dukarska
Poznań University of
Life Sciences,
Poznań, Poland

Editorial Office
MDPI
St. Alban-Anlage 66
4052 Basel, Switzerland

This is a reprint of articles from the Special Issue published online in the open access journal *Materials* (ISSN 1996-1944) (available at: https://www.mdpi.com/journal/materials/special_issues/woodbased_construction).

For citation purposes, cite each article independently as indicated on the article page online and as indicated below:

LastName, A.A.; LastName, B.B.; LastName, C.C. Article Title. *Journal Name* **Year**, *Volume Number*, Page Range.

ISBN 978-3-0365-7802-6 (Hbk)
ISBN 978-3-0365-7803-3 (PDF)

Contents

About the Editors

Radosław Mirski

Professor Radosław Mirski works in the Department of Mechanical Wood Technology at Poznań University of Life Sciences, Poland. As of 2019, he is the head of this department. His research interests focus on improving the properties of wood-based materials, including the development of new technologies for their production, assessing the effects of aging and technological factors on the stability and load-bearing capacity of wood-based plastics, using non-wood lignocellulosic raw materials in the production of materials for construction, and improving material efficiency in wood processing. He is also interested in the application of computer science in the design and diagnosis of electrical machinery and equipment. Currently, he devotes most of his attention to problems in the field of timber construction, particularly the manufacture and testing of composite structural beams and the production of new wood-based boards from wood by-products intended for the construction industry. His activities are documented not only by numerous scientific publications and patents but also through cooperation with industry for the implementation of new solutions. In total, he is the author (or co-author) of more than 190 papers, 80 of them in reputable journals with an IF impact factor, and the holder of 8 patents. He has received numerous awards and award nominations for his scientific activities and collaborations with industry. A project he led entitled "Improving process and material efficiency in the lumber industry", funded by the National Center for Research and Development, within the framework of the "Environment, Agriculture and Forestry" BIOSTRATEG III program, received a European quality certificate issued by the Qualitas Foundation.

Dorota Dukarska

Dorota Dukarska, Ph.D., works in the Department of Mechanical Wood Technology at Poznań University of Life Sciences, Poland. The main thrusts of her scientific and research activities are related to the issues of the manufacturing and properties of wood-based materials depending on the raw materials, binding agents, or technological parameters used. Her research problems focus on determining the impact of various factors on the hygienic properties of wood-based materials for use in interior fitments and furniture manufacturing, the modification of adhesive resins to increase their reactivity and improve binding properties, the use of various types of nanomaterials in the manufacturing process of wood-based materials, and the use of alternative raw materials in the manufacturing process of composite materials. The realization of the above-mentioned trends is evidenced in 65 articles, 22 of them in reputable journals with an IF impact factor.

Preface to "Wood-Based Materials in Building"

The high strength of wood, combined with its relatively low density, makes it a widely used material in the broader construction industry. However, despite its many advantages, wood has defects that limit its range of applications in building construction. For this reason, in modern timber construction, new solutions and wood-based materials are being introduced to increase the durability, stiffness, and load-bearing capacity of wooden constructions. The main topics of this Special Issue were knowledge on the possibility of reinforcing laminated timber beams, the strength of glulam–concrete composite beams and the connections of individual components of timber construction, innovative solutions for the connection of lightweight wood frame panelized roofs, the effect of fire retardation of wood on its strength depending on the time of accelerated aging, and the production of innovative wood-based and insulating materials for the broadly defined construction industry. The presented reprint contains 11 high-quality original scientific and research papers by 27 authors from various research centers including Poland, the Czech Republic, Austria, Canada, and China. These papers, published in the Special Issue entitled "Wood-Based Materials in Building" in the journal *Materials*, represent examples of the latest solutions and achievements in the field of modern timber construction. The Guest Editors would like to thank all of the authors who contributed to this Special Issue. The Guest Editors would also like to thank the Section Managing Editor of the journal *Materials* and the editor of the Special Issue, Sybil Zhang, for her professionalism, kindness, and all of the assistance provided during the publication process.

Radosław Mirski and Dorota Dukarska
Editors

materials

MDPI

Editorial

Wood-Based Materials in Building

Dorota Dukarska * and Radosław Mirski

Department of Mechanical Wood Technology, Faculty of Forestry and Wood Technology, Poznań University of Life Sciences, 60-627 Poznań, Poland

* Correspondence: dorota.dukarska@up.poznan.pl

Wood is a widely used building material. It is characterized by a high strength-to-weight ratio, predictable fire behavior, good performance in seismic zones, and it is easy to use in the construction of prefabricated buildings. In addition, wood reduces energy consumption during construction and reduces a building's overall environmental impact, has lower embedded energy compared to steel and concrete, and has a positive effect on a building's carbon footprint [1]. The use of wood in building constructions is limited by its tendency to crack, twist fibers, and it can be difficult to obtain the right dimensions and shapes for use. As a result, it is being replaced by new-generation wood-based materials. Therefore, the aim of this Special Issue is to present the latest knowledge and current trends in the production of innovative wood-based materials, including composite materials for modern wood constructions, and to provide new solutions to ensure better strength parameters and safer wood constructions. Such solutions include the reinforcement of ashlar glulam beams, proposed by Wdowiak-Postulak [2], using carbon fiber reinforced plastic (CFRP) cords and carbon laminates made of carbon fibers embedded in an epoxy resin matrix. Two types of reinforcement were tested, i.e., internal strengthening, in which carbon cords are placed into cut grooves in the last and penultimate lamella, and an external surface of near-surface mounted carbon laminates, which are glued to the bottom surface of the beam to reinforce the laminated ashlar beams. The effectiveness of the reinforcement of the beams was evaluated in a four-point bending test. It was found that reinforcing the glulam beams of ashlar with carbon cords increases their load-bearing capacity by about 36%, and with carbon cords and carbon laminates by about 45%. At the same time, this type of beam reinforcement reduces the amount of displacement of the timber materials. From a practical point of view, it is important that this type of beam reinforcement is used in the construction of new structures, as well as the renovation of existing ones.

For multi-story floors, glulam-concrete composite beams (GCC) have been used for years, in which bending tensile forces are mainly carried by laminated wood, and compressive forces by concrete. Compared to typical glulam beams, GCC beams are characterized by, among other things, better load-bearing capacity, flexural strength and stiffness, better sound insulation, and greater thermal mass [3]. Du et al. [4], conducting experimental studies and finite element modeling, determined the properties of GCC beams depending on the height of the glulam beam, the spacing of the shear connectors, the thickness of the timber board interlayer, and the thickness of the concrete slab. It was shown that the failure mechanism of this type of beam is the combination of bend and tensile failure in the glulam beam, and that the weakening of interfacial interaction leading to a sharp increase in slip in the interfacial region occurs at a load corresponding to 28% of the maximum load. Increasing the height of the glulam beam results in a significant increase in the flexural capacity and stiffness of the GCC beams. On the other hand, increasing the spacing of the shear connectors decreases the ultimate bearing capacity and bending stiffness of the beams. The timber boards used as formwork for pouring concrete, placed on top of the glulam beam, have no significant effect on the flexural performance of GCC beams. It is clear that the bending bearing capacity and flexural stiffness of the composite beams increase as the thickness of the concrete slab increases. It is noteworthy that the finite element method and

Citation: Dukarska, D.; Mirski, R. Wood-Based Materials in Building. *Materials* **2023**, *16*, 2987. https://doi.org/10.3390/ma16082987

Received: 7 March 2023
Accepted: 7 April 2023
Published: 9 April 2023

numerical simulation used by the authors make it possible to accurately predict the failure mode and change characteristics of GCC composite beams during the loading process.

The permanent preservation of the form and safety of wooden constructions is ensured not only by the structural elements with adequate load-bearing capacity and strength but also by the properties of connectors and connections of individual components. Among the most common connectors in wooden constructions are dowel-type fasteners, which include screws, dowels, and bolts. According to Johanides et al. [5,6], in order for them to perform their function, it is necessary to know their mechanical behavior under load and the relationship between load and slip, stress distribution, and possible different failure modes. Therefore, the authors conducted a series of tests on the basis of which they determined the load-carrying capacity, and the rotational stiffness of a semi-rigid connection of a rung and two stands using dowel-type mechanical fasteners. These tests were further validated through numerical models. Two types of fasteners were evaluated, i.e., those made from a combination of bolts and dowels, and those made from high-strength fully threaded screws. In the first case, the load-carrying capacity and rotational stiffness were found to be higher than the values estimated according to the standard for the ultimate load condition during the entire loading process. The second type of connection from fully threaded screws also showed a higher load carrying capacity compared to the design capacity, but its rotational stiffness did not reach values higher than those estimated for the ultimate limit state for the load level corresponding to 80% of the ultimate limit state. Therefore, as the authors concluded, both types of connections are safe and reliable until the ultimate limit state is reached.

An important aspect of current research is numerical modeling, which is an excellent tool for understanding the behavior of joints in wood constructions [5,6]. The numerical analysis of single-step joints, applied by Braun et al. [7], made it possible to satisfactorily determine the stiffness and predict the forces at the onset of local failure of single- and double-step joints. In doing so, it was found that the prediction was more accurate for single-step joints, due to the fact that the model was calibrated for this type of joint, and that the joint itself is less susceptible to geometric inaccuracies. The developed model is recommended for the future, nondestructive testing of various types of wood joints to estimate their stiffness and failure mode.

An innovative solution for connecting light timber-framed roof elements has been proposed by Islam et al. [8]. The apex connection developed by the authors is expected to reduce the workload both at the construction site and at the roof panel manufacturing plant, in order to allow multiple panels to be lifted at the same time, and to streamline their transportation and installation at the site. In addition, the fastener itself is collapsible and has a self-locking mechanism that eliminates the installation steps of the panel connection on-site. To demonstrate the proposed solution, the authors prepared a 3D printout of the developed joint, which shows its effectiveness in providing a folding and unfolding mechanism as well as a self-locking mechanism for a lightweight panel roof. In addition, a finite element analysis was carried out to determine the strength requirements of this connection according to different load cases. The results of this analysis as well as the prepared 3D model indicate that it is useful and significantly improves the transportation and installation of the panel roof, mainly by providing a mechanism for its folding before installation. They also demonstrated that it can withstand the load in its unfolded state at service.

The safety of wood construction relies on proper construction technique, the quality of the engineered wood, and fire resistance. The fire safety of the structure is one of the basic requirements to be met when designing, constructing, and using a wooden house. For this reason, flame retardants are used for wood and wood-based materials, which are designed to, among other things, reduce the spread of fire, weight loss, and the rate of heat release. However, the use of flame retardants affects the mechanical properties of the wood. Grześkowiak et al. [9] determined the effect of wood flame retardants on the compressive strength and elastic modulus of wood as a function of accelerated aging time. The wood

was treated with solutions of chemical compounds included in the flame retardant formulations, i.e., monoammonium phosphate, boric acid, sodium tetraborate (borax), urea, monoammonium sulphate and diammonium phosphate, as well as commercially available formulations. In addition, to determine the progressive changes in the wood over time, a proprietary accelerated aging cycle was developed to simulate conditions in temperate climates. The process included 0, 8, and 16 cycles, and each cycle consisted of the following phases: heating at 130 °C for 24 h, then freezing at −15 °C for 24 h, reheating to 130 °C for 24 h, conditioning at 40–45 °C and 90% relative humidity for 24 h, and refreezing at −15 °C for 24 h. Of the non-aged wood samples tested, wood treated with urea, boric acid borax, and monoammonium phosphate showed the lowest compressive strength. A significant decrease in the modulus of elasticity was also observed for the last compound. In contrast, after a full aging process of 16 cycles, wood treated with urea, diammonium phosphate, and boric acid showed the highest compressive strength values. In the case of elastic modulus, the best results were obtained using monoammonium phosphate. Protecting the wood with a commercial formulation gave positive results, but only for a maximum of eight aging cycles.

One of the research directions presented in this Special Issue is the possibility of using wood by-products from primary wood processing in the production of wood-based and insulation materials for the wider construction industry. In the sawmill industry, during the primary processing of wood raw material, in addition to losses due to desorption changes, material losses of up to 50% of the wood raw material originally intended for production are also generated [10]. These losses primarily involve wood chips, sawdust, and bark, which must be managed. Mirski et al. [11] demonstrated the possibility of managing ground bark and sawdust from pine roundwood processing lines as a partial substitute for wood chips during the production of wood-based boards glued with urea–formaldehyde (UF) resin. In the produced boards, the proportions of wood chips to bark were 70:30, 60:40, and 50:50, while that of sawdust was 70:30. Regarding the results of the study, the authors showed that the most homogeneous structure and the most favorable properties are characterized by boards in which the weight ratio of wood chips to finer particles (i.e., sawdust or bark) is 70:30. They also found that the partial substitution of sawdust for bark increases the homogeneity of the board cross-section, and contributes to a significant reduction in formaldehyde emissions and water absorption. However, a potential limitation of its application in industrial practice is the variability of the chemical composition of the bark. Therefore, further research is needed, taking into account the influence of factors such as wood species, habitat, age, size, and quality of the debarked log on board properties.

The bark has a unique chemical composition and contains numerous organic compounds such as tannins, lignin, cellulose, catechins, gallocatechins, flavonoids, and proanthocyanidins [12–14]. For this reason, Walkiewicz et al. [15] used the powdered bark of various tree species as UF resin fillers in the process of plywood production. Birch, beech, maple, pine, and spruce bark were considered. Replacing the traditional filler (i.e., rye flour commonly used in the plywood industry) with maple bark did not affect the bond quality of the plywood produced with it. In other cases, a significant decrease in tensile strength values was noted, especially in the case of spruce bark. Despite these decreases, the obtained values still exceeded the normative requirements, i.e., they were above 1 N/mm^2. The decrease in the bond quality of plywood glued with resin with the addition of different bark species is due to its chemical composition, which can affect the resin curing process and lower the pH of the adhesive mixture. The consequence of this can be the occurrence of resin pre-curing and a decrease in the strength of the adhesive bond. In addition, spruce bark causes a decrease in the elastic modulus of plywood and its bending strength, especially in the perpendicular direction. However, the presence of lignin as well as tannins in the bark contributed to a favorable reduction in formaldehyde emissions, which was clearly observed for birch, beech, maple, and pine bark. Only in the case of spruce bark was a deterioration in the hygienic quality of the plywood produced.

By-products from the wood industry have also become a source of fillers that can be used in the production of polymer-based composites. Dukarska et al. [16] showed that pine sawdust is a material with a high application potential in the production of polyurethane (PUR) composite foams. The authors determined the effect of modification of a rigid PUR foam with a closed-cell structure with various amounts of sawdust, with particle sizes in the range of 0.315–1.25 mm, on the kinetics of the foam foaming process, its structure, and selected functional properties. It was shown that the introduction of up to 10% by weight of sawdust into the structure of foams does not significantly affect the course of the foaming process, while such an amount of filler allows them to reduce their thermal conductivity coefficient and significantly reduce their brittleness, while maintaining the required dimensional stability. This is accompanied by a slight decrease in the compressive strength of the foams, a decrease in their flexural strength, and an increase in water absorption. However, despite the slight decrease in the values of the above parameters, composite foams containing up to 10% sawdust are characterized by favorable properties comparable to rigid PUR foams currently available on the market. The introduction of larger amounts of sawdust into the polyurethane matrix, i.e., at the levels of 15% and 20%, results in serious changes in the cellular structure of PUR foams, which, as a consequence, leads to a significant decrease in almost all the studied physical and mechanical parameters. Thus, as the authors propose, rigid PUR foams made with a 10% addition of pine sawdust can be used as thermal insulation materials in the construction industry, for example for door insulation. However, they can also be used in the refrigeration and heating industries, for example, for the insulation of refrigerated furniture or boilers. The significantly reduced brittleness of this type of foam also allows it to be used in the production of usable items such as ceiling and wall decorations.

The current technological and social trends require the construction sector to implement the principles of sustainable development. An important element of this concept is the principle of wooden construction based mainly on wood and wood-based materials, which counteracts climate change by storing carbon dioxide in wood and reducing the consumption of high-emission materials such as concrete and steel. The introduction of new and innovative solutions improves the energy efficiency of buildings, their functionality, and reduces their negative impact on the natural environment. The works presented in this Special Issue exemplify the current directions of research in modern wooden construction in accordance with the concept of sustainable development.

Author Contributions: Conceptualization, D.D. and R.M.; formal analysis, D.D. and R.M.; writing and editing, D.D. All authors have read and agreed to the published version of the manuscript.

Funding: This research was funded by the National Centre for Research and Development, grant number BIOSTRATEG3/344303/14/NCBR/2018.

Conflicts of Interest: The authors declare no conflict of interest.

References

1. Wimmers, G. Wood: A Construction Material for Tall Buildings. *Nat. Rev. Mater.* **2017**, *2*, 17051. [CrossRef]
2. Wdowiak-Postulak, A. Strengthening of Structural Flexural Glued Laminated Beams of Ashlar with Cords and Carbon Laminates. *Materials* **2022**, *15*, 8303. [CrossRef] [PubMed]
3. Yeoh, D.; Fragiacomo, M.; De Franceschi, M.; Koh, H.B. State of the Art on Timber-Concrete Composite Structures: Literature Review. *J. Struct. Eng.* **2011**, *137*, 1085–1095. [CrossRef]
4. Du, H.; Yuan, S.; Liu, P.; Hu, X.; Han, G. Experimental and Finite Element Study on Bending Performance of Glulam-Concrete Composite Beam Reinforced with Timber Board. *Materials* **2022**, *15*, 7998. [CrossRef] [PubMed]
5. Johanides, M.; Lokaj, A.; Dobes, P.; Mikolasek, D. Numerical and Experimental Analysis of the Rotational Stiffness of a Timber Semi-Rigid Dowel-Type Connection. *Materials* **2022**, *15*, 5622. [CrossRef] [PubMed]
6. Johanides, M.; Lokaj, A.; Dobes, P.; Mikolasek, D. Numerical and Experimental Analysis of the Load-Carrying Capacity of a Timber Semi-Rigid Dowel-Type Connection. *Materials* **2022**, *15*, 7222. [CrossRef] [PubMed]
7. Braun, M.; Pełczyński, J.; Al Sabouni-Zawadzka, A.; Kromoser, B. Calibration and Validation of a Linear-Elastic Numerical Model for Timber Step Joints Based on the Results of Experimental Investigations. *Materials* **2022**, *15*, 1639. [CrossRef] [PubMed]

8. Islam, M.S.; Chiu, Y.H.; Chen, Z. Novel Apex Connection for Light Wood Frame Panelized Roof. *Materials* **2022**, *15*, 7457. [CrossRef] [PubMed]
9. Grześkowiak, W.Ł.; Molińska-Glura, M.; Przybylska, M. The Influence of the Accelerated Aging Process on the Compressive Strength of Wood Treated with Components of a Salt Fire Retardant. *Materials* **2022**, *15*, 4931. [CrossRef] [PubMed]
10. Mirski, R.; Derkowski, A.; Dziurka, D.; Dukarska, D.; Czarnecki, R. Effects of a Chipboard Structure on Its Physical and Mechanical Properties. *Materials* **2019**, *12*, 3777. [CrossRef] [PubMed]
11. Mirski, R.; Derkowski, A.; Kawalerczyk, J.; Dziurka, D.; Walkiewicz, J. The Possibility of Using Pine Bark Particles in the Chipboard Manufacturing Process. *Materials* **2022**, *15*, 5731. [CrossRef] [PubMed]
12. Jansone, Z.; Muizniece, I.; Blumberga, D. Analysis of Wood Bark Use Opportunities. *Energy Procedia* **2017**, *128*, 268–274. [CrossRef]
13. Bianchi, S.; Kroslakova, I.; Janzon, R.; Mayer, I.; Saake, B.; Pichelin, F. Characterization of Condensed Tannins and Carbohydrates in Hot Water Bark Extracts of European Softwood Species. *Phytochemistry* **2015**, *120*, 53–61. [PubMed]
14. Valentín, L.; Kluczek-Turpeinen, B.; Willför, S.; Hemming, J.; Hatakka, A.; Steffen, K.; Tuomela, M. Scots Pine (*Pinus sylvestris*) Bark Composition and Degradation by Fungi: Potential Substrate for Bioremediation. *Bioresour. Technol.* **2010**, *101*, 2203–2209. [CrossRef] [PubMed]
15. Walkiewicz, J.; Kawalerczyk, J.; Mirski, R.; Dziurka, D.; Wieruszewski, M. The Application of Various Bark Species as a Fillers for UF Resin in Plywood Manufacturing. *Materials* **2022**, *15*, 7201. [CrossRef] [PubMed]
16. Dukarska, D.; Walkiewicz, J.; Derkowski, A.; Mirski, R. Properties of Rigid Polyurethane Foam Filled with Sawdust from Primary Wood Processing. *Materials* **2022**, *15*, 5361. [CrossRef] [PubMed]

materials

MDPI

Article

Strengthening of Structural Flexural Glued Laminated Beams of Ashlar with Cords and Carbon Laminates

Agnieszka Wdowiak-Postulak

Faculty of Civil Engineering and Architecture, Kielce University of Technology, 25-314 Kielce, Poland; awdowiak@tu.kielce.pl; Tel.: +48-41-34-24-480

Abstract: Changes in the condition of existing timber structures can be caused by fatigue or biological attack, among other things. Replacing damaged timber is still very expensive, so it seems more advisable to repair or reinforce damaged elements. Therefore, in order to improve the static performance analysis of timber structures, reinforcement applications in timber elements are necessary. In this experimental study, technical-scale glulam beams measuring 82 × 162 × 3650 mm, which were reinforced with carbon strands and carbon laminates, were tested in flexure. A four-point bending test was used to determine the effectiveness of the reinforcement used in the timber beams. Internal strengthening (namely, glued carbon cords placed into cut grooves in the last and penultimate lamella) and an external surface of near-surface mounted (NSM) carbon laminates glued to the bottom surface of the beam were used to reinforce the laminated ashlar beams. As a result of this study, it was found that the bending-based mechanical properties of ash wood beams reinforced with carbon fibre-reinforced polymer composites were better than those of the reference beams. In this work, the beams were analysed in terms of the reinforcement variables used and the results were compared with those for the beams tested without reinforcement. This work proves the good behaviour of carbon fibre reinforced plastic (CFRP—Carbon fibre reinforced polymer) cords when applied to timber beams and carbon laminates. This study illustrated the different reinforcement mechanisms and showed their structural properties. Compared to the reference samples, it was found that reinforcement with carbon strings or carbon laminates increased the load-bearing capacity, flexural strength and modulus of elasticity, and reduced the amount of displacement of the timber materials, which is an excellent alternative to the use of ashlar and, above all, inferior grade materials due to the current shortage of choice grade. Experimental results showed that, with the use of carbon fibre (carbon cords SikaWrap® FX-50 C—Sika Poland Sp. z o.o., Warsaw), the load bearing capacity increased by 35.58%, or with carbon cords SikaWrap® FX-50 C and carbon laminates S&P C-Laminate type HM 50/1.4 - S&P Poland Sp. z o.o., Malbork, by 45.42%, compared to the unreinforced beams.

Keywords: glued laminated beams; fibre-reinforced timber; load-bearing capacity; stiffness; ductility; modulus of elasticity; bending test; carbon cords; carbon laminates; knots

Citation: Wdowiak-Postulak, A. Strengthening of Structural Flexural Glued Laminated Beams of Ashlar with Cords and Carbon Laminates. *Materials* **2022**, *15*, 8303. https://doi.org/10.3390/ma15238303

Academic Editor: Tomasz Sadowski

Received: 6 November 2022
Accepted: 21 November 2022
Published: 23 November 2022

Publisher's Note: MDPI stays neutral with regard to jurisdictional claims in published maps and institutional affiliations.

1. Introduction

Wood is anisotropic, hygroscopic and organic [1–4]. It should be remembered, also, that wood has many beneficial properties [5,6]. It represents a material that is advantageous for use in structures and in non-structural areas [7]. There is currently a rapid increase in the use of wood materials, primarily for structural applications. However, there are also certain limitations that allow the use of wood in the structural area. These limitations are: fibre twists, knots, cracks, difficulties in finding materials with the desired shapes and sizes, changes in production methods, production methods, use of materials with low strength properties in production, a high waste rate when using solid wood material, and the joining of short pieces. Therefore, wood as a material can be strengthened by supporting it with fibre-reinforced polymers both to increase the resistance of the strength properties of the joints of the structures to be obtained by using the wood material, and to repair damage

caused by external factors such as material deterioration of previously built structures or due to earthquakes [1,8,9].

Wood construction makes an important contribution to the global energy consumption of greenhouse gas emissions. This has a significant impact on renewable materials, primarily timber structures. Although wood is a natural composite and is one of the oldest materials used in construction, it is important to remember that the use of wood and wood-based materials for structural purposes is still used today [4]. The use of timber as a structural element is the oldest known technique, especially in structural engineering projects, as an example of high deadweight construction. This is because these materials have a high strength-to-weight ratio and can be considered as highly sustainable materials. Recently, there has been a growing fondness for the use of timber in construction projects. This is triggered by its ability to hold dynamic loads and its mechanical properties, hence the many research works [10–15]. Currently, there are various structural timber products, and glulam is one of these products, described as one of the most efficient composite building materials. These glulam components consist of different layers of laminated timber, which are bonded together using a high-strength adhesive material to create a uniform component. Moreover, this causes a decrease in natural heterogeneities, such as knots occurring in the wood material [11–19]. Glulam elements make it possible to obtain elements with different dimensions and avoid inconsistencies in their properties. In recent years, a number of researchers have looked into the scope of glulam beams, so various experimental studies have been carried out. In a study by Anshari et al. [20], compressed timber layers in pre-cut rectangular holes were used to reinforce glulam beams. The study confirmed that the use of pressed timber layers as a reinforcing material is economically and environmentally effective. Another study [21] presented an investigation of the feasibility of glulam beams, the purpose of which was to determine the effective gluing factor, stating in its conclusions that the gluing parameters must be adjusted depending on the timber species. Another study [22] presented an investigation of the mechanical properties of the glue in a rod embedded in a glulam beam, where the results of an experimental pull-out test of this rod showed that failure occurred as a result of the rod slipping into the glulam beam and the delamination of the shear bond. Subsequently, the paper [23] demonstrated and concluded that reinforcement played an important role in the change of the failure form from brittle to ductile, which represented an increase in the load carrying capacity of the reinforced beams. Subsequent experimental studies [24] investigated bonded beams and carbon composites as reinforcing materials. Afterwards, it was found that the type and position of the reinforcement had a direct influence on the mechanical properties of the whole element. Subsequently, in [25], the influence of the toe joint profile of glued beams made of hardwood and its behaviour on the tensile strength was determined. As a result, it was suggested that the species studied could be used to produce glulam with a high tensile strength.

In recent years, the demand for wood has increased significantly, while timber is now a popular building material due to its ability to be used as a lightweight construction material. Ease of production or its unique physical and mechanical properties and low density are also enhanced by its attractive appearance. Due to its environmental protection or low energy requirements, wood is a commonly used construction material. Reinforcing or joining of wooden materials is usually done with steel elements. It is important to remember, however, that steel elements detach from the wood material over time and corrode. This decreases the quality of the environment over time, damages human health, shortens the life of the wooden element and also creates environmental problems. Therefore, nowadays most historic and existing wooden structures need to be safely repaired or reinforced. Known repair work, as well as insect infestation in various parts of the wooden elements over time, as well as fungal activity or decay, etc., can also cause environmental problems. On the other hand, leaving such elements that should be replaced for various reasons can cause serious problems both in terms of cost and structural safety. It would therefore be more appropriate to replace the damaged element rather than replace all the elements used

in the building. Changes can be applied by using a dowel, a nail, or a blotting technique. However, this may not have the desired static result. On the other hand, reinforcing timber structures with FRP does not take a lot of time and at the same time provides an advantage also aesthetically [6]. Therefore, it is advisable to use man-made or natural fibres, whether based on basalt, glass, carbon, aramid, jute, etc., used in the study to reinforce wood [26–39]. It should be noted that performance reinforcing polymer (FRP) composites support the use, the care and reinforcement, of damaged structures. Their characteristics include their low height, high strength, high resistance to action and convenience and installation. Types of FRP include carbon fibre reinforced polymer (CFRP), glass fibre reinforced polymer (GFRP) and basalt fibre reinforced polymer (BFRP) composites. Due to the use of pultrusion technology, CFRP sheets can be rapidly developed with high forming properties. On the basis of experimental studies, the use of CFRP duct instead of externally bonded CFRP board was found to be a very effective way to renew or reinforce structures. This has the effect that the build-up rate of the CFRP plate can help 20–30% when the source is used. In addition, by using a specific compressed CFRP plate, load and shear capacity, deflection performance and crack growth can be effectively achieved. In addition, when providing prestressed CFRP for structural reinforcement, the end result creates the effect of the properties of the CFRP exposed to the generating temperature, water absorption and attachment with the necessity of loading. Although some analysis has been carried out to investigate the performance of FRP to study the environment, it should be noted that it is difficult to obtain the effect of the pressure level on the degradation of mechanical properties [40]. The paper [41] presents the results of a four-point bending test of fifteen small-size glulam specimens reinforced with glass (GFRP) or carbon (CFRP) cords, differing in the type of adhesive (epoxy resin or melamine glue). It was found that the effectiveness of the proposed technique was compromised by inadequate soaking of the installed cords and by too much resin. The reinforcements used were able to induce compressive failure of the upper timber layer once the beam cracked. In contrast, specimens reinforced with basalt cords showed better performance in terms of both strength and ductility. The average increase in strength was about 25%, while the average increase in ductility was about 40%, relative to unreinforced specimens. In an experimental paper [42], a programme for strengthening cross-laminated timber beams using carbon fibre reinforced polymer (CFRP) and glass fibre reinforced polymer (GFRP) composite sheets was presented. Encouraging results were found: the percentage increase in flexural stiffness was 26.29% and 45.76% for 2.5% and 5% addition of GFRP composite sheets on the tension side of the beam, respectively. However, for the same percentage addition of GFRP, the increase in flexural strength was 36.91% and 40% compared to the unreinforced beam. For a 1.67% and 3.33% addition of CFRP composite sheet to the tension side of the beam, the percentage increase in flexural stiffness compared to the unreinforced beam was 36.19% and 64.12%. Furthermore, the increase in flexural strength for the respective percentage additions of CFRP was 45.86% and 50.62%.

Due to its orthotropic natural properties, it must be taken into account that wood is a complex material and, therefore, analytical methods to describe its basic workings are limited. The presence of knots or cracks or skewness of the fibres also has a significant impact on the mechanical behaviour of a wood component, especially in the tensile zone that is present. For this reason, the material properties of wood can vary even between the same wood species, so many parameters are important and necessary to fully describe its modelling.

Based on an analysis of the literature, there has been some minor research carried out on carbon cord-reinforced laminated beams. In contrast, there has been virtually no research involving reinforcement with inferior carbon ropes or laminates with a reinforcement scheme such as that in the work below. Therefore, this paper presents the results of an experimental study carried out on glulam beams of medium and inferior quality class, with the aim of determining the effectiveness of an innovative strengthening technique involving

the use of CFRP cords, instead of rods and CFRP laminates. Based on these considerations, further experimental studies are needed, for example by considering circular grooves.

2. Materials and Methods

2.1. Materials

Ash was the hardwood species that was chosen for the flexural testing of beams reinforced with CFRP materials. Obviously, the properties of this species are similar even to those of pine, primarily used in the construction industry, primarily in the manufacture of glulam or CLT (Cross Laminated Timber). It is a fast-growing, leaf-shedding and medium-sized tree, around 25–35 m in height and up to around 100 cm in diameter. In contrast to the trunks of trees growing in forests, its compactness is well-grown, long, straight, up to a height of about 20 m, and free of branches. In its slow-growing state, the tree is prone to bifurcation. The bark, up to about 50 years of age, is smooth and greenish-grey, then brown, almost black, and cracked. The proportion of bark is about 9–14% of the trunk volume with bark. Ash is found throughout Europe, from southern Scandinavia to the northern Mediterranean coastline (but not on the Apennine or Peloponnese peninsulas), and in Spain only in the north. In Poland, it is a wild forest tree ranked among the most valuable, noble species of native deciduous trees. It also requires fertile, deep, plump, moist or wet soils. It is very sensitive to frost. It does not form solid stands. It is found in river valleys, where it forms stands together with alder and oak.

The lamellas came from timber elements with strength classes D18—($f_{m,k}$—18 MPa, $f_{t,0,k}$ —11 MPa, $f_{c,0,k}$ —18 MPa, $E_{0,mean}$ —9500 MPa, G_{mean}–590 MPa) oraz D24—($f_{m,k}$ —24 MPa, $f_{t,0,k}$ —14 MPa, $f_{c,0,k}$ —21 MPa, $E_{0,mean}$ —10,500 MPa, G_{mean}—620 MPa), [43]. Smooth sawn timber beams, with a density of approximately 670 kg/m3, were reinforced with carbon fibre SikaWrap® FX-50 C-carbon fibre cord, and SikaWrap® FX-50 C and S&P C-Laminate type HM 50/1.4-carbon laminate.

According to the manufacturer, SikaWrap® FX-50 C—Sika Poland Sp. z o.o., Warsaw [44] is a rope of unidirectionally aligned carbon fibres, encased in a foil sleeve, used as a surface mounted reinforcement, and provides a connector for anchoring SikaWrap® mats. Unidirectionally aligned carbon fibres in a SikaWrap® FX-50 C foil sleeve sheath with a dry fibre tensile strength of 4 GPa, 240 GPa dry fibre tensile modulus and a dry fibre density of 1.82 g/cm^3. Sikadur®-330—Sika Poland Sp. z o.o., Warsaw [45] epoxy resin was used to bond the carbon fibre cords in the bonded beams in layers. The hardener and resin were mixed at a ratio of 1 to 4 by weight. Sikadur®-330 has the following parameters: flexural modulus E~3 800 MPa, tensile strength ~30 MPa, tensile modulus ~4500 MPa.

According to the manufacturer, S&P C-Laminates—S&P Poland Sp. z o.o., Malbork [46] are finished composite products made from carbon fibres embedded in an epoxy resin matrix. They are designed for the reinforcement of steel, reinforced concrete masonry and timber structures. Technical data are as follows: tensile strength $\geq$2800 N/mm^2, modulus of elasticity $\geq$205 kN/mm^2 and density 1.6 g/cm^3. S&P Resin 55 HP—S&P Poland Sp. z o.o., Malbork [47] liquid epoxy resin was used to bond the carbon fibre laminates in the sandwich bonded beams to achieve a good wood—FRP bond. From the experimental studies already carried out, it was found that the best performance was obtained for the liquid epoxy resin, which penetrates very well into the pores of the wood; see [26]. S&P Resin 55 HP is a two-component, solvent-free adhesive based on epoxy resin with an amine hardener. The manufacturer's technical data are as follows: modulus of elasticity $\geq$3200 N/mm^2, compressive strength $\geq$ 100 N/mm^2 and mixing ratio of components A:B is 4.2:1.8.

The wood species used in the study was ash, which has recently been increasingly used in the production of wood composites, and above all for structural purposes. For fibre composites, on the other hand, if high tensile strength is desired, then carbon fibres are an excellent material. Carbon fibre-reinforced polymers are the most common reinforcement applications used in industry. Other types of commonly used fibres are already significantly inferior to carbon fibres in terms of their modulus of elasticity or tensile strength, which makes them a suitable choice for reinforcing wooden beams in particular. In addition,

carbon fibres have a high fatigue resistance, so that they can withstand significant stresses (for a certain number of cycles) without breaking. In addition, they are also non-combustible and have a low coefficient of thermal expansion. Although natural fibres appear to be a better choice in terms of their sustainability, natural fibres have a significantly lower tensile strength compared to carbon fibres. In contrast, natural fibres reduce greenhouse gas emissions. In this research, carbon fibre cords were used instead of natural fibres due to the potential increase in the mechanical properties of the composite. In contrast, the impact on greenhouse gas creation potential could be offset if recycled carbon fibres were used instead of virgin carbon fibres.

2.2. Samples Preparation

The timber samples were selected from pieces with natural defects, such as knots, to investigate the possibility of which fibres could address the natural defects in the timber. The timber samples were cut from the same trunk (with the timber fibres parallel to the length of the beam) to reduce differences that could affect the comparison of results. All the timber elements from which the glued laminated beams were made were visually sorted by strength methods, dividing them into sorting classes: KS—medium quality class, and KG—lower quality class, according to PN-D-94021:2013-10 [48]. The experimental tests mainly focused on the analysis of the increase in load-bearing capacity compared to the load-bearing capacity of unreinforced elements.

The timber beams were grooved in designed square patterns for the placement of the reinforcement, so as to provide an opportunity to lay the carbon fibres as cords on the timber beams, The carbon fibres were laminated onto the beams using an epoxy resin mix and allowed to dry for 24 h.

Considering the type of reinforcement material, 15 unreinforced and reinforced laminated timber beams were designed and designated as NCFRP (5 units) as unreinforced beams, followed by CFRP1 (5 units) as reinforced with carbon strands with a degree of strengthening of 2.51% and CFRP2 (5 units) as reinforced with both carbon strands and carbon laminates with a degree of strengthening of 3.07%.

Four grooves were made along the length of the timber beams; next, the cords were placed in the cut-out, then these were bonded to the timber using epoxy resin. This reinforcement technique would allow significant bending strength to be achieved in the designed beams while maintaining shallow depths. It would therefore allow for a long-span structure with reduced dimensions and a significant visual effect.

All the beams were made with the same external section size: their length was 3650 mm, the span between supports was 3000 mm, the height was 162 mm and the width was 82 mm. The beams, designated CFRP1, were reinforced with carbon fibre cords of approximately 10 mm in diameter and 3750 mm in length. The CFRPs were bonded in holes of approximately 14 mm to the compressed carbon fibres using Sikadur®-330 epoxy adhesive. The square holes around the carbon cords were filled with this epoxy adhesive. S&P Resin 55 HP epoxy adhesive, on the other hand, was applied to the primed surfaces using a roller to a thickness of 1 mm. Substrate preparation was carried out by planing the beam elements. The resulting dust was removed with a hoover. The surface was primed using S&P Resin 55 HP system adhesive immediately before bonding with S&P C-Laminate. A diagram of the reinforcement including dimensions is shown in Figure 1. The prepared beams were stored for 1 week before bending tests. Prior to testing the beams, all elements were stored at a temperature of 20 ± 2 °C and a relative humidity of 65 ± 5%. The moisture level was checked with an electric moisture meter at 12%.

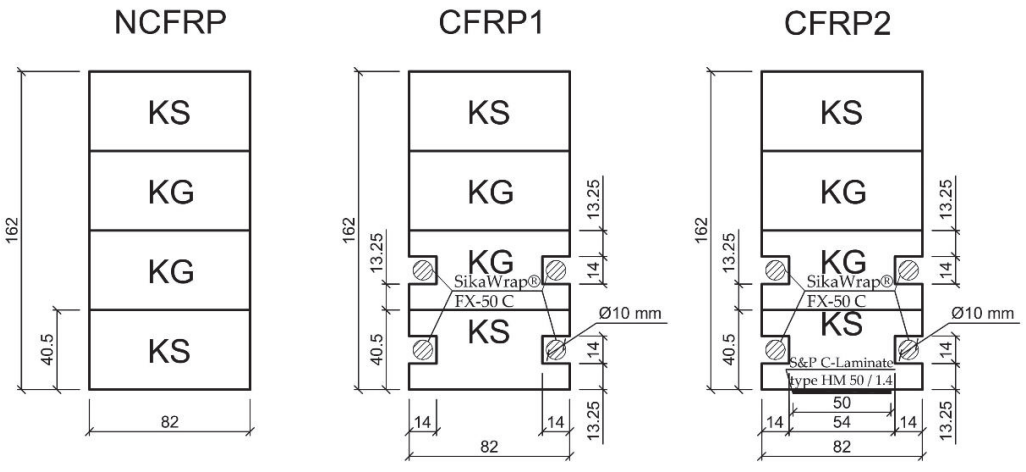

Figure 1. Cross-section of the laminated beams.

2.3. Test Methods

The bending tests were carried out on timber beams according to EN 408+A1:2012 [49] and EN 1995-1-1:2010 [50]. All the beams were tested at a span of 3000 mm in four-point bending. Steel plates, 50 mm wide and 15 mm thick, were placed at the bearing and support points to relieve displacement rotation and to recreate a simply supported beam. A freely supported glulam beam is shown in Figure 2. The four-point bending experimental test was carried out using a mechanical testing machine. In order to delineate the change in strain at the mid-span of the specimen during the entire loading process, the measuring points were evenly distributed along the height. The deformations were tested using a 'Demec' extensometer. The span of the support points was taken as 203.2 mm. The deflection tests, on the other hand, were determined at the centre of the beam span using dial gauges. The four-point bending test as a representation of the experimental setup is shown in Figure 2.

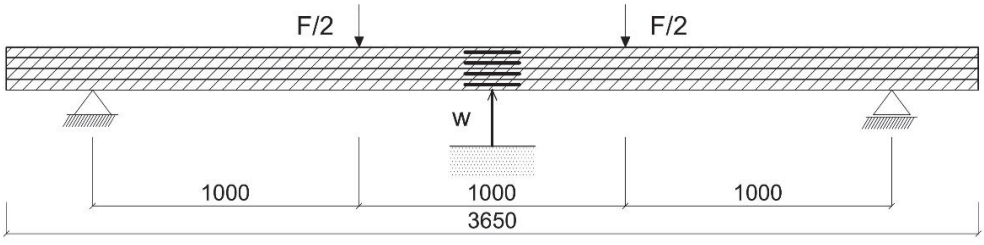

Figure 2. Four-point bending test.

3. Results

In this study, laminated beams were reinforced with carbon fibre: SikaWrap® FX-50 C or S&P C-Laminate type HM 50/1.4 carbon fibre CFRP. The reference and reinforced beams were subjected to bending tests.

3.1. Load-Displacement Responses

Load-displacement diagrams and the bending strength and modulus of elasticity values obtained in the test are given in Figures 3–5.

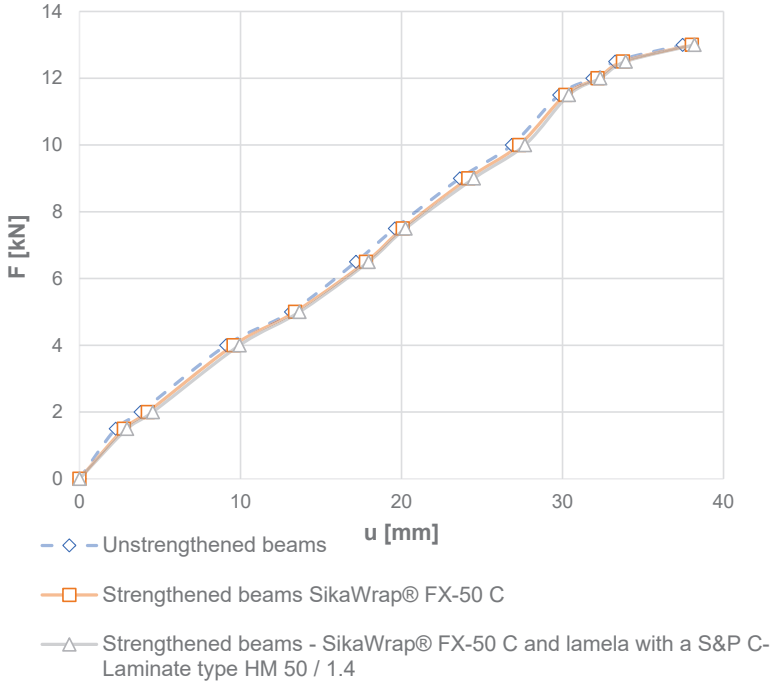

Figure 3. Load-displacement diagrams of FRP-strengthened and unstrengthened beams.

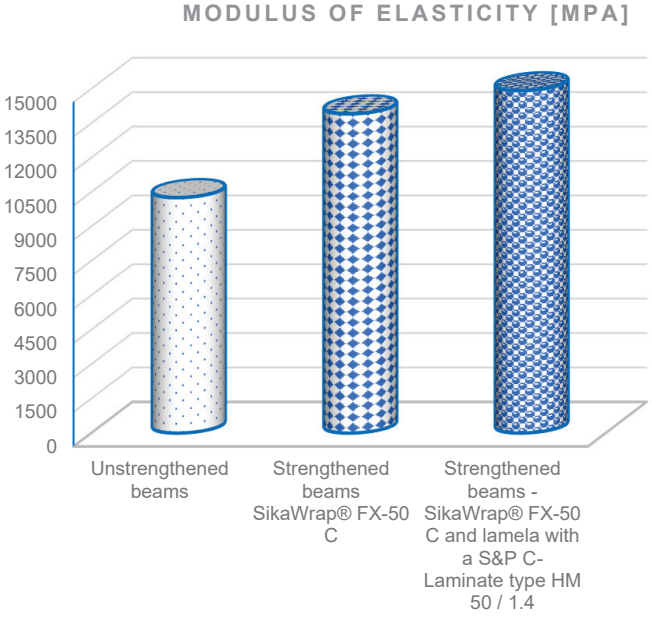

Figure 4. Diagrams of the moduli of elasticity of strengthened and unstrengthened beams.

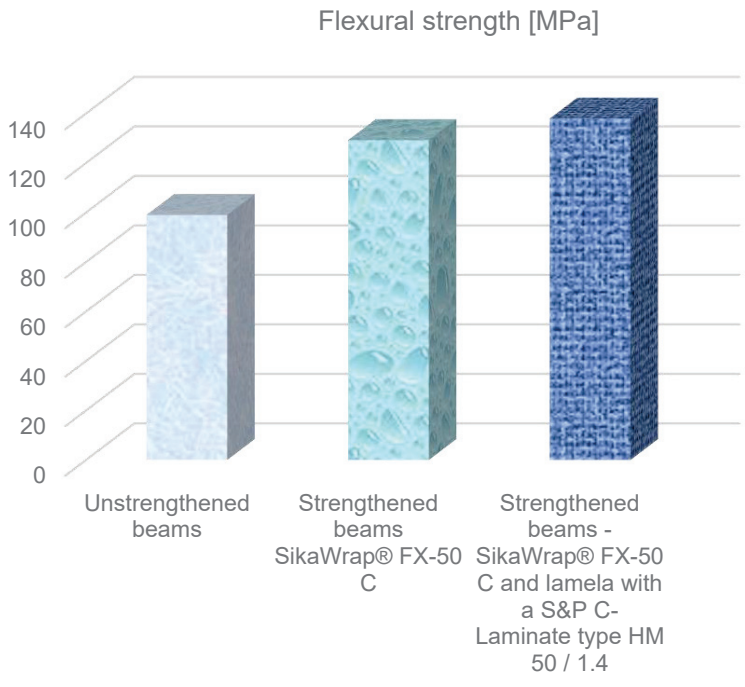

Figure 5. Bending strength diagrams of the strengthened and reference beams.

From the tests, it was found that the load capacity of the elements reinforced with carbon fibre SikaWrap® FX-50 C increased by 35.58% or with SikaWrap® FX-50 C and S&P C-Laminate type HM 50/1.4 carbon fibre CFRP by 45.42% with the reference beams. It was found that the displacement volume with the SikaWrap® FX-50 C reinforced beam increased by 15.22% and with the SikaWrap® FX-50 C reinforced beam and S&P C-Laminate type HM 50/1.4 CFK carbon fibre CFRP laminates by 19.49%, compared to the reference beams.

After analysing Figures 4 and 5, it was found that beams reinforced with SikaWrap® FX-50 C carbon fibre–carbon ropes, had a flexural strength (129.22 MPa) and modulus of elasticity (13,910 MPa), while beams reinforced with SikaWrap® FX-50 C and S&P C-Laminate type HM 50/1.4 had a flexural strength (137.97 MPa) and modulus of elasticity (14,920 MPa). It was found that the flexural strength value of the reinforced SikaWrap® FX-50 C beam increased by 31.53%, SikaWrap® FX-50 C and S&P C-Laminate type HM 50/1.4 by 39.36%, whereas the modulus of elasticity of the SikaWrap® FX-50 C increased by 35.58%, and SikaWrap® FX-50 C I laminate S&P C-Laminate type HM 50/1.4 by 45.42%.

3.2. Deformations of Unstrengthened and Strengthened Beams

The variation of the bending strain of the reinforced beams at the height of the section in the middle span and the FRP materials used are shown in Figures 6–8. The figures show that the compressive strain is negative, while the tensile strain is positive. In contrast, the strain at the height of the glued beam varies linearly, which is obviously consistent with the assumption of a planar section. Note that the neutral axis in some cases of SikaWrap® FX-50 C or S&P C-Laminate type HM 50/1.4 reinforced beams shifts downwards. In the experimental process of loading laminated timber beams, the timber in the compression zone is in a plastic state, while it can be seen that the applied reinforcements, i.e., SikaWrap® FX-50 C or S&P C-Laminate type HM 50/1.4 CFRP in the tension zone, have an increasingly significant effect on the static performance analysis of the beams.

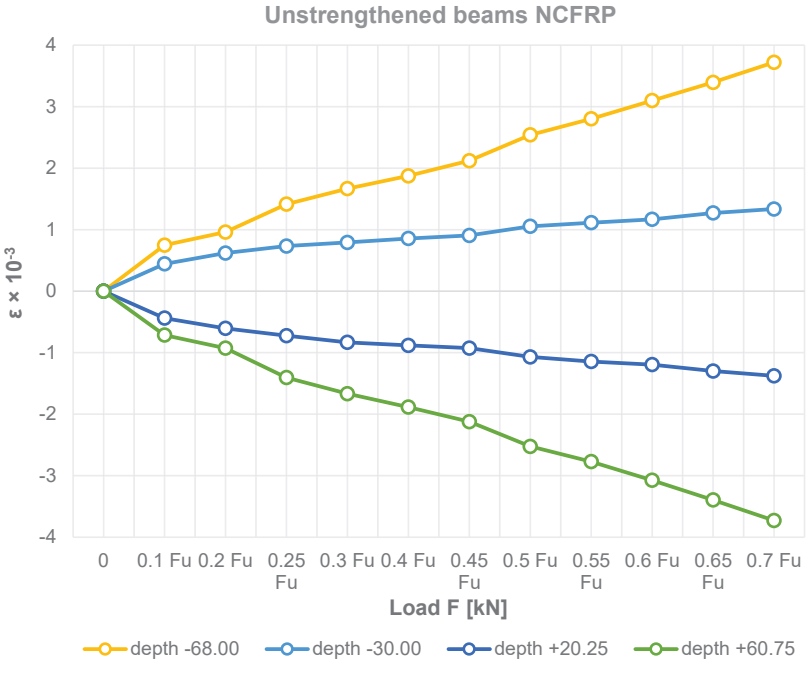

Figure 6. The distribution of deformations in timber beams at the section height.

3.3. Effect of CFRP Reinforcement on Beam Bending

As can be seen in the experimental results in Figures 3–8, the elastic modulus of the FRP materials increased with the increasing percentage of reinforcement. The lower the elastic modulus, the smaller the deformation was. In the case of beam elements reinforced with carbon strings and carbon laminates, it proved to be the most effective, providing up to a 39.36% additional increase in load capacity compared to the unreinforced condition (see Figures 6–8).

Based on the experimental tests carried out, due to the selective placement of the FRP material in the areas of the beam subjected to stronger tension, the wood fibres in the upper part of the beam produced plastic compressive deformation (see Figures 7 and 8).

Figures 3–8 clearly show a significant increase in the load carrying capacity of the carbon fibre reinforced beams compared to the reference beams. Furthermore, in Figure 3, it can be seen that the elongation of the beam improved significantly after strengthening. It can be seen from the experimental study that the more the beams were reinforced, the more they showed a plastic curve.

On the basis of the research, it was also found that beam elements can also be used for building structures as well as components that can also be subjected to sudden impact loads such as from earthquakes at the same time. It should further be noted that, on the basis of the bending test, it was noted in order to increase the ductility of the reinforced section, it is recommended that the timber elements do not have natural defects. Furthermore, it was noted that, by analysing the strain distribution, fibre reinforcement in the tensile zone of the member maximises the effective use of the material in the compressive zone. In the experimental tests, it was further noted that during the tests the laminated beams or reinforcing materials did not slip as well as creep.

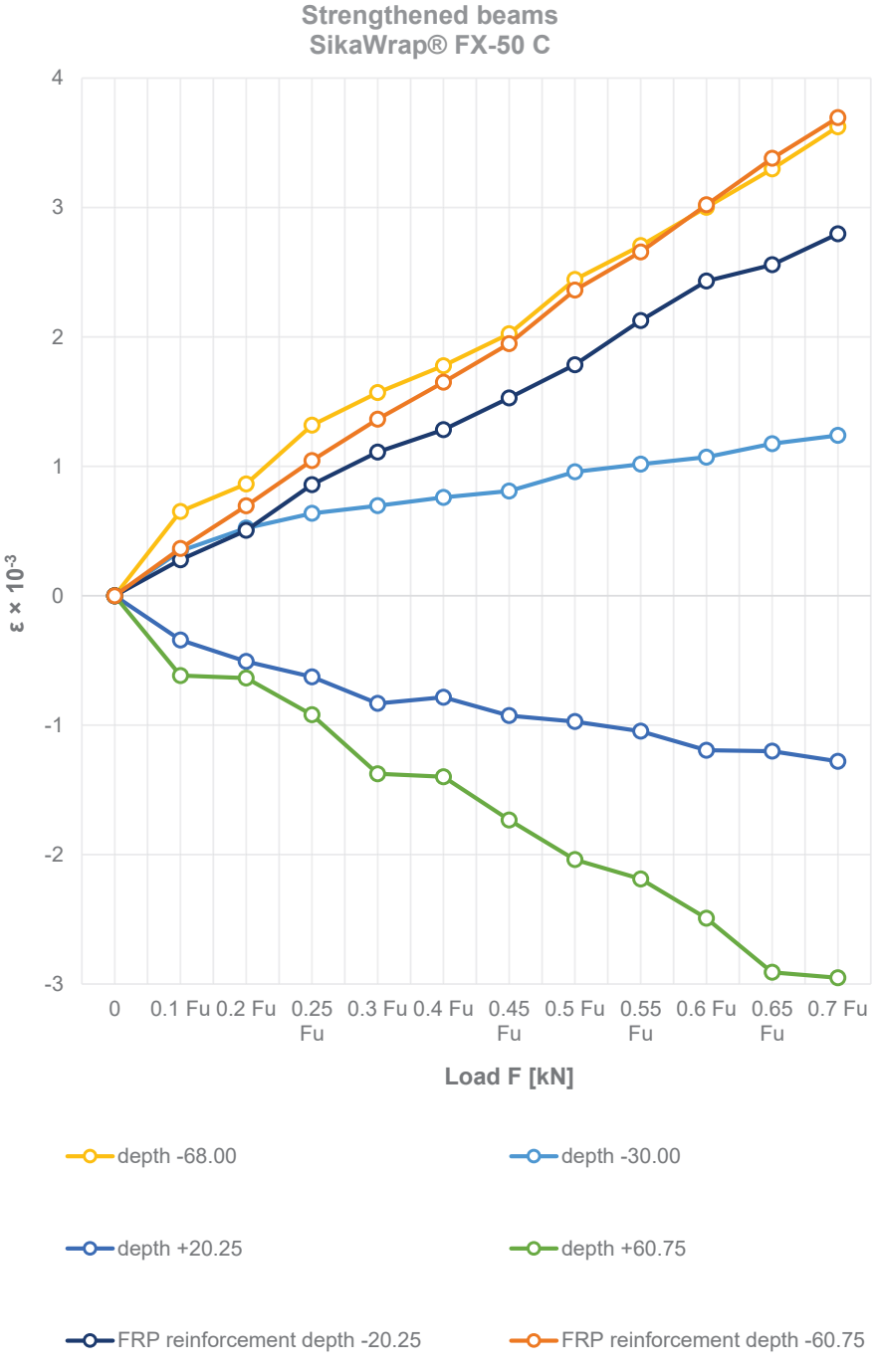

Figure 7. The distribution of deformation in timber beams and FRP materials at the section height.

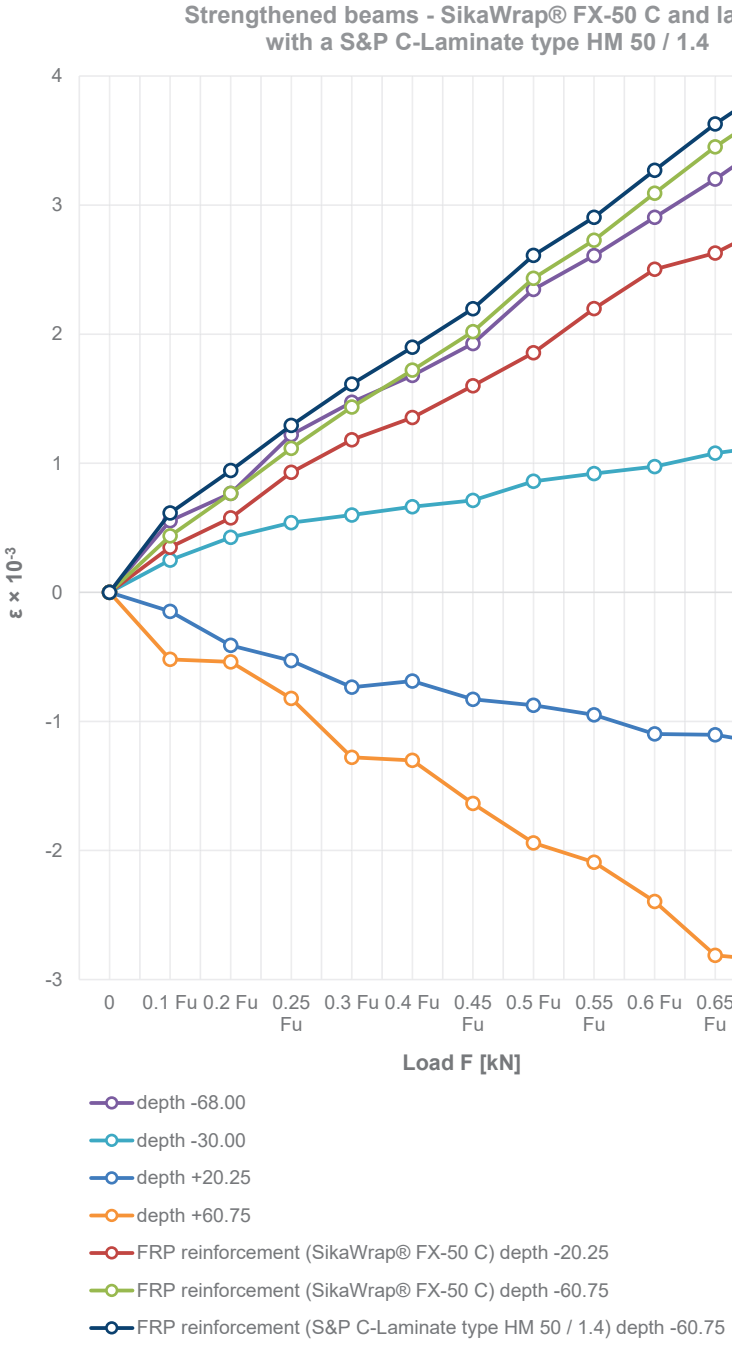

Figure 8. The distribution of deformation in timber beams and FRP materials at the section height.

For the group of beams reinforced with carbon cords or ropes and carbon laminates, the compressive strain was slightly lower than the tensile strain at the initial loading

stage. The strain distribution in the four-point bending of reinforced beam elements was initially characterised by elastic deformation of the laminated beams, followed by an initial elastic-plastic deformation, then elastic-plastic deformation. Subsequently, the deformation reached the elastic final tensile deformation in the tensile zone, improved by carbon reinforcement.

From the beginning of the load up to about 70 per cent of the failure load, the object–load–displacement curve was linear (Figure 3), which at the same time shows linear elastic characteristics. Thereafter, until the final load point was reached, the curve is non-linear. Thus, it can be seen that the laminated beam behaved plastically to a certain extent as the load increased. Subsequently, the beam underwent failure, in which the stiffness of the laminated beam increased continuously with the increasing load to the effect of reaching total failure. In contrast, once reinforcement was applied in the tension zone, the ductility of the sandwich glued beam was then fully exploited and failure occurred in the compression zone. In some beams, the failure occurred from vertical cracks in the middle zone. In addition, the remaining beams experienced wood fibre cracking longitudinally in the shear zone between the support and the point of force application. The failure in most of the unreinforced beams was related to longitudinal cracking as delamination of the wood grain, most commonly in the wood defects, was present. Three beams failed with no cracks, and no separation of the CFRP laminate. The failure was associated with longitudinal cracking as destruction between the support and the load application point, usually at the top of the section. On some beams, the longitudinal crack appeared in the lower part of the section. That is, it was related to shear. There was usually no peeling of the CFRP laminate from the glue or the glue from the timber. On the other hand, the beam behaved differently when it was subjected to rapid damage related to the peeling off of the CFRP laminate. The destruction occurred from the tearing of part of the timber member from the lower edge of the beam near the support; this was associated with shear cracks and carbon cords.

In this study, no CFRP reinforcement failed. The yield strength of the CFRP is higher than the yield strength of wood. It was observed in the study that complete failure occurred when the mid-span deflection was over 60.16 mm. This value is considered a high value, which provides good results from the point of view of ductility, as a result of which people have enough time to escape from the building before collapse. The study also concluded that there was a significant increase in ductility. It was noted that, even after the final collapse, the beams were still united. Therefore, there was no catastrophic failure when the beams were reinforced with CFRP. What is important, as a ductile material in design, is that it is possible to make ductile timber beams by adequate reinforcement of the tension zone, where it is possible to design reinforced timber beams up to yield strength, as is the case with steel structures.

4. Conclusions

On the basis of experimental tests carried out on glued laminated timber beams made of ash reinforced with Sika Wrap® FX-50 C carbon strings and S&P C-Laminate type HM 50/1.4 carbon laminates, it was concluded that:

(1) Research has shown that ashlar timber used for glulam beams has become an important and attractive alternative in today's construction industry. It can be seen that wood is now being used to supplement or even replace concrete structures in composite and hybrid systems. On the basis of the study, it was also noted that the FRP reinforcement technology used (SikaWrap® FX-50 C carbon cords or S&P C-Laminate type HM 50/1.4 carbon cords) for the reinforcement of ashlar timber elements is structurally very effective and can also complement concrete structures. It should be noted that wood beams reinforced with carbon fibre in the form of cords or laminates can be used both to repair existing structures and to build new ones. It should also be noted that carbon fibres as FRP materials also have a high deformation tolerance and a low coefficient of thermal expansion.

(2) In a four-point bending experimental study, the effect of carbon reinforcement on the properties of the wood material of laminated beams made of ash graded KS and KG was investigated. Compared to reference samples, it was found that reinforcement with carbon strings or carbon laminates increased the load capacity, bending strength and modulus of elasticity, and the magnitude of displacements of the timber materials, which is an excellent alternative to the use of ash and, above all, inferior grade materials due to the current shortage of choice grade.

(3) With reference to the experimental studies carried out regarding the four-point test of the effectiveness of the applied reinforcement in the form of cords or CFRP laminates in laminated reinforced beams, there was an average increase in the ultimate load of 30.51% and 39.36% for reinforcement ratios of 2.51% and 3.07%, respectively. With this performance of reinforced members, this allows for the use of lower height members, which can be an alternative for projects with architectural constraints.

(4) Based on the tests, it was found that laminated beams with an applied reinforcement ratio of 2.51% and 3.07% showed higher average displacements of 15.22% and 19.49%, respectively. In addition, it was noted that, at higher loads and higher displacements, the reinforced beams exhibited more ductile behaviour.

The results confirmed the analyses of experimental studies, which showed the effectiveness of the use of cords or carbon laminates in increasing the load-bearing capacity of beams, as well as ductility. In addition, load-displacement and strain diagrams are shown as part of the verification of the study, enabling a procedure for the dimensioning of components reinforced with cord and carbon laminates. However, further research is needed with different types of wood or reinforcement, as well as with different dimensions and loads.

Funding: The APC (Open Access) was funded by 02.0.12.00/1.02.001; SUBB.BKWM.22.001.

Institutional Review Board Statement: Not applicable.

Informed Consent Statement: Not applicable.

Data Availability Statement: Not applicable.

Acknowledgments: Sincere acknowledgements to Sika Poland Sp. z o.o. and S&P Polska Sp. z o.o. for the epoxy adhesives provided for the experimental tests.

Conflicts of Interest: The author declares no conflict of interest.

References

1. Kılınçarslan, Ş.; Şimşek Türker, Y. Ahşap Malzemelerin Islanabilirlik Özelliği Üzerine Isıl İşlem Uygulamasının Etkisi. *Mühendislik Bilimleri Ve Tasarım Derg.* **2020**, *8*, 460–466. [CrossRef]
2. Sahin, H.T.; Arslan, M.B.; Korkut, S.; Sahin, C. Colour Changes of Heat-Treated Woods of Red-Bud Maple, European Hophornbeam and Oak. *Color Res. Appl.* **2011**, *36*, 462–466. [CrossRef]
3. Sahin, C.K.; Onay, B. Alternatıve Wood Species for Playgrounds Wood from Fruit Trees. *Wood Research* **2020**, *65*, 149–160. [CrossRef]
4. Sahin, C.; Topay, M.; Var, A.A. A Study on Some Wood Species for Landscape Applications: Surface Color, Hardness and Roughness Changes at Outdoor Conditions. *Wood Res.* **2020**, *65*, 395–404. [CrossRef]
5. Şimşek Türker, Y. Strengthening of Wood Materials Using Composites. In Proceedings of the 7th International Conference on Computational and Experimental Science and Engineering (ICCESEN2020), Antalya, Turkey, 21–25 October 2020; pp. 244–249.
6. Kilinçarslan, Ş.; Türker, Y. Strengthening of Solid Beam with Fiber Reinforced Polymers. *Turk. J. Eng.* **2022**, *7*, 166–171. [CrossRef]
7. Fridley, K.J. Wood and Wood-Based Materials: Current Status and Future of a Structural Material. *J. Mater. Civ. Eng.* **2002**, *14*, 91–96. [CrossRef]
8. Foliente, G.C. Hysteresis Modeling of Wood Joints and Structural Systems. *J. Struct. Eng.* **1995**, *121*, 1013–1022. [CrossRef]
9. Saribiyik, M.; Akgül, T. GFRP Bar Element to Strengthen Timber Connection Systems. *Sci. Res. Essays* **2010**, *5*, 1713–1719.
10. Harrach, D.; Muayad, H.; Majid Movahedi, R. Reliability-based numerical analysis of glulam beams reinforced by CFRP plate. *Sci. Rep.* **2022**, *12*, 13587.
11. Ramage, M.H.; Burridge, H.; Busse-Wicher, M.; Fereday, G.; Reynolds, T.; Shah, D.U.; Wu, G.; Yu, L.; Fleming, P.; Densley-Tingley, D.; et al. The wood from the trees: The use of timber in construction. *Renew. Sustain. Energy Rev.* **2017**, *68*, 333–359. [CrossRef]

12. Van De Lindt, J.W.; Pei, S.; Pryor, S.E.; Shimizu, H.; Isoda, H. Experimental Seismic Response of a Full-Scale Six-Story Light-Frame Wood Building. *J. Struct. Eng.* **2010**, *136*, 1262–1272. [CrossRef]
13. Ceccotti, A.; Sandhaas, C.; Okabe, M.; Yasumura, M.; Minowa, C.; Kawai, N. SOFIE project—3D shaking table test on a seven-storey full-scale cross-laminated timber building. *Earthq. Eng. Struct. Dyn.* **2013**, *42*, 2003–2021. [CrossRef]
14. Herzog, T.; Natterer, J.; Schweitzer, R.; Volz, M.; Winter, W. *Timber Construction Manual*; Walter de Gruyter: Basel, Switzerland, 2012. [CrossRef]
15. Monahan, J.; Powell, J. An embodied carbon and energy analysis of modern methods of construction in housing: A case study using a lifecycle assessment framework. *Energy Build.* **2011**, *43*, 179–188. [CrossRef]
16. Yadav, R.; Kumar, J. Engineered wood products as a sustainable construction material: A review. *Eng. Wood Prod. Constr.* **2021**. [CrossRef]
17. Dietsch, P.; Tannert, T. Assessing the integrity of glued-laminated timber elements. *Constr. Build. Mater.* **2015**, *101*, 1259–1270. [CrossRef]
18. Frangi, A.; Fontana, M.; Mischler, A. Shear behaviour of bond lines in glued laminated timber beams at high temperatures. *Wood Sci. Technol.* **2004**, *38*, 119–126. [CrossRef]
19. Falk, R.H.; Colling, F. Laminating Effects in Glued-Laminated Timber Beams. *J. Struct. Eng.* **1995**, *121*, 1857–1863. [CrossRef]
20. Anshari, B.; Guan, Z.; Kitamori, A.; Jung, K.; Komatsu, K. Structural behaviour of glued laminated timber beams pre-stressed by compressed wood. *Constr. Build. Mater.* **2012**, *29*, 24–32. [CrossRef]
21. Bourreau, D.; Aimene, Y.; Beauchêne, J.; Thibaut, B. Feasibility of glued laminated timber beams with tropical hardwoods. *Eur. J. Wood Wood Prod.* **2013**, *71*, 653–662. [CrossRef]
22. Navaratnam, S.; Thamboo, J.; Ponnampalam, T.; Venkatesan, S.; Chong, K.B. Mechanical performance of glued-in rod glulam beam to column moment connection: An experimental study. *J. Build. Eng.* **2022**, *50*, 104131. [CrossRef]
23. Issa, C.A.; Kmeid, Z. Advanced wood engineering: Glulam beams. *Constr. Build. Mater.* **2005**, *19*, 99–106. [CrossRef]
24. Rescalvo, F.J.; Timbolmas, C.; Bravo, R.; Valverde-Palacios, I.; Gallego, A. Improving ductility and bending features of poplar glued laminated beams by means of embedded carbon material. *Constr. Build. Mater.* **2021**, *304*, 124469. [CrossRef]
25. Morin-Bernard, A.; Blanchet, P.; Dagenais, C.; Achim, A. Glued-laminated timber from northern hardwoods: Effect of finger-joint profile on lamellae tensile strength. *Constr. Build. Mater.* **2020**, *271*, 121591. [CrossRef]
26. Wdowiak, A.; Brol, J. Effectiveness of Reinforcing Bent Non-Uniform Pre-Stressed Glulam Beams with Basalt Fibre Reinforced Polymers Rods. *Materials* **2019**, *12*, 3141. [CrossRef]
27. Brol, J.; Wdowiak-Postulak, A. Old Timber Reinforcement with FRPs. *Materials* **2019**, *12*, 4197. [CrossRef]
28. Brol, J.; Wdowiak, A. *The Use of Glass and Aramid Fibres for the Strengthening of Timber Structures*; Annals of Warsaw University of Life Sciences, Forestry and Wood Technology: Warsaw, Poland, 2017; pp. 128–138.
29. Brol, J.; Nowak, T.; Wdowiak, A. *Numerical Analysis and Modelling of Timber Elements Strengthened with FRP Materials*; Annals of Warsaw University of Life Sciences, Forestry and Wood Technology: Warsaw, Poland, 2018; pp. 274–282.
30. Wdowiak, A. Analysis of bent timber beam reinforcement with the application of composite materials. *Struct. Environ.* **2016**, *8*, 10–16.
31. Wdowiak, A. Właściwości Strukturalno—Wytrzymałościowe Zginanych Belek Drewnianych Wzmocnionych Kompozytami Włóknistymi [Structural and Strength Properties of Bent Wooden Beams Reinforced with Fibre Composites]. Ph.D. Thesis, Kielce University of Technology, Kielce, Poland, 12 April 2019.
32. Wdowiak, A.; Kroner, A. Wpływ niejednorodności struktury zginanych belek z drewna klejonego na efekt ich wzmocnienia. *Mater. Bud.* **2017**, *1*, 87–89. [CrossRef]
33. Wdowiak, A.; Brol, J. Methods of strength grading of structural timber—Comparative analysis of visual and machine grad-ing on the example of Scots pine timber from four natural forest regions of Poland. *Struct. Environ.* **2019**, *11*, 210–224. [CrossRef]
34. Wdowiak-Postulak, A.; Świt, G. Behavior of Glulam Beams Strengthened in bending with BFRP Fabrics. *Civ. Environ. Eng. Rep.* **2021**, *31*, 1–14. [CrossRef]
35. Kamionka, L.; Wdowiak-Postulak, A.; Hajdenrajch, A. Nowoczesne budownictwo drewniane w technologii CLT na przykładzie budynku Bioklimatycznej Jednostki Modularnej. *Mater. Bud.* **2022**, 49–51. [CrossRef]
36. Wdowiak-Postulak, A. Basalt Fibre Reinforcement of Bent Heterogeneous Glued Laminated Beams. *Materials* **2020**, *14*, 51. [CrossRef]
37. Wdowiak-Postulak, A. Natural Fibre as Reinforcement for Vintage Wood. *Materials* **2020**, *13*, 4799. [CrossRef] [PubMed]
38. Wdowiak-Postulak, A.; Brol, J. Ductility of the Tensile Zone in Bent Wooden Beams Strengthened with CFRP Materials. *Materials* **2020**, *13*, 5451. [CrossRef]
39. Wdowiak-Postulak, A. Ductility, load capacity and bending stiffness of Scandinavian pine beams from waste timber strengthened with jute fibres. *Drewno* **2022**, *65*. [CrossRef]
40. Xian, G.; Guo, R.; Li, C.; Wang, Y. Mechanical performance evolution and life prediction of prestressed CFRP plate exposed to hygrothermal and freeze-thaw environments. *Compos. Struct.* **2022**, *293*, 115719. [CrossRef]
41. Fossetti, M.; Minafò, G.; Papia, M. Flexural behaviour of glulam timber beams reinforced with FRP cords. *Constr. Build. Mater.* **2015**, *95*, 54–64. [CrossRef]
42. Nadir, Y.; Nagarajan, P.; Ameen, M.; Muhammed, M.A. Flexural stiffness and strength enhancement of horizontally glued laminated wood beams with GFRP and CFRP composite sheets. *Constr. Build. Mater.* **2016**, *112*, 547–555. [CrossRef]

43. *PN-EN 338:2016-06*; Structural Timber—Strength Classes. Polish Committee for Standardization: Warsaw, Poland, 2016.
44. Product Information Sheet Sika Poland Sp. z o.o. Available online: https://pol.sika.com/content/dam/dms/plcon/8/sikawrap_fx-50_c.pdf (accessed on 15 October 2022).
45. Product Information Sheet Sika Poland Sp. z o.o. Available online: https://pol.sika.com/content/dam/dms/plcon/e/sikadur_-330.pdf (accessed on 15 June 2021).
46. Carbon Fibre Composite Tapes Embedded in a Matrix of Epoxy Resin - S&P Poland Sp. z o.o. Available online: https://www.sp-reinforcement.pl/sites/default/files/field_product_col_doc_file/c-laminates_polska_ver012019-low.pdf (accessed on 15 January 2019).
47. Two-Component Adhesive for FRP Mats on an Epoxy Resin Basis - S&P Poland Sp. z o.o. Available online: https://www.sp-reinforcement.pl/sites/default/files/field_product_col_doc_file/resin55_hp_polska_ver20190326_web.pdf (accessed on 15 March 2019).
48. *PN-D-94021:2013-10*; Softwood Structural Sawn Timber Sorted Using Strength Methods. Polish Committee for Standardization: Warsaw, Poland, 2013.
49. *PN-EN 408+A1:2012*; Timber Structures—Structural Timber and Glued Laminated Timber—Determination of Some Physical and Mechanical Properties. Polish Committee for Standardization: Warsaw, Poland, 2012.
50. *PN-EN 1995-1-1:2010 Eurocode 5*; Design of Timber Structures. Part 1-1: General. Common Rules and Rules for Buildings. Polish Standards Committee: Warsaw, Poland, 2010.

materials

MDPI

Article

Experimental and Finite Element Study on Bending Performance of Glulam-Concrete Composite Beam Reinforced with Timber Board

Hao Du [1,*], Shengnan Yuan [1], Peiyang Liu [1], Xiamin Hu [2] and Guohui Han [2]

[1] College of Civil Engineering, Nanjing Forestry University, Nanjing 210037, China
[2] College of Civil Engineering, Nanjing Tech University, Nanjing 211816, China
* Correspondence: duhaodc@163.com

Abstract: In this research, experimental research and finite element modelling of glulam-concrete composite (GCC) beams were undertaken to study the flexural properties of composite beams containing timber board interlayers. The experimental results demonstrated that the failure mechanism of the GCC beam was the combination of bend and tensile failure of the glulam beam. The three-dimensional non linear finite element model was confirmed by comparing the load-deflection curve and load-interface slip curve with the experimental results. Parametric analyses were completed to explore the impacts of the glulam beam height, shear connector spacing, timber board interlayer thickness and concrete slab thickness on the flexural properties of composite beams. The numerical outcomes revealed that with an increase of glulam beam height, the bending bearing capacity and flexural stiffness of the composite beams were significantly improved. The timber boards were placed on top of the glulam members and used as the formwork for concrete slab casting. In addition, the flexural properties of composite beams were improved with the increase of the timber board thickness. With the elevation of the shear connector spacing, the ultimate bearing capacity and bending stiffness of composite beams were decreased. The bending bearing capacity and flexural rigidity of the GCC beams were ameliorated with the increase of concrete slab thickness.

Keywords: glulam-concrete composite beam; timber board interlayer; bending performance; finite element model; parametric study

Citation: Du, H.; Yuan, S.; Liu, P.; Hu, X.; Han, G. Experimental and Finite Element Study on Bending Performance of Glulam-Concrete Composite Beam Reinforced with Timber Board. *Materials* **2022**, *15*, 7998. https://doi.org/10.3390/ma15227998

Academic Editors: Radosław Mirski and Dorota Dukarska

Received: 8 October 2022
Accepted: 9 November 2022
Published: 12 November 2022

1. Introduction

The glulam-concrete composite (GCC) beam is a novel structural element in which the glulam member and the concrete slab fit together through shear connections. Due to the sufficient composite effect provided by shear connections, the material properties of the glulam and concrete are better utilized, as tensile forces from bending are primarily resisted by the glulam and compressive forces are resisted by the concrete [1,2]. The GCC beam exhibits better bending, bearing capacity and flexural rigidity than the pure glulam beam, and displays greater acoustic insulation, better vibration comfort, and superior fire protection ability [3–5]. Over the past ten years, the GCC beam has been extensively utilized to reinforce and strengthen timber slabs in existent and newly-built multistory buildings. In different practical uses of GCC beam, especially in the restoration of timber architectures, the timber boards are placed on top of glulam members and can be used as the formwork for concrete slab casting [6].

Up to now, substantial experimental studies on the structural behaviors of GCC beams have been published [7–10]. Clouston et al. [11] performed bend tests on GCC beams with steel toothed plate connectors. It was verified that composite beams exhibited excellent mechanical properties. Persaud et al. [12] conducted experimental studies on the flexural properties of GCC beams with screw connectors. The outcomes revealed that the flexural bearing capacity and rigidity of GCC beams were significantly higher than

those of pure glulam beams. Khorsandnia et al. [13] completed experimental research on the short-term behavior of GCC beams with different forms of shear connectors (lag screws, SFS and triangular notched connectors). Through nonlinear regression, analytical models were established for investigating the load-slip behavior of the three types of connections. Schanack et al. [14] found that during the stress process of GCC beams with screw connectors, the cracking of concrete slabs reduced the stiffness of concrete, which resulted in the increase of the deflection deformation and section stress of composite beams. Hong et al. [15] conducted bending tests to investigate the effects of shear connection ratio and concrete type on the bending performance of GCC beam. The outcomes revealed that the failure modes of the GCC beam were tensile brittle failure and finger joint failure of the glulam beams. Giv et al. [16] used adhesive to connect the concrete slab and glulam beam, and carried out experimental research and theoretical analysis pertaining to the shear bonding performance of the adhesive and the flexural performance of the composite beams. Du et al. [17] conducted experimental research on the fire behavior of GCC beams with timber board to study the effects of the timber board thickness and load ratio, and established the mechanical model for analyzing the flexural bearing capacity and rigidity of GCC beams in the presence of fire.

There are multiple numerical research and theoretical analyses regarding the structural behavior of GCC beams. The existent finite element (FE) models for GCC beams can be separated into 1D, 2D, and 3D. Lukaszewska et al. [8] established one-dimensional FE models of timber-GCC floors. The glulam beam and concrete slab were emulated as two parallel beams, and the shear connectors were simulated by discrete nonlinear spring elements. The shear lag effects on the concrete slab were ignored, which might induce computational outcome overestimation when the broad slab was utilized. Crocetti et al. [18] developed two-dimensional FE models for timber-concrete composite beams produced via simulating the concrete slab with multi-layer shell elements and emulating the timber beam by beam elements. The discrete steel reinforcement bars were assumed as the steel layers with the identical section area, and the interface connections were defined by the non-linear springs. Thereby, the shear lag effects on concrete slabs and the impairment plasticity behaviors of concrete were covered by the model. The research conducted by Monteiro et al. [19] proved that two-dimensional FE models exhibited remarkable accuracy based on the test outcomes, particularly for composite beams with comparatively larger slab widths. Nevertheless, given that timber was a kind of orthotropic material, neglecting the effect from weak orientations could cause the slight overestimation of the bending performances of the GCC beam. To thoroughly reveal the influence of material performance and the interplay between the members, solid elements with the specific definitions of the stress-strain and contact associations were used in three-dimensional FE models. The studies validated that three-dimensional FE models could precisely describe the load-deflection, stress distributional status, and slip behavior of timber-concrete composite beams [20–22].

Up to now, few researches on the structural performance of GCC beams containing timber board interlayers have been completed. Here, the experimental research on glulam-concrete composite beams was undertaken to study the flexural properties of composite beams containing timber board interlayer. Then, the three-dimensional non-linear finite element model was developed and confirmed by comparing the load-deflection curve and load-interface slip curve with the experimental results. Based on the finite element studies, the influences of the glulam beam height, shear connector spacing, timber board interlayer thickness and concrete slab thickness on the flexural properties of composite beams were investigated.

2. Bending Tests

2.1. Composite Beam Sample

One full-scale GCC beam with inclined fasteners was constructed and loaded by the four-point bending approach. In the composite beam sample, the glulam beam was connected to the concrete slab using shear connectors (Figure 1). The glulam beam was

150 mm wide, 300 mm high and 3900 mm long. The concrete slab was 80 mm thick and 800 mm wide. The concrete slab was enhanced with steel meshes utilizing 8 mm reinforcement bars with a spacing of 150 mm in two orientations. A timber board was placed on the top of the glulam beam and utilized as formwork for concrete slab casting. The inclined screw exhibited higher shear bearing capacity and slip modulus than that of screws inserted vertically. Thus, an overall 19 horizontal cross-wise pairs of inclined screw fasteners were used for connecting. The embedment lengths into concrete and timber of the screw connectors were 70 and 100 mm, respectively. The glulam beam comprised evenly glued laminated larch timber. The mean density of the timber was 0.526 g/cm^3, and the mean water content was 12.8%. The compressive elasticity modulus and compressive strength of the lumber were obtained through material tests according to ISO 3787 [23]. The average compressive elastic modulus was 11,580 N/mm^2, the compressive strength parallel to the timber grain was 39.6 N/mm^2, and the tensile strength parallel to the timber grain was 84.89 N/mm^2. The mean compressive strength of the concrete was 35.8 N/mm^2.

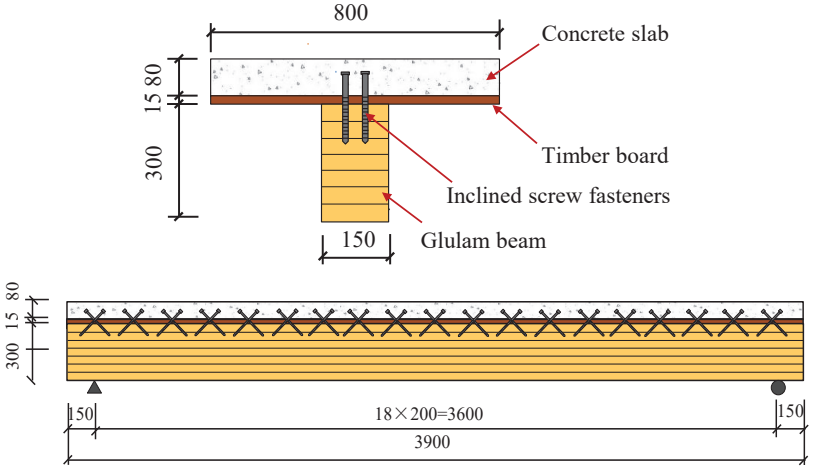

Figure 1. Dimensions of composite beam specimen GCCB.

The four-point bending loads were applied to the beam specimen using a 300 kN hydraulic jack. Firstly, the applied loads were applied at a rate of 0.2 kN/s to 10% of the anticipated ultimate load, and then the loads were released to verify the efficiency of the bending test setup and measurement equipment. After that, the load increased at a rate of 0.2 kN/s until it reached the ultimate load. For obtaining the relative slips between the concrete slab and the glulam beam, two displacement meters were mounted at the end of the GCC specimen.

2.2. Test Results

At the beginning of loading period, there was no observable relative slip because of the strong bonding effect at the interfacial region. With an increased level of the applied load, a small relative slip was identified. For the composite beam sample, when the applied load was elevated to approximately 85% of the ultimate load, cone expulsion failure happened on the concrete layer around inclined screw fasteners (Figure 2a). The total collapse happened on the testing sample because of the combination of bend and tensile failure in the glulam beam (Figure 2b). Figure 3a displays the association between the loads and mid-span deflections acquired from the bend test. The design of the glulam-concrete beam is usually controlled by deflection. The corresponding mid-span deflection under serviceability limit state Δ_{SLS} was based on GB 50,005 [24], $\Delta_{SLS} = l/250$. At the beginning of loading, the GCC beam displayed linear elasticity behavior. When the load was elevated to about 60%

of the maximum load, the applied loads presented an analogous parabolic increase with the elevation of the mid-span deflections. The flexural stiffness of GCC beam was lower, and diminished continuously. When it attained the maximal load, with the elevation of deflections, the loads decreased remarkably because of the brittle failure of the glulam beam. Figure 3b presents the association between the loads and interface slips at the end of the GCC beam. With the bending loading elevated, the relative slips at the at the interfacial region increased because of the bending deformation of screw fasteners under longitudinal shearing force.

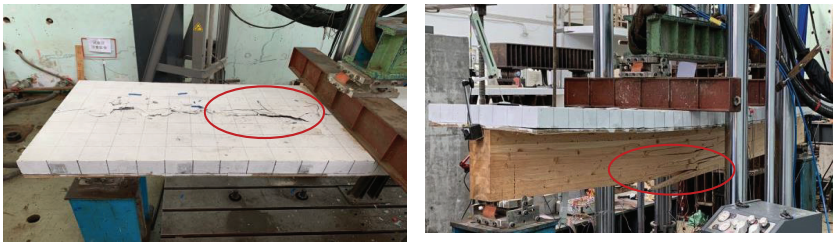

(**a**) (**b**)

Figure 2. Failure mode of composite beam specimen. (**a**) Cone failure of concrete slab, (**b**) Tensile failure of glulam beam.

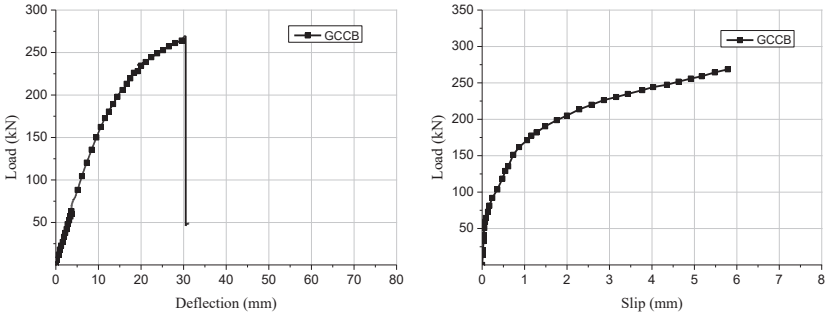

(**a**) (**b**)

Figure 3. Test results of composite beam specimen. (**a**) Load-deflection curve, (**b**) Load-slip curve.

3. Finite Element Model

3.1. Constitutive Model of Materials

To sufficiently consider the effect of the failure mechanisms on the flexural behavior of GCC beams containing interlayers, three-dimensional (3D) FE models were established by the commercially available FE software ABAQUS. In the FE models, the damage plasticity model was utilized to realize the modeling of the physical performances of concrete. The concrete damage elicited by cracking or crushing causes a decrease in the elasticity modulus of the concrete. The tensile behavior of concrete was hypothesized to be linear up to the uniaxial tensile strength equal to $f_t = f'_c/10$. According to Eurocode 2 [25], the compression uniaxial stress-strain association for concrete can be identified by the formula below:

$$\frac{\sigma_c}{f_{cm}} = \frac{k\eta - \eta^2}{1 + (k-2)\eta} \quad (1)$$

where: $\eta = \varepsilon_c/\varepsilon_{c1}$; ε_{c1} = the strain at peak stress; $k = 1.05E_{cm} \times |\varepsilon_{c1}|/f_{cm}$; E_{cm} = elasticity modulus of concrete; f_{cm} = cylinder compression strength of concrete.

The timber was simulated as an orthotropic material. It was hypothesized that both rigidity and intensity in the radial or tangential orientations were identical. The association between elasticity modulus in the grain and cross grain orientation as well as the association between elastic modulus and shearing modulus are specified in standard EN 338 [26]. The orthotropic yield standard put forward by Hill [27] was utilized to realize the definition of glulam, which has been evidenced to have precise delineation of timber performances [28].

The steel material properties of screw fasteners were defined as isotropic elastic-plastic constitutive. The yield strength and ultimate tensile strength of screw fasteners were 375 MPa and 462 MPa, which were measured from material tests.

3.2. Element Type and Interface Simulation

The composite beam specimen was mainly composed of the concrete slab, glulam beam, screw fasteners and steel bars. The screw section cutting of the threaded section was considered in the screw modeling. The net section diameter was used for the screw modeling. The 8-node solid linear elements with reduced integration C3D8R were utilized to model the concrete slab, glulam beam and screw fasteners. The T3D2 truss element was utilized to simulate the steel reinforcement in the concrete slab. The global size of the element meshed in the connection model was 10 mm, and for the beam model, the relevant size was 100 mm. The interplay between the steel bars and concrete were analyzed through the "Embedded region" option. The longitudinal spacing and transverse spacing of screw fasteners were 200 mm and 50 mm, respectively. Both tangential and normal contact behaviours were identified in the FE model to simulate interaction among screw fasteners, concrete slab and glulam beam. The option "Hard Contact" was selected to identify the normal contact behaviours, and "Penalty" was chosen for identifying tangential behaviourd through postulating the timber-concrete frictional coefficient of 0.7. The model diagram of the GCC beam after defining boundary and load conditions is shown in Figure 4.

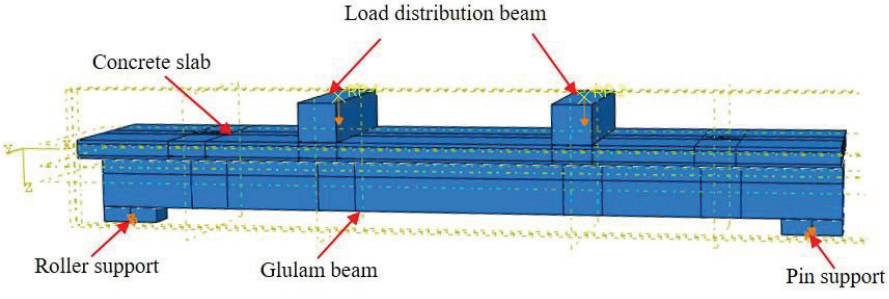

Figure 4. Model diagram of GCC beam after defining boundary and load conditions.

3.3. Validation and Discussion

Figure 4 displays the stress distributional status of the GCC beam at the maximal load. When the composite beam model reached the limit state, the midspan bottom of the glulam beam achieved the ultimate tensile stress (Figure 5a). In addition, the maximum principal stress distribution of the concrete slab indicated that the cone expulsion failure occurred at the inclined screw fasteners (Figure 5b). The outcomes revealed that the numerical simulation could precisely predict the failure mode and the change characteristics of the composite beam in the loading process. Figure 6 presents the numerical simulation results of the load-deflection relationship and load-interface slip curve for the GCC beam. As shown in Figure 5, the developed finite element model adequately predicted the load-deflection relationship and load-interface slip curve, particularly in the elasticity range. With the elevation of the applied load, the cracks appeared on the weak surface of the

glulam member under the combination of bending and shear effects, which resulted in reduction of the stiffness and load carrying capacity. The maximal bearing capacity of the composite beam forecasted by the finite element modelling was a little lower than the testing outcomes. The main reason was the simplified constitutive law of timber utilized in the finite element modelling. At the beginning of loading, the slip displacement was small because of the strong bonding effect at the concrete-timber interfacial region. When the loading was elevated to approximately 28% of the maximum load, with the applied loads increased, the attenuated composite actions at the interfacial region led to a rapid increase of the interface slips.

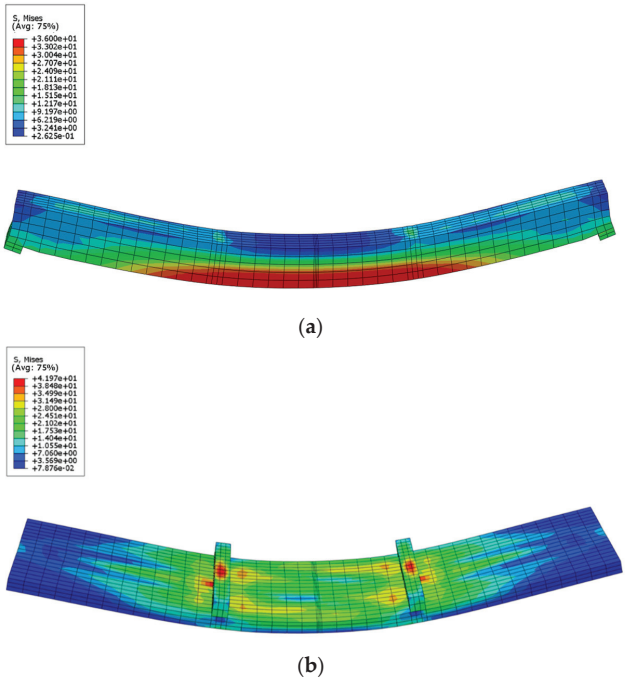

Figure 5. Stress distributions of GCC beam at maximum load. (**a**) Glulam beam, (**b**) Concrete slab.

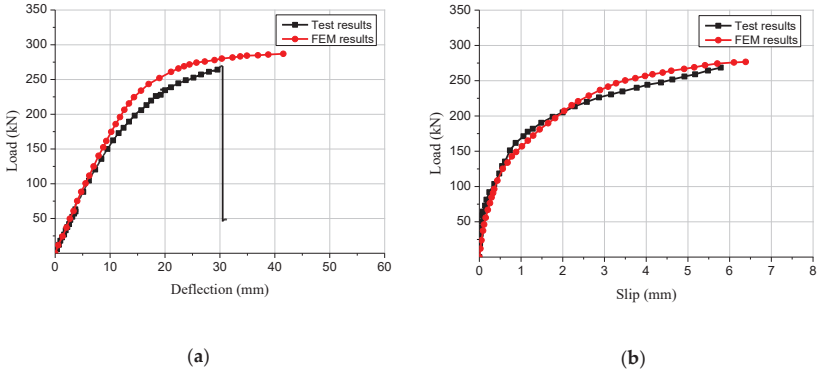

Figure 6. Comparison between the test and finite element results. (**a**) Load-deflection curve, (**b**) Load-slip curve.

4. Parametric Study

4.1. Section Height of Glulam Beam

To reveal the impact of the glulam beam section size on the flexural performance of composite beams, different sizes of the glulam beams (150 mm × 300 mm, 150 mm × 200 mm, 150 mm × 100 mm and 150 mm × 400 mm) were simulated. The numerical simulation results of the composite beam with different glulam beam section size are presented in Figure 7. When the section height of the glulam beam increased from 300 mm to 400 mm, the elastic bending capacity of the GCC beams increased by 51.4% and the ultimate bearing capacity increased by 59.4%. When the section height decreased from 300 mm to 200 mm, the elastic bearing capacity was reduced by 42.9% and the maximal load carrying capacity was reduced by 38.2%. The comparison results showed that the section height of the glulam beam could significantly affect the flexural bearing capacity. Through the analysis of the load-deflection curves, it was found that the flexural rigidity of the composite beam was improved with the increase of the glulam beam section height. In addition, the increasing section height of the glulam beam could significantly ameliorate the deformation-resistance capability of GCC beam.

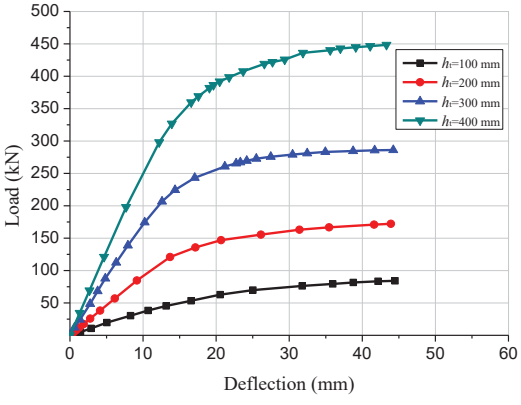

Figure 7. Comparison of load-deflection curves of composite beams with different beam heights.

4.2. Screw Connector Spacing

The shear connections play an important role in GCC beams through transferring shear forces among the glulam and concrete members and preventing detachment mechanisms. Four finite element models of the GCC beams with 100, 200, 300 and 400 mm spacing of inclined screw fasteners were simulated and analyzed to research the influence of shear connector ratio on the flexural properties. The load-deflection curves of GCC beams with different shear connector spacings are displayed by Figure 8. The numerical results revealed that the ultimate bending bearing capacity of the GCC beams with 100, 200 and 300 mm spacing of screw connectors increased by 13.5%, 7.6% and 4.0%, respectively, compared to that of the composite beam with 400 mm spacing of screw connectors. In addition, the flexural stiffness of the GCC beams was improved by 6.3%, 20.0% and 33.6%, respectively, compared to that of the composite beam with 400 mm spacing of screw connectors. Thus, the bending bearing capacity and flexural stiffness of the composite beams decreased with the increase of the screw fasteners spacing, which was mainly due to the decrease of the composite action between the glulam beam and the concrete slab.

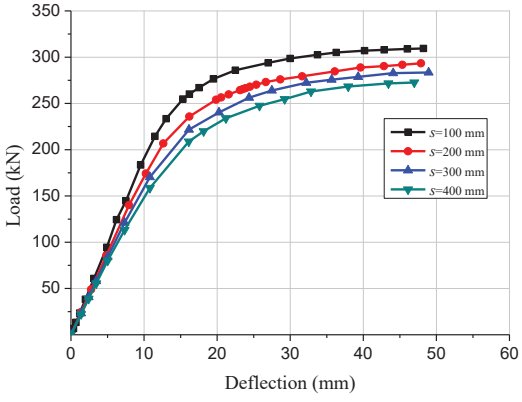

Figure 8. Comparison of load-deflection curves of composite beams with different screw connector spacing.

4.3. Thickness of Timber Board

Timber boards may be utilized as the permanent formwork for concrete casting. This can not only create convenience for the construction, but also keep the integral beauty of the timber structures. Five finite element models of GCC beams with various timber board thicknesses were established to study the impacts of timber board thickness on the structural properties. The load-deflection curves of the GCC beams are presented in Figure 9. The numerical simulation outcomes revealed that when the timber board thickness increased from 0 mm to 10 mm, the flexural stiffness and ultimate bending bearing capacity of the composite beams displayed no obvious difference, which indicated that the presence of the timber board had no significant effect on the mechanical performance of GCC beam. The maximal bending bearing capacity of the GCC beams with 15, 20 and 30 mm timber board thickness was improved by 3.2%, 7.5% and 10.8%, respectively, compared to that of the composite beam with 10 mm timber board thickness. It was discovered that the bending bearing capacity and flexural stiffness of the composite beams was enhanced with the elevation of the timber board thickness.

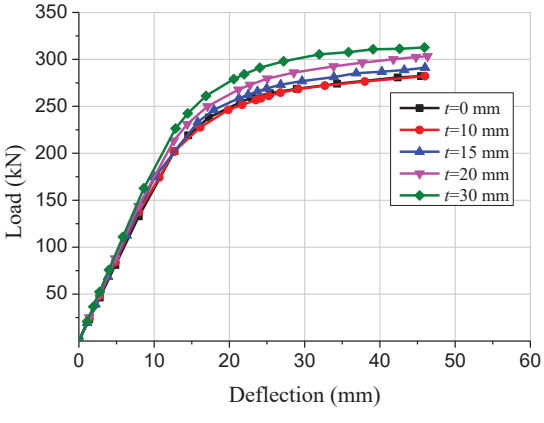

Figure 9. Comparison of load-deflection curves of composite beams with different timbe board thicknesses.

4.4. Thickness of Concrete Slab

Five finite element models of GCC beams with various concrete slab thicknesses were established to study the impact of concrete slab thickness on the mechanical properties.

The load-deflection curves of the GCC beams with 60, 70, 80, 90 and 100 mm concrete slab thickness are displayed in Figure 10. The numerical simulation outcomes revealed that the ultimate bending bearing capacity of the GCC beams with 70, 80, 90 and 100 mm concrete slab thickness increased by 6.4%, 7.6% and 4.0%, respectively, compared to that of the composite beam with 60 mm concrete slab thickness. In addition, the flexural stiffness of the GCC beams was increased by 6.2%, 12.7%, 19.2% and 26.1%, respectively, compared to that of the composite beam with 60 mm concrete slab thickness. The numerical results indicated that the bending bearing capacity and flexural rigidity of the composite beams were enhanced with the increase of concrete slab thickness.

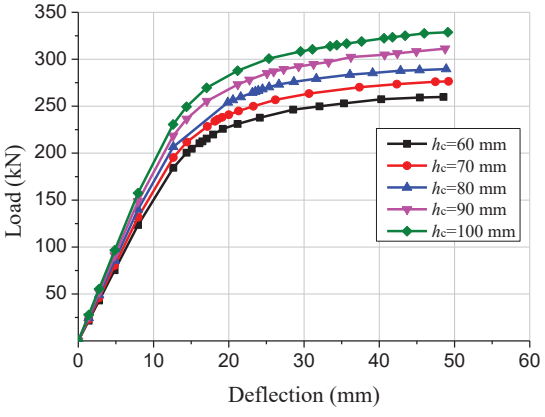

Figure 10. Comparison of load-deflection curves of composite beams with different concrete slab thicknesses.

5. Conclusions

To study the flexural performance of GCC beam containing interlayer, experimental research and finite element modelling of the composite beam were conducted. The finite element studies were performed to investigate the impacts of the glulam beam height, shear connector spacing, timber board thickness and concrete slab thickness on the structural properties of GCC beam.

(1) The experimental results demonstrated that the failure mechanism of the GCC beam was the combination of bend and tensile failure in the glulam beam. At the beginning of loading, the slip displacement was small because of the strong bonding effect at the concrete-timber interfacial region. When the loading was elevated to approximately 28% of the maximum load, with the applied loads increased, the attenuated composite actions at the interfacial region led to a rapid increase of the interface slips.

(2) The finite element results showed that the numerical simulation could precisely predict the failure mode and the change characteristics of the composite beam in the loading process. The developed finite element model adequately predicted the load-deflection relationship and load-interface slip curve, particularly in the elasticity range. For the elastic-plastic stage, the predicted deflection of the GCC beam deviated from the test results due to the nonlinear bending performance. The elastic-plastic damage constitutive model of glulam needs to be optimized.

(3) The parametric study results showed that with increase of the glulam beam height, the bending bearing capacity and flexural stiffness of the GCC beam were significantly improved. With the shear connectors spacing increased, the ultimate bearing capacity and bending stiffness of the composite beam were decreased. The existence of timber board had no significant effect on the flexural performance of the composite beams. The bending bearing capacity and flexural stiffness of the composite beams were enhanced with the increase of the concrete slab thickness.

Author Contributions: Conceptualization, H.D. and S.Y.; methodology, H.D.; software, H.D.; validation, H.D., S.Y. and P.L.; formal analysis, G.H.; investigation, H.D.; resources, X.H.; data curation, S.Y.; writing—original draft preparation, H.D.; writing—review and editing, H.D.; visualization, S.Y.; supervision, X.H.; project administration, H.D.; funding acquisition, H.D. All authors have read and agreed to the published version of the manuscript.

Funding: The research was funded by National Natural Science Foundation of China (52208257) and Natural Science Foundation of Colleges and Universities of Jiangsu Province (22KJB560023).

Institutional Review Board Statement: Not applicable.

Informed Consent Statement: Not applicable.

Data Availability Statement: Not applicable.

Conflicts of Interest: The authors declare no conflict of interest.

References

1. Ceccotti, A. Composite concrete-timber structures. *Prog. Struct. Eng. Mater.* **2002**, *4*, 264–275. [CrossRef]
2. Yeoh, D.; Fragiacomo, M.; Franceschi, M.D.; Boon, K.H. State of the art on timber-concrete composite structures: Literature review. *J. Struct. Eng.* **2011**, *137*, 1085–1095. [CrossRef]
3. Du, H.; Hu, X.; Xie, Z.; Wang, H.C. Study on shear behavior of inclined cross lag screws for glulam-concrete composite beams. *Constr. Build. Mater.* **2019**, *224*, 132–143. [CrossRef]
4. Du, H.; Hu, X.; Sun, Z.; Meng, Y.; Han, G. Load carrying capacity of inclined crossing screws in glulam-concrete composite beams with interlayer. *Compos. Struct.* **2020**, *245*, 112333. [CrossRef]
5. Xie, Z.; Hu, X.; Du, H.; Zhang, X. Vibration behavior of timber-concrete composite floors under human-induced excitation. *J. Build. Eng.* **2020**, *32*, 101744. [CrossRef]
6. Jorge, L.F.C.; Lopes, S.M.R.; Cruz, H.M.P. Interlayer influence on timber-LWAC composite structures with screw connections. *J. Struct. Eng.* **2011**, *137*, 618–624. [CrossRef]
7. Gutkowski, R.; Brown, K.; Shigidi, A.; Natterer, J. Laboratory tests of composite wood-concrete beams. *Constr. Build. Mater.* **2008**, *22*, 1059–1066. [CrossRef]
8. Lukaszewska, E.; Fragiacomo, M.; Johnsson, H. Laboratory tests and numerical analyses of prefabricated timber-concrete composite floors. *J. Struct. Eng.* **2010**, *136*, 46–55. [CrossRef]
9. Wang, Z.; Wei, Y.; Li, N.; Zhao, K.; Ding, M. Flexural behavior of bamboo-concrete composite beams with perforated steel plate connections. *J. Wood Sci.* **2020**, *66*, 1–20. [CrossRef]
10. Chen, S.; Wei, Y.; Ding, M.; Zhao, K.; Zheng, K. Combinatorial design and flexural behavior of laminated bamboo-timber composite beams. *Thin-Walled Struct.* **2022**, *181*, 109993. [CrossRef]
11. Clouston, P.; Bathon, L.; Schreyer, A. Shear and bending performance of a novel wood-concrete composite system. *J. Struct. Eng.* **2005**, *131*, 1404–1412. [CrossRef]
12. Persaud, R.; Symons, D. Design and testing of a composite timber and concrete floor system. *Struct. Eng.* **2005**, *84*, 22–36.
13. Khorsandnia, N.; Valipour, H.R.; Crews, K. Experimental and analytical investigation of short-term behaviour of LVL-concrete composite connections and beams. *Constr. Build. Mater.* **2012**, *37*, 229–238. [CrossRef]
14. Schanack, F.; Ramos, Ó.R.; Reyes, J.P.; Low, A.A. Experimental study on the influence of concrete cracking on timber concrete composite beams. *Eng. Struc.* **2015**, *84*, 362–367. [CrossRef]
15. Hong, W.; Jiang, Y.; Fang, Y.; Hu, X. Experimental study and theoretical analysis of glulam-concrete composite beams connected with ductile shear connectors. *Adv. Struct. Eng.* **2019**, *23*, 1168–1178. [CrossRef]
16. Giv, A.N.; Fu, Q.; Yan, L.; Kasal, B. Interfacial bond strength of epoxy and PUR adhesively bonded timber-concrete composite joints manufactured in dry and wet processes. *Constr. Build. Mater.* **2021**, *311*, 125356.
17. Du, H.; Hu, X.; Xie, Z.; Meng, Y. Experimental and analytical investigation on fire resistance of glulam-concrete composite beams. *J. Build. Eng.* **2021**, *44*, 103244. [CrossRef]
18. Crocetti, R.; Sartori, T.; Tomasi, R. Innovative timber-concrete composite structures with prefabricated FRC slabs. *J. Struct. Eng.* **2015**, *141*, 04014224. [CrossRef]
19. Monteiro, S.R.S.; Dias, A.; Lopes, S.M.R. Bi-dimensional numerical modeling of timber–concrete slab-type structures. *Mater. Struct.* **2015**, *48*, 3391–3406. [CrossRef]
20. Fragiacomo, M.; Balogh, J.; To, L.; Gutkowski, R.M. Three-dimensional modeling of long-term structural behavior of wood-concrete composite beams. *J. Struct. Eng.* **2014**, *140*, A4014006. [CrossRef]
21. Oudjene, M.; Meghlat, E.; Ait-Aider, H.; Lardeur, P.; Khelifa, M.; Batoz, J.-L. Finite element modelling of the nonlinear load-slip behaviour of full-scale timber-to concrete composite T-shaped beams. *Compos. Struct.* **2018**, *196*, 117–126. [CrossRef]
22. Wei, Y.; Wang, Z.; Chen, S.; Zhao, K.; Zheng, K. Structural behavior of prefabricated bamboo-lightweight concrete composite beams with perforated steel plate connectors. *Arch. Civ. Mech. Eng.* **2021**, *21*, 1–21. [CrossRef]

23. *ISO 3787: 1976*; Wood-Tests Methods-Determination of Ultimate Stress in Compression Parallel to Grain. ISO: Geneva, Switzerland, 1976.
24. *GB 50005*; Standard for Design of Timber Structures. Standardization Administration of China: Beijing, China, 2017.
25. *EN 1992-1-1: 2004*; Eurocode 2: Design of Concrete Structures, Part 1-1: General Rules and Rules for Buildings. CEN: Brussels, Belgium, 2004.
26. *EN 338: 2015*; Structural Timber-Strength Classes. European Committee for Standardization: Brussels, Belgium, 2015.
27. Hill, R. *The Mathematical Theory of Plasticity*; Clarendon Press: Oxford, UK, 1950.
28. Dias, A.; Van de Kuilen, J.; Lopes, S.; Cruz, H. A non-linear 3D FEM model to simulate timber–concrete joints. *Adv. Eng. Softw.* **2007**, *38*, 522–530. [CrossRef]

materials

MDPI

Article

Numerical and Experimental Analysis of the Rotational Stiffness of a Timber Semi-Rigid Dowel-Type Connection

Marek Johanides [1,2,*], Antonin Lokaj [1], Pavel Dobes [2] and David Mikolasek [1]

[1] Department of Structures, Faculty of Civil Engineering, VSB-Technical University of Ostrava, 708 00 Ostrava, Czech Republic
[2] Centre for Building Experiments and Diagnostics, Faculty of Civil Engineering, VSB-Technical University of Ostrava, 708 00 Ostrava, Czech Republic
* Correspondence: marek.johanides@vsb.cz

Abstract: The paper deals with the analysis of the rotational stiffness of a semirigid connection created from a system of two stands and a rung. The connection was made from glued laminated timber with metal mechanical dowel-type fasteners. Not only a common combination of bolts and dowels but also fully threaded screws were used for the connection. The aim of the research and its motivation was to replace commonly used fasteners with more modern ones, to shorten and simplify the assembly time, and to improve the load-carrying capacity of this type of connection. Each of these two types of connection was loaded to the level of 60%, 80%, and 100% of the ultimate limit state value. Subsequently, the rotational stiffness was determined for each load level after five loading and unloading cycles. This paper presents the results and comparison of the experimental testing and the numerical modeling. The obtained results were also compared with the assumption according to the currently valid standard.

Keywords: bolts; dowels; dowel-type fasteners; FEM; frame connection; fully threaded screws; glued laminated timber; numerical model; rotational stiffness

Citation: Johanides, M.; Lokaj, A.; Dobes, P.; Mikolasek, D. Numerical and Experimental Analysis of the Rotational Stiffness of a Timber Semi-Rigid Dowel-Type Connection. *Materials* **2022**, *15*, 5622. https://doi.org/10.3390/ma15165622

Academic Editors: Radosław Mirski and Dorota Dukarska

Received: 27 July 2022
Accepted: 12 August 2022
Published: 16 August 2022

1. Introduction

Stiffness is an important property of connections in timber structures. When designing and assessing a structure, it is necessary to take into account not only the load-carrying capacity but also the deformation behavior in order to ensure sufficient reliability of the structure. In 1949, Granholm [1] began to deal with the issue of deformation capacity of structures after the fall of a formwork of the Sandö Bridge, which was located in Sweden in the 1930s. The failure of the structure was caused by ignoring the nonlinear deformation behavior of fasteners in connections. The scientist found that the stiffness was not constant and varied depending on the load level and deformation of the connection. A decrease in connection stiffness can be observed with increasing deformation. In 1963, Granholm [2] determined the tangent and secant stiffness along the entire curve of a load–deformation diagram for a nail connection. The stiffness was calculated based on 70 load–deformation curves for a nail diameter of 5.6 mm and a length of 150 mm. The scientist also emphasized consideration the friction between the timber elements in the connection. In the case of the collapse of the aforementioned bridge formwork, the stiffness at failure was only about 20–25% of the initial values.

Ehlbeck [3] identified some parameters that influence the load–deformation behavior. These parameters are divided into four main parts. The dimensions and material properties of fasteners represent the first part. These properties include the size, length, diameter, surface treatment, and bending properties of the fastener. The second part includes mechanical properties of fasteners, such as slip moduli and yield moment. The third part contains configurations of fasteners, i.e., number of shear planes, thickness of timber element, predrilling of holes, and spacing and distances for fasteners. The last part of

influences includes loading conditions. These can be static or dynamic, short term or long term, and also loading rate. The identification of these parameters means that the stiffness values given in the design codes are only rough estimates, due to the great variability of material properties [3].

In 1981, Dubas and Gehri [4] stated that the standard at the time took into account only the slip modulus corresponding to the ultimate limit state. This failure stiffness was too conservative for the serviceability limit state due to the strong dependence of the respective stiffness value on the respective load value. It was also emphasized that the initial slip of the connection is usually smaller for tested connections than for actual connections made on the construction site in practice. This is due to greater accuracy and precision under laboratory conditions. They also stated that the initial slip can be observed for all types of connections, even for predrilled ones. It is possible to expect an initial slip of 0.50–1.00 mm depending on the fastener diameter or timber drying. There are very few experiments and scientific work that have evaluated the effect of moisture content on connection stiffness 2020 [5]. That latter work assumes that the most deformations in the connection occur in the timber element, so the same moisture content dependence can be applied to the connection stiffness. Furthermore, the paper states that as the moisture content of the timber element increases, its modulus of elasticity decreases and thus the deformation increases. However, this idea needs to be verified by several studies.

In experimental tests by Ehlbeck and Werner in 1988 [6], it was observed that deformation under the allowable load according to DIN 1052 [7] increased with increasing fastener diameter. They derived an equation for calculation of the slip modulus. This was later modified by Ehlbeck and Larsen [8], and became the standard equation for the calculation of the slip modulus. This relationship was and is still under investigation. Jorissen [9] also dealt with this relation in his dissertation and found that in the case of multiple fastener connections, the stiffness values were significantly lower than assumed by the current standard approach. This is explained by the clearances for holes and the nonuniform load distribution of individual fasteners during loading.

Nowadays, the slip modulus for fasteners (translational stiffness) is calculated on the basis of the equations given in Eurocode 5 [10]. However, this standard does not specify a procedure for calculating rotational stiffness. Rotational stiffness can be calculated on the basis of the equations given in the scientific literature [11] using the slip modulus according to Eurocode 5 [9].

Dowel-type fasteners, such as screws, bolts, and dowels, are one of the most popular fasteners in timber structures [12,13]. They are easy to use, cheap, and available everywhere. In order to effectively apply dowel-type connections, it is crucial to understand their mechanical behavior under loading. It is desirable to know the relationship between load and slip, stress distribution, or possible different failure modes. The mechanical behavior of connections in timber structures is a complex problem that is influenced by a number of factors [14]. The most important factors are the geometry and arrangement of the connection (i.e., spacing, edge and end distances) [15], the material characteristics, the type of timber [16], and the method of loading.

The load-carrying capacity and stiffness of connections are influenced not only by mechanical properties of fasteners but also by mechanical properties of timber. The stiffness is mainly affected by the timber density. The findings described in [17,18] can be used to determine the mechanical properties and to classify the structural timber. It is possible to use selected nondestructive experimental testing [19,20], dynamic testing [21], and a nondestructive vibrational method [22] in order to determine these mechanical properties. A semidestructive method can also be used to determine the density and moisture content of timber [23].

Nowadays, numerical modeling should also be included as an important part of experiments. Numerical modeling is an excellent tool to understand the behavior of connections in timber structures. Dobeš [24], Braun [25], and Kupniewska [26] dealt with the calibration and validation of numerical models according to experimental tests. The

papers stated that numerical modeling was especially suitable for determining the stress in individual elements of the connection and determining the locations of stress peaks. However, the exact prediction of the load–deformation response is often problematic, because the response of the tested connection is influenced by many factors that can hardly be taken into account in the numerical model (e.g., unpredictable initial slip and the gradual increase in stiffness in the initial consolidation phase of the connection when the contact between the timber and the fastener is just forming).

The paper is focused on the experimental determination of the rotational stiffness of a semirigid connection, with subsequent validation of a numerical model. The fist variant of the connection is made of a combination of bolts and dowels in Experiment A. The second variant of the connection is made of high tensile fully threaded screws in Experiment B. The fasteners in Experiment A are used in practice, so it is a common combination. Knowledge on the design of such a semirigid connection can be found elsewhere [27–29]. However, the fasteners in Experiment B are not commonly used in practice. The presented paper is a follow-up of previous research [30–32]. Papers [30,31] dealt with determining the rotational stiffness and load-carrying capacity of a timber frame corner. However, this structure was much larger and made of larger cross-sections with greater number of fasteners. The aim was to create a connection with higher load-carrying capacity using the same structural elements. Johanides [32] dealt with smaller timber frame corners. The paper determined and compared the ductility of these two types of connection (bolts and dowels vs. fully threaded screws).

This paper brings knowledge about the results of analytical, experimental, and numerical determination of the rotational stiffness of a semirigid connection with mechanical fasteners. The reader can view the results of a comparison of two types of fasteners and form his/her own opinion on the advantages and disadvantages of individual fasteners based on the presented data.

2. Materials and Methods

2.1. Description of Structure and Geometry

The tested specimens corresponded to actual connections used in practice. The arrangement and loading of test specimens was designed to correspond with the actual state of the connection in a real load-carrying structure. The air temperature was 21 °C and the relative air humidity 55% during the experimental testing.

The structural system for the experiments was created from a semirigid connection of two stands and a rung. These structural elements were made of spruce timber, which is the most used structural timber in Central Europe for structural practice due to its availability. The disadvantage of this timber is its low durability in the outdoor environment. The connection was made of dowel-type metal fasteners. Two identical structural systems were created with different types of fasteners. Experiment A contained a combination of bolts and dowels as fasteners. Experiment B contained fully threaded screws. Glued laminated timber of the strength class GL24h was used. Four-point bending tests were performed to verify the properties of the used timber. Results of the tests have already been published [32]. The stands were made of a cross-section of 100/300 mm and the rung was made of a cross-section of 100/300 mm. The material properties of the fasteners were also experimentally verified by tensile tests [32]. Bolts and dowels in Experiment A were made of steel, grade 10.9. The outer diameter of the threaded shank was 8 mm, the inner diameter was 7.25 mm. The bolt length was 360 mm and the dowel length was 300 mm. Holes for fasteners were predrilled with an 8 mm-diameter drill to get connections without initial slip. The fully threaded bolts in Experiment B were made of steel, grade 10.9. The outer diameter of the screw was 8 mm, the inner diameter of the screw was 5 mm, and the length was 300 mm. Holes for fasteners were predrilled with a 5 mm-diameter drill, also in order to eliminate the initial slip.

The arrangement of fasteners in both experiments was identical. They were located on one symmetrical circle with a radius r = 90 mm, with 10 pieces. The arrangement (see Figure 1) was determined according to [11].

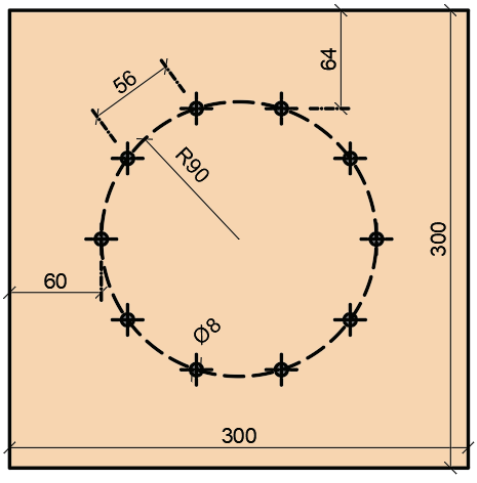

Figure 1. The arrangement of fasteners.

It was necessary to create the boundary conditions of the structure to carry out these experiments. A steel structure was designed and made to ensure the correct boundary conditions. A steel sheet of the desired shape was fastened to the steel structure by bolts and subsequently the stand of the semirigid connection was fastened to the plate using 24 bolts with a diameter of 8 mm. This connection was calculated and designed for 400% of the estimated load that would cause the connection failure. The entire steel structure was placed on a reinforced concrete floor at the required distance from the testing machine so the load could be applied to the required position on the rung. After the correct positioning of the steel structure, the rear part of the steel structure was loaded with a steel box with a weight of 1000 kg against its overturning and displacement. A schematic illustration of the experiment is shown in Figure 2.

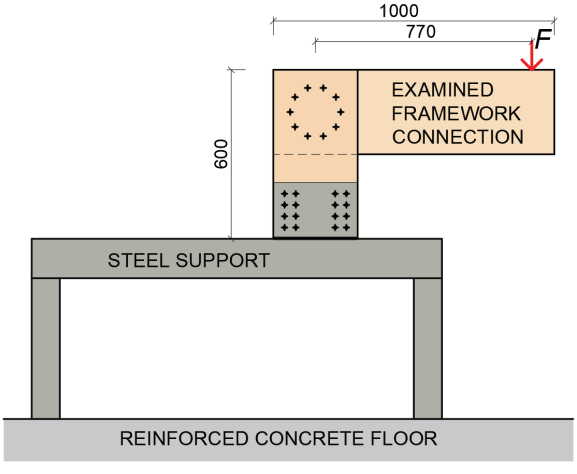

Figure 2. Schematic illustration of the experiment.

2.2. Description of the Testing Machine

The experiments were performed using a LabTest 6.1200 electromechanical testing machine from Labortech (Opava, Czech Republic) [33] with a maximum force of 1200 kN. This testing machine allows tensile, compressive static, and cyclic dynamic testing. The test speed of the testing machine ranges from 0.0005 to 250 mm/min. The machine and testing procedure is controlled by computer software.

2.3. Position of Gauge Sensors

To evaluate the rotational stiffness from the tests, it was necessary to obtain the most accurate input data for the calculation. This was achieved by using the force gauge sensors (see Figure 3 on the right), which was located under the crosshead. The ALMEMO FKA0255 gauge sensor records force up to 50 kN with an accuracy of ±0.20% in pressure and ±0.10% tension. Furthermore, it was necessary to fit the strain gauge sensors correctly (see Figure 3 on the left), according to the scheme in Figure 4. An Almemo FWA100TR gauge sensor with a range of 0–100 mm with an accuracy of ±0.002 mm was used to record the deformation. Both sensors were from Ahlborn (Holzkirchen, Germany) [34].

Figure 3. Strain gauge sensor (on the left); force gauge sensor (on the right).

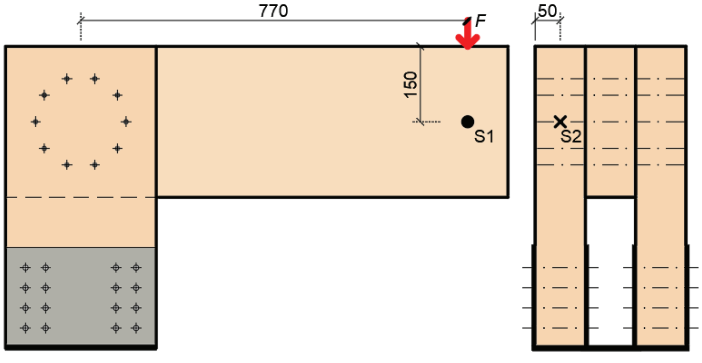

Figure 4. Position of strain gauge sensors: front view (on the left), side view (on the right).

2.4. Determination of the Rotational Stiffness

The system for loading (see Figure 2) included several influences that cause the vertical movement of the rung end. These components must be subtracted to determine the actual deformation caused by the rotational stiffness of the frame connection. The following text therefore focuses on determination of the deformation caused by the rotational stiffness.

The first important factor is the semirigid connection between the lower part of the stand and the supporting steel structure (see Figure 5). This connection causes an inclination of the stand during loading, and subsequently a vertical displacement of the rung end. Therefore, one strain gauge sensor is placed horizontally (S2 in Figure 4). It records the horizontal displacement (inclination) of the stand. It is then possible to determine this vertical deformation based on the obtained data.

It is also necessary to take into account deformations of the individual segments (see Figure 6), caused by the bending moment and the shear force. These deformations can be determined analytically according to cross-sectional characteristics and dimensions of the individual segments, for example, by means of the force method.

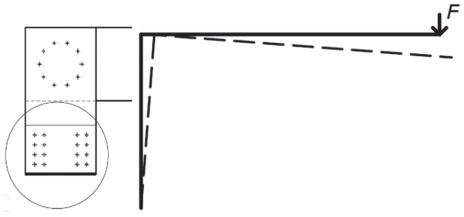

Figure 5. Semirigid connection between the stand and the steel plate (on the left); deformation due to inclination (on the right).

Figure 6. Deformation of segments due to bending moment and shear force.

The actual value of the deformation caused by the rotational stiffness can be obtained if the abovementioned effects of the vertical displacements are subtracted from the total displacement measured by the sensor S1 (see Figure 4). Based on the obtained value of deformation, it is possible to determine the course of rotational stiffness depending on the applied load (see Figure 7). It can subsequently be compared with the value from the numerical model and analytical calculation [11].

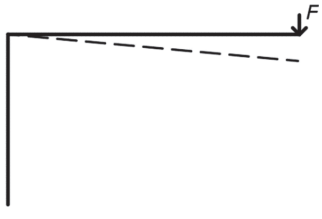

Figure 7. Deformation of the rung end caused by the rotational stiffness of the frame connection.

2.5. Description of the Loading Procedure of Quasi-Static Tests

The aim of the quasi-static cyclic testing was to investigate the behavior of the semirigid connection at different load levels. The rotational stiffness values for the individual load levels were determined based on the obtained data.

The idea of such testing is built on a practical basis. This means that building structures are designed with consideration of the ultimate limit state. The limit value of the load-carrying capacity must not be exceeded in a real structure; otherwise, there is a risk of permanent damage of the supporting structure, or its collapse [10]. For this reason, the rotational stiffness of the connection beyond the ultimate limit state was not investigated. The selection of individual load levels for the cyclic testing was chosen strategically as follows.

1. The first value for loading was calculated as 60% of the ultimate limit state value of load-carrying capacity. This load represents a common design situation of most load-carrying structures.
2. The second value for loading was calculated as 80% of the ultimate limit state value of load-carrying capacity. This load is also a common design situation of some load-carrying structures.

3. The third value for loading was calculated as 100% of the ultimate limit state value of load-carrying capacity. This load represents the maximum load of load-carrying structures in practice.

The tensile load was generated by electrohydraulic cylinders. During the test, the time, tensile force, and deformation (i.e., crosshead displacement) were continuously recorded. Strain gauge sensors were installed on the structures in order to enable a correct evaluation of the results (see Section 2.3).

The test specimens were subjected to nondestructive tests before the cyclic testing to determine the moisture content and density of the used timber. The timber density is the main factor in the analytical calculation of the slip modulus of fasteners according to Eurocode 5 [10] and thus also the rotational stiffness according to Koželouh [11].

It is important to note that a new unloaded connection was used for each test to achieve correct results. Using an already loaded specimen would affect the results, as a consequence of embedment of timber or irreversible permanent deformation of fasteners.

The following loading procedure is a modified approach of the authors, which is based on the standard EN 26891 [35].

1. Calculation of the maximum force F_{ed} for the tested connection (i.e., 100% ULS);
2. Loading of the specimen to 60% F_{ed}, then holding for 30 s;
3. Unloading to 10% F_{ed}, then holding for 30 s;
4. Repeating steps 2 and 3 four times, until a total of 5 load cycles is done.

The procedure mentioned in the text above was also applied to test specimens at 80% and 100% F_{ed}.

Table 1 shows the values that determine the course of the experimental loading for Experiment A (bolts and dowels) and Experiment B (fully threaded screws) at 60% of the ultimate limit state value. The load-carrying capacity of the connection F_{ed} was calculated as the design value (using modification factor k_{mod} = 0.90 and partial factor for material properties γ_{con} = 1.30). This value represents the maximum load-carrying capacity of the connection and was calculated according to Eurocode 5 [10] and the literature [10].

Table 1. The course of the 60% ULS experiment setup.

Loading Step	Bolts and Dowels		Fully Threaded Screws	
	From (kN)	To (kN)	From (kN)	To (kN)
Step 1	0	4.93	0	6.31
Step 2	Hold		Hold	
Step 3	4.93	0.85	6.31	1.05
Step 4	Hold		Hold	
Step 5	0.85	4.93	1.05	6.31
Step 6	Hold		Hold	
Repeating steps 3, 4, 5 four times.				

The loading speed was chosen as constant in kN/min according to the selected loading schemes. The total testing time of one specimen was 30 min.

Figure 8 shows the graphic course of individual experimental tests.

2.6. Experimental Testing

All the experiments were carried out at the Centre for Building Experiments and Diagnostics at VSB—Technical University of Ostrava, Czech Republic. Figure 9a shows Experiment A, a combination of bolts and dowels. Figure 9b shows Experiment B, fully threaded screws. The load was applied to the connection using a steel cylinder with a diameter of 50 mm. A rubber pad with a thickness of 10 mm was placed under this cylinder to eliminate local damage of the timber rung during loading.

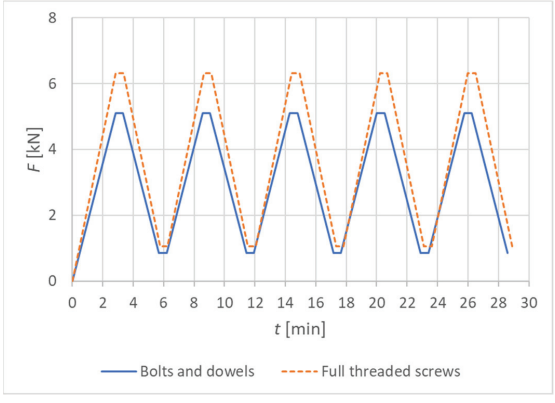

Figure 8. The course of individual experiments.

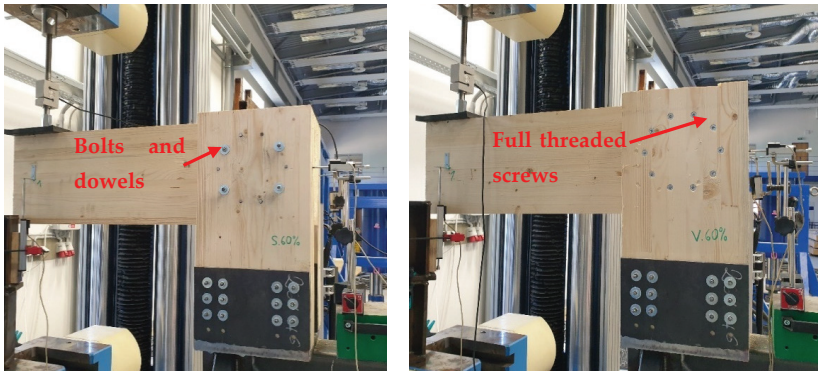

(**a**) (**b**)

Figure 9. Experimental specimens: (**a**) Experiment A, bolts and dowels; (**b**) Experiment B, fully threaded screws.

2.7. Numerical Modeling

The numerical model was created in the Ansys 21 software in the Workbench 21 environment (Canonsburg, PA, USA) [36]. The models used 3D finite elements with the support of material nonlinearity, geometric nonlinearity, and contact elements. The material model of timber was considered to be orthotropic with the Hill yield criterion to predict plastic behavior, [37]. Steel elements were considered isotropic with plastic behavior based on the Von Mises yield criterion [37]. The load–deformation response of the numerical model would not be sufficiently accurate without considering the orthotropy of timber and the plastic behavior of materials. Mikolášek [38] and Gunderson and Goodman [39] were also used to gain the material characteristics of timber for the numerical models. The material characteristics of timber are shown in Table 2, and the material characteristics of steel are shown in Table 3.

Table 2. Elastic constants of the material model for timber.

Timber Properties	Value	Unit
Young's modulus in *X*	9200	MPa
Young's modulus in *Y*	740	MPa
Young's modulus in *Z*	400	MPa
Poisson's ratio in *XY*	0.47	-
Poisson's ratio in *YZ*	0.25	-
Poisson's ratio in *XZ*	0.37	-
Shear modulus in *XY*	650	MPa
Shear modulus in *YZ*	38	MPa
Shear modulus in *XZ*	700	MPa

Table 3. Elastic constants of the material model of fasteners.

Steel Properties	Value	Unit
Young's modulus	190,000	MPa
Poisson's ratio	0.30	-

The modulus of elasticity of fasteners was determined on the basis of the experience of the authors.

The values of the plastic behavior of timber (see Table 4), and the plastic behavior of steel (see Table 5) were obtained based on an experimental testing. The results of the testing have already been published in [31].

Table 4. Values for the plastic behavior of the material model for timber.

Hill Yield Criterion	Value	Unit
Yield strength in *X*	32	MPa
Yield strength in *Y*	1	MPa
Yield strength in *Z*	1	MPa
Yield strength in *XY*	6	MPa
Yield strength in *YZ*	3	MPa
Yield strength in *XZ*	6	MPa

Table 5. Values for the plastic behavior of the material model for steel.

Bolts and Dowels		
Yield strength	670	MPa
Ultimate strength	970	MPa
Hardening modulus	1000	MPa
Fully Threaded Screws		
Yield strength	690	MPa
Ultimate strength	1075	MPa
Hardening modulus	1000	MPa

Figures 10 and 11 show individual numerical models that were used for the analysis of the rotational stiffness at different load levels after five cycles of loading and unloading. The connection with bolts and dowels (Experiment A) contained 125,000 nodes, 32,467 finite elements and 375,000 equations. The connection with fully threaded screws (Experiment B) contained 78,557 nodes, 15,868 elements, and 218,729 equations.

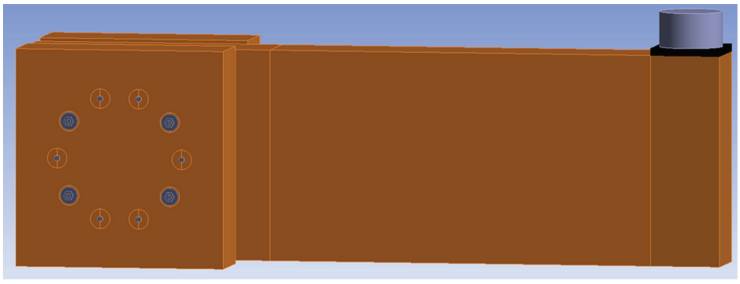

Figure 10. Numerical model for Experiment A, bolts and dowels.

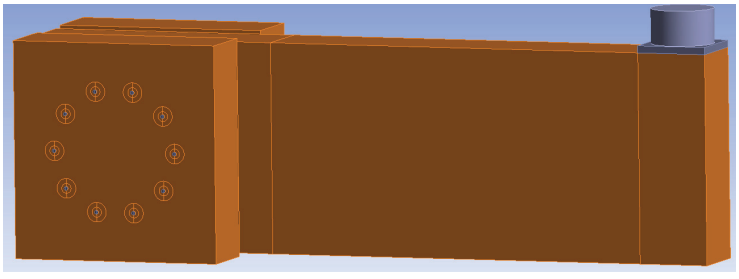

Figure 11. Numerical model for Experiment B, fully threaded screws.

Thanks to carefully placed strain gauge sensors and analytical calculations described in Section 2.3, it was possible to choose a fixed support for the stands as boundary conditions. After subtracting the already mentioned external influences causing the deformation of the rung, we can get the deformation caused by the rotational stiffness of the connection. Figure 12 shows the selected boundary conditions of the numerical model (the fixed support of the stands).

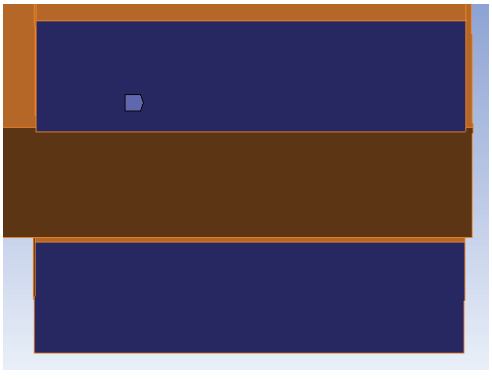

Figure 12. Boundary conditions of the numerical models.

It is very important to correctly apply the load into the numerical model. Figure 13 shows the finite-element mesh for both numerical models for applying the load using the press head (cylinder) of the testing machine. The model was loaded by a vertical displacement (displacement controlled loading), which represented the actual loading by the cylinder during the experimental testing.

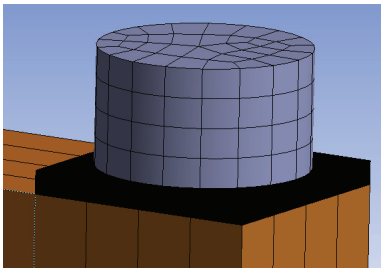

Figure 13. Finite-element mesh for applying load.

The mesh was created from 3D hexahedral finite elements. The finite-element mesh was divided into several subregions with different finite-element sizes with respect to the estimated areas of increased local stress concentrations. A finer mesh was chosen around the contact of the fastener with the timber element. A ratio of 3:1 (length to height) for the finite elements of the subregions was set to obtain optimal results. The interface between individual elements was simulated using frictional contacts. The coefficient of friction between timber–timber elements was 0.40, steel–steel 0.10, and timber–steel 0.30. Figure 14 shows the finite-element mesh for Experiment A (bolts and dowels). Figure 15 shows the finite-element mesh for Experiment B (fully threaded screws).

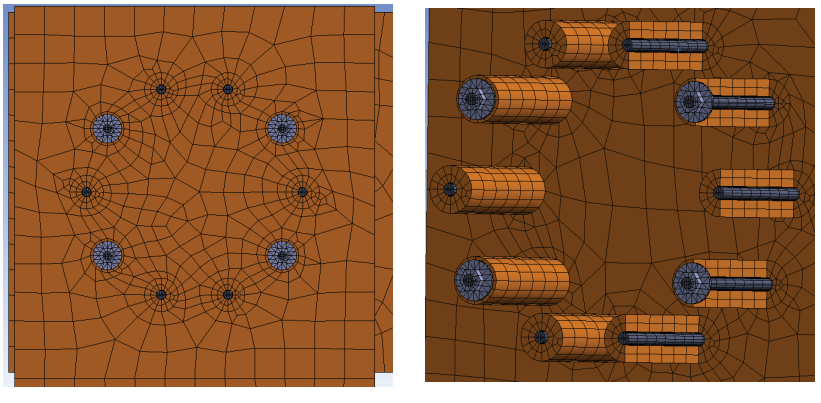

Figure 14. Finite-element mesh for Experiment A, bolts and dowels.

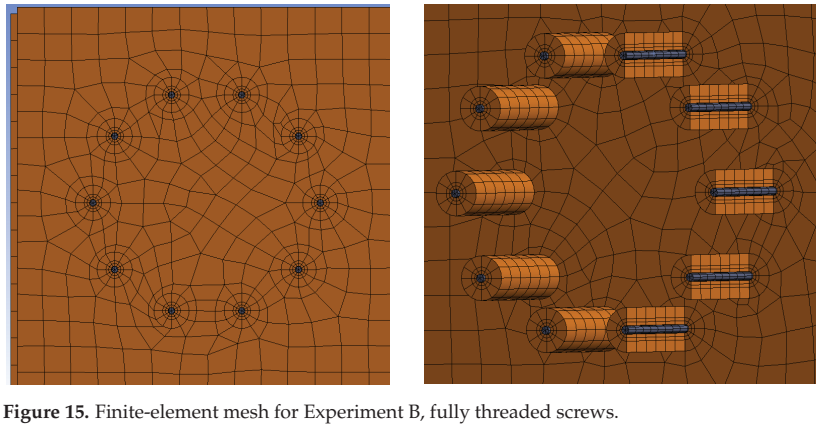

Figure 15. Finite-element mesh for Experiment B, fully threaded screws.

3. Results

3.1. Results of Experimental Testing

3.1.1. Experiment A, Bolts and Dowels

Figure 16 shows load–deformation curves from the experimental testing. The deformation u represents the actual vertical deformation of the rung end after subtracting all the influences that were explained in Section 2.3. The loading procedure was carried out according to the explanation in Section 2.4, and the position of the load is shown in Figure 4.

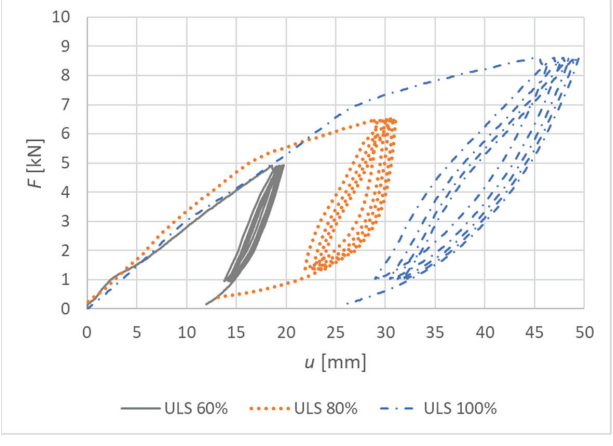

Figure 16. Load–deformation curves of nondestructive quasi-static cyclic testing for individual specimens made from a combination of bolts and dowels (Experiment A).

Figure 17 shows the curves of the rotational stiffness depending on the load level for the connection made from a combination of bolts and dowels. The figure also indicates the rotational stiffness values calculated for the ultimate limit state according to Eurocode 5 [10].

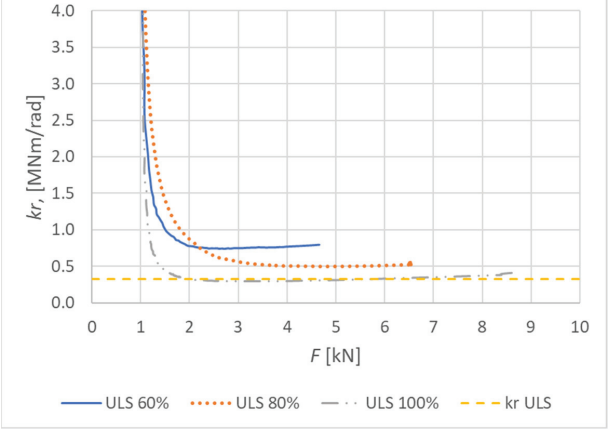

Figure 17. Course of rotational stiffness of a semirigid connection for specimens made from a combination of bolts and dowels (Experiment A).

The results of the individual tests are listed in Tables 6–8. The first column indicates the load level. The second column shows the maximum force achieved during the test. The third column shows the corresponding value of the bending moment. The fourth column shows the actual deformation caused by the rotational stiffness of the semirigid

connection. The fifth column contains the calculated value of the rotational stiffness based on the experimental data. The sixth and the seventh columns contain the standard deviation value and the average value of the experimental data. The eighth column contains the calculated rotational stiffness according to Eurocode 5 [10]. The ninth column shows the ratio between the rotational stiffness obtained experimentally and the rotational stiffness calculated according to Eurocode 5 [10].

Table 6. Results of quasi-static cyclic testing for Experiment A at 60% ULS.

Load Level	$F_{60\%\ ULS}$ [kN]	$M_{60\%\ ULS}$ [kNm]	u [mm]	$k_{r,\ 60\%\ ULS}$ [MNm/rad]	$SD_{,kr,60}$ [MNm/rad]	$AVG_{,kr,60}$ [MNm/rad]	$k_{r,\ u,\ EC5}$ [MNm/rad]	Test/u [-]
60% ULS	4.93	3.80	3.06	0.955	0.023	0.917	0.323	2.96
			3.13	0.934				2.89
			3.21	0.911				2.82
			3.25	0.899				2.78
			3.27	0.894				2.77

Table 7. Results of quasi-static cyclic testing for Experiment A at 80% ULS.

Load Level	$F_{80\%\ ULS}$ [kN]	$M_{80\%\ ULS}$ [kNm]	u [mm]	$k_{r,\ 80\%\ ULS}$ [MNm/rad]	$SD_{,kr,80}$ [MNm/rad]	$AVG_{,kr,80}$ [MNm/rad]	$k_{r,\ u,\ EC5}$ [MNm/rad]	Test/u [-]
80% ULS	6.50	5.01	6.85	0.563	0.005	0.554	0.323	1.74
			6.92	0.558				1.73
			6.98	0.553				1.71
			7.02	0.550				1.70
			7.04	0.548				1.70

Table 8. Results of quasi-static cyclic testing for Experiment A at 100% ULS.

Load Level	$F_{100\%\ ULS}$ [kN]	$M_{100\%\ ULS}$ [kNm]	u [mm]	$k_{r,\ 100\%\ ULS}$ [MNm/rad]	$SD_{,kr,100}$ [MNm/rad]	$AVG_{,kr,100}$ [MNm/rad]	$k_{r,\ u,\ EC5}$ [MNm/rad]	Test/u [-]
100% ULS	8.66	6.67	12.58	0.408	0.002	0.401	0.323	1.26
			12.63	0.406				1.26
			12.68	0.404				1.25
			12.69	0.404				1.25
			12.70	0.404				1.25

Figure 18 shows the course of the rotational stiffness of the connection. It was created on the basis of the individual load levels. It is possible to observe a decreasing trend in the level of rotational stiffness with the increasing load.

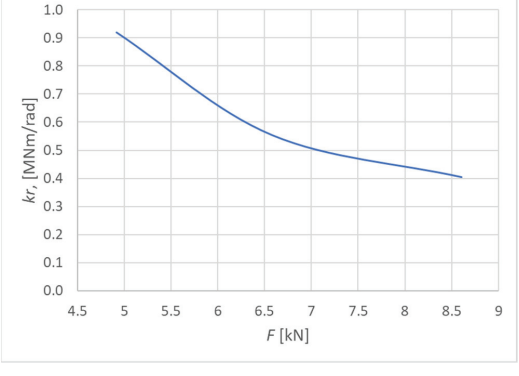

Figure 18. Trend of rotational stiffness for Experiment A.

3.1.2. Experiment B, Fully Threaded Screws

Figure 19 shows load–deformation curves from the experimental testing. The deformation u represents the actual vertical deformation of the rung end after subtracting all the influences that were explained in Section 2.3. The loading procedure were carried out according to the explanation in Section 2.4, and the position of the load is shown in Figure 4.

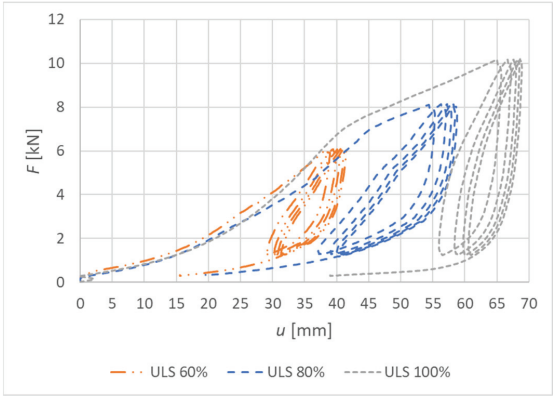

Figure 19. Load–deformation curves of nondestructive quasi-static cyclic testing for individual specimens made from fully threaded screws (Experiment B).

Figure 20 shows the curves of the rotational stiffness depending on the load level for the connection made from fully threaded screws. The figure also indicates the rotational stiffness values calculated for the ultimate limit state according to Eurocode 5 [10].

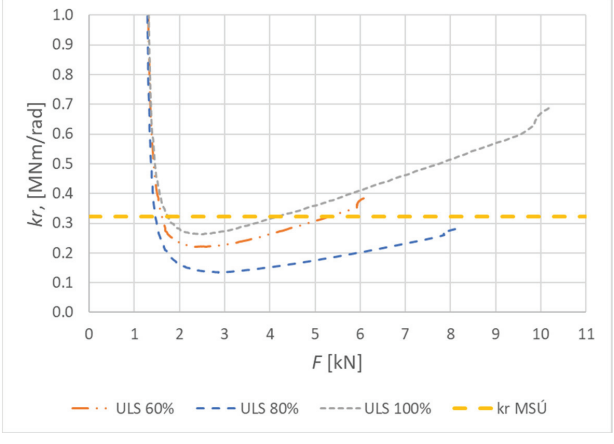

Figure 20. Course of rotational stiffness of a semirigid connection for specimens made from fully threaded screws (Experiment B).

The results of the individual tests are listed in Tables 9–11. The first column indicates the load level. The second column shows the maximum force achieved during loading. The third column shows the corresponding value of the bending moment. The fourth column shows the actual deformation caused by the rotational stiffness of the semirigid connection. The fifth column contains the calculated value of the rotational stiffness based on the experimental data. The sixth and the seventh columns contain the standard deviation value and the average value of the experimental data. The eighth column contains the calculated rotational stiffness according to Eurocode 5 [10]. The ninth column shows the

ratio between the rotational stiffness obtained experimentally and the rotational stiffness calculated according to Eurocode 5 [10].

Table 9. Results of quasi-static cyclic testing for Experiment B at 60% ULS.

Load Level	$F_{60\%\ ULS}$ [kN]	$M_{60\%\ ULS}$ [kNm]	u [mm]	$k_{r,\ 60\%\ ULS}$ [MNm/rad]	$SD_{,kr,60}$ [MNm/rad]	$AVG_{,kr,60}$ [MNm/rad]	$k_{r,\ u,\ EC5}$ [MNm/rad]	Test/u [-]
60% ULS	6.31	4,86	9.39	0.383	0.002	0.386	0.323	1.19
			9.28	0.388				1.20
			9.34	0.385				1.19
			9.33	0.386				1.19
			9.33	0.386				1.19

Table 10. Results of quasi-static cyclic testing for Experiment B at 80% ULS.

Load Level	$F_{80\%\ ULS}$ [kN]	$M_{80\%\ ULS}$ [kNm]	u [mm]	$k_{r,\ 80\%\ ULS}$ [MNm/rad]	$SD_{,kr,80}$ [MNm/rad]	$AVG_{,kr,80}$ [MNm/rad]	$k_{r,\ u,\ EC5}$ [MNm/rad]	Test/u [-]
80% ULS	8.10	6.24	15.28	0.314	0.000	0.313	0.323	0.97
			15.32	0.313				0.97
			15.33	0.313				0.97
			15.35	0.313				0.97
			15.36	0.313				0.97

Table 11. Results of quasi-static cyclic testing for Experiment B at 100% ULS.

Load Level	$F_{100\%\ ULS}$ [kN]	$M_{100\%\ ULS}$ [kNm]	u [mm]	$k_{r,\ 100\%\ ULS}$ [MNm/rad]	$SD_{,kr,100}$ [MNm/rad]	$AVG_{,kr,100}$ [MNm/rad]	$k_{r,\ u,\ EC5}$ [MNm/rad]	Test/u [-]
100% ULS	10.17	7.83	8.77	0.688	0.069	0.784	0.323	2.13
			8.08	0.746				2.31
			7.67	0.787				2.44
			7.51	0.803				2.48
			6.73	0.896				2.77

Figure 21 shows the course of the rotational stiffness of the connection. It was created on the basis of the individual load levels. It is possible to observe an increase in the rotational stiffness with the increasing load.

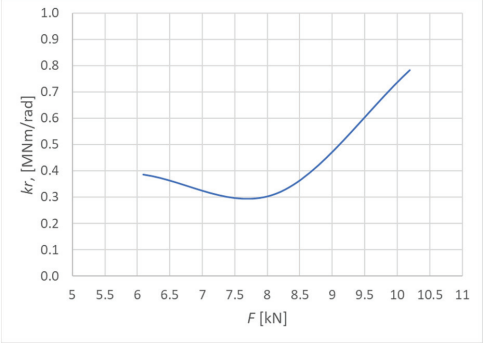

Figure 21. Trend of rotational stiffness for Experiment B.

3.2. Results of the Numerical Modeling

3.2.1. Experiment A, Bolts and Dowels

Figure 22 shows load–deformation curves from the numerical models. The deformation u represents the vertical deformation of the rung end in the numerical model.

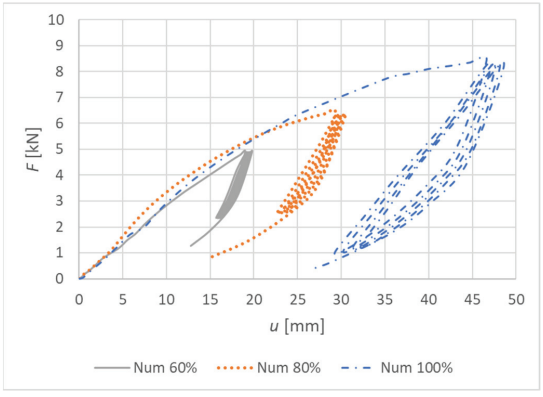

Figure 22. Load–deformation curves of quasi-static numerical modeling for individual specimens made from a combination of bolts and dowels (Experiment A).

Figure 23 shows the normal stress perpendicular to the grain in the individual elements of the connection at a load level of 60% ULS. As can be seen, the maximum tensile stress perpendicular to the grain (1 MPa) is locally concentrated mainly near the holes.

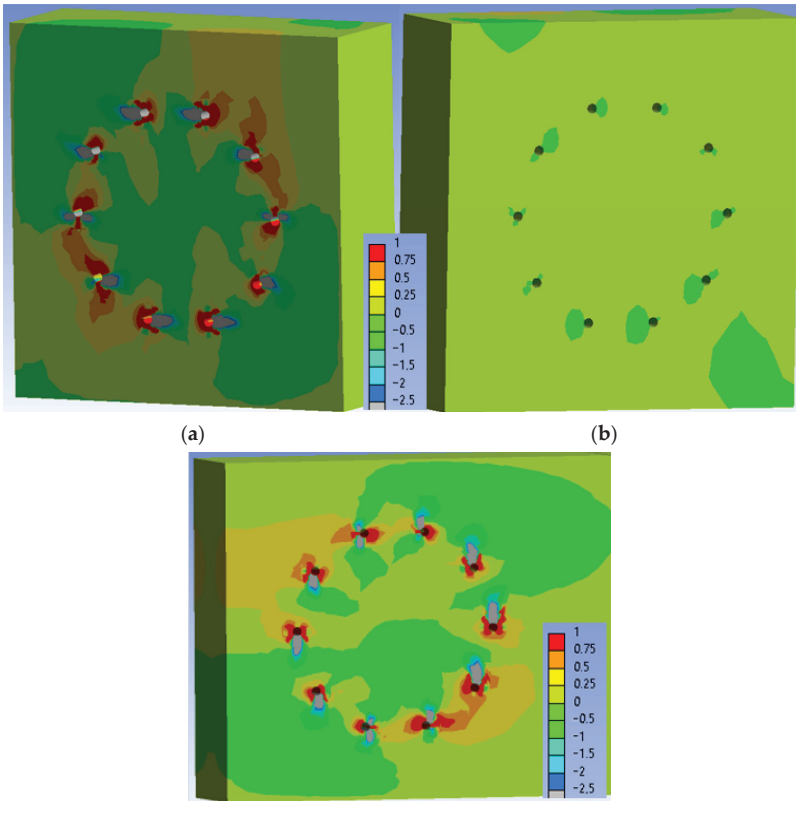

Figure 23. Tensile stress perpendicular to the grain [MPa] at 60% ULS, Experiment A: (**a**) inner side of the stand; (**b**) outer side of the stand; (**c**) rung.

Figure 24 shows the normal stress perpendicular to the grain in the individual elements of the connection at a load level of 80% ULS. The maximum tensile stress perpendicular to the grain (1 MPa) is also concentrated mainly near the holes at this load level. However, the stress in the critical area of the connection (marked in Figure 24c) increased to values of 0.25–0.50 MPa. This stress did not cause any visible cracks in the timber elements during the testing.

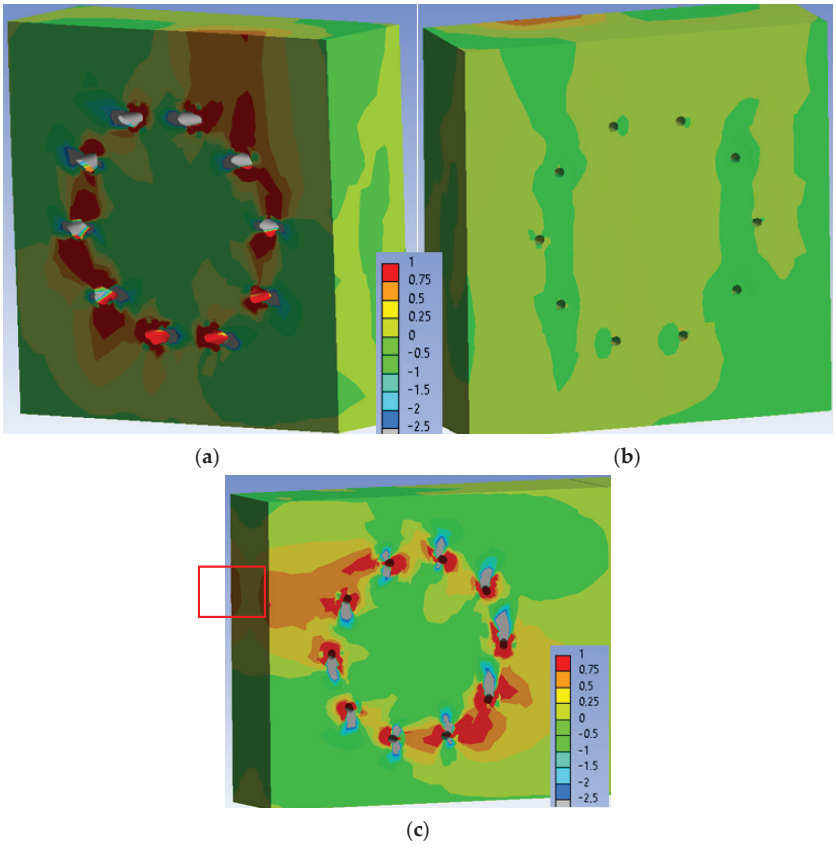

Figure 24. Tensile stress perpendicular to the grain [MPa] at 80% ULS, Experiment A: (**a**) inner side of the stand; (**b**) outer side of the stand; (**c**) rung.

Figure 25 shows the normal stress perpendicular to the grain in the individual elements of the connection at a load level of 100% ULS. Areas of the maximum tensile stress perpendicular to the grain (1 MPa) continue to expand around the holes at this load level. The stress in the critical area of the connection (marked in Figure 25c) remained unchanged with values of 0.25–0.50 MPa. This stress did not cause any visible cracks in the timber elements during the testing.

The results of the individual numerical models are listed in Tables 12–14. The first column indicates the load level. The second column shows the maximum force achieved during loading. The third column shows the corresponding value of the bending moment. The fourth column shows the actual deformation caused by the rotational stiffness of the semirigid connection. The fifth column contains the calculated value of the rotational stiffness based on the numerical model. The sixth and the seventh columns contain the standard deviation value and the average value of the experimental data. The eighth column contains the calculated rotational stiffness according to Eurocode 5 [10]. The

ninth column shows the ratio between the rotational stiffness obtained from the numerical analysis and the rotational stiffness calculated according to Eurocode 5 [10].

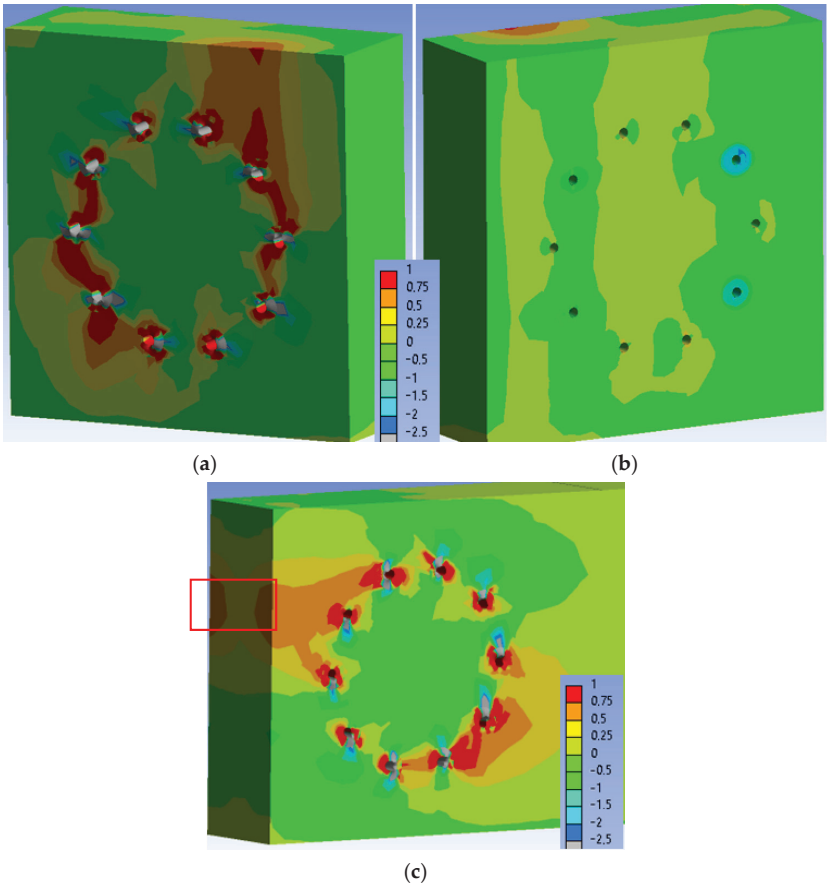

Figure 25. Tensile stress perpendicular to the grain [MPa] at 100% ULS, Experiment A: (**a**) inner side of the stand; (**b**) outer side of the stand; (**c**) rung.

Table 12. Results of quasi-static cyclic numerical modeling for Experiment A at 60% ULS.

Load Level	$F_{60\%,num}$ [kN]	$M_{60\%,num}$ [kNm]	u [mm]	$k_{r,60\%,num}$ [MNm/rad]	$SD_{,kr,num,60}$ [MNm/rad]	$AVG_{,kr,num,60}$ [MNm/rad]	$k_{r,u,EC5}$ [MNm/rad]	Num/u [-]
60% ULS	4.93	3.80	3.32	0.880	0.010	0.887	0.323	2.72
			3.32	0.880				2.72
			3.32	0.880				2.72
			3.25	0.889				2.75
			3.23	0.905				2.80

Table 13. Results of quasi-static cyclic numerical modeling for Experiment A at 80% ULS.

Load Level	$F_{80\%,\,num}$ [kN]	$M_{80\%,\,num}$ [kNm]	u [mm]	$k_{r,\,80\%,\,num}$ [MNm/rad]	$SD_{,kr,num,80}$ [MNm/rad]	$AVG_{,kr,num,80}$ [MNm/rad]	$k_{r,\,u,\,EC5}$ [MNm/rad]	Num/u [-]
80% ULS	6.50	5.01	6.71	0.575	0.022	0.609	0.323	1.72
			6.51	0.593				1.84
			6.32	0.611				1.89
			6.12	0.631				1.95
			6.09	0.634				1.96

Table 14. Results of quasi-static cyclic numerical modeling for Experiment A at 100% ULS.

Load Level	$F_{100\%,\,num}$ [kN]	$M_{100\%,\,num}$ [kNm]	u [mm]	$k_{r,\,100\%,\,num}$ [MNm/rad]	$SD_{,kr,num,100}$ [MNm/rad]	$AVG_{,kr,num,100}$ [MNm/rad]	$k_{r,\,u,\,EC5}$ [MNm/rad]	Num/u [-]
100% ULS	8.66	6.67	14.67	0.350	0.013	0.370	0.323	1.08
			14.25	0.360				1.11
			13.84	0.371				1.15
			13.43	0.382				1.18
			13.32	0.385				1.19

3.2.2. Experiment B, Fully Threaded Screws

Figure 26 shows load–deformation curves from the numerical models. The deformation u represents the vertical deformation of the rung end in the numerical model.

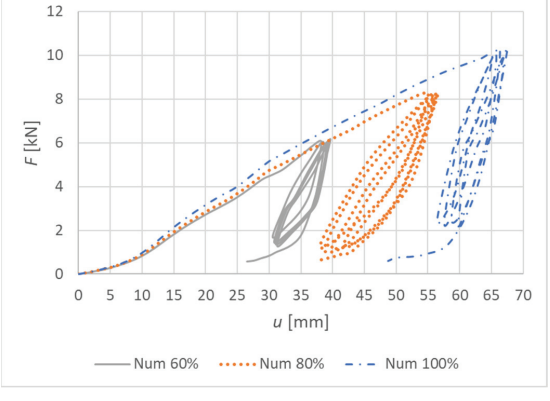

Figure 26. Load–deformation curves of quasi-static numerical modeling for individual specimens made from fully threaded screws (Experiment B).

Figure 27 shows the normal stress perpendicular to the grain in the individual elements of the connection at a load level of 60% ULS.

Figure 28 shows the normal stress perpendicular to the grain in the individual elements of the connection at a load level of 80% ULS. The maximum tensile stress perpendicular to the grain (1 MPa) is also concentrated mainly near the holes at this load level. The stress in the critical area of the connection (marked in Figure 28c) increased to values of 0.25–0.50 MPa in very small range.

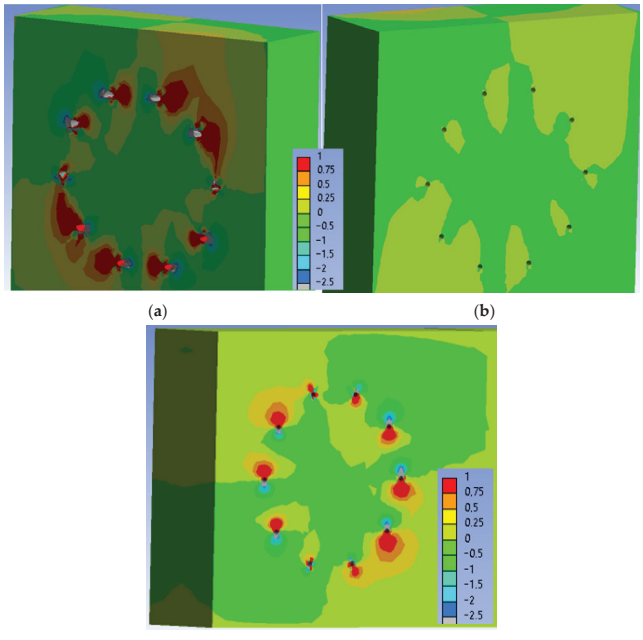

Figure 27. Tensile stress perpendicular to the grain [MPa] at 60% ULS, Experiment B: (**a**) inner side of the stand; (**b**) outer side of the stand; (**c**) rung.

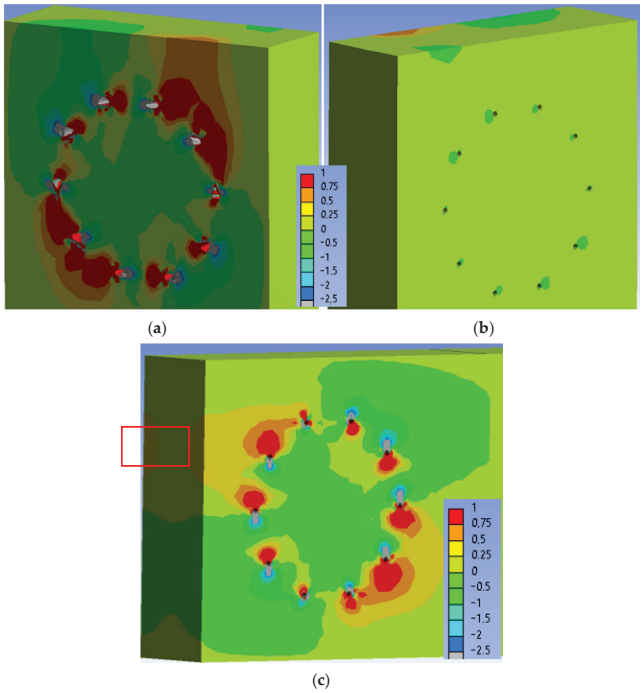

Figure 28. Tensile stress perpendicular to the grain [MPa] at 80% ULS, Experiment B: (**a**) inner side of the stand; (**b**) outer side of the stand; (**c**) rung.

Figure 29 shows the normal stress perpendicular to the grain in the individual elements of the connection at a load level of 100% ULS. Areas of the maximum tensile stress perpendicular to the grain (1 MPa) continued to expand around the holes at this load level. The stress in the critical area of the connection (marked in Figure 29c) remained unchanged with values of 0.25–0.50 MPa. The area of this stress did not increase significantly.

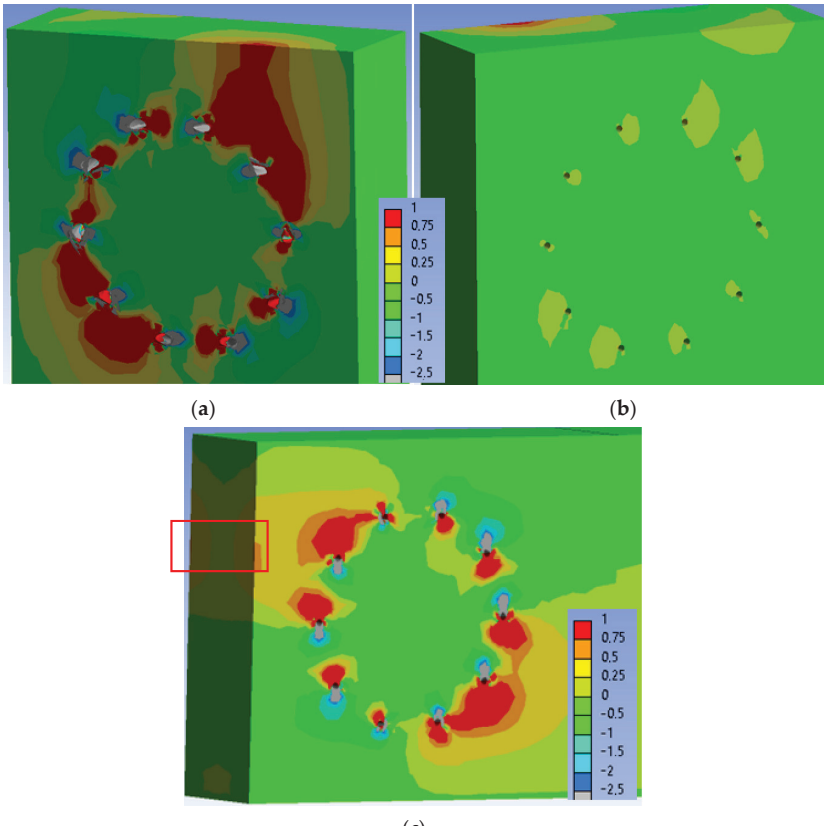

Figure 29. Tensile stress perpendicular to the grain [MPa] at 100% ULS, Experiment B: (**a**) inner side of the stand; (**b**) outer side of the stand; (**c**) rung.

The results of the individual numerical models are listed in Tables 15–17. The first column indicates the load level. The second column shows the maximum force achieved during loading. The third column shows the corresponding value of the bending moment. The fourth column shows the actual deformation caused by the rotational stiffness of the semirigid connection. The fifth column contains the calculated value of the rotational stiffness based on the numerical model. The sixth and the seventh columns contain the standard deviation value and the average value of the experimental data. The eighth column contains the calculated rotational stiffness according to Eurocode 5 [10]. The ninth column shows the ratio between the rotational stiffness obtained from the numerical analysis and the rotational stiffness calculated according to Eurocode 5 [10].

Table 15. Results of quasi-static cyclic numerical modeling for Experiment B at 60% ULS.

Load Level	$F_{60\%,num}$ [kN]	$M_{60\%,num}$ [kNm]	u [mm]	$k_{r,60\%,num}$ [MNm/rad]	$SD_{,kr,num,60}$ [MNm/rad]	$AVG_{,kr,num,60}$ [MNm/rad]	$k_{r,u,EC5}$ [MNm/rad]	Num/u [-]
60% ULS	6.31	4.86	7.68	0.469	0.007	0.457	0.323	1.45
			7.81	0.461				1.43
			7.92	0.454				1.41
			8.02	0.449				1.39
			7.92	0.454				1.41

Table 16. Results of quasi-static cyclic numerical modeling for Experiment B at 80% ULS.

Load Level	$F_{80\%,num}$ [kN]	$M_{80\%,num}$ [kNm]	u [mm]	$k_{r,80\%,num}$ [MNm/rad]	$SD_{,kr,num,80}$ [MNm/rad]	$AVG_{,kr,num,80}$ [MNm/rad]	$k_{r,u,EC5}$ [MNm/rad]	Num/u [-]
80% ULS	6.31	6.24	17.09	0.281	0.024	0.304	0.323	0.87
			17.53	0.274				0.85
			15.92	0.302				0.93
			14.59	0.329				1.02
			14.39	0.334				1.03

Table 17. Results of quasi-static cyclic numerical modeling for Experiment B at 100% ULS.

Load Level	$F_{100\%,num}$ [kN]	$M_{100\%,num}$ [kNm]	u [mm]	$k_{r,100\%,num}$ [MNm/rad]	$SD_{,kr,num,100}$ [MNm/rad]	$AVG_{,kr,num,100}$ [MNm/rad]	$k_{r,u,EC5}$ [MNm/rad]	Num/u [-]
100% ULS	10.17	7.83	10.36	0.582	0.038	0.638	0.323	1.80
			9.85	0.612				1.89
			9.50	0.635				1.97
			8.97	0.672				2.08
			8.78	0.687				2.13

4. Discussion

When testing the specimens by nondestructive quasi-static cyclic loading, the audible signals of the specimen failure did not occur, due to the low load level. This also applies to the 100% of the ultimate limit state. Each specimen was loaded with a value of about 2 kN before the start of the cyclic testing, in order to eliminate the concave shape of load–deformation curves. The fasteners were activated, and the initial consolidation of the connection and the initial slip took place by loading with this small force.

An interesting course shown in Figure 30 can be observed by comparing the trends of rotational stiffness with the increasing load. The connection using bolts and dowels loses its rotational stiffness with the increasing load. On the contrary, the rotational stiffness of the connection using screws increases with the increasing load. The increase in rotational stiffness can be attributed to the axial forces that are generated in fasteners during its transverse loading. The transverse loading leads to the deformation of fasteners and thus to the loss of rotational stiffness in the initial phase of the loading. Increasing loading begins to generate axial forces in screws [40]. The transverse deformation is straightened again, thanks to the thread along the entire screw length. This phenomenon results in a gradual increase in the rotational stiffness during loading. Such a phenomenon does not occur with the connection using bolts and dowels, because the number of bolts is low and the effect of the washer and nut is not sufficient.

The results according to Eurocode 5 [9] represent a method for calculation of slip modulus. Possible variations of the results were created for comparison in order to capture the real rotational stiffness value using an analytical equation as accurately as possible. The rotational stiffness value from the last cycle (i.e., the fifth cycle) is used in the following tables.

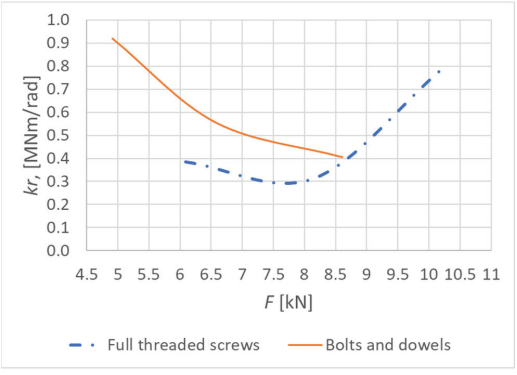

Figure 30. Comparison of the rotational stiffness trends.

Table 18 shows results obtained using the individual approaches. The third column represents the rotational stiffness value obtained experimentally. The fourth column contains the value obtained by the numerical modeling. The rotational stiffness value calculated according to Eurocode 5 [10] using the outer fastener diameter and the standard value of timber density is shown in the fifth column. The sixth column contains the values calculated according to Eurocode 5 [10] using the inner fastener diameter and the standard value of timber density. The rotational stiffness value calculated according to Eurocode 5 [10] using the actual measured timber density and diameter of the fastener shank is shown in the seventh column.

Table 18. Comparison of rotational stiffness results.

Type of Fastener	Test	$k_{r,\,test}$ [MNm/rad]	$k_{r,\,num}$ [MNm/rad]	$k_{r,\,EC5}$ [MNm/rad]	$k_{r,\,RS}$ [MNm/rad]	$k_{r,\,RSD}$ [MNm/rad]
Bolts and dowels	60% ULS	0.894	0.905	0.323	0.293	0.299
	80% ULS	0.548	0.634			
	100% ULS	0.404	0.385			
Fully threaded screws	60% ULS	0.386	0.454		0.202	0.206
	80% ULS	0.313	0.334			
	100% ULS	0.896	0.687			

It can be seen in the table that all values (with the exception of screws to a load level of 80% ULS) are above the value of rotational stiffness calculated according to the standard equation for the slip modulus. From the point of view of a safer design, it is necessary to take into account the actual inner diameter, because it has a huge influence on the calculated values. The standard states the use of the fastener diameter, but does not define whether its actual inner core diameter or outer thread diameter. Based on the presented results, it is desirable to recommend the use of the inner core diameter of the fastener.

It is also possible to see relatively good accuracy with the numerical modeling. The numerical models thus provide details that are difficult to achieve during experimental testing, e.g., the stress curves during loading. No elements of connections were broken during experimental testing. The numerical models also correctly assumed this fact.

5. Conclusions

The paper was focused on the issue of the semirigid connection, which was composed of a timber rung and two stands using dowel-type fasteners. Six specimens were tested by quasi-static nondestructive cyclic loading. Three specimens were made from a combination of bolts and dowels and three specimens from fully threaded screws. The work required the creation of analytical assumptions, which were the basis for the design of the experimental testing and were subsequently used to compare the results.

Experimental testing proved that the connection created from a combination of bolts and dowels (Experiment A) is safe and reliable until the ultimate limit state. The rotational stiffness of this connection is higher than the standard estimate for the ultimate limit state during the entire loading process.

Testing further showed, that the connection created from fully threaded screws (Experiment B) was also safe and reliable until the ultimate limit state. The rotational stiffness of this connection was not higher than the standard estimate for the ultimate limit state for a load level corresponding to 80% ULS. The experiment indicates that in order to achieve more accurate results of rotational stiffness according to Eurocode 5 [9], it is necessary to use the inner core diameter of the fastener shank for the calculation of the slip modulus. Alternatively, it is possible to use the diameter of the fastener shank and the actual measured timber density. However, from a practical point of view, it is almost impossible to use the actual measured timber density for the standard calculations. The obtained data showed that the use of the inner core diameter of the fastener and the standard value of timber density for the standard calculations is sufficiently accurate.

The issue of determining the load-carrying capacity of connections in timber structures according to the European standards for the design of timber structures Eurocode 5 [10] is still under development. The proposed experiments should also contribute to this trend. The experiments were focused on determining the rotational stiffness of a semirigid connection of a rung and two stands using dowel-type mechanical fasteners.

The data from the experiments can be used for the practical design of this type of semirigid connection from the point of view of the rotational stiffness.

Author Contributions: Conceptualization, M.J.; validation, D.M. and A.L.; data curation, M.J.; methodology, P.D.; visualization, M.J.; formal analysis and writing—original draft, M.J.; supervision, A.L.; writing—review and editing, M.J. and P.D. All authors have read and agreed to the published version of the manuscript.

Funding: This research was funded by VSB-TUO by the Ministry of Education, Youth and Sports of the Czech Republic. The supported project has the number 2022/55 of the Student Research Grant Competition of the VSB—Technical University of Ostrava.

Institutional Review Board Statement: Not applicable.

Informed Consent Statement: Not applicable.

Data Availability Statement: Data are contained within the article.

Acknowledgments: Experimental measurements and research were carried out thanks to VSB—Technical University of Ostrava. The work was supported by the Student Research Grant Competition of the VSB—Technical University of Ostrava under identification number 2022/55.

Conflicts of Interest: The authors declare no conflict of interest.

References

1. Granholm, H. *Om Sammansatta Balkar och Pelare med Särskild Hänsyn Till Spikade Träkonstruktionr. Handlingar 88*; Chalmers Tekniska Högskola: Sweden, Gothenburg, 1949.
2. Granholm, H. *Der Einsturz des Bogengerüstes der Sandöbrücke*; Verlag der Akademie der Wissenschaften und der Literatur: Mainz, Germany, 1963.
3. Ehlbeck, J. Load-carrying capacity and deformation characteristics of nailed joints. In Proceedings of the CIB-W18, Paper 12-7-1, Bordeaux, France, 29 October 1979.
4. Dubas, P.; Gehri, E.; Steurer, T. *Einführung in die Norm SIA 164 (1981)–Holzbau*; Publication No. 81-1; Baustatik und Stahlbau; ETH: Zürich, Switzerland, 1981.
5. Lokaj, A.; Dobes, P.; Sucharda, O. Effects of Loaded End Distance and Moisture Content on the Behavior of Bolted Connections in Squared and Round Timber Subjected to Tension Parallel to the Grain. *Materials* **2020**, *13*, 5525. [CrossRef] [PubMed]
6. Ehlbeck, J.; Werner, H. Untersuchungen über die Tragfähigkeit von Stabdübelverbindungen. *Holz Roh Werkst.* **1988**, *46*, 281–288. [CrossRef]
7. Stoy, W. *Holz-Nagelbau nach DIN 1052, 3. Ausgabe, 1940. 4. Ergänzte und Verbesserte Auflage*; Schriftenreihe der Reichsarbeitsgemeinschaft Holz e. V; Reichsnährstandsverlag: Berlin, Germany, 1942.

8. Ehlbeck, J.; Larsen, H.J. Eurocode 5 design of timber structures: Joints. In *International Workshop on Wood Connectors*; Barnes, M., Brauner, A., Galligan, W., Leichti, R., Soltis, L., Eds.; Forest Products Society: Madison, WI, USA, 1993.
9. Jorissen, A. Double Shear Timber Connections with Dowel Type Fasteners. Ph.D. Thesis, Delft University of Technology, Delft, The Netherlands, 1998.
10. *EN 1995-1-1*; Eurocode 5: Design of Timber Structures—Part 1-1: General—Common Rules and Rules for Buildings. Czech Standards Institute: Praha, Czech Republic, 2006.
11. Kozelouh, B. *Timber Structures According to Eurocode 5; STEP 1: Design and Construction Materials; Translated by Bohumil Kozelouh*; KODR: Zlin, Czech Republic, 1998; ISBN 80-238-2620-4. (In Czech)
12. Solarino, F.; Giresini, L.; Chang, W.-S.; Huang, H. Experimental Tests on a Dowel-Type Timber Connection and Validation of Numerical Models. *Buildings* **2017**, *7*, 116. [CrossRef]
13. Vavrusova, K.; Mikolasek, D.; Lokaj, A.; Klajmonova, K.; Sucharda, O. Determination of carrying capacity of steel-timber joints with steel rods glued-in parallel to grain. *Wood Res.* **2016**, *61*, 733–740.
14. Vassiliou, V.; Barboutis, I.; Kamperidou, V. Strength of Corner and Middle Joints of Upholstered Furniture Frames Constructed with Black Locust and Beech Wood. *Wood Res.* **2016**, *61*, 495–504.
15. Cai, Y.; Young, B. Effects of end distance on thin sheet steel bolted connections. *Eng. Struct.* **2019**, *196*, 109331. [CrossRef]
16. Požgaj, A.; Kürjatko, S. Wood properties of spruce from forests affected by pollution in Czechoslovakia. *IAWA J.* **1986**, *7*, 405–410. [CrossRef]
17. Mirski, R.; Dziurka, D.; Chuda-Kowalska, M.; Wieruszewski, M.; Kawalerczyk, J.; Trociński, A. The Usefulness of Pine Timber (*Pinus sylvestris* L.) for the Production of Structural Elements. Part I: Evaluation of the Quality of the Pine Timber in the Bending Test. *Materials* **2019**, *13*, 3957. [CrossRef]
18. Mirski, R.; Dziurka, D.; Chuda-Kowalska, M.; Kawalerczyk, J.; Kuliński, M.; Łabęda, K. The Usefulness of Pine Timber (*Pinus sylvestris* L.) for the Production of Structural Elements. Part II: Strength Properties of Glued Laminated Timber. *Materials* **2020**, *13*, 4029. [CrossRef]
19. Nowak, T.; Karolak, A.; Sobótka, M.; Wyjadłowski, M. Assessment of the Condition of Wharf Timber Sheet Wall Material by Means of Selected Non-Destructive Methods. *Materials* **2019**, *12*, 1532. [CrossRef]
20. Nowak, T.; Patalas, F.; Karolak, A. Estimating Mechanical Properties of Wood in Existing Structures—Selected Aspects. *Materials* **2021**, *14*, 1941. [CrossRef] [PubMed]
21. Bragov, A.; Igumnov, L.; dell'Isola, F.; Konstantinov, A.; Lomunov, A.; Iuzhina, T. Dynamic Testing of Lime-Tree (Tilia Eu-ropoea) and Pine (Pinaceae) for Wood Model Identification. *Materials* **2020**, *13*, 5261. [CrossRef] [PubMed]
22. Olaoye, K.; Aguda, L.; Ogunleye, B. Prediction of Mechanical Properties of Hardwood Species Using the Longitudinal Vib-ration Acoustic Method. *For. Prod. J.* **2021**, *71*, 391. [CrossRef]
23. Martínez, R.D.; Balmori, J.-A.; Llana, D.F.; Bobadilla, I. Wood Density and Moisture Content Estimation by Drilling Chips Extraction Technique. *Materials* **2020**, *13*, 1699. [CrossRef]
24. Dobes, P.; Lokaj, A.; Mikolasek, D. Load-Carrying Capacity of Double-Shear Bolted Connections with Slotted-in Steel Plates in Squared and Round Timber Based on the Experimental Testing, European Yield Model, and Linear Elastic Fracture Mechanics. *Materials* **2022**, *15*, 2720. [CrossRef]
25. Braun, M.; Pełczyński, J.; Al Sabouni-Zawadzka, A.; Kromoser, B. Calibration and Validation of a Linear-Elastic Numerical Model for Timber Step Joints Based on the Results of Experimental Investigations. *Materials* **2022**, *15*, 1639. [CrossRef]
26. Burawska-Kupniewska, I.; Beer, P. Near-Surface Mounted Reinforcement of Sawn Timber Beams-FEM Approach. *Materials* **2021**, *14*, 2780. [CrossRef] [PubMed]
27. Zhou, S.; Li, Z.; Feng, S.; Zhu, H.; Kang, S. Effects of bolted connections on behaviour of timber frames under combined vertical and lateral loads. *Constr. Build. Mater.* **2021**, *293*, 123542. [CrossRef]
28. Wang, M.; Song, X.; Gu, X.; Tang, J. Bolted glulam beam-column connections under different combinations of shear and bending. *Eng. Struct.* **2019**, *181*, 281–292. [CrossRef]
29. Wang, X.T.; Zhu, E.C.; Niu, S.; Wang, H.J. Analysis and test of stiffness of bolted connections in timber structures. *Constr. Build. Mater.* **2021**, *303*, 124495. [CrossRef]
30. Johanides, M.; Kubíncová, L.; Mikolášek, D.; Lokaj, A.; Sucharda, O.; Mynarčík, P. Analysis of Rotational Stiffness of the Timber Frame Connection. *Sustainability* **2021**, *13*, 156. [CrossRef]
31. Johanides, M.; Mikolasek, D.; Lokaj, A.; Mynarcik, P.; Marcalikova, Z.; Sucharda, O. Rotational Stiffness and Carrying Capacity of Timber Frame Corners with Dowel Type Connections. *Materials* **2021**, *14*, 7429. [CrossRef] [PubMed]
32. Johanides, M.; Lokaj, A.; Mikolasek, D.; Mynarcik, P.; Dobes, P.; Sucharda, O. Timber Semirigid Frame Connection with Improved Deformation Capacity and Ductility. *Buildings* **2022**, *12*, 583. [CrossRef]
33. LaborTech. Available online: https://www.labortech.cz (accessed on 25 November 2021).
34. Ahlborn. Available online: https://www.ahlborn.com (accessed on 25 November 2021).
35. *EN 26891*; Timber Structures. Joints Made with Mechanical Fasteners. General Principles for the Determination of Strength and Deformation Characteristics. Czech Office for Standards. Metrology and Testing: Praha, Czech Republic, 1994.
36. Ansys. Available online: https://www.ansys.com/ (accessed on 25 November 2021).
37. Brožovský, Jiří a Alois Materna. Metoda Konečných Prvkůve Stavební Mechanice. 2012. Available online: https://docplayer.cz/414068-Metoda-konecnych-prvku-ve-stavebni-mechanice.html (accessed on 1 July 2022).

38. David, M. *Numerické Modelování Vybraných Spojů Dřevěných Konstrukcí*; Disertační práce; Vysoká škola báňská–Technická univerzita: Ostrava, Czech Republic, 2012.
39. Gunderson, R.A.; Goodman, J.R.; Bodig, J. Plate Tests for Determination of Elastic Parameters of Wood. *Wood Sci.* **1973**, *5*, 241–248.
40. Larsen, H.J.; Reestrup, V. Tests on screws in wood. *Bygn. Medd.* **1969**, *1*, 3–36.

materials

MDPI

Article

Numerical and Experimental Analysis of the Load-Carrying Capacity of a Timber Semi-Rigid Dowel-Type Connection

Marek Johanides [1,2,*], Antonin Lokaj [1], Pavel Dobes [2] and David Mikolasek [1]

[1] Department of Structures, Faculty of Civil Engineering, VSB-Technical University of Ostrava, 708 00 Ostrava, Czech Republic
[2] Department Centre of Building Experiments, Faculty of Civil Engineering, VSB-Technical University of Ostrava, 708 00 Ostrava, Czech Republic
* Correspondence: marek.johanides@vsb.cz

Abstract: The paper deals with the analysis of the load-carrying capacity of a timber semi-rigid connection created from a system of two stands and a rung. The connection was made from glued laminated timber with metal mechanical dowel-type fasteners. Not only a common combination of bolts and dowels, but also fully threaded screws were used for the connection. The aim of the research and its motivation was to replace these commonly used fasteners with more modern ones, to shorten and simplify the assembly time, and to improve the load-carrying capacity of this type of connection. Each of these two types of connections was loaded statically, with a slow increase in force until failure. The paper presents results of the experimental testing. Three specimens were made and tested for each type of the connection. Experimental results were subsequently compared with numerical models. The achieved results were also compared with the assumption according to the currently valid standard. The results indicate that a connection using fully threaded screws provides a better load-carrying capacity.

Keywords: bolts and dowels; dowel-type fasteners; FEM; frame connection; fully threaded screws; glued laminated timber; numerical model; rotational stiffness

Citation: Johanides, M.; Lokaj, A.; Dobes, P.; Mikolasek, D. Numerical and Experimental Analysis of the Load-Carrying Capacity of a Timber Semi-Rigid Dowel-Type Connection. *Materials* **2022**, *15*, 7222. https://doi.org/10.3390/ma15207222

Academic Editors: Radosław Mirski and Raffaele Landolfo

Received: 12 September 2022
Accepted: 14 October 2022
Published: 17 October 2022

Publisher's Note: MDPI stays neutral with regard to jurisdictional claims in published maps and institutional affiliations.

1. Introduction

Since the mid-1950s, many countries have carried out extensive research in the area of wood-based materials and their fasteners. Special regulations for construction procedures were necessary in some countries because of the different species of timber. This led to various theories, which resulted in even more significant differences in design criteria. The progress in timber engineering design soon showed the need for more extensive research in the behavior of timber structures, including their connections. Experimental tests made in Forest Products Laboratory *Wilson 1917* [1] were among the first instances of research in the area of nailed connections.

The current model for the determination of the load-carrying capacity of dowel-type connections under a lateral load is the European yield model, abbreviated as EYM. The EYM theory arose from the research of the Danish scientist *Johansen 1941* [2], when he first applied this theory to timber fasteners. Eight years later, *Johansen 1949* [3] published an original article about EYM in English. Some of his research remained unfinished, and the results were unpublished for years. Finally, this research was completed and published by *Larsen 1977* [4]. The theory was based on, and later experimentally verified on single-shear and double-shear connections with one nail by *Möller 1951* [5]. Other researchers followed up on the groundbreaking research in the area of the design of connections in timber structures. American scientist *Kuenzi 1955* [6] dealt with a permissible transverse load of single-shear and double-shear nailed and bolted connections. The scientific articles by Johansen and Möller were complemented with the load–deformation response of nailed and bolted connections. It was found that the plastic deformation of a fastener causes

non-linearity and contributes significantly to the load-carrying capacity of the connection. He presented the idea of a fastener as a beam on an elastic foundation (supported by so-called Winkler springs; see *Winkler 1867* [7]). The derived relations were valid for the elastic branch of the load–deformation curve of the connection. However, they became the basis for further research in the modeling of dowel-type connections using nonlinear parameters for embedment in timber; for example, the ariticle by *Foschi 2000* [8].

Meyer 1957 [9] tested nailed connections with different qualities of timber and nails, and proved that the load-carrying capacity of the connection is significantly influenced by the thickness and the embedment strength of the used timber. *Doyle 1964* [10] observed that there is a dependence between the load-carrying capacity and the end distance, the spacings parallel to the grain, and the fastener diameter. *Mack 1966* [11] created an analytical model for transversely loaded nailed connections, where the load–deformation response to short-term loading is influenced by many mutual independent factors. *Larsen and Reestrup 1969* [12] investigated screwed connections and found that the conditions in a transversely loaded screwed connection differ slightly from a bolted connection due to the thread of the screw. This meant that different values of the fastener yield moment had to be considered. *Norén 1974* [13] stated different formulas for different types of connections in timber structures. *Larsen 1973* [14] proposed a supporting rationale for the EYM theory in the Scandinavian countries. Afterwards, *Larsen 1979* [15] proposed a theoretical background and approximations for screwed connections. The findings were later included into the *CIB Structural Timber Design Code 1983* [16]. The EYM model was further refined depending on the angle between the applied force and the grain direction; see *Smith and Whale 1986* [17]. It was proven that the direction of the applied force has no influence on the load-carrying capacity of connections with dowel-type fasteners up to a diameter of 8 mm. This work also became the basis for a standard relationship for the embedment strength. *Ehlbeck and Werner 1992* [18] followed up on this scientific article and investigated the load-carrying capacity of dowel-type connections depending on various selected parameters. *Blaß 2000* [19] dealt with the bending properties of dowel-type metal fasteners. He derived an empirical relationship that is used in the current standard for the calculation of the yield moment. Currently, the load-carrying capacity of connections is calculated on the basis of the relationships given in *Eurocode 5* [20]. This standard provides sufficient findings for determining the load-carrying capacity of transversely loaded connections in timber structures. However, the standard does not provide the procedure for calculating the load-carrying capacity of a connection loaded by the bending moment. Therefore, *Koželouh 1998* [21] was used to determine this load-carrying capacity.

Dowel-type fasteners, such as screws, bolts, and dowels, are one of the most popular fasteners in timber structures, not only in timber-to-timber connections—*Solarino 2017* [22] and *Vavrusova 2016* [23]—but also in steel-to-timber and aluminum-to-timber connections; see *Chybiński, Polus 2022* [24], *Chybiński, Polus 2022* [25]. In order to effectively apply dowel-type connections, it is crucial to understand their mechanical behavior under loading. It is desirable to know the relation between the load and slip, stress distribution, or possible different failure modes. The mechanical behavior of connections in timber structures is a complex problem that is influenced by a number of factors. The most important factors are the geometry and arrangement of the connection (i.e., spacings, edge, and end distances) as in *Cai 2019* [26], the material characteristics, the timber species as in *Požgaj 1986* [27], and the method of loading.

The load-carrying capacity and stiffness of connections are influenced by mechanical properties of fasteners and timber. The findings described in *Mirski 2019* [28] and *Mirski 2020* [29] can be used to determine the mechanical properties and to classify the structural timber. It is possible to use selected non-destructive experimental testing, as in *Nowak 2019* [30] and *Nowak 2021* [31]; dynamic testing, as in *Bragov 2020* [32]; and the non-destructive vibrational method described in *Olaoye 2021* [33] in order to determine these mechanical properties. A semi-destructive method can also be used to determine the density and moisture content of timber, as described in *Martínez 2020* [34].

Nowadays, numerical modeling is definitely an important part of experimental testing. It can be an excellent tool for the understanding of the behavior of connections in timber structures. *Dobeš 2022* [35], *Braun 2022* [36], and *Kupniewska 2021* [37] dealt with the calibration and validation of numerical models according to experimental tests.

This paper is focused on the experimental determination of the load-carrying capacity of a semi-rigid connection. The experimental tests are further validated by numerical models. The fist variant of the connection is made of a combination of bolts and dowels in Experiment A. The second variant of the connection is made of high-tensile fully threaded screws in Experiment B. The fasteners in Experiment A are commonly used in practice. Findings on the design of such a semi-rigid connection can be found in *Shu-Rong 2021* [38], *Mingqian 2019* [39], and *Wang 2021* [40]. On the other hand, the fasteners in Experiment B are not commonly used in practice. The presented paper is a follow-up research of *Johanides 2020* [41] and *Johanides 2021* [42]. These papers dealt with determining the rotational stiffness and load-carrying capacity of a timber frame corner, which was made of larger cross-sections with a greater number of fasteners. Small semi-rigid connections with the two already mentioned types of fasteners were subsequently created for a detailed analysis of the connection. The article by *Johanides 2022* [43] dealt with the determination and comparison of the ductility of this connection. The article by *Johanides 2022* [44] dealt with the determination and comparison of the rotational stiffness of this connection. The latest information from the series of tests is presented in this article, which deals with the determination of the load-carrying capacity.

The paper brings findings about the results of the analytical, experimental, and numerical determination of the load-carrying capacity of a semi-rigid connection with mechanical fasteners.

2. Materials and Methods

2.1. Description of Construction and Geometry

The tested specimens corresponded to actual connections used in practice. The arrangement and loading of test specimens was designed to correspond with the actual state of the connection in a real load-carrying structure. The air temperature was 21 °C and the relative air humidity was 55% during the experimental testing. The measurement was performed using TFA DC 106 device.

The structural system for the experiments was created from a semi-rigid connection of two stands and a rung. These structural elements were made of spruce timber, which is the most used structural timber in Central Europe for structural practice due to its availability. The disadvantage of this timber species is its low durability in the outdoor environment. The connection was made with dowel-type metal fasteners. Two identical structural systems were created with different types of fasteners. Experiment A contained a combination of bolts and dowels as fasteners. Experiment B contained fully threaded screws. Glued laminated timber of the strength class GL24h was used. Four-point bending tests were performed to verify the properties of the used timber. Results of the tests have already been published in *Johanides 2022* [43]. The stands were made of a cross-section of 100/300 mm and the rung was made of a cross-section of 100/300 mm. The material properties of the fasteners were also experimentally verified by tensile tests in *Johanides 2022* [43].

The fasteners used in experiment A consisted of bolts and dowels. These were created from a threaded rod with an outer diameter of 8 mm and a core diameter of 7.25 mm. The length of the bolt was 360 mm and the length of the dowels was 300 mm. The fasteners used in experiment B consisted of fully threaded screws with a diameter of 8 mm and a core diameter of 5 mm. Both used materials of fasteners were made of steel, grade 10.9. In addition, the holes for these fasteners were pre-drilled to minimize the initial slip of the connection.

The arrangement was identical for both experiments. The fasteners were located on one symmetrical circle r = 90 mm, with 10 pieces. The arrangement (see Figure 1) was determined according to *Koželouh 1998* [21].

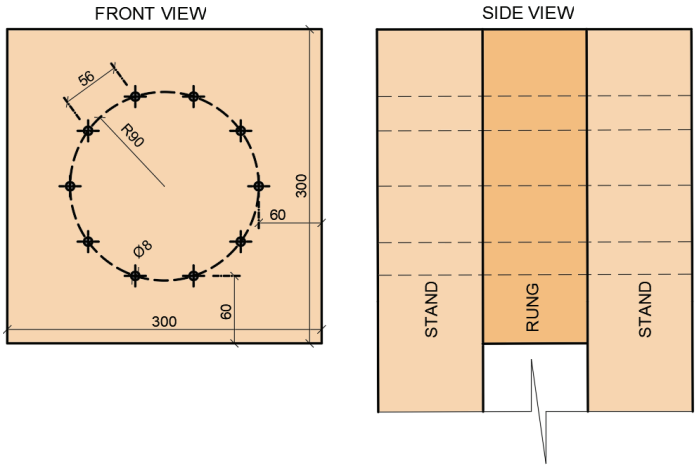

Figure 1. A location of fasteners in test specimens.

The boundary conditions of the structure were created for the execution of the experiments. They were supported by using an auxiliary steel structure. This structure was designed and built for approximately three times the estimated applied force. Timber stands were then attached to the steel structure using 24 bolts with a diameter of 8 mm. The entire steel structure was placed on the reinforced concrete floor and centered at the required distance from the press head so that the press head pressed exactly at the desired location of the rung. After the correct setting of the steel structure, its rear part (Figure 2 on the left) was loaded with a steel cube of 1000 kg. This cube ensured the elimination of the tensile forces caused by the load. The right part did not need to be loaded in any way because only the compressive force was transmitted to this part of the structure. The schematic illustration of the experiment is shown in Figure 2.

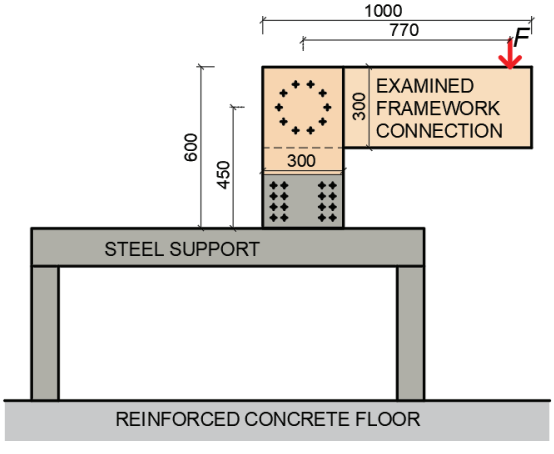

Figure 2. Schematic illustration of the investigated structural system.

2.2. Description of the Testing Machine

The experiments were performed using a LabTest 6.1200 electromechanical testing machine from *Labortech* (Opava, Czech Republic) [45] with a maximum force of 1200 kN. The testing machine is designed for tensile, compressive, static, and cyclic dynamic testing. The machine allows for testing using displacement controlled load. The testing speed

varies from 0.0005 mm/min to 250 mm/min. The machine also allows for testing using force-controlled load up to 1200 kN, with a measurement accuracy of 1%. Control of the test device is provided by a PC with software.

2.3. Description of the Testing

The aim of the static testing was to investigate the total load-carrying capacities of the semi-rigid connection and the failure mode.

Specimens were subjected to a displacement-controlled loading (see Figure 3) after fastening to the auxiliary steel structure. The testing was aimed at determining the maximum load-carrying capacity, and therefore the deformation was measured by the displacement of the crosshead. The loading course was carried out in accordance with the standard *EN 26891* [46]. This standard specifies requirements and test methods for connections in timber structures using mechanical fasteners. The following loading procedure was prescribed:

1. Estimation of the maximum force F_{est} for the tested connection based on experience, calculation, or pretests;
2. Loading of the specimen to 40% of the estimated maximum force, $0.4 \cdot F_{est}$, then holding for 30 s;
3. Unloading to 10% of the estimated maximum force, $0.1 \cdot F_{est}$, then holding for 30 s;
4. Reloading until the specimen fails.

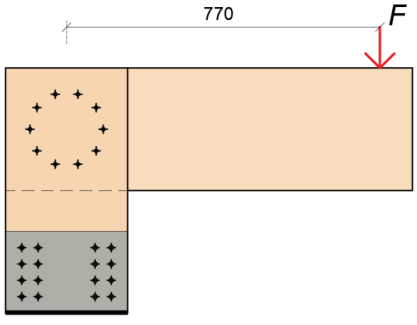

Figure 3. The position of the applied load and deformation measurement.

Table 1 shows the values that determine the course of the experimental loading for Experiment A (bolts and dowels) and Experiment B (fully threaded screws). The load-carrying capacity of the connection F_{ed} was calculated as the design value (using modification factor k_{mod} = 0.90 and partial factor for material properties γ_c = 1.30). This value represents the maximum load-carrying capacity of the connection and was calculated according to *Eurocode 5* [20] and the literature *Koželouh 1998* [21].

Table 1. The course of the experimental testing *Johanides 2022* [43].

Loading Step	Bolts and Dowels		Fully Threaded Screws	
	From (kN)	To (kN)	From (kN)	To (kN)
Step 1	0	4.90	0	6.08
Step 2	Hold		Hold	
Step 3	4.90	1.23	6.08	1.52
Step 4	Hold		Hold	
Step 5	1.23	8.58	1.52	10.63
Step 6	8.58	12.26	10.63	15.19

The loading speed was chosen as constant in kN/min according to the selected loading schemes. The total testing time of one specimen was 15 min.

Figure 4 shows the graphic course of individual experimental tests.

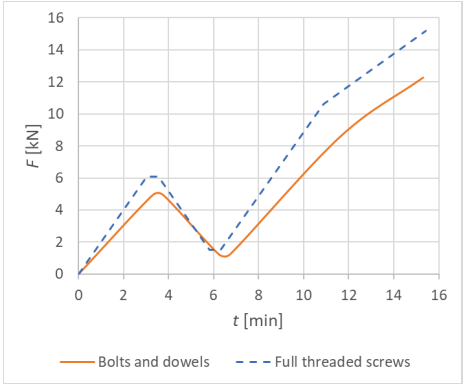

Figure 4. Course of the loading; see *Johanides 2022* [43].

2.4. Experimental Testing

All of the experiments were carried out at the Centre for Building Experiments and Diagnostics at VSB—Technical University of Ostrava, Czech Republic. Figure 5a shows Experiment A, a combination of bolts and dowels. Figure 5b shows Experiment B, fully threaded screws. The load was applied to the connection using a steel cylinder with a diameter of 50 mm. A rubber pad with a thickness of 10 mm was placed under this cylinder to eliminate local damage of the timber rung during loading.

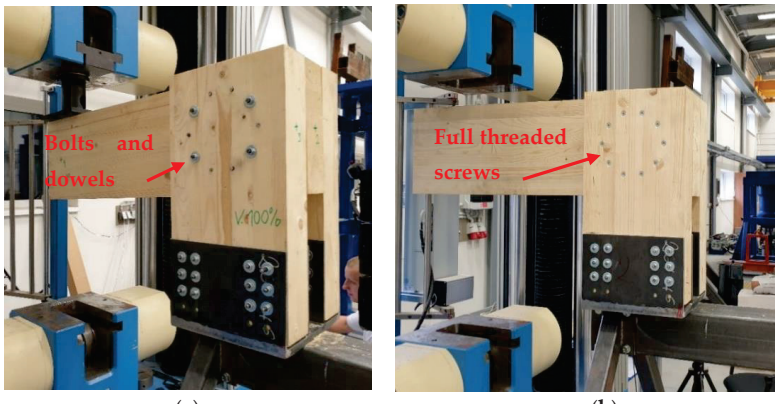

(**a**) (**b**)

Figure 5. Experimental specimens: (**a**) Experiment A, bolts and dowels; (**b**) Experiment B, fully threaded screws; see *Johanides 2022* [43].

2.5. Numerical Modeling

Ansys^{TM} *21* software in the *Workbench 21* environment [47] was used to create the numerical model. The geometry of the model was made up of 3D volume finite elements, which included physical, geometric nonlinearity, and contact elements. The material model of timber was considered orthotropic (see Figure 6) with plastic behavior. The condition of plasticity was created by Hill in *Brožovský 2012* [48]. Neglecting the orthotropy of timber would result in an insufficient representation of the behavior. The dissertation of *Mikolášek 2012* [49] and the publication *Gunderson and Goodman 1973* [50] were used to select the parameters of the material characteristics.

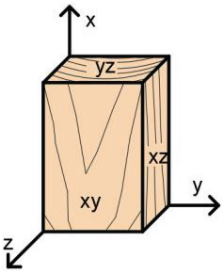

Figure 6. Orthotropy of timber.

The material characteristics of timber are shown in Table 2, and the material characteristics of steel are shown in Table 3. The modulus of elasticity of fasteners was determined on the basis of the experience of the authors.

Table 2. Elastic constants of the material model for timber; see *Johanides 2022* [44].

Timber Properties	Value	Unit
Young's modulus in *X*	9200	MPa
Young's modulus in *Y*	740	MPa
Young's modulus in *Z*	400	MPa
Poisson's ratio in *XY*	0.47	-
Poisson's ratio in *YZ*	0.25	-
Poisson's ratio in *XZ*	0.37	-
Shear modulus in *XY*	650	MPa
Shear modulus in *YZ*	38	MPa
Shear modulus in *XZ*	700	MPa

Table 3. Elastic constants of the material model of fasteners; see *Johanides 2022* [44].

Steel Properties	Value	Unit
Young's modulus	190,000	MPa
Poisson's ratio	0.30	-

The values of the plastic behavior of timber (see Table 4) and the plastic behavior of steel (see Table 5) were obtained based on an experimental testing. The results of the testing have already been published in [43].

Table 4. Values for the plastic behavior of the material model for timber; *Johanides 2022* [44].

Hill Yield Criterion	Value	Unit
Yield strength in *X*	32	MPa
Yield strength in *Y*	1	MPa
Yield strength in *Z*	1	MPa
Yield strength in *XY*	6	MPa
Yield strength in *YZ*	3	MPa
Yield strength in *XZ*	6	MPa

The Hill yield criterion allows us to set a single value for the hardening modulus of all directions. It was set to 10 MPa for a good numerical convergence.

Figure 7 shows individual numerical models that were used for the analysis of the load-carrying capacity. The connection with bolts and dowels (Experiment A) contained 253,961 nodes, 67,432 finite elements, and 730,642 equations. The connection with fully threaded screws (Experiment B) contained 237,743 nodes, 61,565 finite elements, and 678,822 equations.

Table 5. Values for the plastic behavior of the material model for steel; see *Johanides 2022* [44].

Bolts and Dowels		
	Value	**Unit**
Yield strength	670	MPa
Ultimate strength	970	MPa
Hardening modulus	1000	MPa
Fully Threaded Screws		
	Value	**Unit**
Yield strength	690	MPa
Ultimate strength	1075	MPa
Hardening modulus	1000	MPa

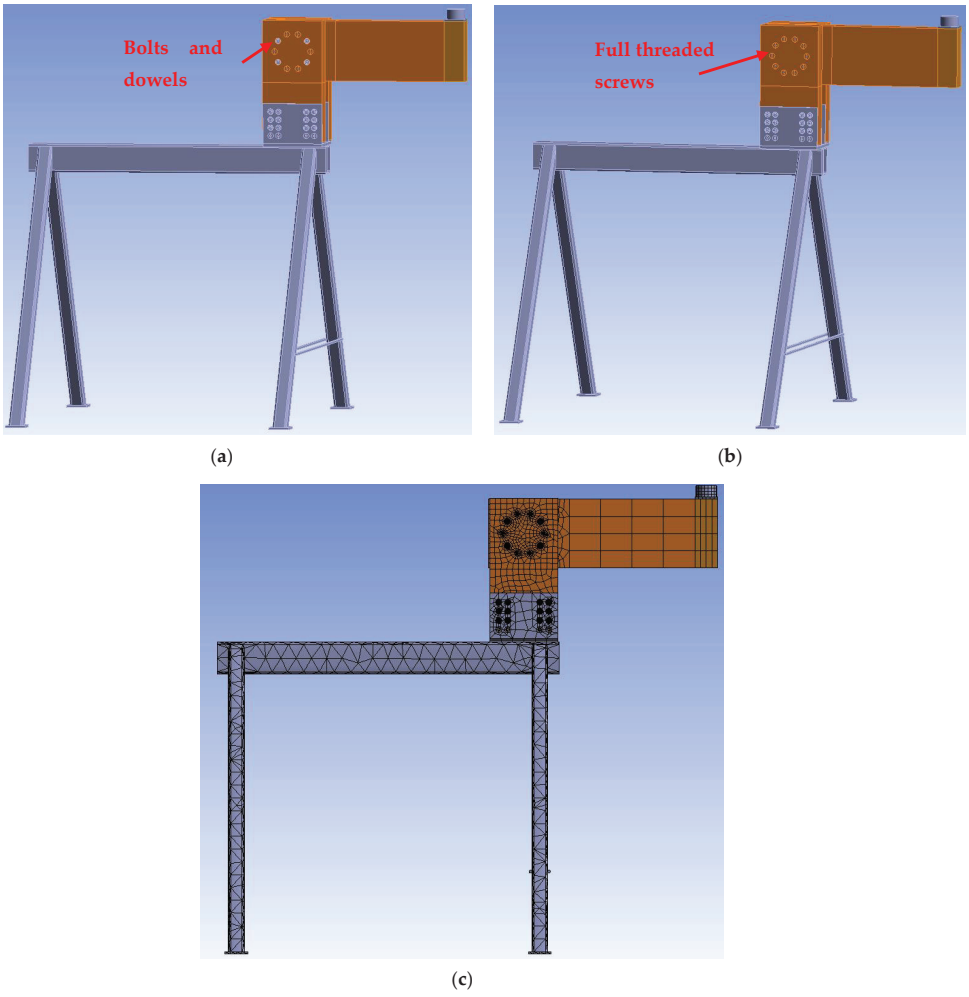

Figure 7. Numerical models: (**a**) Experiment A, bolts and dowels; (**b**) Experiment B, fully threaded screws; (**c**) finite element mesh in the overall model view.

Figure 8 shows the boundary conditions of the numerical model. A vertical displacement of all stands of the auxiliary steel structure was disabled. In addition, a vertical force of 5 kN was applied to each rear stand to prevent the vertical displacement and the overturning of the steel structure. Such a choice of boundary conditions ensured the real conditions that were used during the experimental testing.

Figure 8. Boundary conditions of the numerical models.

It is very important to correctly apply the load into the numerical model. Figure 9 shows the finite element mesh for both numerical models for applying the load using the press head (cylinder) of the testing machine. The model was loaded as vertical displacement (displacement-controlled loading), which represented the actual loading by the cylinder during the experimental testing. The numerical model used the Newton–Raphson incremental–iterative method. The number of increments was the selected logic setting of the Ansys^{TM} software [47], with an initial step of 0.001 s and a maximum step of 0.04 s.

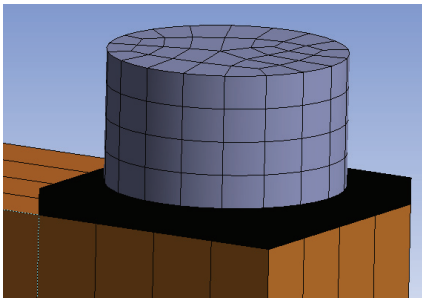

Figure 9. Finite element mesh for applying load.

The finite element mesh was created from 3D finite elements. Tetrahedral finite elements were used for most of the steel structure, and hexahedral elements were used for the timber structure and fasteners. A finer mesh of finite elements was created around contact of timber with fasteners. The finite element ratio of 3:1 (length to height of finite elements) was used based on general FEM modeling recommendations; see *Brožovský 2012* [48]. Frictional contacts were used between the individual segments of the structure. The coefficient of friction between timber–timber elements was 0.40, steel–steel 0.10, and timber–steel 0.30 [51]. The interaction between the steel cylinder and the rubber pad was created using a coefficient of friction of 0.50. This rubber pad was firmly connected to the timber in order to achieve a good convergence. Figure 10 shows the finite element mesh for Experiment A, bolts and dowels. Figure 11 shows the finite element mesh for Experiment B, fully threaded screws.

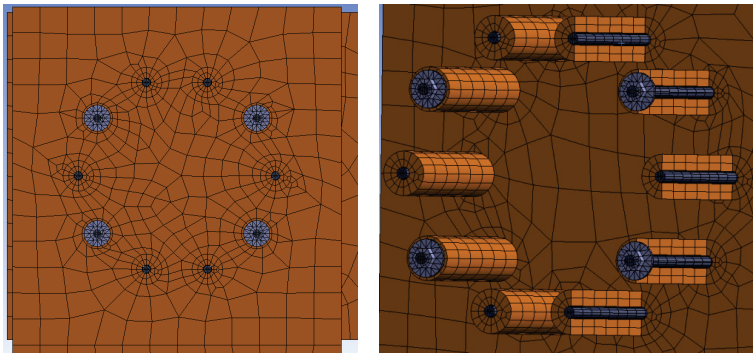

Figure 10. Finite element mech for Experiment A, bolts and dowels.

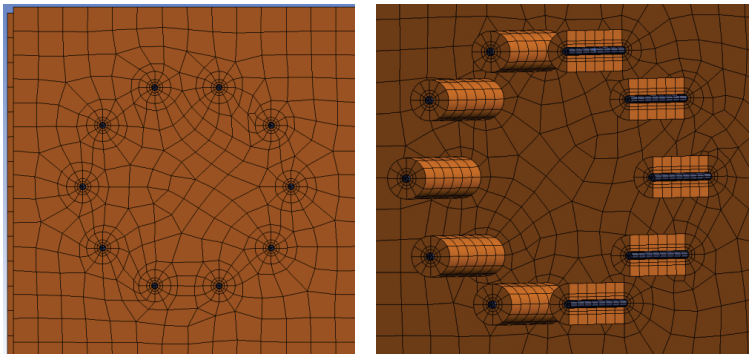

Figure 11. Finite element mech for Experiment B, fully threaded screws.

3. Results

3.1. Results of Experimental Testing

3.1.1. Experiment A, Bolts and Dowels

Figure 12 shows broken specimens after the quasi-static destructive experimental testing. Each specimen was broken in the rung when the tensile stress perpendicular to the grain was exceeded. It is important to state that the failure occurred in timber outside the glued joint between individual lamellas.

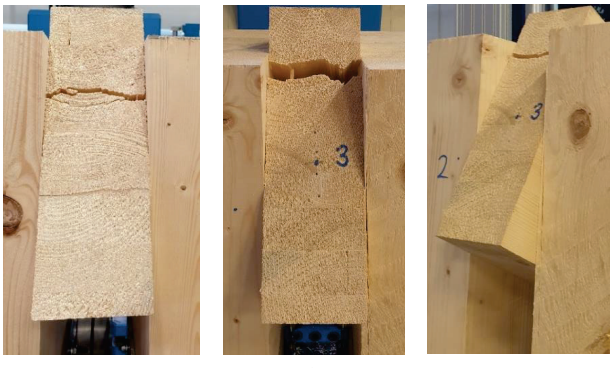

(**a**) (**b**) (**c**)

Figure 12. Experiment A, bolts and dowels: (**a**) test 1; (**b**) test 2; (**c**) test 3.

Figure 13 shows load–deformation curves from the experimental testing for Experiment A, bolts and dowels.

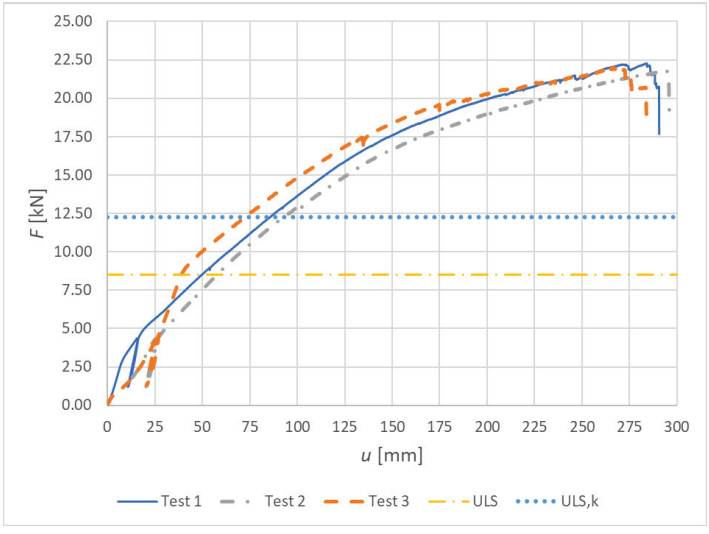

Figure 13. Experiment A: Load–deformation curves of destructive quasi-static cyclic testing for individual specimens made from a combination of bolts and dowels.

3.1.2. Experiment B, Fully Threaded Screws

Figure 14 shows broken specimens after the quasi-static destructive experimental testing. Even when testing specimens with fully threaded screws, each specimen was broken in the rung when the tensile stress perpendicular to the grain was exceeded. The failure also occurred in timber outside the glued joint between individual lamellas.

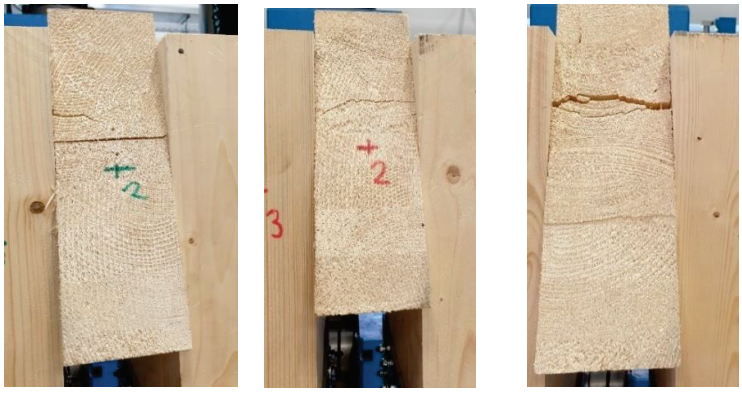

(**a**) (**b**) (**c**)

Figure 14. Experiment B, fully threaded screws: (**a**) test 1; (**b**) test 2; (**c**) test 3.

Figure 15 shows load–deformation curves from the experimental testing for Experiment B, fully threaded screws.

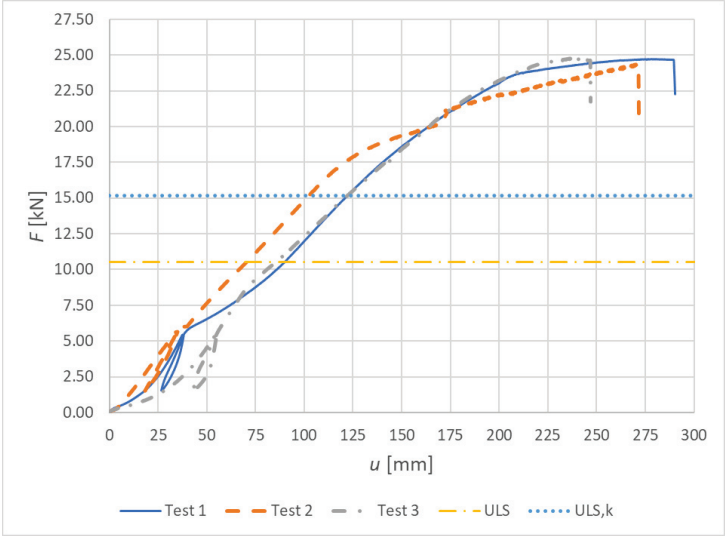

Figure 15. Experiment B: Load–deformation curves of destructive quasi-static cyclic testing for individual specimens made from fully threaded screws.

3.2. Tabular Results of the Experimental Testing

The results of the individual tests are listed in Tables 6 and 7. The first column indicates the specimen number. The second column shows the maximum force achieved during loading (i.e., the actual load-carrying capacity). The third column shows the calculated load-carrying capacity according to *Eurocode 5* [20] (using modification factor k_{mod} = 0.90 and partial factor for material properties γ_{con} = 1.30). The fourth column contains the calculated load-carrying capacity without using the modification and partial factor. The fifth column shows the ratio between the load-carrying capacity based on the experimental testing and calculation according to *Eurocode 5* [20] using the modification and partial factor. The sixth column shows the ratio between the load-carrying capacity based on the experimental testing and calculation according to *Eurocode 5* [20] without using the modification and partial factor. The seventh column shows the maximum value of the vertical displacement of the rung end. The eighth column shows the maximum bending moment calculated from the value in the second column.

Table 6. Results of Experiment A, bolts and dowels; see *Johanides 2022* [43].

Specimen	$F_{max,test}$ (kN)	$F_{max,d}$ (kN)	$F_{max,k}$ (kN)	d (-)	k (-)	u (mm)	M (kNm)
1	22.29			2.62	1.82	290.60	17.16
2	21.78	8.51	12.26	2.56	1.78	295.67	16.77
3	22.02			2.59	1.80	283.56	16.96

Table 7. Results of Experiment B, fully threaded screws; see *Johanides 2022* [43].

Specimen	$F_{max,test}$ (kN)	$F_{max,d}$ (kN)	$F_{max,k}$ (kN)	d (-)	k (-)	u (mm)	M (kNm)
1	24.72			2.35	1.63	290.50	19.03
2	24.37	10.52	15.19	2.32	1.60	271.85	18.76
3	24.65			2.34	1.62	247.10	18.98

3.3. Results of Numerical Modeling

3.3.1. Experiment A, Bolts and Dowels

Figure 16 shows the load–deformation curve from the numerical modeling for Experiment A, bolts and dowels. The values of the maximum achieved deformation and load-carrying capacity are shown in Table 8.

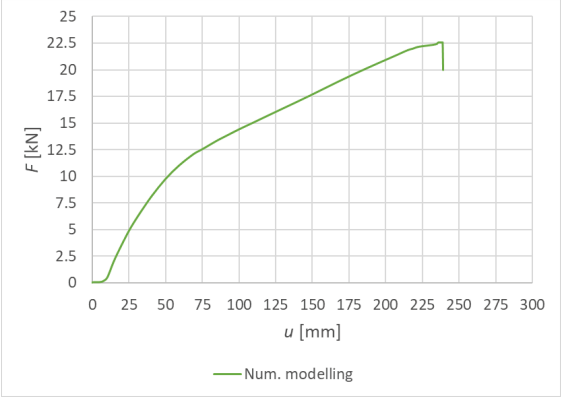

Figure 16. Experiment A: Load–deformation curves of quasi-static numerical modeling for individual specimens made from a combination of bolts and dowels.

Table 8. Results of numerical modeling, Experiment A.

F_{num} (kN)	u (mm)	M (kNm)
22.60	238.64	17.40

Figure 17 shows the overall deformation of the connection, including the deformation of the auxiliary steel structure. This deformation describes the actual behavior of the entire structure during loading.

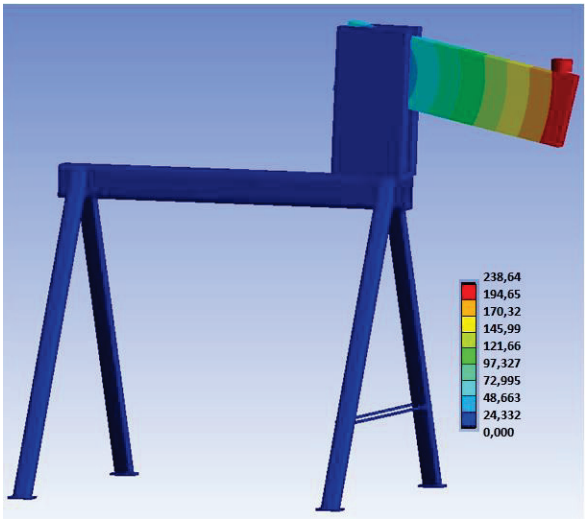

Figure 17. Overall deformation of the structure (mm) for Experiment A.

Figure 18 shows an "X-ray" view of the connection. It is possible to observe the embedment of timber around the holes for fasteners and the formation of two plastic hinges in fasteners.

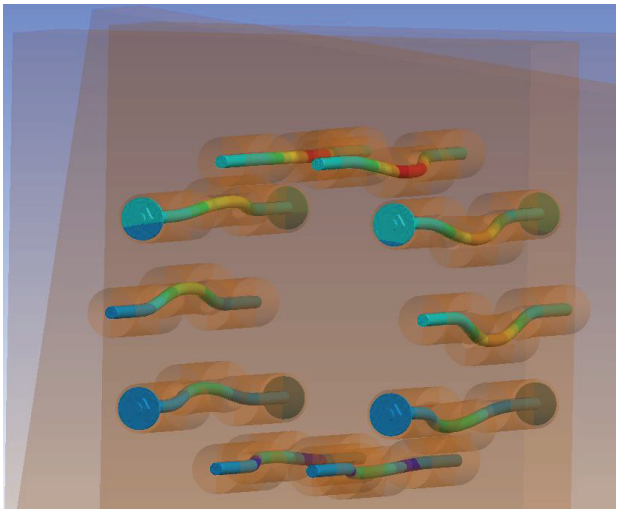

Figure 18. Overall deformation of fasteners (bolts and dowels) for Experiment A.

Figure 19 shows the overall deformation of a dowel. The deformation after the experimental testing with a value of 35.10 mm is above. The deformation from the numerical model with a value of 23.52 mm is below.

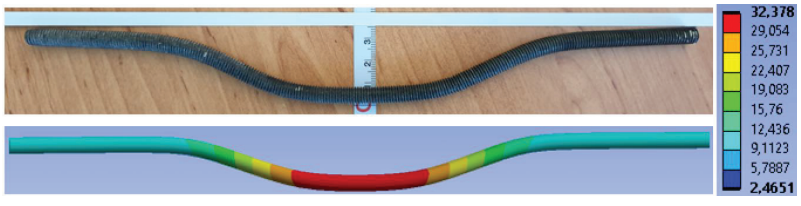

Figure 19. Deformation of a dowel (mm).

Figure 20 shows the overall deformation of a bolt. The deformation after the experimental testing with a value of 24.30 mm is above. The deformation from the numerical model with a value of 16.62 mm is below.

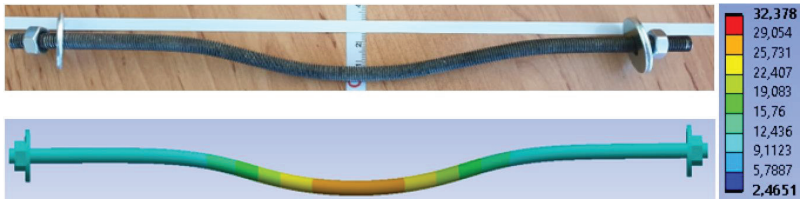

Figure 20. Deformation of a bolt (mm).

Figure 21 shows the stress and deformation in fasteners at a connection collapse in the numerical analysis. The stress during the collapse reaches the ultimate strength and the maximum plastic deformation reaches the value of 6.08%. On the basis of the experimental

testing of used bolts and dowels (see the publication *Johanides 2022* [43]), it can be concluded that the numerical model did not fail due to the rupture of the fasteners. This fact was also verified and confirmed by the experimental testing of those connections. Figure 22 shows the detailed stress distribution and plastic deformation in one fastener.

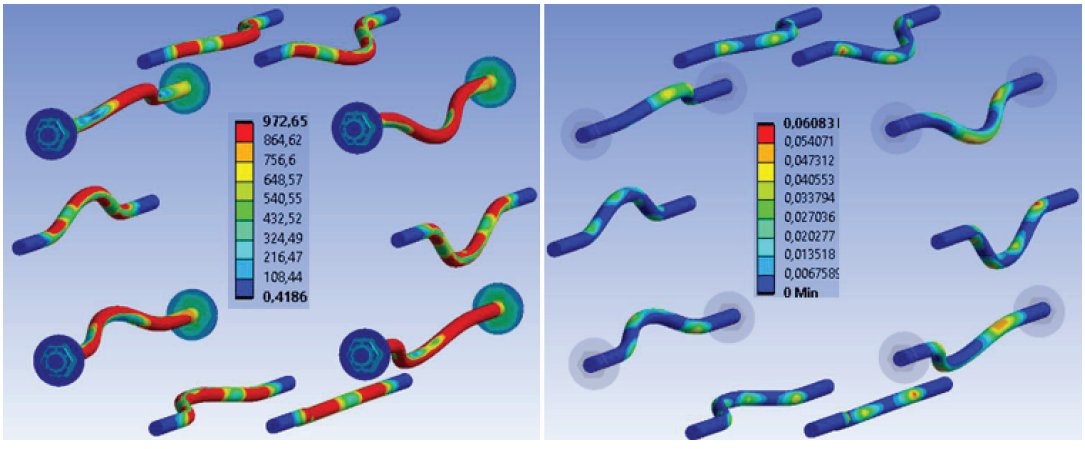

Figure 21. Experiment A: Stress in fasteners during connection collapse (MPa) (**left**), plastic deformation in fasteners during connection collapse (-) (**right**).

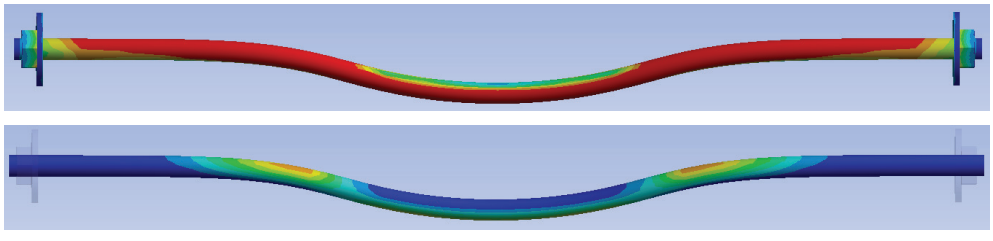

Figure 22. Experiment A: Detailed stress (MPa) (**above**), detailed plastic deformation (-) (**below**) (colour scale valid form the previous figure).

Figure 23 on the right shows the tensile stress perpendicular to the grain in the rung. When the numerical model collapses, the maximum stress (1 MPa) is found in a large area of timber. It can be especially observed in the critical area, which is marked in a red frame. Figure 23 on the left shows the collapse during the experimental testing. It can be seen that the failure occurred in the rung, precisely in the mentioned critical area. On the basis of these findings, it can be concluded that the numerical model failed because the tensile strength perpendicular to the grain in timber was exceeded.

Figure 24 shows the tensile stress perpendicular to the grain in the stands. When the numerical model collapses, the maximum stress (1 MPa) is also found in a relatively large area of timber, but is not found through the entire cross-sectional area. Therefore, the second critical area of the connection (marked in Figure 24) could remain undamaged during the experimental testing. After exceeding the tensile stress perpendicular to the grain, the timber could be damaged from the inside of the connection with various cracks. However, this fact could not be detected during the experimental testing because this area was not visible.

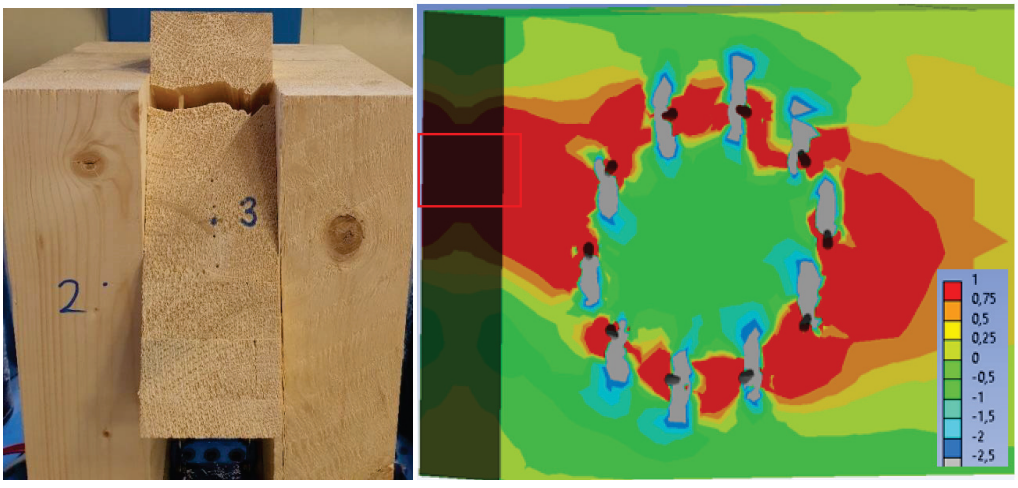

Figure 23. Experiment A: Collapse of the connection during experimental testing (on the (**left**)), tensile stress perpendicular to the grain from the numerical model (MPa) (on the (**right**)).

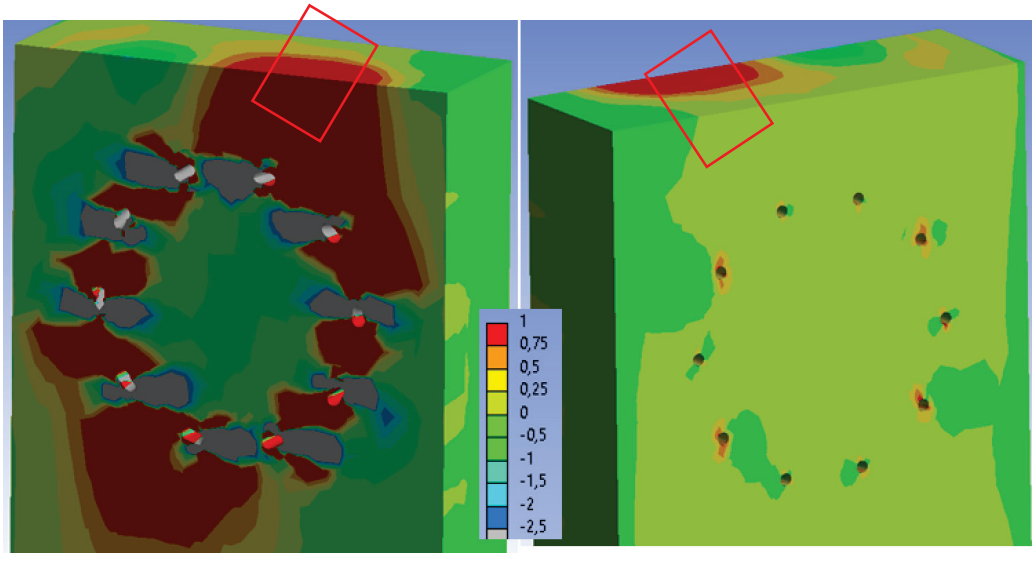

Figure 24. Experiment A: Collapse of the connection during experimental testing (on the (**left**)), tensile stress perpendicular to the grain from the numerical model (MPa) (on the (**right**)).

3.3.2. Experiment B, Fully Threaded Screws

Figure 25 shows the load–deformation curve from the numerical modeling for Experiment B, fully threaded screws. The values of the maximum achieved deformation and load-carrying capacity are shown in Table 9.

Table 9. Results of numerical modeling, Experiment B.

F_{num} (kN)	u (mm)	M (kNm)
25.75	228.65	19.83

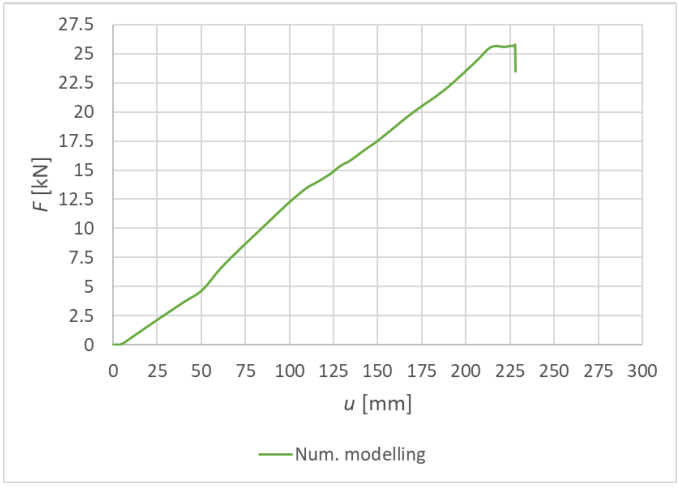

Figure 25. Experiment B: Load–deformation curves of quasi-static numerical modeling for individual specimens made from fully threaded screws.

Figure 26 shows the overall deformation of the connection, including the deformation of the auxiliary steel structure. This deformation describes the actual behavior of the entire structure during loading.

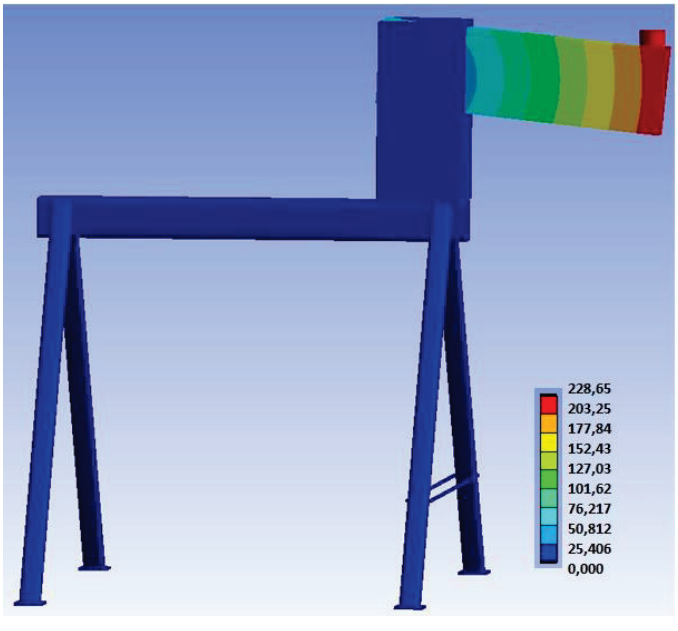

Figure 26. Overall deformation of the structure (mm) for Experiment B.

Figure 27 shows an "X-ray" view of the connection. It is possible to observe the embedment of timber around the holes for fasteners and the formation of two plastic hinges in fasteners.

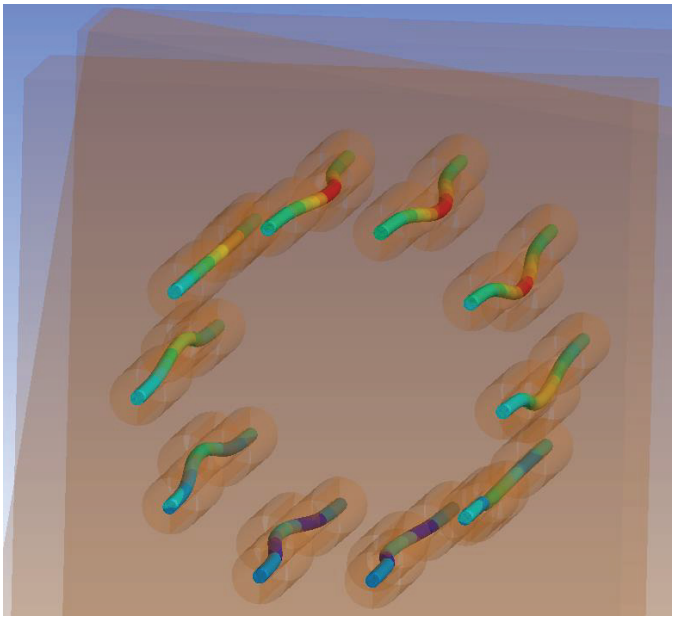

Figure 27. Overall deformation of fasteners (fully threaded screws) for Experiment B.

Figure 28 shows the overall deformation of a fully threaded screw. The deformation after the experimental testing with a value of 22.30 mm is above. The deformation from the numerical model with a value of 18.47 mm is below.

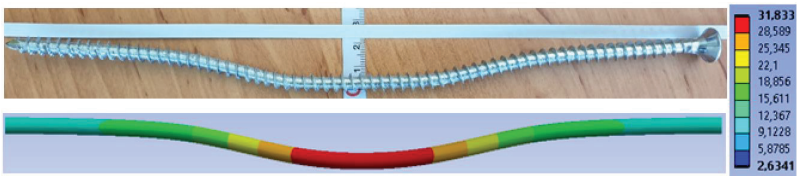

Figure 28. Deformation of a fully threaded screw (mm).

Figure 29 shows the stress and deformation in fasteners at a connection collapse in the numerical analysis. The stress during the collapse reaches the ultimate strength and the maximum plastic deformation reaches the value of 3.68%. On the basis of the experimental testing of used fully threaded screws (see the publication *Johanides 2022* [43]), it can be concluded that the numerical model did not fail due to the rupture of the fasteners. This fact was also verified and confirmed by the experimental testing of those connections. Figure 30 shows the detailed stress distribution and plastic deformation in one fastener.

Figure 31 on the right shows the tensile stress perpendicular to the grain in the rung. When the numerical model collapses, the maximum stress (1 MPa) is found in a large area of timber. It can be especially observed in the critical area, which is marked in a red frame. Figure 31 on the left shows the collapse during the experimental testing. It can be seen that the failure occurred in the rung, precisely in the mentioned critical area. On the basis of these findings, it can be concluded that the numerical model failed because the tensile strength perpendicular to the grain in timber was exceeded.

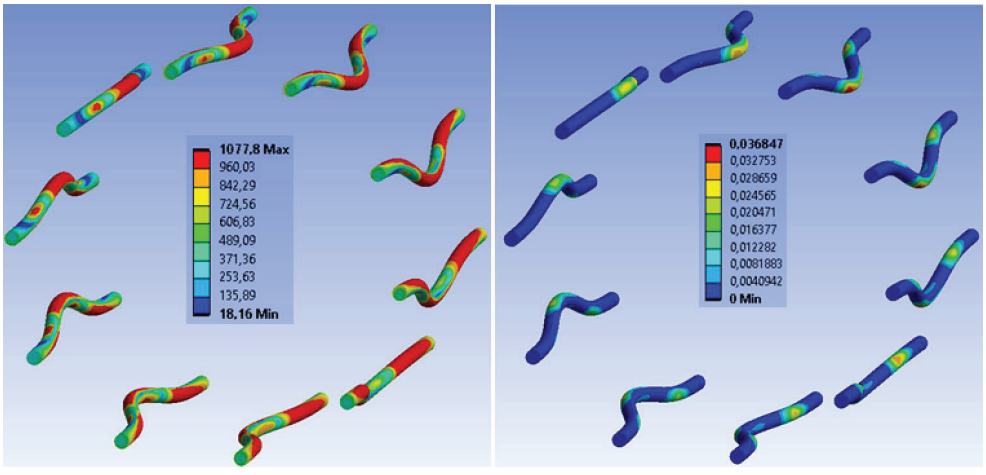

Figure 29. Experiment B: Stress in fasteners during connection collapse (MPa) (on the (**left**)), plastic deformation in fasteners during connection collapse (-) (on the (**right**).

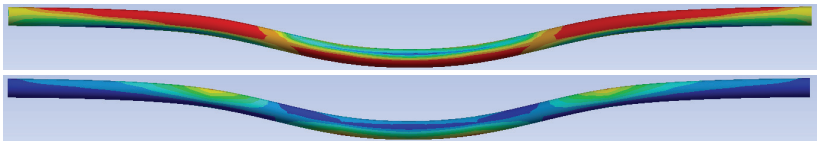

Figure 30. Experiment B: Detailed stress (MPa) (**above**), detailed plastic deformation (-) (**below**) (colour scale valid form the previous figure).

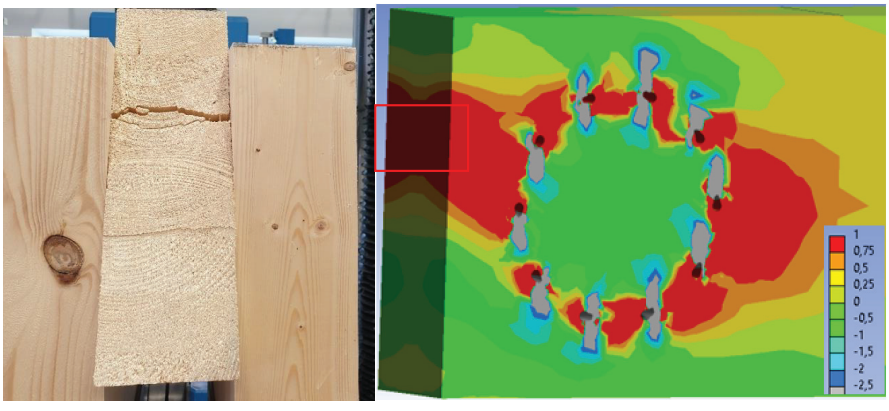

Figure 31. Experiment B: Collapse of the connection during experimental testing (on the (**left**)), tensile stress perpendicular to the grain from the numerical model (MPa) (on the (**right**)).

Figure 32 shows the tensile stress perpendicular to the grain in the stands. When the numerical model collapses, the maximum stress (1 MPa) is also found in a relatively large area of timber, but is not found through the entire cross-sectional area. Therefore, the second critical area of the connection (marked in Figure 32) could remain undamaged during the experimental testing.

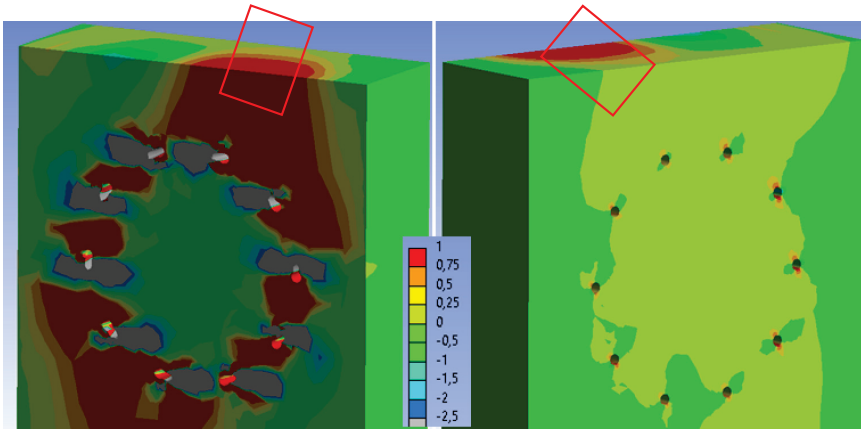

Figure 32. Experiment B: Collapse of the connection during experimental testing (on the (**left**)), tensile stress perpendicular to the grain from the numerical model (MPa) (on the (**right**)).

4. Discussion

Figure 33 shows the load–deformation curves of Experiment A—numerical modeling (continuous curve) and experimental testing (dashed, dot-dashed, and double-dot-dashed curves). It is possible to observe a relatively good agreement of the real load-carrying capacities with the numerical analysis. The course of the numerical curve best matches the experimental test 3.

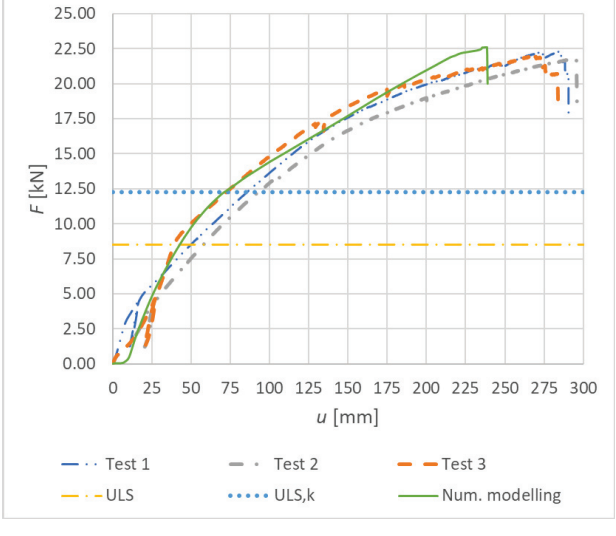

Figure 33. Load–deformation curves for Experiment A.

Results of the experimental testing and numerical modeling are given in Table 10. The table shows the maximum vertical deformation, the maximum force, and the corresponding bending moment at the point of connection failure. This value is compared with the value obtained from the numerical model. The maximum difference between the numerical value and the experimental value is 3.76%, and the minimum one is 1.40%. This agreement of the maximum load-carrying capacity can be considered as sufficiently accurate.

Table 10. Results of Experiment A (bolts and dowels).

Method	Specimen	*u* (mm)	*F* (kN)	*M* (kNm)	Difference *F* (%)	Difference *u* (%)
Numerical model	-	238.4	22.60	17.40	-	-
Experimental test	1	290.60	22.29	17.16	1.40	17.96
	2	295.67	21.78	16.77	3.76	19.37
	3	283.56	22.02	16.96	2.59	15.93

Less accuracy was achieved for the maximum deformation of the rung end. The maximum difference between the numerical model and the experimental test is 18.86%, and the minimum one is 15.84%. This inaccuracy could be caused by local imperfections in timber, local cracks in timber during loading, or the different modulus of the elasticity of the individual glued lamellas. These imperfections could not be taken into account in the numerical model.

Figure 34 shows the load–deformation curves of Experiment B—numerical modeling (continuous curve) and experimental testing (dashed, dot-dashed, and double-dot-dashed curves). The course of the numerical curve best matches the experimental tests 1 and 3.

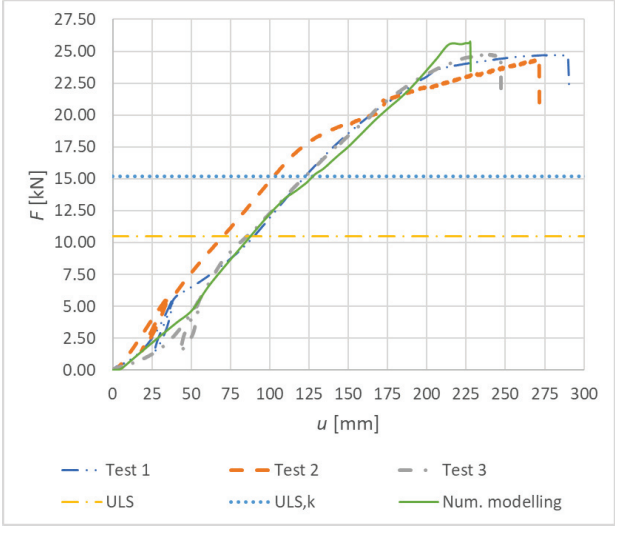

Figure 34. Load–deformation curves for Experiment B.

Results of the experimental testing and numerical modeling are given in Table 11. The table shows the maximum vertical deformation, the maximum force, and the corresponding bending moment at the point of connection failure. This value was compared with the value obtained from the numerical model. The maximum difference between the numerical value and the experimental value is 5.70%, and the minimum one is 4.20%. Although the achieved agreement of the maximum load-carrying capacity is worse compared to Experiment A (bolts and dowels), it can be considered as sufficiently accurate. Less accuracy was again achieved for the maximum deformation of the rung end. The maximum difference between the numerical model and the experimental test is 21.58%, and the minimum one is 7.81%. Even with great effort, it was not possible to achieve a better accuracy.

Table 11. Results of Experiment B (fully threaded screws).

Method	Specimen	*u* (mm)	*F* (kN)	*M* (kNm)	Difference *F* (%)	Difference *u* (%)
Numerical model	-	227.80	25.75	19.83	-	-
Experimental test	1	290.50	24.72	19.03	4.20	21.58
	2	271.85	24.37	18.76	5.70	16.20
	3	247.10	24.65	18.98	4.48	7.81

5. Conclusions

The paper was focused on the issue of the semi-rigid connection, which was composed of a timber rung and two stands using dowel-type fasteners. Six specimens were tested by quasi-static destructive cyclic loading. Three specimens were made from a combination of bolts and dowels and three specimens from fully threaded screws. The work required the creation of analytical assumptions, which were the basis for the design of the experimental testing and were subsequently used to compare the results.

First, a consolidation of the connection occurred during the initial phase of the loading. This phenomenon could be demonstrated on the load–deformation curve with a concave shape.

According to preliminary analytical and numerical calculations, the experimental testing of the real specimens resulted in an expected failure of connections in the area of the rung by tension perpendicular to the grain.

The actual measured load-carrying capacity of specimens made from a combination of bolts and dowels reached higher values compared to the design (ultimate limit state) load-carrying capacity calculated according to the standard. The actual load-carrying capacity was 2.54 times higher for the experimental test 1, 2.48 times higher for the experimental test 2, and 2.51 times higher for the experimental test 3.

The actual measured load-carrying capacity of specimens made from fully threaded screws also reached higher values compared to the design (ultimate limit state) load-carrying capacity calculated according to the standard. The actual load-carrying capacity was 2.08 times higher for the experimental test 1, 2.05 times higher for the experimental test 2, and 2.07 times higher for the experimental test 3.

It can be concluded that both types of the semi-rigid connection are sufficiently safe and reliable from the point of view of the load-carrying capacity.

Results of the numerical modeling were satisfactorily accurate in all cases compared to results of the experimental testing. Using the calibration of the numerical model according to the experimental data, it was possible to detect and describe stresses and deformations of the entire structure, as well as its details that are not visible at first sight during the experimental testing. Subsequently, it is possible to carry out analyses of different variations by removing or adding fasteners. This would save time, material, and money, because it would not be necessary to carry out further experimental testing.

The issue of determining the load-carrying capacity of connections in timber structures according to the European standards for the design of timber structures *Eurocode 5* [20] is still under development. The proposed experiments should also contribute to this trend. The experiments were focused on determining the load-carrying capacity of a semi-rigid connection of a rung and two stands using dowel-type mechanical fasteners. The data from the experiments can be used for the practical design of this type of a semi-rigid connection from the point of view of the load-carrying capacity.

Author Contributions: Conceptualization, M.J.; validation, D.M. and A.L.; data curation, M.J.; methodology, P.D.; visualization, M.J.; formal analysis and writing—original draft, M.J.; supervision, A.L; writing—review and editing, M.J. and P.D. All authors have read and agreed to the published version of the manuscript.

Funding: This research was funded by VSB-TUO by the Ministry of Education, Youth and Sports of the Czech Republic. The supported project has the number 2022/55 of Student Research Grant Competition of the VSB-Technical University of Ostrava.

Institutional Review Board Statement: Not applicable.

Informed Consent Statement: Not applicable.

Data Availability Statement: Data are contained within the article.

Acknowledgments: Experimental measurements and research were carried out thanks to VSB Technical University of Ostrava. The work was supported by the Student Research Grant Competition of the VSB-Technical University of Ostrava under identification number 2022/55.

Conflicts of Interest: The authors declare no conflict of interest.

References

1. Wilson, T.R.C. Tests made to determine lateral resistance of wire nails. *Eng. Rec.* **1917**, *75*, 303–304.
2. Johansen, K.W. *Forsög med Träforbindelser. Danmarks Tekniske Höjskole Medd. No. 10*; Laboratoriet for bygningsteknik: Copenhagen, Denmark, 1941. (In Danish)
3. Johansen, K.W. *Theory of Timber Connections*; International association for bridge and structural engineering: Zurich, Switzerland, 1949; pp. 249–262.
4. Larsen, H.J.K.W. Johansen's nail tests. *Bygn. Medd.* **1977**, *48*, 9–30.
5. Möller, T. En ny metod för beräkning av spikförband. In *Report No. 117*; Chalmers University of Technology: Chalmersplatsen, Sweden, 1951.
6. Kuenzi, E.W. Theoretical design of nailed or bolted connection under lateral load. In *Report No: D1951*; States Department of Agriculture, Forest Service, Forest Laboratory Products: Madison, WI, USA, 1955.
7. Winkler, E. Die lehre von elastizitatunffestigheit. *Dominicus Prague Czechoslov.* **1867**.
8. Foshi, R.O. Modeling the hysteretic response of mechanical connections for wood structures. In Proceedings of the 6th World Conference of Timber Engineering, Whistler, CA, Canada, 31 July–3 August 2000.
9. Meyer, A. Die Tragfähigkeit von Nagelverbindungen bei statischer Belastung. *HOLZ Als Roh-Und Werkst.* **1957**, *15*, 96–109. [CrossRef]
10. Doyle, D.V. *Performance of connections with eight bolts in laminated Douglas-fir*; U.S. Forest Service Research Paper FPL 10; U.S. Forest Service: Missoula, MT, USA, 1964.
11. Mack, J.J. The strength and stiffness of nailed connections under short-duration loading. In *Division of Forest Products*; Commonwealth Scientific and Industrial Research Organization: South Melbourne, Australia, 1966.
12. Larsen, H.J.; Reestrup, V. Tests on screws in wood. *Bygningsstatiske Medd.* **1969**, *1*, 3–36.
13. Norén, B. Formler för hallfasthet hos mekaniska träförband. In *Formulas Indicating the Strength of Mechanical Wood Connections*; Medd. Series B, No. 226; Svenska Träforskningsinstitutet: Stockholm, Sweden, 1974. (In Swedish)
14. Larsen, H.J. The yield load of bolted and nailed connections. In Proceedings of the International Union of Forestry Research Organizations Working Group on Structural Utilization, Pretoria, South Africa, 22 September–12 October 1973.
15. Larsen, H.J. Design of bolted connections. In *International Council for Building Research Studies and Documentation, Working Commission W 18—Timber Structures*; Karlsruhe Institute of Technology: Bordeaux, France, 1979.
16. CIB. Structural timber design code. In *International Council for Building Research Studies and Documentation, Working Group W18—Timber Structures*, 6th ed.; CIB-W18: St. Andrews, NB, Canada, 1983.
17. Smith, I.A.; Whale, L.R.J. Mechanical timber connections. In *TRADA Research Report 18/86*; TRADA: High Wycombe, UK, 1986.
18. Ehlbeck, J.; Werner, H. *Tragfähigkeit von Laubholzverbindungen mit stabförmigen Verbindungsmitteln. Versuchsanst. für Stahl, Holz und Steine, Abt. Ingenieurholzbau*; Universität Karlsruhe: Karlsruhe, Germany, 1992.
19. Blass, H.J.; Bienhaus, A.; Krämer, V. Effective bending capacity of dowel-type fasteners. *Proc. PRO* **2000**, *22*, 71–80.
20. *EN 1995-1-1*; Eurocode 5: Design of Timber Structures—Part 1-1: General—Common Rules and Rules for Buildings. Czech Standards Institute: Praha, Czech Republic, 2006.
21. *Timber Structures According to Eurocode 5; STEP 1: Design and Construction Materials*; Translated by Bohumil Kozelouh; KODR: Zlin, Czech Republic, 1998; ISBN 80-238-2620-4. (In Czech)
22. Solarino, F.; Giresini, L.; Chang, W.-S.; Huang, H. Experimental Tests on a Dowel-Type Timber Connection and Validation of Numerical Models. *Buildings* **2017**, *7*, 116. [CrossRef]
23. Vavrusova, K.; Mikolasek, D.; Lokaj, A.; Klajmonova, K.; Sucharda, O. Determination of carrying capacity of steel-timber connections with steel rods glued-in parallel to grain. *Wood Res.* **2016**, *61*, 733–740.
24. Chybiński, M.; Polus, Ł. Mechanical Behaviour of Aluminium-Timber Composite Connections with Screws and Toothed Plates. *Materials* **2022**, *15*, 68. [CrossRef]
25. Chybiński, M.; Polus, Ł. Experimental Study of Aluminium-Timber Composite Bolted Connections Strengthened with Toothed Plates. *Materials* **2022**, *15*, 5271. [CrossRef]

26. Cai, Y.; Young, B. Effects of end distance on thin sheet steel bolted connections. *Eng. Struct.* **2019**, *196*, 109331. [CrossRef]
27. Požgaj, A.; Kürjatko, S. Wood properties of spruce from forests affected by pollution in Czechoslovakia. *IAWA J.* **1986**, *7*, 405–410. [CrossRef]
28. Mirski, R.; Dziurka, D.; Chuda-Kowalska, M.; Wieruszewski, M.; Kawalerczyk, J.; Trociński, A. The Usefulness of Pine Timber (*Pinus sylvestris* L.) for the Production of Structural Elements. Part I: Evaluation of the Quality of the Pine Timber in the Bending Test. *Materials* **2019**, *13*, 3957. [CrossRef] [PubMed]
29. Mirski, R.; Dziurka, D.; Chuda-Kowalska, M.; Kawalerczyk, J.; Kuliński, M.; Łabęda, K. The Usefulness of Pine Timber (*Pinus sylvestris* L.) for the Production of Structural Elements. Part II: Strength Properties of Glued Laminated Timber. *Materials* **2020**, *13*, 4029. [CrossRef] [PubMed]
30. Nowak, T.; Karolak, A.; Sobótka, M.; Wyjadłowski, M. Assessment of the Condition of Wharf Timber Sheet Wall Material by Means of Selected Non-Destructive Methods. *Materials* **2019**, *12*, 1532. [CrossRef] [PubMed]
31. Nowak, T.; Patalas, F.; Karolak, A. Estimating Mechanical Properties of Wood in Existing Structures—Selected Aspects. *Materials* **2021**, *14*, 1941. [CrossRef]
32. Bragov, A.; Igumnov, L.; dell'Isola, F.; Konstantinov, A.; Lomunov, A.; Iuzhina, T. Dynamic Testing of Lime-Tree (Tilia Eu-ropoea) and Pine (Pinaceae) for Wood Model Identification. *Materials* **2020**, *13*, 5261. [CrossRef] [PubMed]
33. Olaoye, K.; Aguda, L.; Ogunleye, B. Prediction of Mechanical Properties of Hardwood Species Using the Longitudinal Vib-ration Acoustic Method. *For. Prod. J.* **2021**, *71*, 391. [CrossRef]
34. Martínez, R.D.; Balmori, J.-A.; Llana, D.F.; Bobadilla, I. Wood Density and Moisture Content Estimation by Drilling Chips Extraction Technique. *Materials* **2020**, *13*, 1699. [CrossRef] [PubMed]
35. Dobes, P.; Lokaj, A.; Mikolasek, D. Load-Carrying Capacity of Double-Shear Bolted Connections with Slotted-In Steel Plates in Squared and Round Timber Based on the Experimental Testing, European Yield Model, and Linear Elastic Fracture Mechanics. *Materials* **2022**, *15*, 2720. [CrossRef]
36. Braun, M.; Pełczyński, J.; Al Sabouni-Zawadzka, A.; Kromoser, B. Calibration and Validation of a Linear-Elastic Numerical Model for Timber Step Connections Based on the Results of Experimental Investigations. *Materials* **2022**, *15*, 1639. [CrossRef]
37. Burawska-Kupniewska, I.; Beer, P. Near-Surface Mounted Reinforcement of Sawn Timber Beams-FEM Approach. *Materials* **2021**, *14*, 2780. [CrossRef] [PubMed]
38. Zhou, S.R.; Li, Z.Y.; Feng, S.Y.; Zhu, H.; Kang, S.B. Effects of bolted connections on behaviour of timber frames under combined vertical and lateral loads. *Constr. Build. Mater.* **2021**, *293*, 123542. [CrossRef]
39. Wang, M.; Song, X.; Gu, X.; Tang, J. Bolted glulam beam-column connections under different combinations of shear and bending. *Eng. Struct.* **2019**, *181*, 281–292. [CrossRef]
40. Wang, X.T.; Zhu, E.C.; Niu, S.; Wang, H.J. Analysis and test of stiffness of bolted connections in timber structures. *Constr. Build. Mater.* **2021**, *303*, 124495. [CrossRef]
41. Johanides, M.; Kubincova, L.; Mikolasek, D.; Lokaj, A.; Sucharda, O.; Mynarcik, P. Analysis of Rotational Stiffness of the Timber Frame Connection. *Sustainability* **2021**, *13*, 156. [CrossRef]
42. Johanides, M.; Mikolasek, D.; Lokaj, A.; Mynarcik, P.; Marcalikova, Z.; Sucharda, O. Rotational Stiffness and Carrying Capacity of Timber Frame Corners with Dowel Type Connections. *Materials* **2021**, *14*, 7429. [CrossRef]
43. Johanides, M.; Lokaj, A.; Mikolasek, D.; Mynarcik, P.; Dobes, P.; Sucharda, O. Timber Semirigid Frame Connection with Improved Deformation Capacity and Ductility. *Buildings* **2022**, *12*, 583. [CrossRef]
44. Johanides, M.; Lokaj, A.; Dobes, P.; Mikolasek, D. Numerical and Experimental Analysis of the Rotational Stiffness of a Timber Semi-Rigid Dowel-Type Connection. *Materials* **2022**, *15*, 5622. [CrossRef] [PubMed]
45. LaborTech. Available online: https://www.labortech.cz (accessed on 25 November 2021).
46. *EN 26891*; Timber Structures. Joints Made with Mechanical Fasteners. General Principles for the Determination of Strength and Deformation Characteristics. Czech Office for Standards. Metrology and Testing: Praha, Czech Republic, 1994.
47. ANSYS. Available online: https://www.ansys.com/ (accessed on 25 November 2021).
48. Brožovský, J.; Alois, M. Metoda konečných Prvkůve Stavební Mechanice. 2012. Available online: https://docplayer.cz/414068-Metoda-konecnych-prvku-ve-stavebni-mechanice.html (accessed on 15 May 2022).
49. Mikolášek, D. *Numerické Modelování Vybraných Spojů Dřevěných Konstrukcí. Disertační Práce*; Vysoká škola báňská–Technická univerzita Ostrava: Ostrava, Czech Republic, 2012.
50. Gunderson, R.A.; Goodman, J.R.; Bodig, J. Plate Tests for Determination of Elastic Parameters of Wood. *Wood Sci.* **1973**, *5*, 241–248.
51. The Engineering Tool Box. Available online: https://www.engineeringtoolbox.com/friction-coefficients-d_778.html (accessed on 15 May 2022).

materials

MDPI

Article

Calibration and Validation of a Linear-Elastic Numerical Model for Timber Step Joints Based on the Results of Experimental Investigations

Matthias Braun [1,*,†], Jan Pełczyński [2,†], Anna Al Sabouni-Zawadzka [2] and Benjamin Kromoser [1]

[1] Institute of Structural Engineering, University of Natural Resources and Life Sciences (BOKU), 1190 Vienna, Austria; benjamin.kromoser@boku.ac.at
[2] Faculty of Civil Engineering, Warsaw University of Technology, 00-637 Warsaw, Poland; j.pelczynski@il.pw.edu.pl (J.P.); a.sabouni@il.pw.edu.pl (A.A.S.-Z.)
* Correspondence: m.braun@boku.ac.at; Tel.: +43-147-6548-7537
† These authors contributed equally to this work.

Abstract: The paper is dedicated to the numerical analysis of a single-step joint, enabling the prediction of stiffness and failure modes of both single- and double-step joints. An experimental analysis of the geometrically simplest version, the single-step joint, serves as a reference for the calibration of the subsequent finite element model. The inhomogeneous and anisotropic properties of solid timber make detailed modelling computationally intensive and strongly dependent on the respective specimen. Therefore, the authors present a strategy for simplified but still appropriate modelling for the prediction of local failure at certain load levels. The used mathematical approach is based on the linear elasticity theory and orthotropic material properties. The finite element calculations are performed in the environment of the software Abaqus FEA. The calibrated numerical model shows a good conformity until first failures occur. It allows for a satisfactory quantification of the stiffness of the connection and estimation of the force when local failure begins and is, therefore, recommended for future, non-destructive research of timber connections of various shapes.

Keywords: timber–timber joints; single-step joint; double-step joint; resource efficient construction; digital image correlation; finite element analysis

Citation: Braun, M.; Pełczyński, J.; Al Sabouni-Zawadzka, A.; Kromoser, B. Calibration and Validation of a Linear-Elastic Numerical Model for Timber Step Joints Based on the Results of Experimental Investigations. *Materials* **2022**, *15*, 1639. https://doi.org/10.3390/ma15051639

Academic Editors: Radosław Mirski and Dorota Dukarska

Received: 28 January 2022
Accepted: 20 February 2022
Published: 22 February 2022

1. Introduction

We are currently confronted with a steadily increasing CO_2 concentration in the atmosphere, resulting in global warming [1]. A large part (~40%) of the global CO_2 emissions is caused by the construction industry [2]. The comparison of different construction materials shows that timber exhibits advantageous properties with regard to these environmental aspects, as it stores part of the CO_2 absorbed during the growth phase of the trees [3]. Unfortunately, a scarcity of the raw material has been observed on the present market, resulting in, among other things, a strong price increase. If timber is to be used in larger quantities as a construction material, a higher degree of utilisation is, therefore, essential.

An outstanding example of efficient material use is timber truss systems which have optimal load-bearing behaviour while highly utilising the construction material [4]. Unfortunately, the high effort in design and production make the manufacturing and application of these structures in this day and age a rarity. New, upcoming possibilities, such as digital tools and CNC machines, enable an automation of the design and production process and allow for the improvement of the profitability in order to, yet again, be able to compete with other systems such as plate girders [4]. A key factor in the functionality and efficiency of timber truss systems is the joints.

Previous research by the Institute of Structural Engineering at BOKU showed that timber–timber step joints represent very efficient solutions for the transfer of compressive

forces. The joints provide a ductile failure behaviour, are easy to produce and are able to transfer comparatively high loads. In addition, no additional steel parts, which normally have a major impact on the environmental performance and economy of such structures, are required. A series of compression tests performed by the authors, investigating different embodiments of step joints, as well as inaccuracies possibly caused by a change of moisture content or production, showed the influence of the geometry on the performance (stiffness and maximum load) [4–7].

The authors of this paper pursued two main goals while driving research forward in this area: (1) Experimental investigation of the load-bearing behaviour of new timber step joint designs with a set focus on maximising the performance (maximum load, stiffness and producibility) [6] (BOKU, Institute of Structural Engineering) and (2) Development of a modelling strategy for timber–timber joints under compression for the best possible prediction of the load-bearing behaviour (Warsaw University of Technology, Faculty of Civil Engineering). The basic research approaches to achieve the defined goals were the implementation of experimental investigations on the one side and increasing sophistication of the finite element model on the other.

A realistic prediction of the load-bearing behaviour prior to construction counts as one of the core disciplines of structural engineering. In addition to analytical models and empirical determined data, finite element (FE) calculations can be added to the well-established prediction tools. However, a careful (material) model calibration based on experimental investigations, especially for materials with a complex behaviour, such as timber, is the basis for a reliable prediction model. The main focus of the presented paper was the investigation of the performance and applicability of a simplified FE model based on linear-elastic material behaviour and an orthotropic constitutive model, allowing for a comparatively low computation effort.

After the introduction, the test setup and test specimens, as well as the results of the performed experimental investigations on a single-step joint, are explained in Section 2. Section 3 is dedicated to the mathematical model used to simulate the behaviour of timber within an orthotropic constitutive model of linear elasticity used for the FE simulation performed with the Abaqus FEA software. Subsequently, Section 4 deals with the computational modelling and the calibration of the material parameters based on the results of the experiments. In Section 5, the linear-elastic model is applied to the geometry of a double-step joint and, again, compared with the results of experimental investigations. Concluding remarks can be found in Section 6.

2. Experimental Investigations

As a first basis for the FE model calibration, a single-step joint (Series A) was chosen. Compared to joints with two (double-step joints) or a number of steps (multi-step joints) the influence of production inaccuracies is lower within the single-step joint, making it easier to identify the individual influencing parameters. Subsequently, the results of experiments on double-step joints (Series B) were used to verify if the calibration could be applied to other geometries. The experimental investigations analysing the load-bearing behaviour of single- and double-step joints were performed in the laboratory of the Institute of Structural Engineering at BOKU.

2.1. Test Setup and Test Specimens

The test setup, consisting of welded HEB160 steel profiles, as well as the geometry of the test specimens (single-step joint), are pictured in Figure 1. The load was applied using a three-axial, servo-hydraulic testing machine in a displacement-controlled manner with a rate of 1 mm/min. A digital image correlation system (DIC-3D™ from the company Correlated Solutions, Irmo, SC, USA) was used to measure the occurring strains on one surface of the specimens while the loads were recorded using an electric load cell. The areas of interest of the timber specimens were painted white and, subsequently, sprinkled using black paint, creating appropriate reference points. Five tests were performed.

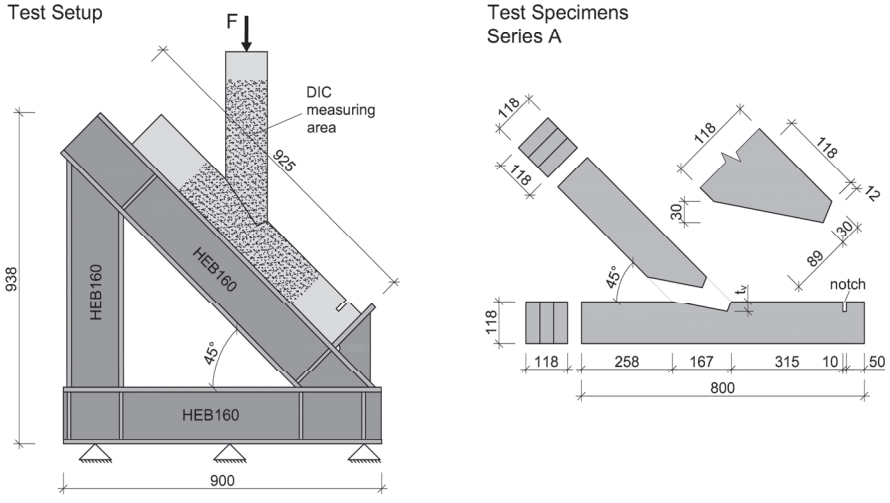

Figure 1. (**Left**): Test setup [4]; (**Right**): Geometry of the Series A test specimens. Measurements in mm.

Laminated timber with a strength class GL24h according to ÖNORM EN 14080:2013 [8] and a cross-section of 118 × 118 mm^2 made of three spruce lamellas was chosen for the specimens. The lamellas were arranged vertically to minimise the influence of local wood defects. The moisture content, varying from 7.3% to 8.9%, was determined using a GANN Hydromette BL H40/HT70 immediately after testing of each specimen. A sufficient length of the shearing path was chosen to create failure by crushing due to compression stress and prevent shear failure. A 30 mm deep notch was cut into the specimens 315 mm from the joint in order to eliminate any influence of the abutment.

2.2. Results of the Experimental Invesitations

The test results of the load-bearing investigations of the five single-step joints of Series A are summarised in Figure 2 (left). A virtual extensometer, shown in Figure 2 (right), was used during post-processing for the determination of the displacement within the evaluation of the tests using the software VIC-3D 9™. The results clearly show that all specimens exhibited an almost linear-elastic behaviour throughout a specific phase of the experiments. When evaluating the mean of all five specimens (A_MV), the linear-elastic phase extended from 19% to 72% of the achieved ultimate force F_{max}. Once the failure occurred in a ductile manner, the tests were stopped, and the post-fractural behaviour was observed. For the calibration of the numerical model, it was necessary to obtain data from one individual specimen because, within VIC-3D 9™, it was not possible to create mean values for points at the exact same location (seen in Section 4.2) for individual specimens. Therefore, the results of one individual specimen were used. As the results of specimen A_5, with the linear-elastic phase ranging from 24 to 82 kN, represented the mean value of this test series best (see Figure 2 left), it was chosen for the calibration.

The DIC system measures displacements of reference points on the surface of the specimen, with all other quantities post-processed mathematically. In Figure 3, the normal strains eyy (in vertical direction) of the surface of specimen A_5 at different load levels are shown to illustrate the propagation with increasing load.

The validation of the subsequently proposed numerical model was performed relying on the displacements. Figures 4 and 5 show the distributions of displacements measured with the DIC system for the chosen specimen A_5 at a load of 70.1 kN. This load was set as the top calibration range for the numerical model and represents approximately 85% of the end of the elastic phase. The figures show that, in addition to the deformations of the specimen itself, vertical and horizontal displacements at the lower edge can be

traced back to deflections of the steel frame. The results from the virtual extensometer, however, indicate that these deflections of the test setup did not affect the results seen in the force-displacement curves presented in Figure 2 (left).

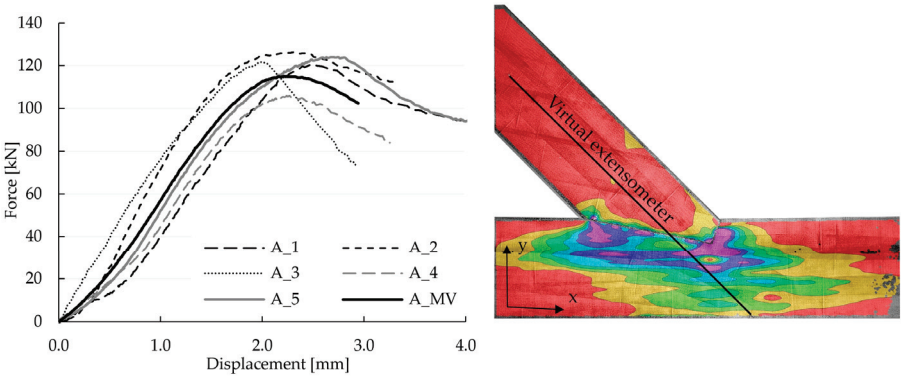

Figure 2. (**Left**): Force-displacement curves of all five test specimens of the single-step joints, as well as the mean value MV of the five specimens; (**Right**): Normal strains eyy at 90% of the ultimate load (124.08 kN) of specimen A_5 and visualisation of the virtual extensometer (based on the DIC measurement) used for the determination of the displacement, as well as the orientation of the coordinate system.

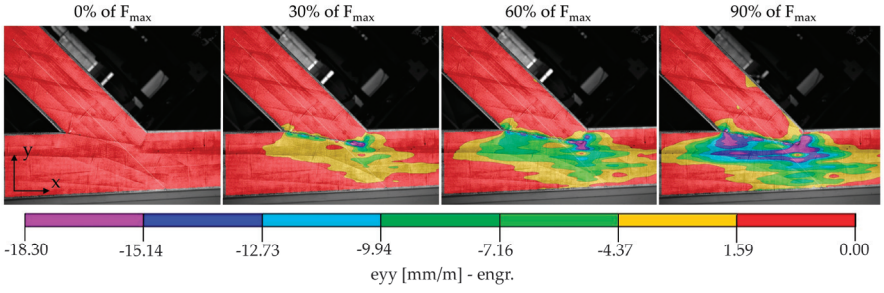

Figure 3. Normal strains eyy of the surface of specimen A_5 measured using the DIC system at 0%, 30%, 60% and 90% of the ultimate load F_{max} at 124.08 kN.

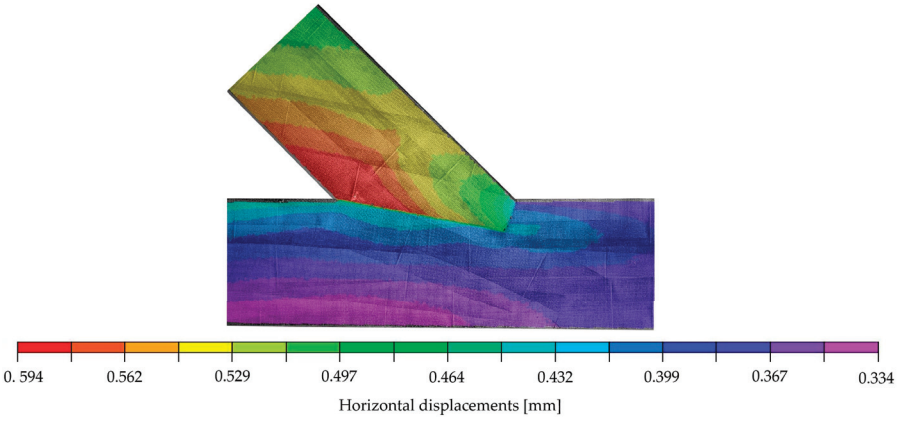

Figure 4. DIC-horizontal displacements on the surface of specimen A_5 at 70.1 kN.

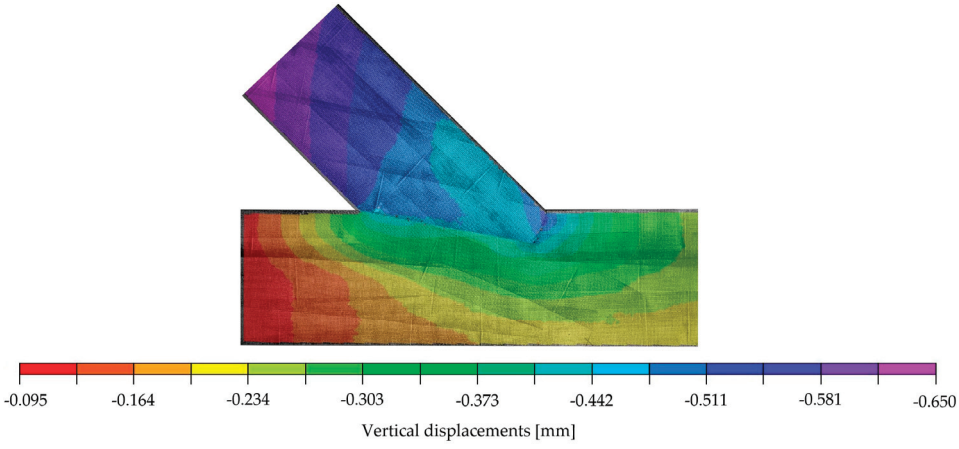

Figure 5. DIC-vertical displacements on the surface of specimen A_5 at 70.1 kN.

3. Mathematical Model of Timber with the Finite Element Implementation

Various experimental tests of timber joints show a strong dependence of the results on the inhomogeneous material properties of the sample, in particular the arrangement and twist of the fibres, as well as the presence of knots [9,10]. Furthermore, the results are dependent on the chosen geometry of the joint and the accuracy of craftsmanship in regard to the execution [7]. A precise prediction of the load-bearing behaviour considering the inhomogeneity of the material, as well as the damage and the accompanying redistribution of forces in certain areas, requires a detailed analysis of the properties of each sample. A very detailed modelling and subsequent numerical analysis in terms of non-linear-elastic, elastic-plastic, visco-plastic or fracture mechanics are, therefore, necessary to identify the propagation of the failure. Another approach is to use novel hysteretic models, which are capable of simulating the complex, non-linear behaviour of materials [11–13]. In order to obtain a first assessment of a joint without complicated calculations, the authors proposed to simplify the numerical analysis to a linear-elastic model. Subsequently, it was investigated whether the simplified model allowed for an assessment of the local failure modes, an estimation of the stiffness of the connection (force-displacement relationship) and a prediction of the load at which the onset of failure is to be expected.

In a linear-elastic model, the constitutive relations have the following form [14]:

$$S_{ij} = D_{ijlk} E_{kl} \tag{1}$$

with S_{ij} being the components of the stress tensor, E_{kl} the components of the strain tensor and D_{ijlk} the components of the elasticity tensor. In the orthotropic model, non-zero components of elasticity tensor can be expressed by nine independent technical coefficients [14]: three Young's moduli E_1, E_2, E_3, three Kirchhoff's moduli G_{12}, G_{13}, G_{23} and three independent Poisson's ratios selected from six: $\nu_{12}, \nu_{13}, \nu_{23}, \nu_{21}, \nu_{31}, \nu_{32}$, with dependencies as follows:

$$\frac{\nu_{12}}{E_2} = \frac{\nu_{21}}{E_1}, \frac{\nu_{13}}{E_3} = \frac{\nu_{31}}{E_1}, \frac{\nu_{23}}{E_3} = \frac{\nu_{32}}{E_2} \tag{2}$$

The directions are defined as parallel to the grain (direction 1), perpendicular to the grain (direction 2) and circumferential (direction 3). The technical coefficients are usually determined based on experimental research published in literature or taken from the design standards [15]. In the case of the presented model, the technical coefficients, listed in Section 4.1, were calibrated based on the previously described experimental research.

A theoretical analysis of timber joints within the framework of the theory of elasticity is possible with the use of FE modelling (e.g., [16–18]). Even though only a certain range of

the structural response to the load (linear-elastic phase) is covered by this type of modelling, it is expected that the linear range allows for the determination of the onset of local failure and failure mode. As described in [19], 3D modelling is not always necessary, with 2D models often being sufficient for orthotropic materials [20–22], resulting in simulation time reduction and, therefore, a cost reduction within the assessment process. Since no significant, out-of-plane deformations were observed during the experimental investigations, the use of a 2D model for the presented numerical calculations seemed justified.

A detailed comparison of the modelling results with the results of the experimental investigations is presented in the following sections.

4. Numerical Calculations

4.1. First Step—Numerical Simulation Using Material Properties According to EN 14080

The simulation, based on a geometrical model with dimensions of specimen A_5 (Figure 1) was carried out in Abaqus FEA software. The model itself consisted of two unconnected parts, namely the upper and lower beam. The contact zone of both beams was modelled in terms of unilateral constraints that activate as soon as the elements are pressed against each other, with the possibility of sliding with friction, in accordance with the procedures of Abaqus [23]. In the contact area, surface-to-surface contact was assumed in the initial step, with the option *Adjust only to remove overclosure*. The contact interaction property included *"Hard" Contact Normal behaviour*, with permission for separation after contact and *Tangential behaviour* with the friction coefficient μ. With this model, the contact areas could be calculated frictionlessly when $\mu = 0$.

As a linear-elastic approach was chosen to model the experiment, a 29.6 kN increment between 40.5 kN and 70.1 kN was chosen according to the linear-elastic phase of the results of specimen A_5 (see Figure 6). The increment value was based on the choice of the authors to work within the linear-elastic phase in combination with the available data from the DIC measurements. The resulting linear-elastic model allowed for easy scaling of the results and, therefore, an easy comparison with experimental results taken from different load ranges. In the area of the force application, a rigid body, loaded with a concentrated force $F = 29.6$ kN, modelled the behaviour of the testing machine. A vertical displacement $u_V = 0.211$ mm was imposed at the bottom edge of the lower beam, while a horizontal displacement $u_H = 0.361$ mm was assumed at the right edge to account for the displacements of the steel frame during the experimental investigations within the investigated load range. The geometrical data and the designation of the contact areas, as well as the boundary conditions for the supports, are pictured in Figure 7.

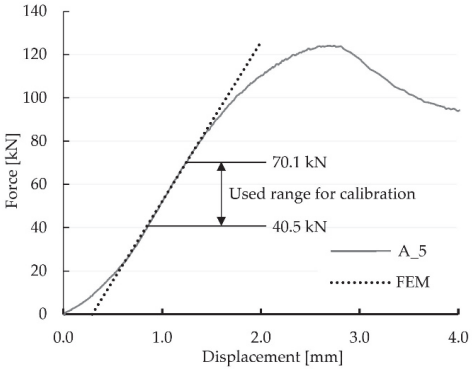

Figure 6. Experimentally, as well as numerically (FEM), determined load-displacement curves of specimen A_5. The FEM line was shifted to the right to facilitate comparability.

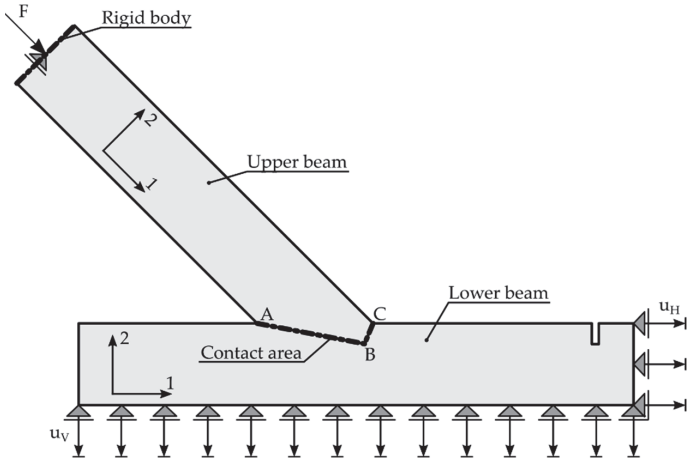

Figure 7. Geometry and designations of the FEM model for the single-step joint. Axis 1 represents the orientation parallel to the grain.

For the 2D plane stress model, with a thickness of 118 mm, 124,538 square elements with linear shape functions and reduced integration (CPS4R) were used. Additionally, 249 triangular elements CPS3 were applied in the areas of less regular mesh. The total number of Gauss points in the model was 124,787. The mesh size of the finite elements was set to approximately 3 mm in general areas and 1 mm close to the contact area in order to provide higher precision of the results. The mesh was generated by Abaqus algorithm with seeding conditions provided by the authors.

The orthotropic properties in the computational model were oriented according to the arrangement of the fibres of the upper and lower member (axis 1 according to Figure 7). In the first step of the analysis, the material properties were orthotropic with the mean value parameters taken from the design standard [8] for timber class GL24h: $E_1 = 11,500$ MPa, $E_2 = E_3 = 300$ MPa, $\nu_{12} = \nu_{13} = \nu_{23} = 0.35$ and $G_{12} = G_{13} = G_{23} = 650$ MPa. The coefficient of friction μ was assumed to be 0 and, thus, frictionless. The force-displacement relation of the experiments showed non-linear behaviour at the beginning of the tests. Once the initial phase [6,7] was overcome, the connection could be seen as a perfect fit, resulting in a linear-elastic phase until a load of approximately 83 kN, corresponding to 72% of the averaged ultimate load. Subsequently, a loss of stiffness was noticeable until the ultimate load was reached, and the load began to drop. As mentioned before, a linear computational model only leads to a linear response of the structure, and progressive damage cannot be reproduced. Therefore, the numerical calculation was done for a 29.6 kN increment. Figures 8 and 9 show displacement fields obtained from the numerical analysis at a force of 29.6 kN.

The stiffness k of the numerical model, defined as the ratio of 29.6 kN to the relative displacement of the extensometer points (see Figure 2 (right)), was equal to 90.08 kN/mm. This value indicated a poor approximation of the experimental results, of 72.1 kN/mm for specimen A_5 (the mean stiffness of the test series was 68.2 kN/mm), resulting in the decision of the authors to further calibrate the model using the results of the experiments.

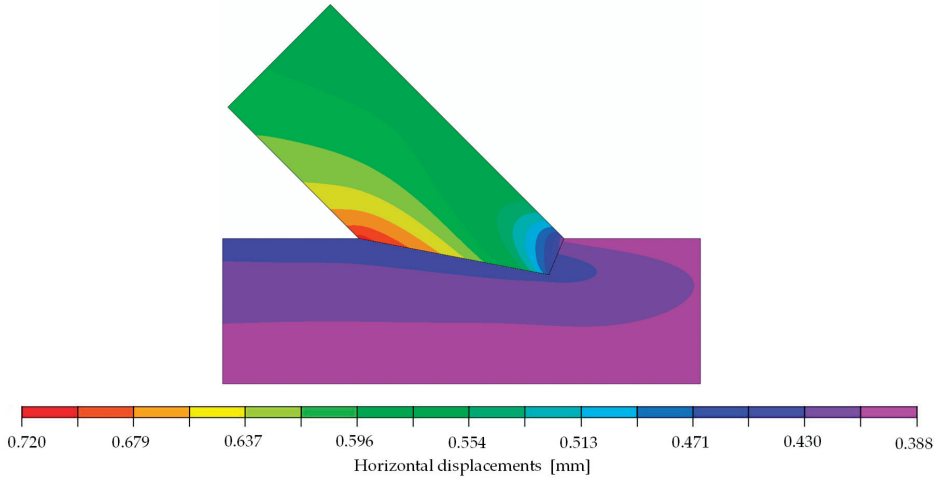

Figure 8. Horizontal displacements of numerical model at 29.6 kN [mm].

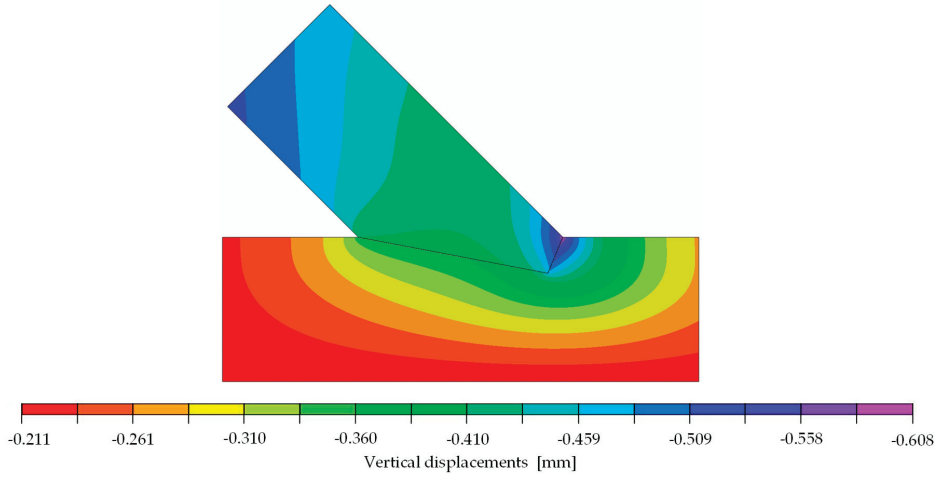

Figure 9. Vertical displacements of numerical model at 29.6 kN [mm].

4.2. Calibration of the Numerical Model According to the Results of the Experimental Investiagions

The following material parameters were re-evaluated during the calibration of the linear-elastic model, with the parameters taken as variable: Young's modulus, both in the longitudinal (E_1) and transversal (E_2) direction, Kirchhoff's modulus G_{12} and the friction factor μ. It was assumed that the geometry of the joint was modelled accurately and, therefore, geometrical factors were not used as calibration candidates. As already described in the previous section and clearly displayed in Figure 6, a load increment of 29.6 kN was chosen for the linear-elastic modelling, starting from a load of 40.5 kN up to a load of 70.1 kN. The vertical and horizontal displacements of 150 inspect points placed in the DIC post-processing, pictured in Figure 10, were used as reference points for the calibration.

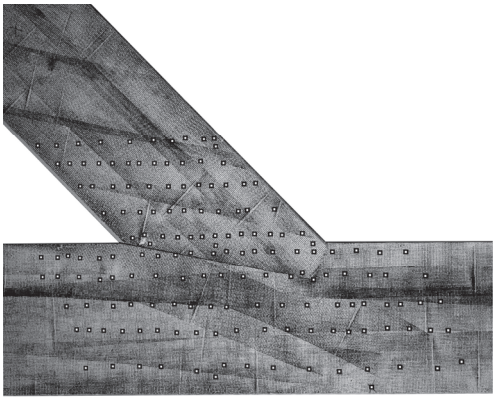

Figure 10. A total of 150 inspect points placed on the surface in the DIC post-processing to extract the displacements for the calibration of the numerical model.

During the calibration, with the process illustrated in Figure 11, 850 numerical models incorporating different parameters were automatically generated using Python and, subsequently, calculated using Abaqus. The displacement values of the defined inspect points were then evaluated using the previously programmed Python code with the implemented coordinates (see Figure 10) before being automatically transferred to an Excel file. In order to determine the most adequate parameters, resulting in a model matching the experimental results, a verification equation (Equation (3)) comparing the displacement fields was defined as:

$$\|x\|:X,Y \to \mathbb{R},\ \|x\| = \sqrt{\sum_{i=1}^{n}(Y_i - X_i)^2} \tag{3}$$

where X is a set of 150 values taken from numerical model, and Y is the set of 150 values taken from the same places but from the experimental results seen in Figure 10. The calculation of the verification equation, Equation (3), was carried out automatically. With the calculation time of one FEA simulation equalling 84 s, the authors will consider using a more time-efficient approach in future works, for example, the Newton method or a meta-heuristic approach to reduce simulation time [12].

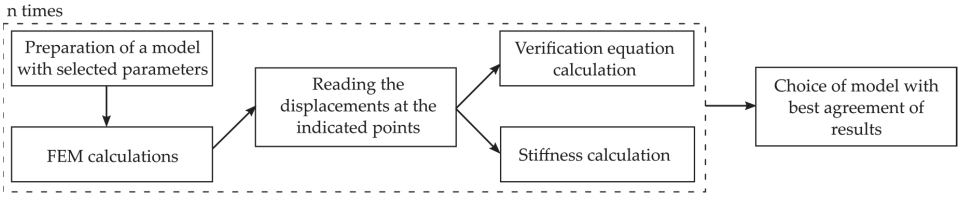

Figure 11. Flowchart of the calibration process.

To compare the investigated models, three values were calculated for each: the horizontal ($\|x_H\|$) and vertical ($\|x_V\|$) displacement field according to the verification equation, Equation (3), and the stiffness k of the numerical model defined as the ratio of 29.6 kN to the relative displacement of the extensometer points (see Figure 2 (right)). The ranges of the parameter values, considered within the calibration, are listed in Table 1.

Table 1. Range of parameter values E_1, E_2, G_{12} and μ.

Parameter	Min	Max
E_1 [MPa]	100	12,650
E_2 [MPa]	10	400
G_{12} [MPa]	50	1000
μ [-]	0.0	0.4

The calibration showed that the set of parameters which provided the best agreement of the numerical results and the laboratory test was: $E_1 = 10,350$ MPa, $E_2 = 196$ MPa, $\nu_{12} = 0.35$, $G_{12} = 728$ MPa and $\mu = 0.0$. This model was characterised by the values $\|x_H\| = 0.77753$, $\|x_V\| = 0.77752$ and $k = 72.11$ kN/mm. A very good compliance of the stiffness values from the numerical analysis (72.11 kN/mm) and the laboratory test (72.10 kN/mm) was achieved. Furthermore, it should be noted that, in the chosen model, very similar results from Equation (3), calculated for both directions, were obtained. Considering all results, the numerical modelling in the linear-elastic range using the orthotropic model showed an acceptable agreement with the experimental results in the linear-elastic range. The correspondence is clearly visible in Figures 12 and 13, where the displacement fields obtained for the selected model are visualised and juxtaposed with those of the experiment. It should be emphasised that the surface conditions of the contact surface are to be seen as stochastic, as they are highly dependent on the accuracy of the samples and the material heterogeneity (e.g., twist of the fibres or small local knots in the timber).

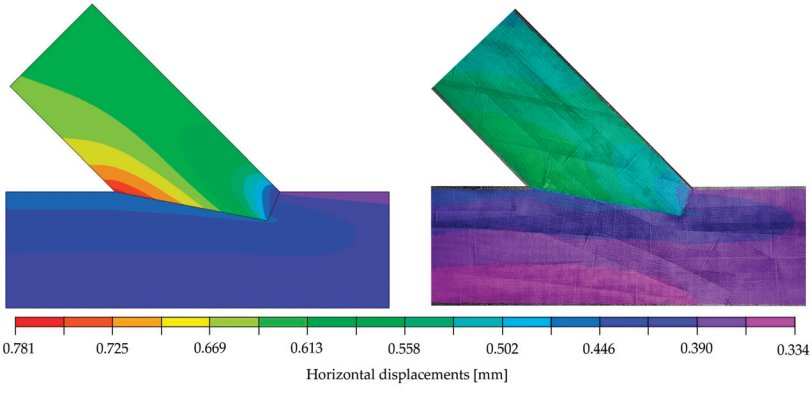

Figure 12. (**Left**): Horizontal displacements of the numerical model at a load of 29.6 kN; (**Right**): DIC-horizontal displacements on the surface of specimen A_5 at 70.1 kN with the initial picture at 40.5 kN (representing a load step of approximately 29.6 kN).

The compliance of the experimental and numerical results obtained for the single-step joint in terms of stiffness and the verification equation, Equation (3), entitled the authors to conduct further computational simulations. In a subsequent step, a stress analysis was performed on the numerical model to determine possible forms of joint failure. A quantitative analysis of the calculated stresses was performed with the following mean values of strength parameters for spruce: tension parallel to the grain 30.00 MPa, compression parallel to the grain 32.00 MPa [24], compression perpendicular to the grain 3.57 MPa and shear 3.85 MPa [25]. The local failure mode was defined as a deformation associated with exceeding related strength parameters in the simulation. The linear computational model only allowed for the indication of the load at which the standard maximum stresses are exceeded. This state can be identified as the beginning of local failure, yet it does not

necessarily lead to a load drop. Due to the assumptions made within the numerical model, progressive damage could not be considered.

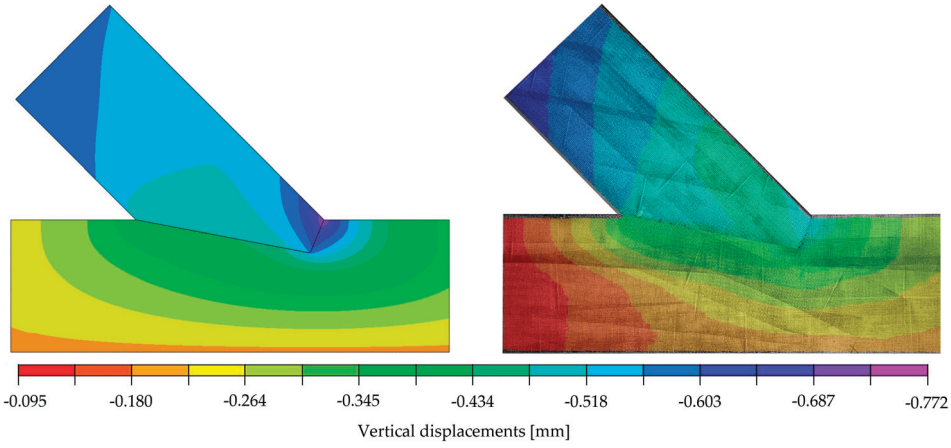

Figure 13. (**Left**): Vertical displacements of the numerical model at a load of 29.6 kN; (**Right**): DIC-vertical displacements on the surface of specimen A_5 at 70.1 kN with the initial picture at 40.5 kN (representing a load step of approximately 29.6 kN).

With the numerical model being linear, it was possible to determine the load value at which a specified stress value exceeded the material strength. The determined load values indicating the location of extreme stress are listed in Table 2. The analysis thereof showed that the first to reach its maximum was shear (load approximately at 50 kN). If the load further increased to 52 kN in the numerical model, compressive failure perpendicular to the grain followed.

Table 2. Location and values of extreme values of stresses in single-step joint with the information of load at which those values reach respective limits.

Stress		Value for 30 kN [MPa]	Strength [MPa]	Limit Load [kN]	Location: Point (Beam)	Figure
parallel to the grain	tension	4.900	30.00	183.7	1 (lower)	Figure 14
	compression	11.000	32.00	87.3	2 (upper)	Figure 14
perpendicular to the grain	tension	0.024	0.50	625.0	3 (upper)	Figure 15
	compression	2.060	3.57	52.0	4 (upper)	Figure 15
shear	positive	2.310	3.85	50.0	5 (lower)	Figure 16
	negative	2.380	3.85	48.5	6 (upper)	Figure 16

The stress distributions at a load of 29.6 kN are shown in Figures 14–16. For the extreme values occurring in places of stress concentrations, the data were not extracted directly from that location but at a distance of 8 mm, allowing for reliable values close enough to the concentration point yet not obscured by the modelling.

Even though the linear model did not allow for the analysis of damage propagation, and the indicated values did not coincide with load-bearing capacity obtained during experimental results, comparing load values taken from the numerical model with those from the experiments showed that an exceedance of the strength values is not necessarily accompanied by a decrease in the joints' stiffness, as seen in Figure 6. In order to cor-

rectly represent the load-bearing capacity, a failure criterion had to be introduced to the numerical model.

When looking at the connection itself, Figure 17 shows a comparison of the joint post loading for both the simulation and the experiment. The upper beam layers separated and shifted relative to each other at the connection point, indicating that the allowable shear stress had been exceeded. In addition, a bending of the aforementioned fibres was noticeable, most likely caused by exceeding the allowable compressive stresses along the fibres. The numerical model indicated that the latter occurs at a load force of 87 kN. The value varied from the actual results due to possible redistributions associated with earlier strength attainment in other directions. Even though the exact failure load could not be calculated using the model, valuable insights regarding failure type could be derived, as is clearly visible in Figure 17, where the joint deformation in both physical and numerical models were in good compliance.

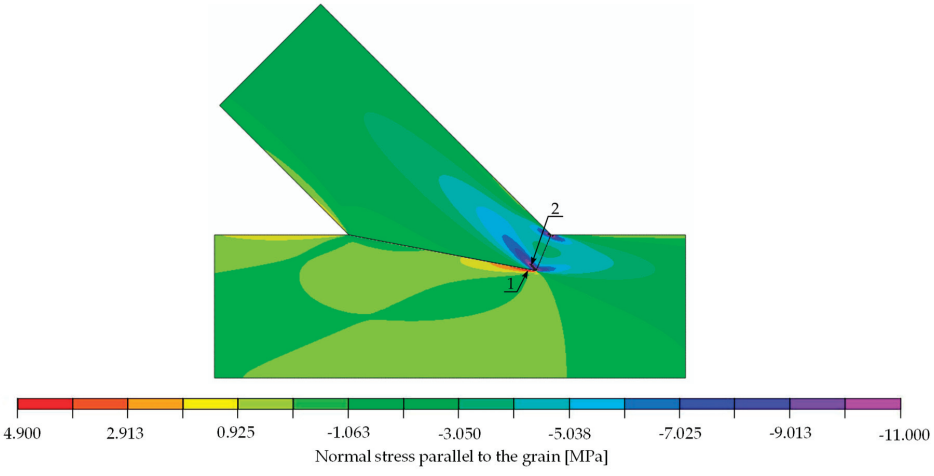

Figure 14. Normal stress parallel to the grain [MPa]. Force 29.6 kN.

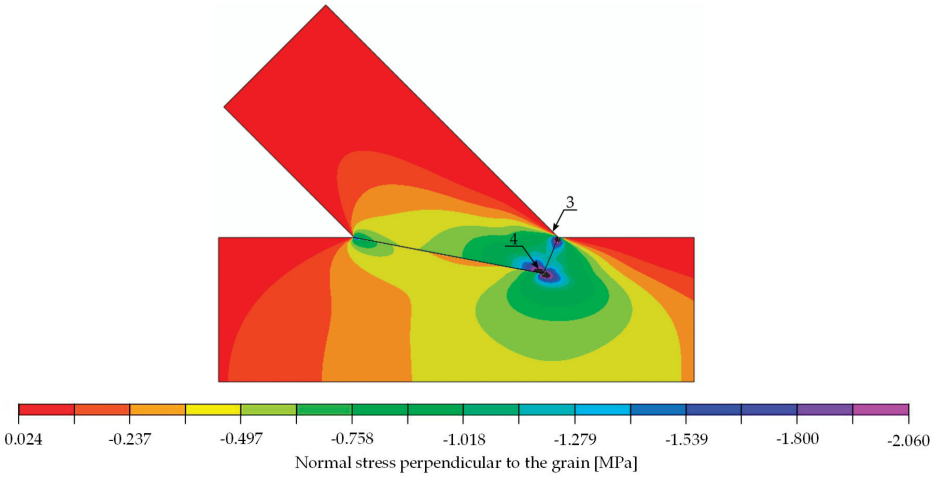

Figure 15. Normal stress perpendicular to the grain [MPa]. Force 29.6 kN.

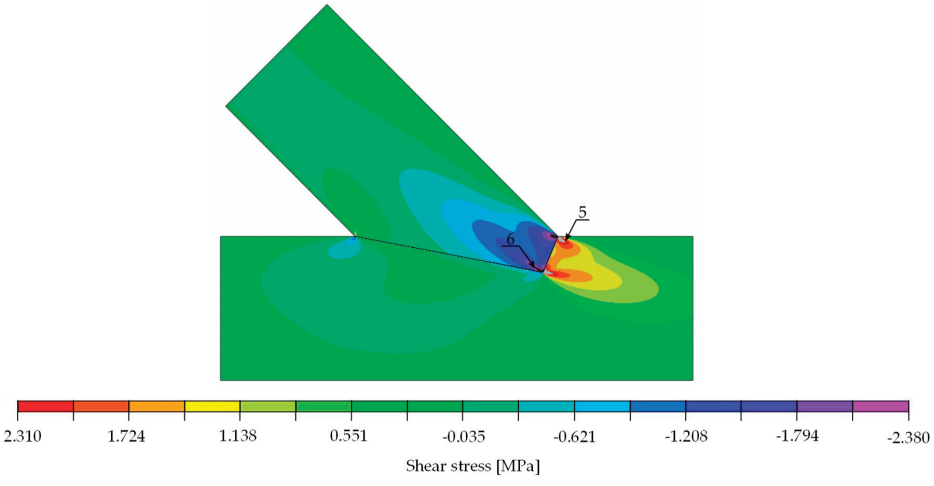

Figure 16. Shear stress [MPa]. Force 29.6 kN.

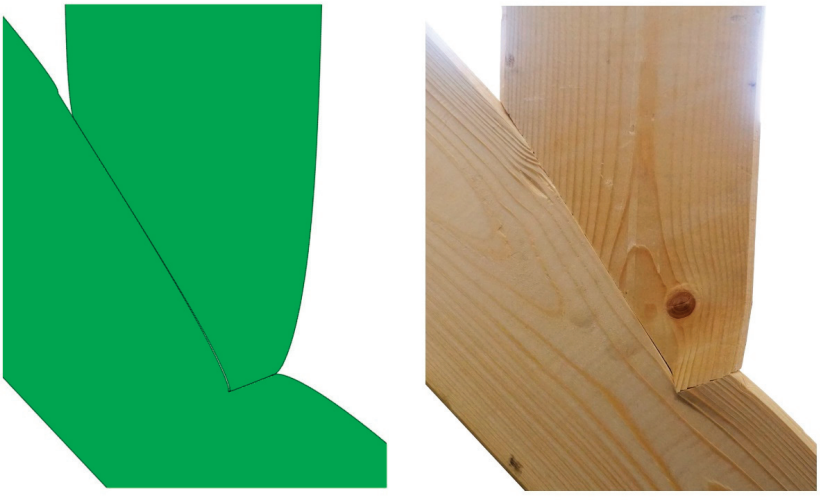

Figure 17. (**Left**): Deformation of numerical model; (**Right**): failure of single-step joint in the experiment.

5. Application of the Calibrated Numerical Model on a Double-Step Joint

The main goal of the authors for the computational analysis was to create a model that could also be applied to other geometries. The results of experimental investigations of double-step joints (Series B) were used to validate the calibrated model, to predict the stiffness and indicate the possible failure mode of the new connection. The geometry of the joint, load introduction point and the geometrical boundary conditions are presented in Figure 18 and can also be found in [1].

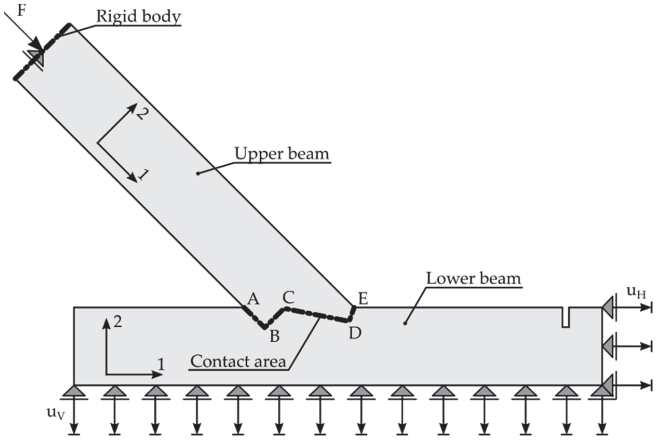

Figure 18. Geometrical data of the FEM model for the double-step joint. Axis 1 represents the orientation parallel to the grain.

The results of the experimental investigation of Series B are presented in Figure 19 in form of a force-displacement diagram, serving as a reference for the validation of the predicted stiffness. The test series consisted of three specimens tested under the same conditions as Series A. Furthermore, the specimens were produced out of the same material.

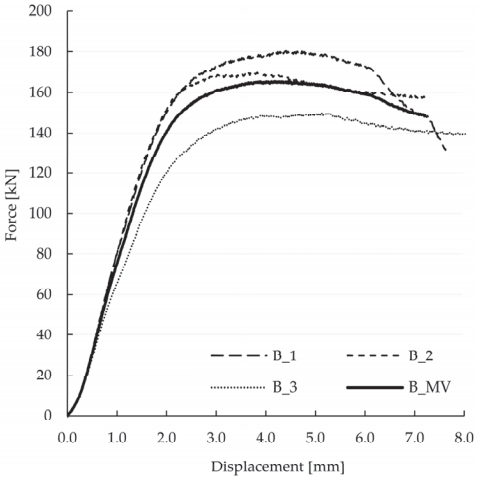

Figure 19. Force-displacement curves of all three single-step specimens, as well as the mean value MV of the three specimens.

The results of the calculations in form of stress distribution and the location where stress equalled material strength (according to Table 3 for the double-step joints) can be seen in Figure 20 (normal stress parallel to the grain), Figure 21 (normal stress perpendicular to the grain) and Figure 22 (shear stress).

Table 3. Stress values and location at a load of 29.6 kN for the double-step joint including the calculation of the limit load for the individual stress (considering the linear progression).

Stress		Value for 29.6 kN [MPa]	Strength [MPa]	Limit Load [kN]	Location: Point (Beam)	Figure
parallel to the grain	tension	4.00	30.00	225.0	1 (lower)	Figure 20
	compression	13.49	32.00	71.2	2 (upper)	Figure 20
perpendicular to the grain	tension	0.33	0.50	45.5	3 (lower)	Figure 21
	compression	1.86	3.57	57.6	4 (lower)	Figure 21
shear	positive	1.73	3.85	66.8	5 (lower)	Figure 22
	negative	1.71	3.85	67.5	6 (upper)	Figure 22

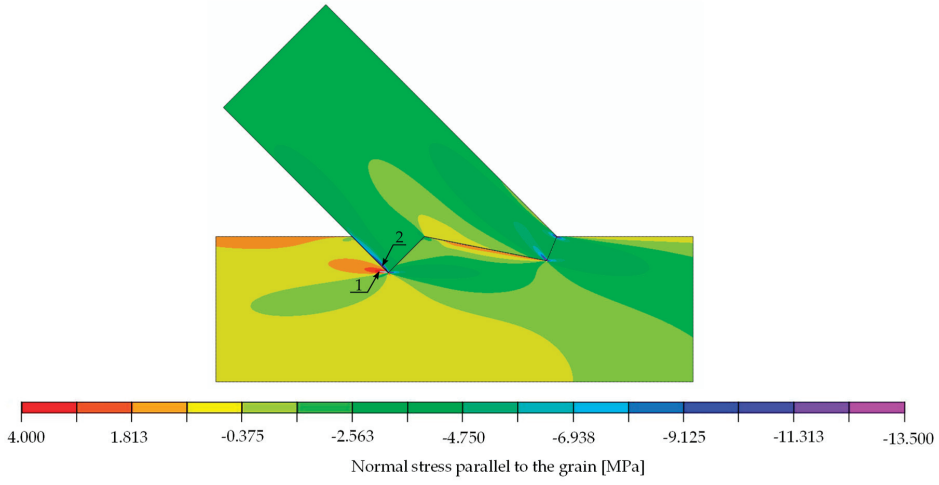

Figure 20. Double-step joint FEM modelling—normal stress parallel to the grain [MPa]. Force 29.6 kN.

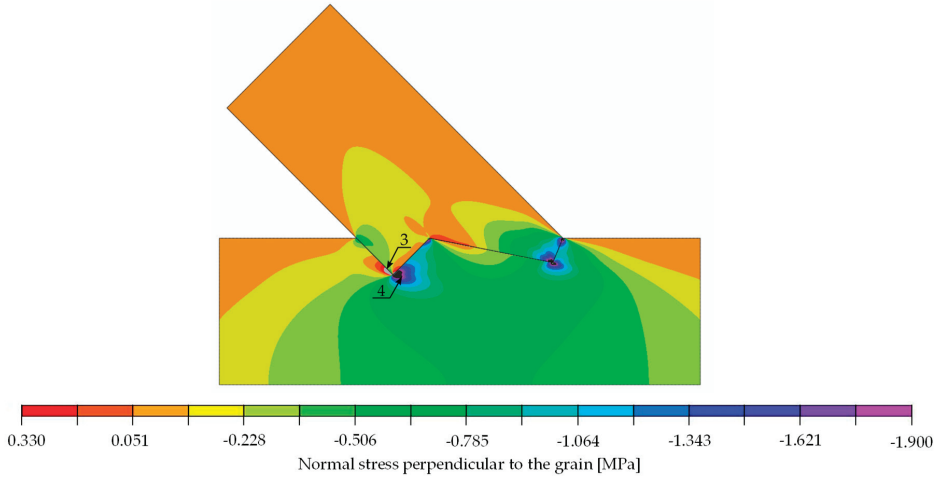

Figure 21. Double-step joint FEM modelling—normal stress perpendicular to the grain [MPa]. Force 29.6 kN.

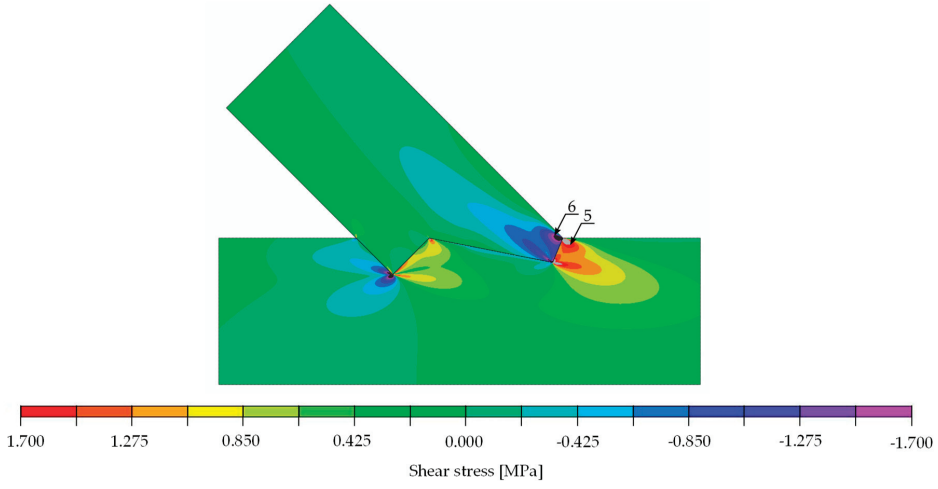

Figure 22. Double-step joint FEM modelling—shear stress [MPa]. Force 30 kN.

The stress values at a load of 29.6 kN, as well as the locations and load values at which the material properties were exceeded, are listed in Table 3 for the double-step joint.

The analysis of Figure 20 through Figure 22 and Table 3 allowed for the prediction of possible local failure modes. Based on the calculations of the single-step joint, the numerical model for the double-step joint was loaded with 29.6 kN. This assumption can be considered correct as the linear range of the specimens starting at 12 kN and ending at 79 kN, as pictured in Figure 19. According to the linear model, the first stress limit reached was that of tensile strength perpendicular to the grain close to point B (see Figure 18) at a load of 45.5 kN, followed by a failure mode related to exceeding the shear stress limit close to point E. The last-mentioned mode is visualised in Figure 23, where the timber layers on the right-hand side of the connection separated and moved relative to each other. The crack visible in Figure 23 was further pre-announced by the distribution of shear stress (shown in Figure 24), where the sign changed within the upper beam (which is related to the change of the direction of shear deformation), suggesting the possibility of a crack occurrence starting at point B in the upper beam.

It should be noted that, according to [6], each analysed specimen of the double-step joint exhibited a slightly different behaviour in the experimental tests, in terms of both the stiffness and the failure modes. During the testing of some samples, the failure modes observed in the numerical analysis occurred nearly simultaneously within the experiments. Furthermore, it should be highlighted that the double-step joint has a higher sensitivity to manufacturing inaccuracies and randomness of the mechanical properties of the wood due to its design. Even though it is not possible to create a general valid numerical model that can accurately predict failure modes of such connections, it was shown within the double-step joint analysis that the proposed linear model could be used to give a general indication of possible damage modes and locations.

Moreover, the calibrated linear model allows for a quantification of the stiffness of the double-step connection. The stiffness k, obtained from the numerical analysis, was calculated to 86.0 kN/mm, while that of the Series B specimens equalled 87.0 kN/mm. The good compliance of the results shows the viability of the proposed linear numerical model in regard to first assessments of timber–timber connections.

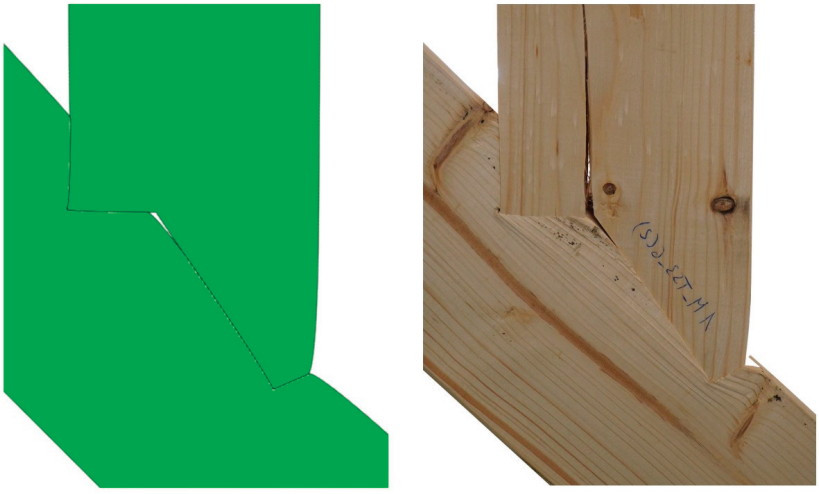

Figure 23. (**Left**): Deformation of numerical model; (**Right**): failure of double-step joint in the experiment.

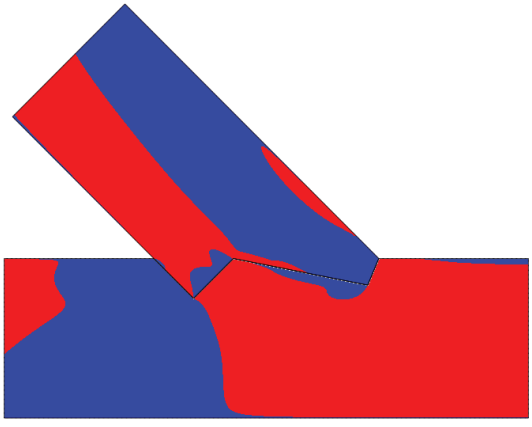

Figure 24. Shear stress distribution: negative (blue) and positive values (red).

6. Concluding Remarks

The authors presented a simplified strategy using a linear-elastic model of an orthotropic body for the numerical simulation of single- and a double-step timber joints under compression. The numerical model was calibrated using the results of experimental investigations on a series of single-step joints. A DIC measurement system allowed for the documentation of the displacements on the surface of the specimens, which made it possible to quantify their rigid movement and deformation. Due to the fact that numerical results obtained with the assumption of material parameters taken from design code did not reflect laboratory tests to a satisfactory degree, the results obtained for the single-step joint were used for the calibration of the FE model with the use of Abaqus software and Python codes, resulting in a calibrated model without specified material parameters.

The presented numerical and experimental analyses were qualitatively consistent and confirm the applicability of the approach. The applied numerical model made it possible to satisfactorily quantify the stiffness of both connections (inclination of the linear-elastic phase in the force-displacement diagrams) and to predict the location of local failures.

However, in the single-step joint, the prediction was more accurate, based on the fact that the model was calibrated for this type of joint, and the connection itself is less prone to inaccuracies of the geometry. The possible local failure modes were identified in places where strength limits were exceeded. However, it should be highlighted that such states do not necessarily lead to a load drop—they only indicate that some local damages occur.

The main advantage of a linear analysis is the speed of calculation and the relative ease of model building. However, interpretation of the results requires knowledge of the mechanical behaviour of timber. The proposed model can be extended by introducing failure criteria such as the Tsai–Wu criterion mentioned in [26]. This would allow for the prediction of the load-bearing capacity of the joint and indicate the failure modes and stiffness of the system. However, one should keep in mind the heterogeneity of the material, which introduces uncertainty in the calculations. According to the authors, crack mechanics modelling of the development of the destruction zone is not advisable if the modelling and computational effort should be kept to a certain boundary due to the scattering of wood characteristics. Inconsistencies of the samples, such as the arrangement of fibres, the presence of small knots and heterogeneity, as well as the inevitable geometrical inaccuracies in the fabrication of samples, should, therefore, be considered.

The proposed numerical model is recommended for future, non-destructive research of timber connections to estimate the stiffness and the failure mode. Possible future directions of research could be related to the analysis of various geometries of joints, including gaps between the connected beams, and optimisation of contact geometry in order to avoid stress concentrations and failure analysis in the frame of crack mechanics.

Author Contributions: Conceptualization, J.P. and B.K.; Methodology, M.B., J.P., A.A.S.-Z. and B.K.; Software, J.P. and A.A.S.-Z.; Validation, B.K. and J.P.; Formal Analysis, B.K. and J.P.; Investigation, M.B.; Resources, B.K.; Data Curation, M.B. and J.P.; Writing—Original Draft Preparation, M.B. and J.P.; Writing—Review and Editing, A.A.S.-Z. and B.K.; Visualization, M.B. and J.P.; Supervision, B.K.; Project Administration, M.B.; Funding Acquisition, B.K. and A.A.S.-Z. All authors have read and agreed to the published version of the manuscript.

Funding: This research received no external funding.

Institutional Review Board Statement: Not applicable.

Informed Consent Statement: Not applicable.

Conflicts of Interest: The authors declare no conflict of interest.

References

1. Anderson, T.R.; Hawkins, E.; Jones, P.D. CO_2, the greenhouse effect and global warming: From the pioneering work of Arrhenius and Callendar to today's Earth System Models. *Endeavour* **2016**, *40*, 178–187. [CrossRef] [PubMed]
2. United Nations Environment Programme. 2019 Global Status Report for Buildings and Construction. 2019. Available online: https://wedocs.unep.org/handle/20.500.11822/30950 (accessed on 6 November 2021).
3. Churkina, G.; Organschi, A.; Reyer, C.P.O.; Ruff, A.; Vinke, K.; Liu, Z.; Schellnhuber, H.J. Buildings as a global carbon sink. *Nat. Sustain.* **2020**, *3*, 269–276. [CrossRef]
4. Kromoser, B.; Braun, M. Towards efficiency in constructive timber engineering—Design and optimization of timber trusses. In Proceedings of the IABSE Congress 2019, New York, NY, USA, 4–6 September 2019.
5. Kromoser, B.; Braun, M. Industrialization of the Design and Production Process of Wooden Trusses. CompWood. 2019. Available online: https://open.lnu.se/index.php/compwood/issue/view/146/Boog%20of%20abstracts (accessed on 10 December 2021).
6. Braun, M.; Pantscharowitsch, M.; Kromoser, B. Experimental investigations on the load-bearing behaviour of traditional and newly developed step joints for timber structures. *Constr. Build. Mater.* **2022**, *323*, 126557. [CrossRef]
7. Braun, M.; Kromoser, B. Under Review-The Influence of Inaccuracies in the Production Process on the Load-Bearing Behaviour of Timber Step Joints. *SSRN J.* **2021**. [CrossRef]
8. CEN. *ÖNORM EN 14080: 2013 08 01: Timber Structures—Glued Laminated Timber and Glued Solid Timber—Requirements*; European Committee for Standardization: Brussels, Belgium, 2013.
9. Kandler, G.; Lukacevic, M.; Füssl, J. Experimental study on glued laminated timber beams with well-known knot morphology. *Eur. J. Wood Prod.* **2018**, *76*, 1435–1452. [CrossRef]
10. Fink, G.; Kohler, J. Model for the prediction of the tensile strength and tensile stiffness of knot clusters within structural timber. *Eur. J. Wood Prod.* **2014**, *72*, 331–341. [CrossRef]

11. Vaiana, N.; Sessa, S.; Marmo, F.; Rosati, L. A class of uniaxial phenomenological models for simulating hysteretic phenomena in rate-independent mechanical systems and materials. *Nonlinear Dyn.* **2018**, *93*, 1647–1669. [CrossRef]
12. Vaiana, N.; Sessa, S.; Rosati, L. A generalized class of uniaxial rate-independent models for simulating asymmetric mechanical hysteresis phenomena. *Mech. Syst. Signal Process.* **2021**, *146*, 106984. [CrossRef]
13. Argilaga, A.; Papachristos, E. Bounding the Multi-Scale Domain in Numerical Modelling and Meta-Heuristics Optimization: Application to Poroelastic Media with Damageable Cracks. *Materials* **2021**, *14*, 3974. [CrossRef]
14. Green, A.E.; Zerna, W. *Theoretical Elasticity*; Courier Corporation: London, UK, 1968.
15. Thelandersson, S.; Larsen, H.J. (Eds.) *Timber Engineering*; Wiley: New York, NY, USA, 2003.
16. Zienkiewicz, O.C.; Taylor, R.L. *The Finite Element Method*, 5th ed.; Butterworth-Heinemann: Oxford, UK; Boston, MA, USA, 2000.
17. Mackerle, J. Finite element analyses in wood research: A bibliography. *Wood Sci. Technol.* **2005**, *39*, 579–600. [CrossRef]
18. Villar-García, J.R.; Vidal-López, P.; Crespo, J.; Guaita, M. Analysis of the stress state at the double-step joint in heavy timber structures. *Mater. Constr.* **2019**, *69*, 196. [CrossRef]
19. Al Sabouni-Zawadzka, A.; Gilewski, W.; Pełczyński, J.; Skowronska, M. 3D Finite Element Stress Analysis of Reinforced Double-Tapered Glulam Beams. *IOP Conf. Ser. Mater. Sci. Eng.* **2019**, *661*, 012068. [CrossRef]
20. Gilewski, W.; Pełczyński, J. The Influence of Orthotropy Level for Perpendicular to Grain Stresses in Glulam Double Tapered Beams. 23rd International Conference Engineering Mechanics. 2017. Available online: https://www.engmech.cz/improc/2017/0342.pdf (accessed on 23 October 2021).
21. Al Sabouni-Zawadzka, A.; Gilewski, W.; Pełczyński, J. Some considerations on perpendicular to grain stress in double-tapered glulam beams. *MATEC Web. Conf.* **2017**, *117*, 00058. [CrossRef]
22. Al Sabouni-Zawadzka, A.; Gilewski, W.; Pełczyński, J. Perpendicular to grain stress concentrations in glulam beams of irregular shape—Finite element modelling in the context of standard design. *Int. Wood Prod. J.* **2018**, *9*, 157–163. [CrossRef]
23. Abaqus Version 6.13. *Simula. ABAQUS User Subroutine Reference Guide*; Abaqus: Providence, RI, USA, 2013.
24. Spaethe, G. *Die Sicherheit Tragender Baukonstruktionen*; Springer: New York, NY, USA, 1992.
25. Bedon, C.; Fragiacomo, M. Numerical analysis of timber-to-timber joints and composite beams with inclined self-tapping screws. *Compos. Struct.* **2019**, *207*, 13–28. [CrossRef]
26. Xu, B.-H.; Bouchaïr, A.; Racher, P. Appropriate Wood Constitutive Law for Simulation of Nonlinear Behavior of Timber Joints. *J. Mater. Civ. Eng.* **2014**, *26*, 04014004. [CrossRef]

materials

MDPI

Article

Novel Apex Connection for Light Wood Frame Panelized Roof

Md Saiful Islam [1,*], Ying Hei Chui [1,*] and Zengtao Chen [2]

[1] Department of Civil and Environmental Engineering, University of Alberta, Edmonton, AB T6G 1H9, Canada
[2] Department of Mechanical Engineering, University of Alberta, Edmonton, AB T6G 1H9, Canada
* Correspondence: mdsaiful@ualberta.ca (M.S.I.); yhc@ualberta.ca (Y.H.C.)

Abstract: Panelized fabrication of light-frame wood buildings has higher productivity than the traditional stick-built method. However, the roof production process is not very efficient due to the structural system and construction method. This study proposes a novel apex connection that allows for a folding mechanism in a panelized light wood frame roof system. Proof of concept of the proposed connection assembly is presented by a 3D printout of the developed connection. Following the steel design code and timber code, the initial estimation of different parameters, such as the pinhole diameter and number screws, were established. A detailed finite element analysis (FEA) was performed to determine the connection strength requirement for different load case scenarios. The results of the FEA and 3D printout of the assembly show that the proposed connection can provide the required folding mechanism before roof installation and can withstand the load in the unfolding state at service.

Keywords: apex connection; folding mechanism; FEA; panelized light frame roof

Citation: Islam, M.S.; Chui, Y.H.; Chen, Z. Novel Apex Connection for Light Wood Frame Panelized Roof. *Materials* **2022**, *15*, 7457. https://doi.org/10.3390/ma15217457

Academic Editors: Radosław Mirski and Dorota Dukarska

Received: 26 August 2022
Accepted: 20 October 2022
Published: 24 October 2022

1. Introduction

The majority of residential buildings constructed in North America are light-frame wood buildings (approximately 90%), mostly in the form of single detached family houses and low-rise multi-story apartments [1,2]. In light wood frame construction, the primary framing material is dimension lumber, which is often utilized in combination with other wood products such as plywood, I-beams, and oriented strand board (OSB) to fabricate a building [3–5]. However, in recent decades, application of engineered lumber such as laminated strand lumber (LSL) has increased due to the dimensional stability of this structural composite lumber product and the adoption of an off-site construction process. For example, an Alberta-based prefab company in Canada uses LSL and OSB to produce light frame walls and their wall production is fully automated, whereas floor production uses wood I-joist in combination with a semiautomated process [6]. This type of light wood frame construction is termed panelized construction. Panelized construction of light wood frame homes is drawing attention in North America due to its design flexibility and on-site assembly cost savings [7,8]. It utilizes manufacturing principles to build light-frame wood buildings. This off-site construction process subdivides a building model into subassemblies, such as wall panels, floor panels, and volumetric roof elements, which are manufactured in a factory environment and then shipped to the site for installation. A light-frame panelized-building production facility typically encompasses several workstations such as wall and floor production lines.

As most construction activities in the panelized construction of light wood frame buildings are performed in a manufacturing environment, it is critical to obtain optimal productivity in the production lines [7,8]. In the current panelized construction process, the roof is built using closely spaced wood trusses that support OSB sheathing and roofing materials (on the upper chord) and drywall ceiling materials (on the lower chord). The entire roof of a single detached home is subdivided into four or five small volumetric units based on the floor area and is manufactured on the roof production line [6]. The fabrication

of roofs follows the same methodology as stick-built construction. For example, the roof trusses are laid out on a setup jig platform (Figure 1a) in the offsite facility according to the building plan, as shown in Figure 1b. Then, other roof components are added (Figure 1c) to manufacture the small roof modules. All the activities in the roof module production are manual and labour intensive. Consequently, current roof production is not as efficient as other building components, such as the wall or floor. Moreover, transporting the roof volumetric units requires a relatively large number of trailers (to be specific, in the case of an Alberta-based home manufacturer, four trailers are required to transport a 1600 sq ft single-family home) and on-site loading and unloading of trusses increases the overall work duration [9]. Therefore, to improve the current roof construction a holistic approach was developed by Islam et al. [10,11]. In this holistic approach, a gable roof was divided into several sub-elements. The dimensions of these sub-elements were aligned with the production line constraints of offsite facility, transportation trailer capacity, crane lifting limitations, and on-site installation considerations. The complete the panelized roof system for a typical two-storey house with a gable roof comprises the following components (Figure 2): (a) Roof panels, (b) support wall panels, (c) celling frames, (d) beams spanning over two support walls, (e) gable ends, and (f) inter-component connections, including the inclined roof panel-to-support wall, ceiling frame-to-load-bearing shear wall, apex connection, and the support wall-to-ceiling frame.

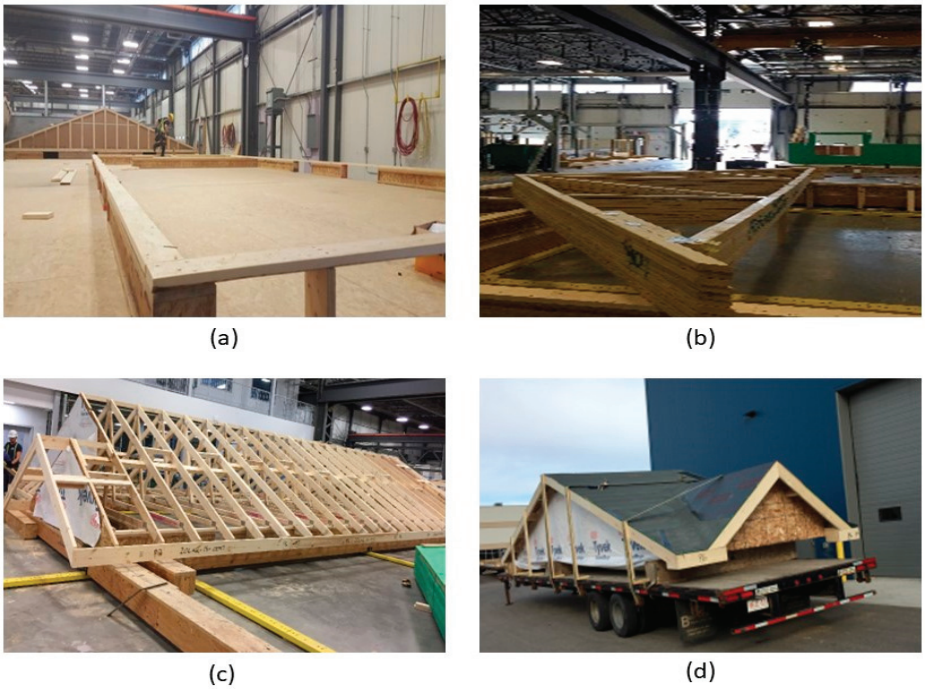

Figure 1. Roof production (**a**) setup jig, (**b**) unloaded truss, (**c**) attaching roof components, and (**d**) small roof module on the transportation trailer (courtesy of ACQBUILT Inc., Edmonton, AB, Canada) [6].

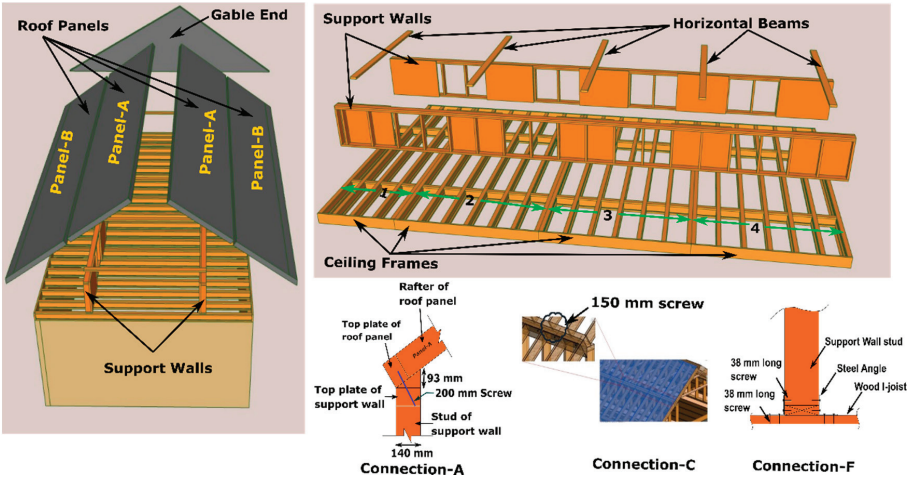

Figure 2. Light wood frame panelized roof concept.

Due to panelization, major components, such as roof panels, ceiling frames and support walls, can be produced in the automated and semi-automated production line of an offsite facility [10]. For instance, the roof panels (panel-A and panel-B in Figure 2) and support walls are produced using LSL and OSB in the wall production line. In contrast, ceiling frames are built using wood I-joist and an LSL rim board. Consequently, major roof component fabrication is expected to require less production time in contrast to the current process due to the utilization of the current wall and floor panel assembly lines. Moreover, transporting the panelized roof requires only one trailer trip in contrast to the current roof system for the same home size [12]. However, in the panelized roof system, all the components are assembled at the site. Consequently, onsite workload increases significantly [9]. Thus, installation of the inter-component connections must be easy to minimize the on-site workload. This paper presents a concept of a novel apex connection that allows assembling two roof panels (Panel-A in Figure 2) at the offsite facility and folding of roof panels while transporting and the self-locking mechanism facilitates easy lifting and installation of the two connecting panels (Figure 3).

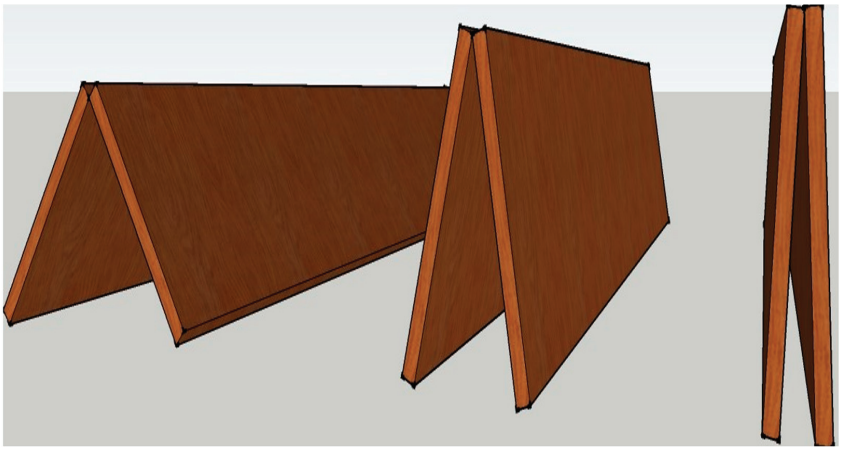

Figure 3. Roof panel folding.

2. Novel Triangular Hinge Apex Connection

The main limitation of the panelized roof system is the increased crane lifting number while installing the roof at the site. To reduce the onsite workload, a novel connection mechanism is developed so that multiple panels can be lifted at once. The apex connection for a panelized roof with an 8/12 slope can be used to connect the two Panels (in this case panel-A as shown in Figure 2). The advantage of this connection is that it is self-locking and foldable. The apex connection can be installed at the offsite facility and thus two panels will form a triangle module that can be folded, as shown in Figure 3. This folded state of the panel facilitates easy transportation to the site and a single crane lift is required for installation. Since the connection facilitates a self-locking mechanism, the roof panel installation requires no additional job once the module reaches the proper roof angle. Thereby, this system is expected to reduce a significant amount of the workload at the site. To demonstrate the folding and locking mechanism of the assembly, a full-scale 3D printout using PLA prototyping material was developed. Figure 4 illustrates the folding and unfolding state of the 3D full-scale printout. A video of the folding mechanism can be found in the Supplementary Materials of this paper. The primary components of the connection are shown in Figure 5 and consist of the following 8 parts:

1. Secondary bars to connect the panel rafter
2. Primary Folding link bars
3. Main lock channel
4. Middle bar
5. Secondary lock channel
6. Side-bars
7. Secondary Folding link bars
8. Pins

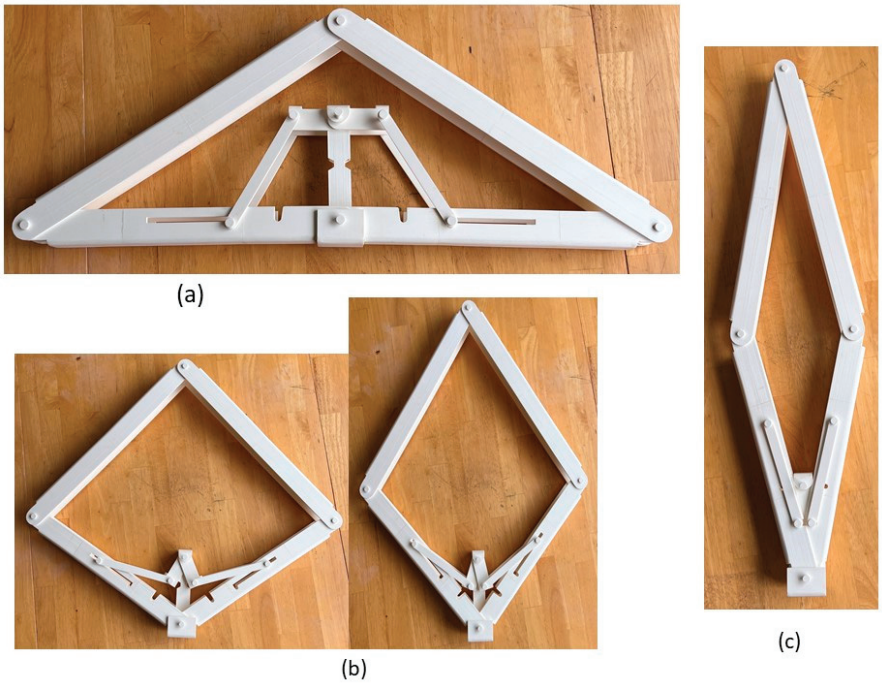

Figure 4. 3D printout of full-scale assembly using PLA prototyping material: (**a**) Unfolded state, (**b**) partial folding state, and (**c**) full folding state.

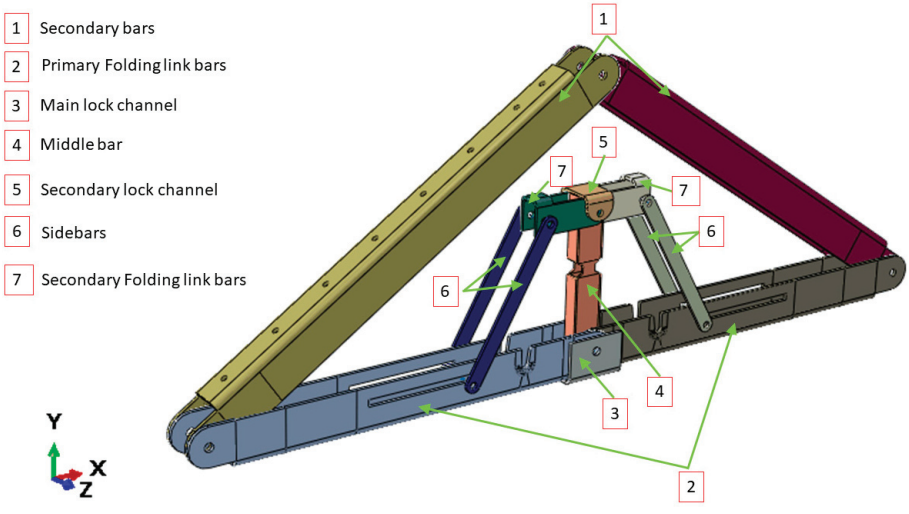

Figure 5. Components of the novel apex connection system for a light frame panelized roof.

The secondary bars are connected to the roof panel rafter using screws, while the primary folding link bars act as rigid link elements when the connection assembly is completely unfolded at the service condition. The primary folding link bar itself has two bars connected using a pin whereas the two secondary bars are tied using pins to the ends of the folding link bars and with each other at the apex point. In order to act as a rigid link, the folding bar has to resist clockwise and counterclockwise rotation depending on the loading condition. The self-locking mechanism is provided through the main lock channel, middle bar, secondary link bars, secondary lock channel and sidebars. It can be observed from Figure 6 that clockwise rotation at point A is resisted by the main lock channel placed at the bottom of the primary folding link bar, whereas counterclockwise rotation is resisted by the secondary lock channel.

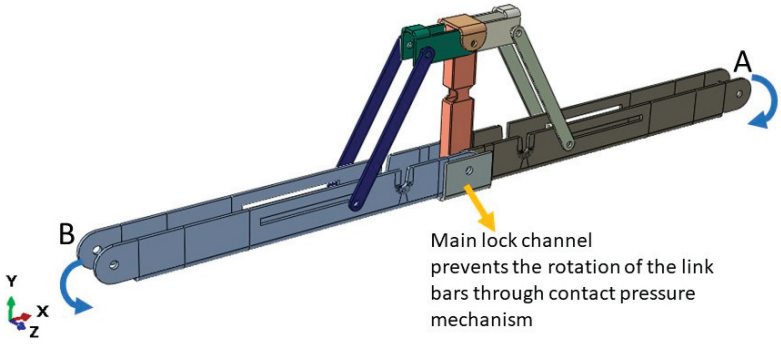

Figure 6. The main lock channel resisting clockwise rotation at point A.

All the components can be fabricated using steel sheet metal (12 gauge and 11 gauge). EN 1993-1-8 [13] provides a general guideline for the edge and end distance of pin holes. Figure 7 shows geometrical requirements for pin-ended members according to EN 1993-1-8. The initial estimate of the hole diameter of the assembly was designed considering the steel design guideline by EN 1993-1-8 [13]. For an 11-gauge plate, (yield strength of plate f_y = 187 MPa, hole diameter d_o = 7.35 mm and design pin force F_{ED} = 8000 N) member the corresponding edge distance and end distance are 10.7 mm and 12.3 mm, respectively.

Hole dimensions of the main link bar are governed by the pin diameter requirement, which primarily depends on the shear capacity of the pin. To analyze the connection, a reasonable diameter of the pin was obtained using the pin connection shear capacity equation of EN 1993-1-8 [13]. Following the design guideline and assuming a design value of pin joint dimensions of the parts of apex connection were determined for numerical analysis. Detailed dimensions of all the components of the novel apex connection for a case study roof slope 8/12 are illustrated in Figures 8–14.

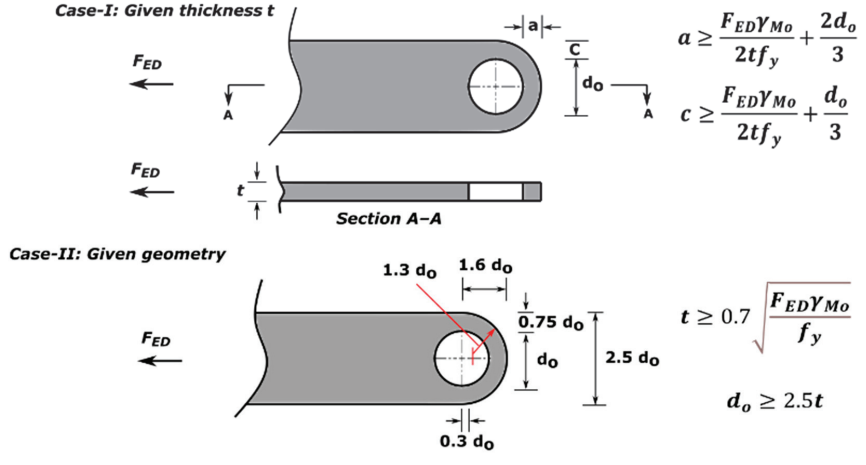

Figure 7. Edge distance and end distance requirement for pin connection according to EN 1993-1-8 [13].

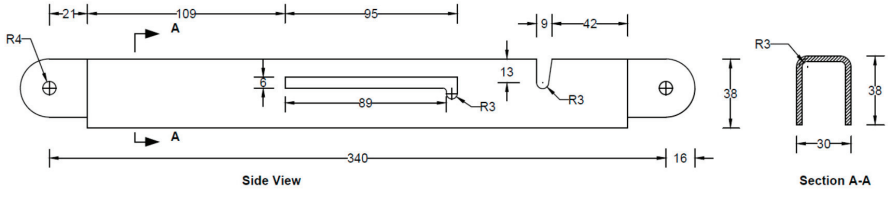

Figure 8. Details of primary folding link bars (all dimensions are in mm, steel plate gauge 11).

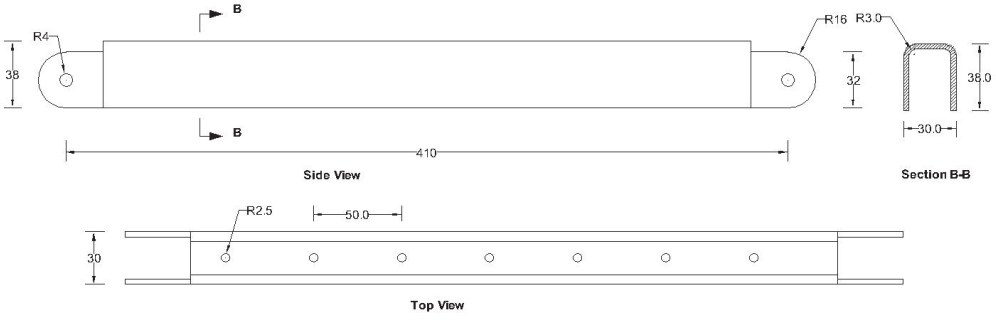

Figure 9. Details of Secondary bars (all dimensions are in mm, steel plate gauge 11).

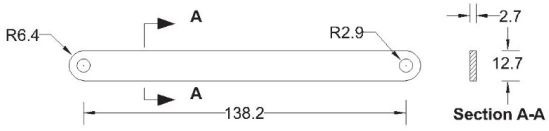

Figure 10. Details of Sidebars (all dimensions are in mm, steel plate gauge 12).

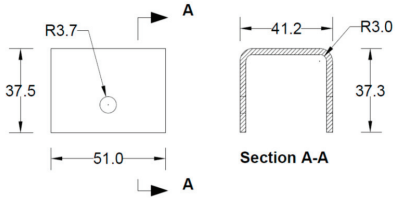

Figure 11. Details of main lock channel (all dimensions are in mm, steel plate gauge 11).

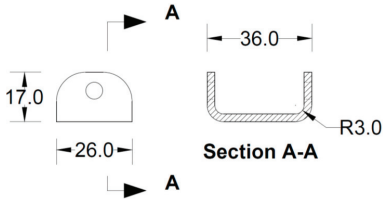

Figure 12. Details of secondary lock channel (all dimensions are in mm, steel plate gauge 12).

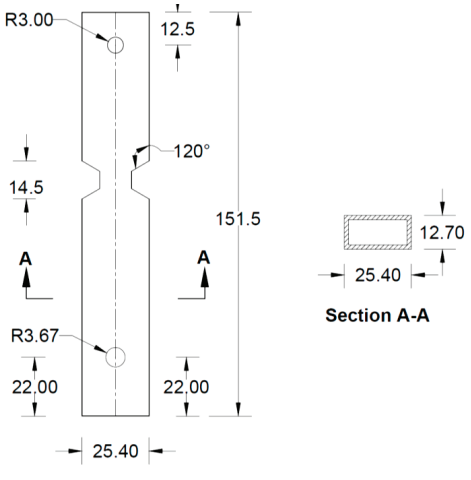

Figure 13. Details of Middle bar (all dimensions are in mm, HSS section).

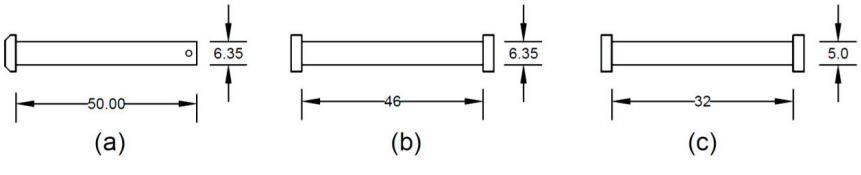

Figure 14. (**a**) Pin for connecting secondary bars at the apex point; (**b**) pin at the middle of the main link bar; and (**c**) Pin for sidebars.

3. Analysis of the Case Study Connection

As can be observed from Figure 3, the apex connection is installed to connect two panels and the main folding bar of the proposed connection at the unfolding state must resist the load at peak of the assembly. This system can be idealized as a statically indeterminate rafter system that has eave support with a collar strut (Figure 15). Using Castigliano's theorem on deflections with enforcement of displacement compatibility at the redundant reaction, unknown forces of the free body diagram shown in Figure 16 can be obtained using Equations (1)–(4) [14].

$$A_x = \frac{wL}{8tan\theta}\left[\frac{-\alpha^2 + 5\alpha + 1}{\alpha}\right], \tag{1}$$

$$B_x = \frac{wL}{8tan\theta}\left[\frac{\alpha^2 - 5\alpha + 3}{(1-\alpha)}\right], \tag{2}$$

$$C_x = \frac{wL}{8tan\theta}\left[\frac{-\alpha^2 + \alpha + 1}{\alpha(1-\alpha)}\right], \tag{3}$$

$$A_y = wL, \tag{4}$$

where:
α = a span factor used to express the location of the interior support or attachment point of the folding link bar
L = horizontal projection of the distance from the eave to the Apex (the distance in the plan).
θ = roof pitch (rafter slope) relative to the horizontal.
x_1 and x_2 = span coordinates measured horizontally, as indicated in Figure 16
w = gravity load including the self-weight of the roof panel expressed as a uniformly distributed load

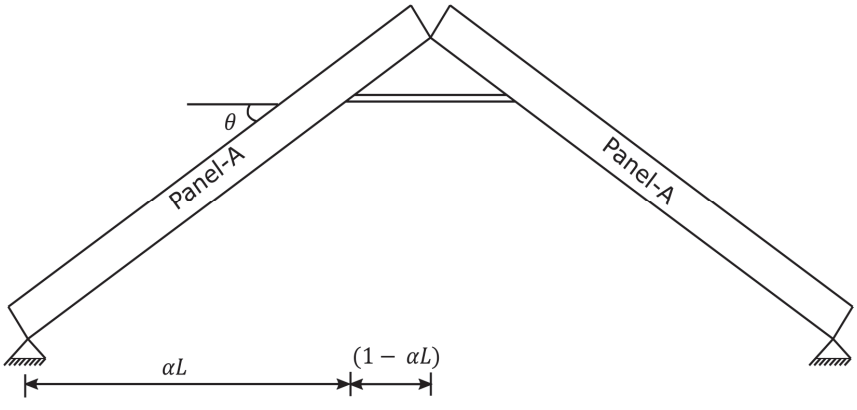

Figure 15. The apex connection idealized as rafter support system eave support with Collar Strut.

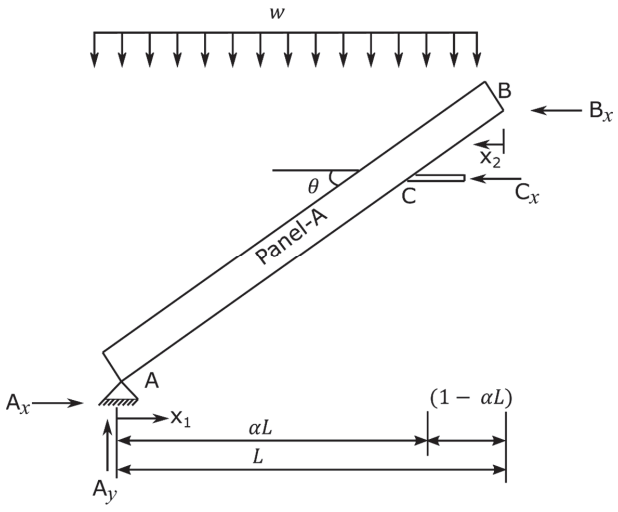

Figure 16. Free body diagram of the system under gravity load.

In this study, the apex connection design is demonstrated for a residential home package provided by an offsite construction company located in Alberta, Canada (11 m × 6.1 m Gabel roof footprint) with a slope of 8/12 and panel-A width of 1944 mm. Both gravity load case and wind load case were considered for a tributary area equal to the apex connection spacing. Assuming 600 mm c/c distance of the apex connections for a factored gravity load of 4 kPa, the axial force (C_x) in the bar and internal hinge force (B_x) at the apex location were calculated using Equations (2) and (3) and led to a solution of 5165 N and 1140 N respectively.

A 2-D finite element model was also developed utilizing commercially available general-purpose FE code, ABAQUS/CAE, distributed by SIMULIA Inc., Palo Alto, CA, USA. A two-node beam element (B31) was used to assemble the two LSL rafters with a cross-section of 140 mm × 38 mm and all the triangle apex connection components were made of steel C-channel section (30 mm × 40 mm × 40 mm) (Figure 17). It was assumed that the main folding bars connected by a pin in the actual connection setup act as one rigid link element. The three beams representing the apex connection, the secondary bar and the primary folding bar are connected by a hinge connector element (CONN3D2) (Points A, B and C in Figure 18). Then, the tie constraint was applied between the rafter and secondary bars of the apex connection. The tie constraint represents the screw connection between the rafter and the secondary bars, assuming that the number of screws provides sufficient rigidity to transfer the load from the rafter to the apex connection assembly. The same magnitude of gravity load was applied according to the previous analytical procedure and a comparison of the results shows that the FE model provides a reasonably close solution (axial force value in the main folding bar = 6570 N and apex hinge force at point B = 1879 N). Thus, the validation of this 2D FEM with the analytical model indicates that a more detailed modelling approach (e.g., contact simulation) can reveal the proper behaviour of this connection mechanism. However, this linear elastic analysis provides the basis to determine the internal forces and thereby an approximate diameter of the pins was obtained using Equation (5) [13].

$$\text{Shear resistance of a pin, } F_v = \frac{0.6\ A\ f_{up}}{\gamma_{M2}}, \tag{5}$$

where d is the diameter of the pin, f_{up} is the ultimate tensile strength of the pin and A is the cross-section area of a pin, and γ_{M2} is the safety factor.

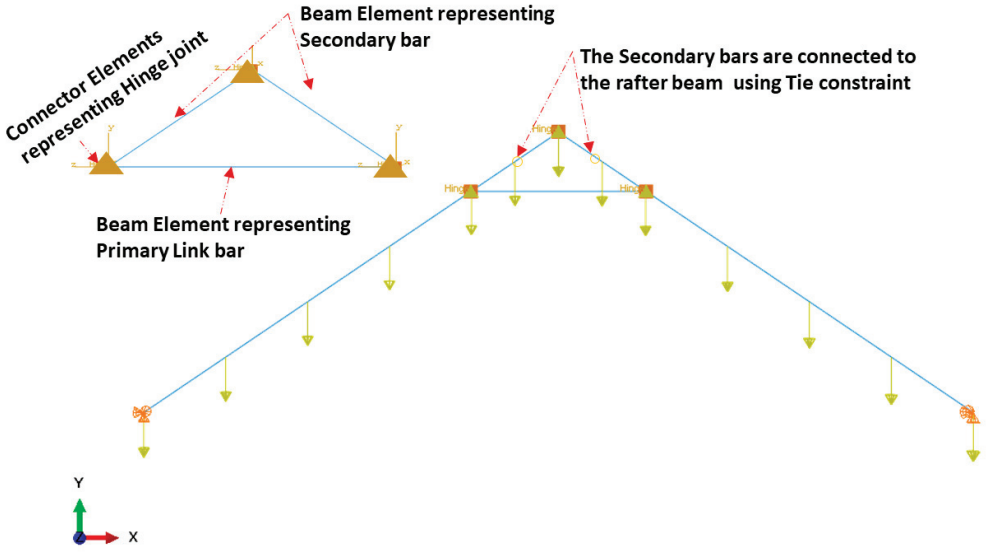

Figure 17. Loading and boundary condition 2-D numerical model of the apex connection.

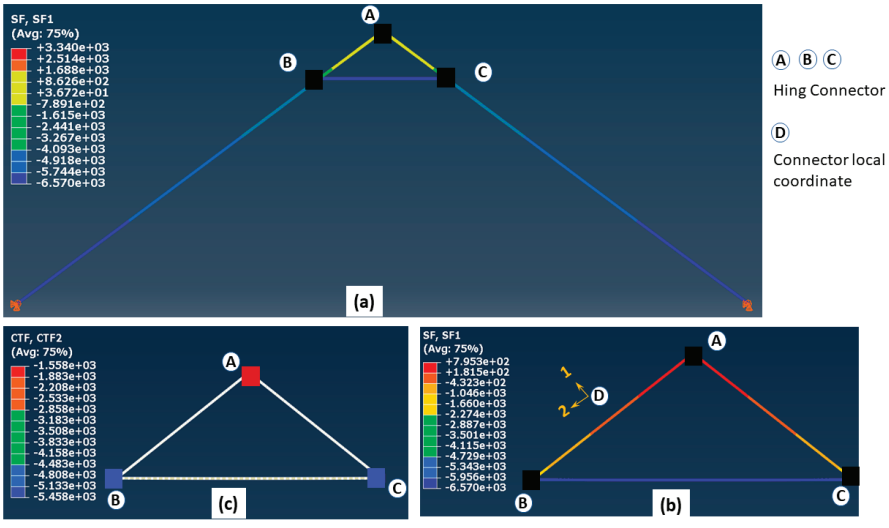

Figure 18. (**a**) Axial forces in the 2D assembly, (**b**) axial force in the apex connection, and (**c**) forces in the pins of apex connection (unit in the figure is N).

4. Screw Connection Requirement of Secondary Bars

In order to connect roof panels with the secondary bars of the proposed apex connection, commercially available screw (Simpson Strong-Tie SD screw), which is an alternative to common 10d nails, can be utilized. The screw nominal diameter and length of the screw are 4.5 mm and 38 mm, respectively. The in-plane component of load along the rafter plane must be resisted by the shear capacity of the screw connection between rafters and the secondary bars. Among all the load cases, gravity load has the highest magnitude. Thus, screw shear capacity was checked for the gravity load case only. Therefore, the number of holes in the secondary bar depends on the number of required screws. The analytical

model for the nail and spike provided in CSA86-19 (Equation (6)) [15] was used to predict the unfactored shear capacity of the screw connection between the secondary bar and rafter. The predicted unfactored shear capacity per screw was 1898 N with the failure mode (e) of Equation (6). In this case study of a roof slope of 8/12, the secondary bar has a dimension of 410 mm between the pin holes (Figure 9) and seven holes are provided to install the screws. Thus, with seven screws, the total factored shear capacity is 10.63 kN. The screw shear force (summation of components of hinge forces of points B and C along the rafter in-plane) was obtained from the 2D analysis (Figure 18c). For the governing load (factored gravity load of 4 kPa), the resultant screw shear was 7.02 kN. Therefore, the number of screws provided for apex connection is safe in the case of in-plane shear resistance. Details of shear capacity analysis can be found in the Appendix A of this paper. The screw connection is also subjected to the highest withdrawal in case of wind load parallel to the ridge direction of the roof. According to the screw manufacturer's technical data sheet, the design withdrawal capacity is 769.5 N per screw [16]. Additionally, the withdrawal force due to a wind withdrawal load is 2.1 kN. Thus, with seven screws, the withdrawal resistance is 5.4 kN. Further, the provided number of screws is sufficient to resist the hourly wind pressure of 0.85 kPa. Thus, providing seven holes in the secondary bar is sufficient to resist both the gravity and wind load in Edmonton, Alberta, Canada. The holes were provided at 50 mm c/c to avoid the splitting of the rafter of the roof panel. It is worthwhile to note that, to accommodate a higher load, the length of the secondary bar must be increased to provide proper screw spacing.

$$N_r = \phi \, N_u n_F \, n_s \tag{6}$$

where:
$N_u = n_u(K_D K_{SF} K_T)$
$\phi = resistance\ factor\ for\ yielding\ failures = 0.8$
$n_u = unit\ lateral\ resistance\ of\ screw$
$n_F = number\ of\ screw\ in\ connection$
$n_s = number\ of\ share\ planes\ per\ screw$

The unit lateral resistance of steel to timber screw connection per share plane is the smallest value calculated in accordance with the failure modes (a) to (f).

$$(a)\ \ f_1 d_F t_1 \tag{7}$$

$$(b)\ \ f_2 d_F t_2 \tag{8}$$

$$(c)\ \ f_1 {d_F}^2 \left(\sqrt{\frac{1}{6} \frac{f_3}{(f_1 + f_3)} \frac{f_y}{f_1}} + \frac{1}{5} \frac{t_1}{d_F} \right) \tag{9}$$

$$(d)\ \ f_1 {d_F}^2 \left(\sqrt{\frac{1}{6} \frac{f_3}{(f_1 + f_3)} \frac{f_y}{f_1}} + \frac{1}{5} \frac{t_2}{d_F} \right) \tag{10}$$

$$(e)\ \ f_1 {d_F}^2 \frac{1}{5} \left(\frac{t_1}{d_F} + \frac{f_2}{f_1} \frac{t_2}{d_F} \right) \tag{11}$$

$$(f)\ \ f_1 {d_F}^2 \sqrt{\frac{2}{3} \frac{f_3}{(f_1 + f_3)} \frac{f_y}{f_1}} \tag{12}$$

where:
$t_1 = head - side\ member\ thickness\ (steel\ plate\ in\ this\ case)$
$d_F = screw\ diamenter$
$f_2 = embedment\ strength\ of\ point\ side\ member\ (LSL) = 50\ G(1 - 0.01 d_F)$
$G = mean\ realtive\ density = 0.5\ for\ LSL$
$t_2 = length\ of\ screw\ penetration$

f_3 = *embedment strength of point side member when failure in screw yielding* $= 110G^{1.8}(1 - 0.01d_F)$
f_y = *screw yield strength* $= 50(16 - d_F)$
f_1 = *embedment strength of steel plate* $= K_{sp}(\phi_{steel}/\phi_{wood})f_u$
$K_{sp} = 2.7$, $\phi_{steel} = 0.80$, $\phi_{wood} = 0.8$

5. 3D Finite Element Modelling of Apex Connection

The actual folding apex connection is inherently three-dimensional in nature and involves complex interactions between the parts. The folding mechanism of apex connections technically represents, in principle, an extremely complex and highly indeterminate analytical problem with a wide range of geometrical nonlinearity and mechanical parameters affecting its behaviour to transfer the force and moment. These parameters include the rectangular slots (95 mm long) and U-shape slots (13 mm × 9 mm) in the primary folding link bar, V-shape cuts (14.5 mm × 7mm) in the Middle bar, contact between the main lock channel and primary link bars, contact between secondary lock channel and secondary link bars, pin bearing mechanism at the hole of main link bars and secondary bars, contact between the sidebar and main link bar (Figures 8–13). Hence, three-dimensional elements were utilized in the FEM to understand the structural behaviour of this connection. Proper element selection for steel connection design is critically important. Abaqus provides several types of elements, such as continuum solid element, shell elements, membrane elements, rigid elements, and beam elements that can be used to simulate steel connections. The behaviour of these elements is characterized by five criteria, such as family, degrees of freedom, number of nodes, formulation, and integration. For example, the solid element library includes first-order (linear) interpolation elements and second-order (quadratic) interpolation elements in one, two, or three dimensions classifying as triangles and quadrilaterals for two dimensions; and tetrahedra, triangular prisms, and hexahedra ("bricks") in three dimensions. Each class of element provides a choice for first-order (linear) interpolation elements and modified second-order interpolation elements in two or three dimensions. It is critical to select the correct element for a particular application to avoid hourglassing, shear and volumetric locking, overly stiff behaviour in bending and slow convergence with mesh refinement. It should be noted that the proposed apex connection may have large plastic deformations and high strain gradients in the pinhole regions of connection, as well as the presence of contact between the lock channel and link bars. As suggested in previous studies [17–19], first-order elements should be used to avoid mesh locking and convergence difficulties associated with contact, while modelling steel connection, 8-node linear brick (C3D8) element is preferable for the apex connection FEM. However, this element shows very high stiffness in bending; consequently, the incompatible mode of these elements (C3D8I) is implemented to improve their bending behaviour [20].

For any numerical modelling, the definition of material property is the most critical step that affects connection ductility and capacity. A detailed literature review of steel connections suggests assuming that the steel in this study is homogenous and isotropic with an elastic modulus of 200 GPa and Poisson's ratio of 0.3 [19,21–23]. Since the variation of mechanical properties of steel is significantly low compared to other construction material, such as wood, in the absence of a coupon test, generic material properties specified in standards used for numerical simulation produces reasonably accurate results [24]. According to ASTM A1008, drawing quality steel sheets (DS) have yield strengths between 150 to 240 MPa [25]. While, for design purposes, selecting the nominal values is a conservative approach, the use of minimum nominal strength material property in numerical simulation underestimates the load-carrying capacity of the steel connection whereas adopting a maximum nominal strength property has the opposite effect [24]. Thus, to obtain proper connection behaviour the typical stress-strain relationship as depicted in Figure 19 [26] is adopted for the elements of all the parts fabricated using steel plate and A36 steel for all pin components (Figure 20) [24]. Since the main focus of the model is to understand the

behaviour of the apex connection, the rafter material (LSL) was assumed to be isotropic with a Young's modulus of 9000 MPa and Poisson's ratio of 0.25.

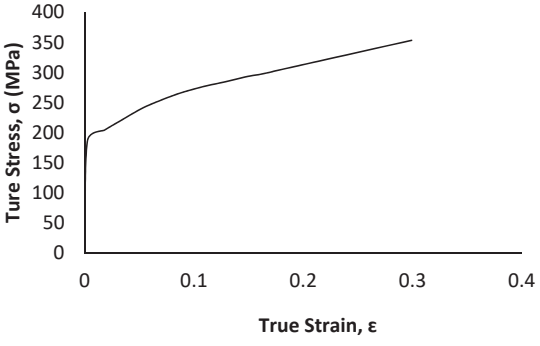

Figure 19. The true stress-true strain curves of an AISI 1008 steel (Data obtained with permission from [26], 2014, Elsevier).

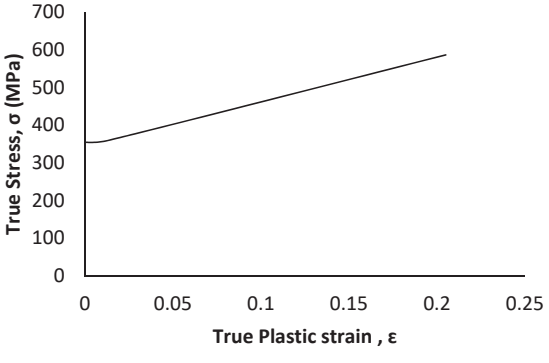

Figure 20. The true stress-true plastic strain curves of A36 steel [24].

In the structural analysis, it is common to make use of reduced or lower-dimensional element types with higher-dimensional element types in a single FE model, which is known as multiscale FEM. This approach is efficient and provides an improved solution to capture local structural features as well as global structural behaviour [27]. Figure 21 illustrates the complete mixed-dimensional FEM assembly of this study. To simplify the model, similar to the analytical approach, only two LSL rafters and the unfolded state of apex connection assembly were incorporated. However, all these components were modelled using solid 3D elements (8-node linear brick element). As can be observed from Figure 5, the apex connection has nine locations that require a hinge mechanism provided by steel pins. Despite well-established design rules and assembly procedures in American and European steel standards, numerous nonlinearities in the vicinity of the pinhole led to overly expensive calculations if fine-scale computation modelling is used. Consequently, to model this large assembly with a considerable number of pin joints, alternative computational strategies are a suitable option [28]. Abaqus provides the connector (CONN3D2) element to model any type of connection such as a hinge or a screw [20]. However, the connector element is a 1D element whereas the other components are 3D objects, so the number of degrees of freedom (DOFs) is not the same for all the objects. Hence, this multi-scale FE simulation requires a reasonable FE coupling method to blend mixed-dimensional finite elements at their interfaces to accomplish both displacement continuity and stress equilibrium. In this regard, the multipoint constraint (MPC) surface method is suitable for the static and dynamic analysis of linear or nonlinear structures

and the interactions between the pin with the assembled elements can be modelled in an average sense with a more rigid way in ABAQUS [28]. The MPC method uses constraint equations for nodal displacements at the interface of mixed-dimensional elements. Thus, to model the hinge mechanism at all locations (as shown in Figure 22), reference points were generated on the center points of the connection and MPC-BEAM constraint was assigned to the hole surface with their corresponding reference point (RP). MPC-BEAM in ABAQUS uses a rigid interface method to connect nodes of different types of elements by creating rigid beams with respect to RP [20]. At each pin location connector element with a hinge, connection property was assigned to join corresponding parts. Tie constraint was applied at the interface between secondary bars and the LSL rafter assuming that the screw connection will act as a rigid joint. In the simulation of steel connection, the boundary condition is deemed to be significant and any inappropriate boundary conditions may cause completely different behaviour. Following the analytical model mentioned in the previous section, the lower two ends of the LSL rafter are assumed to be in the pinned ($U_x = U_y = U_z = 0$) support condition. In actual roof assembly, the OSB sheathing is nailed on the rafters, which provides stability against lateral buckling. To account for this lateral restraint, provided by the continuity of OSB sheathing panels, the rafter edges were assigned as the Z-symmetry coordinate system ($U_z = UR_x = UR_y = 0$), as shown in Figure 21.

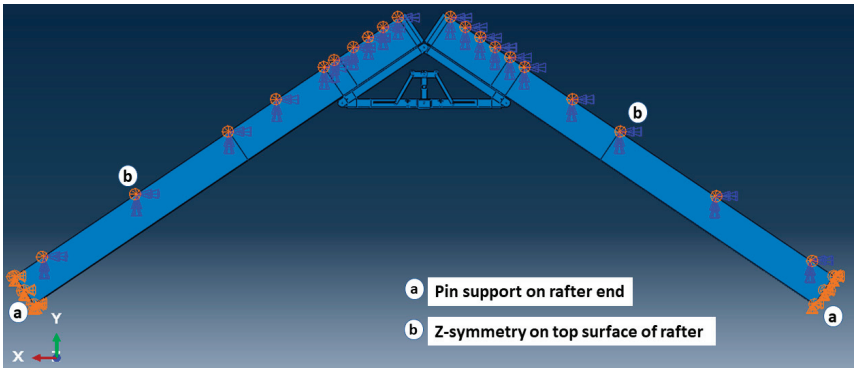

Figure 21. 3D assembly model and boundary condition.

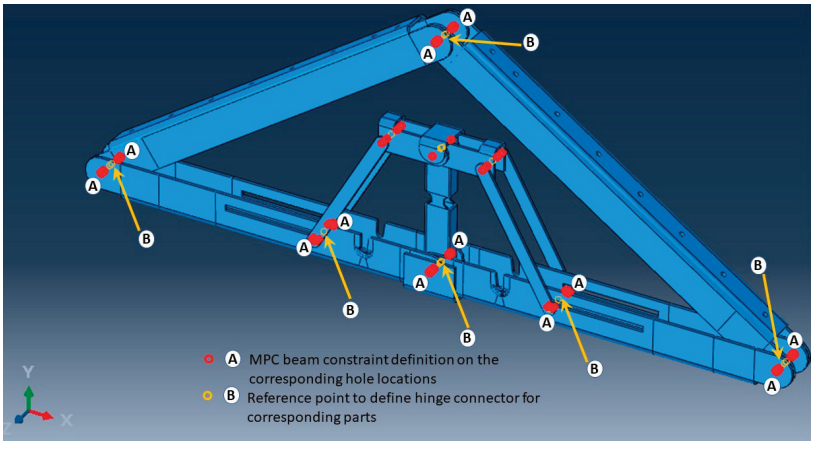

Figure 22. MPC beam constraint location for the hinge connection.

Properly refined element mesh is also an influencing factor for any finite element simulation to obtain reliable results. Due to the presence of slots and pinholes, it was required to partition the complex geometry into several segments and assign an advancing front or medial axis meshing algorithm to generate elements with proper shape factors. For example, the U-shape slot in the main link bar in Figure 23 was partitioned by offsetting the half-circular face of the slot at every 1 mm and creating radial lines at every 9° angle. This technique generated a very refined mesh with a proper shape factor around the face of the model.

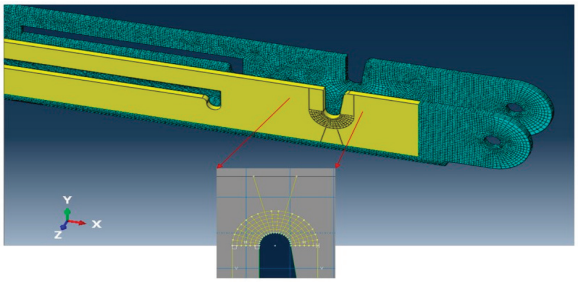

Figure 23. Advanced meshing application.

As mentioned previously, complex interactions exist between the surfaces of different parts of the apex connection to facilitate folding and self-locking mechanism, so this FE modelling requires contact simulations of different components to allow for a transmission of force from one part to another, specifically near the folding location where main lock channel and secondary lock channel provides a self-locking mechanism (Figure 24). In detail, a coulomb coefficient of friction equal to 0.3 is defined for sliding resistance in the surface-based contact approach. It should be noted that the interface of the contact surface must be close and the penalty technique enforcement was used in contact enforcement since this approach has more flexibility and recommended method in steel connection modelling [19].

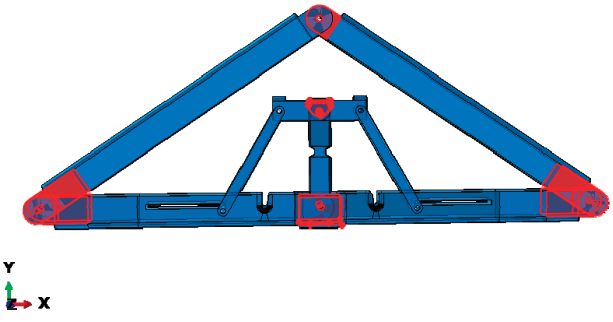

Figure 24. Contact surface interaction locations.

6. Results

Four governing loading combinations from the Canadian Building Code were considered for this numerical analysis. These load combinations account for all the combinations, including gravity load (dead, live and snow) and lateral load (wind load Figure 25), that will lead to maximum effects for both strength and serviceability. The design loads applied to the roof structure were assigned based on the National Building Code of Canada and the building location in Alberta, Canada. These were specified at a snow load of 2.25 kPa, other non-structural components account for another 0.5 kPa of dead load and hourly wind

pressure of 0.85 kPa. Thus, the total factored gravity load was 4 kPa. Wind loads were calculated using the static procedure of NBCC and based on the gust effect and pressure coefficient (as illustrated in Figure 25) for both wind perpendicular to ridge and wind parallel to ridge direction. For both the gravity load and lateral load cases, the partial loading scenario was also checked following the NBCC. The uniformly distributed load was applied on the LSL assuming apex connection spacing of 600 mm c/c since the maximum spacing of the roof panel rafter must not exceed the corresponding value to take advantage of the load sharing system effect.

Load case a: 1.25D + 1.5S +1.0L
Load case b: 0.9D + 1.4W + 0.5S
Load case c: 0.9D + 1.5S + 0.4W
Load case d: 0.9D + 1.4W
where D = dead load, L = live load, S = snow load and W = wind load.

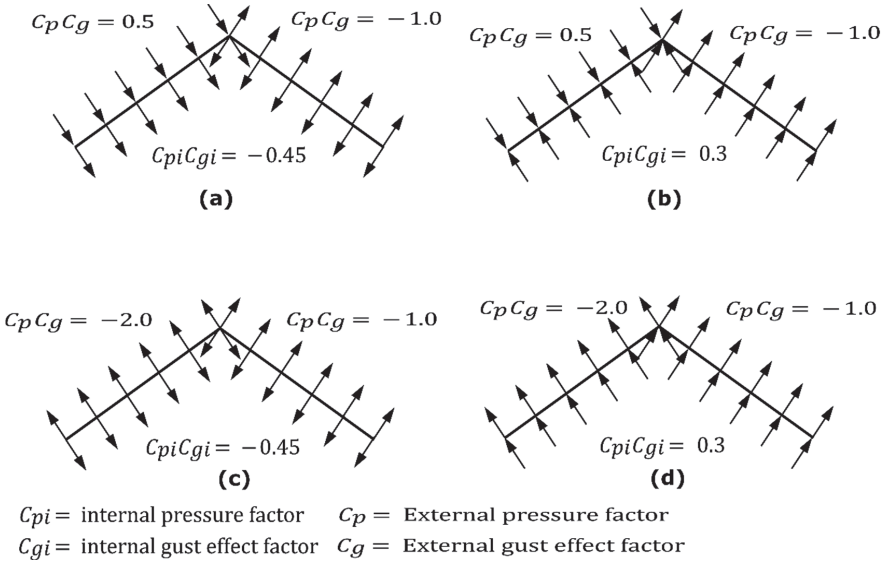

Figure 25. External and internal gust and pressure factors for wind load cases (**a**,**b**) for wind perpendicular to ridge and (**c**,**d**) for wind parallel to ridge.

Figures 26 and 27 show the deflected shape of the assembly under gravity load and von Mises stress of the apex connections parts. Table 1 summarizes the resultant von Mises stress and PEEQ value observed in different load cases. As the link assembly is subjected to both bending and compression for the gravity load, the maximum von Mises stress was observed around the U-slot of the primary folding link bar (Figures 28 and 29). It was observed that the load had the largest impact on the stress distribution in the proximity of the U-slot of the primary folding link bar. Figure 29 depicts the stress distribution near the U-slot indicating the highest stress concentration zone and probability of fracture initiation zone at ultimate failure load. A comparison of the stress contour plotted in Figure 30 shows that all other parts including the main lock channel, middle bar, secondary lock channel, sidebars and secondary folding link bars are within the elastic limit. As expected, among these components, maximum von Mises stress was observed in the contact zone of the main lock channel and secondary lock channel which confirms the effectiveness of the locking mechanism of the assembly. Maximum von Mises stress in the main lock channel and secondary lock channel were 55.2 MPa and 51.2 MPa respectively, whereas the ultimate

strength of AISI 1008 is 353.3 MPa. Thus, the channels are well below the ultimate strength of the material for a factored gravity load of 4 kPa.

Table 1. Summary of results in different load cases.

Part Name	Load Case	Maximum Permissible Plastic Stain (PEEQ) (mm/mm)	Observed Maximum Plastic Strain (PEEQ) (mm/mm)	Maximum Permissible Von Mises Stress (MPa)	Observed Maximum Stress (MPa)
Primary folding link bar (30 mm × 38 mm c-section in Figure 8)	[1] Load case a	0	1.7810×10^{-3}	186.7	199.50
	[2] Load case b		0		81.03
	[2] Load case c		3.7910×10^{-5}		184.66
	[3] Load case d		0		177.56
Secondary bar	[1] Load case a	0	0	186.7	117.61
	[2] Load case b		0		112.95
	[2] Load case c		0		116.72
	[3] Load case d		0		186.76
Main lock channel	[1] Load case a	0	0	186.7	55.10
	[2] Load case b		0		33.59
	[2] Load case c		0		60.58
	[3] Load case d		0		47.75
Secondary lock channel	[1] Load case a	0	0	186.7	51.18
	[2] Load case b		0		50.79
	[2] Load case c		0		51.24
	[3] Load case d		0		50.84
Secondary Folding link bars	[1] Load case a	0	0	186.7	57.47
	[2] Load case b		0		59.18
	[2] Load case c		0		57.26
	[3] Load case d		0		62.61
Side bars	[1] Load case a	0	0	186.7	3.70
	[2] Load case b		0		1.72
	[2] Load case c		0		3.81
	Load case d		0		2.48
Middle bar	[1] Load case a	0		186.7	38.99
	[2] Load case b		0		38.34
	[2] Load case c		0		39.09
	[3] Load case d		0		40.34

Note: [1] Gravity load case, total load = 4 kPa; [2,3] For the load cases wind pressure 0.85 kPa and specified snow load 2.25 kPa.

Figure 26. The deflected shape of the structure for a factored gravity load of 4 kPa.

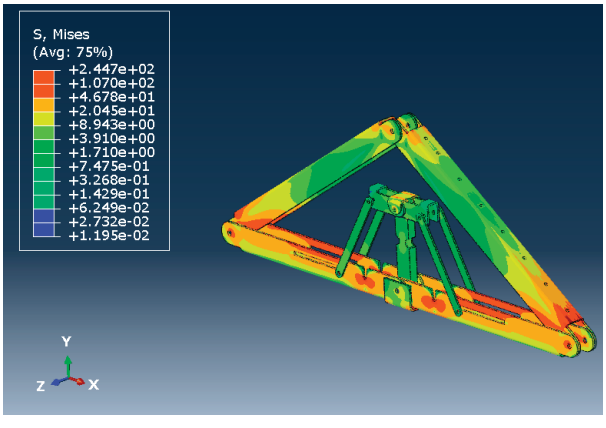

Figure 27. Von Misses stress (MPa) of the Apex connection (factored gravity load of 4 kPa).

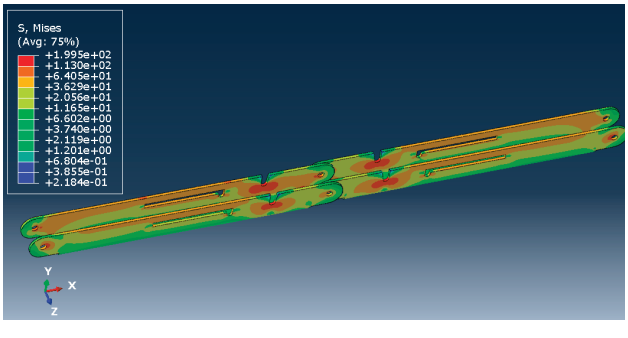

Figure 28. Von Mises Stress (MPa) of primary folding link bars (factored gravity load of 4 kPa).

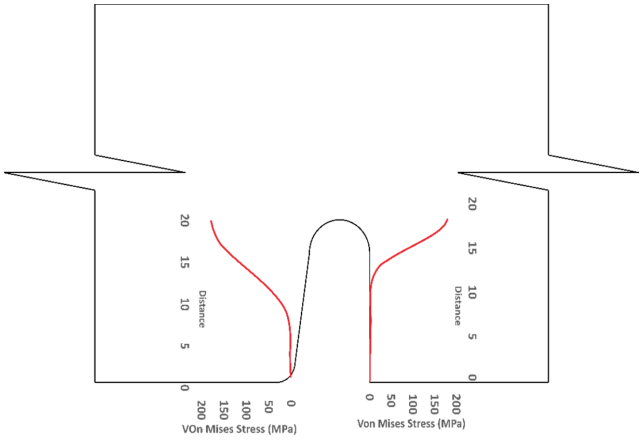

Figure 29. Stress (MPa) distribution near (red line) the vicinity of the U-slot of primary folding link bar.

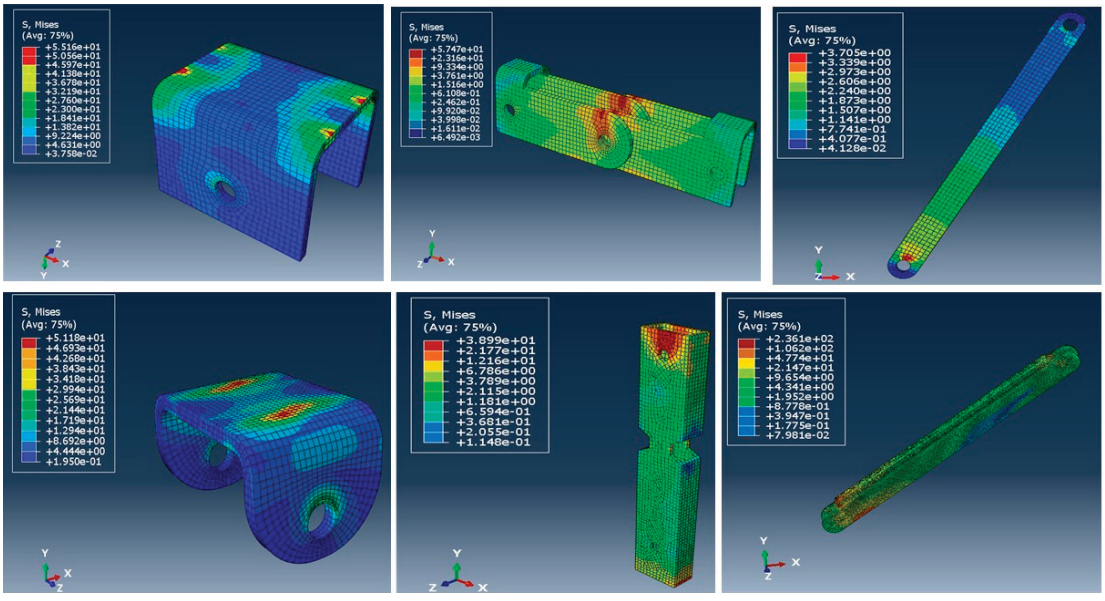

Figure 30. Stress (MPa) contour plot of different parts for a factored gravity load of 4 kPa.

In order to obtain the connection capacity, a benchmark for the failure mechanism and failure criteria for any numerical analysis are required. In the case of the experimental investigation of any connection, the failure point of an assembly can be distinct by observing a situation when the assembly exhibits a substantial loss in load-carrying capacity or the presence of a rupture mechanism. However numerical models continue to obtain results until it fails to converge on a solution which can be different from the actual failure state. Thus, it is important to establish proper failure criteria for the numerical modelling approach. The literature review has revealed that, in the case of steel connection, two types of failure criteria are considered, namely (a) strength criterion and (b) deformation criterion. For example, experimental studies on the bearing resistance of a connection adopted a design equation based on the maximum loads from tests in References [29–32], even though

significantly larger deformation in the specimen was observed. In contrast, according to the later criterion, failure is considered to be the applied load measured at a specific acceptable deformation level depending on the application [33]. For instance, the bearing failure study of cold-formed steel bolted connections by Salih et al. [34] adopted a 3 mm extension limit. Additionally, Eurocode 3 design provisions for steel connections are based on a 3.0 mm deformation limit under ultimate conditions which ensures the deformation under service loads to be 1.0 mm [33]. Thus, for design purposes, deformation-based criteria are more appropriate. Hence, the equivalent plastic strain of a material (PEEQ) in Abaqus, was adopted to implement as a design capacity criterion for the cross-section of the parts. PEEQ is a scalar measurement that is used to represent the material's inelastic deformation and if this variable is greater than zero, the material has yielded. Thus, PEEQ indicates the local ductility and fracture tendency of steel members [35]. In the case of classical (Mises) plasticity, PEEQ is obtained by using the following equation:

$$PEEQ = \overline{\varepsilon_p}|_0 + \int_0^t \sqrt{\frac{2}{3}\dot{\varepsilon_p} : \dot{\varepsilon_p}}dt \tag{13}$$

where $\overline{\varepsilon_p}|_0$ is the initial equivalent plastic strain and $\dot{\varepsilon}_p$ is the tensorial form of plastic strain rate .

In order to investigate the performance of the connection in service, the following hypothesis was adopted:

"The apex connection components must be sized so that all materials remain in the elastic range and their elastic deformations have negligible values. This ensures the deformation of the connection will be returned to its original state after the load is removed."

As can be observed from the deformation and stress distribution of the primary folding link bar, the possible mechanism of failure is fracture propagation near the U-slot. Thus, the design requires avoiding any form of localized plastic deformation near this zone. If the PEEQ value is zero, then it can be concluded that the assembly is in the elastic range under design load. Figures 30–33 illustrate the von Misses stress and PEEQ plot of the apex connection assembly in the most critical load cases. The PEEQ value analysis of all the critical load cases shows non-zero plastic strain for load case-a only (Figure 34). The PEEQ value for a factored gravity load of 4 kPa and the cumulative plastic deformation is concentrated in the middle location of the U-slot; 12 mesh (C3D8I) elements (approximately 64 mm^3 volume) near the U-slot of the primary folding link bar have PEEQ value greater than zero with a maximum value of 1.7810×10^{-3}. As can be observed from Figure 35, the computed strain levels in those 12 elements have exceeded the defined yield value and are in the strain hardening stage. Consequently, there will be a 0.185 mm permanent deformation near the U-slot zone of the one-side main folding link bar. Therefore, the main folding link has the probability of a total of 0.4 mm shortening for a specified gravity load of 4 kPa. This will cause tension force at the secondary bar, ultimately increasing the uplift force on the fastener used to connect the bar with the roof panels. Additionally, the relatively long winter in Canada poses a risk of fatigue and residual stress on the connection, so a PEEQ value equal to zero will be a safe option to ensure that the assembly components remain in the elastic zone. Therefore, it can be concluded that a revised cross-section is required to support a 4 kPa gravity load. However, at a factored load of 2.6 kPa, the cross-section shown in Figure 8 with PEEQ values equal to zero was observed. Thus, the primary folding link bar of the cross-section shown in Figure 8 can be used for a factored gravity load of 2.6 kPa. An enhanced cross-section (Figure 36) is required to support a factored gravity load of 4 kPa, which was obtained by running the numerical model with various trial cross-section sizes until the failure criterion was met. It is worthwhile to note that the initial primary folding link bar (as shown in Figure 8) has a cross-section of 30 mm × 38 mm, whereas the revised cross-section is 30 mm × 50 mm (as illustrated in Figure 36). All other elements, such as the pinhole and u-slot, are the same as initially designed (Figure 8).

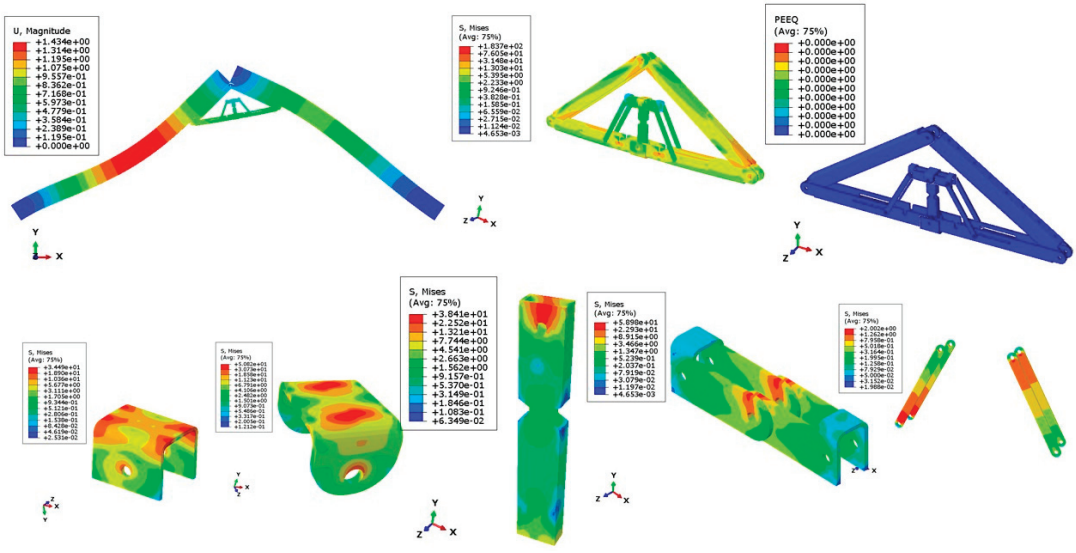

Figure 31. Stress (MPa) in wind load case (100% load removed from one side for hourly wind pressure of 0.85 kPa).

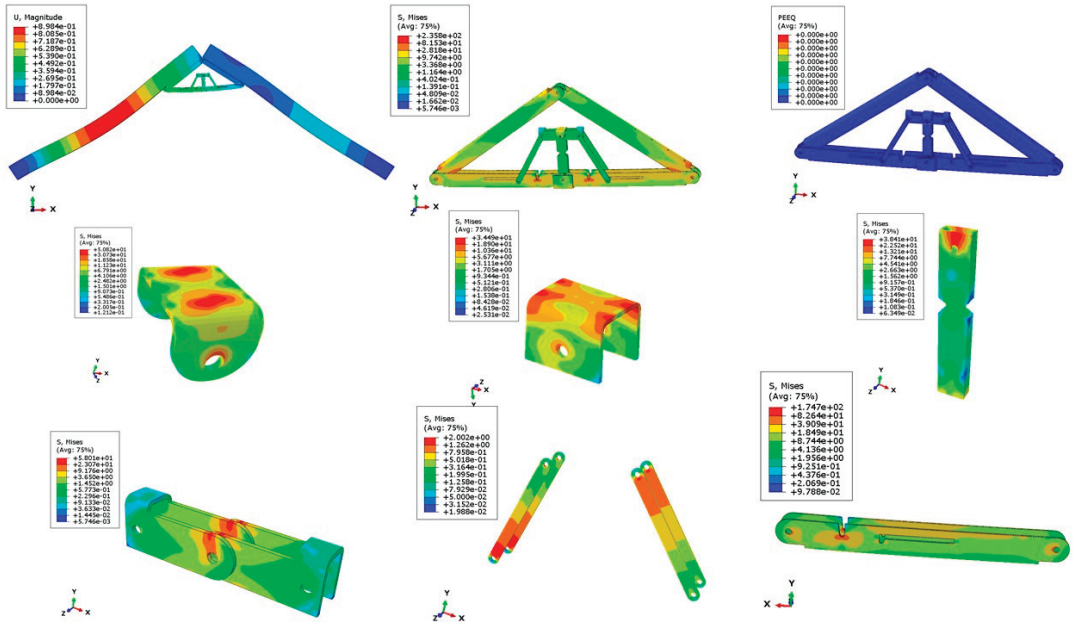

Figure 32. Stress (MPa) in different parts for partial snow load case (specified snow load of 2.25 kPa).

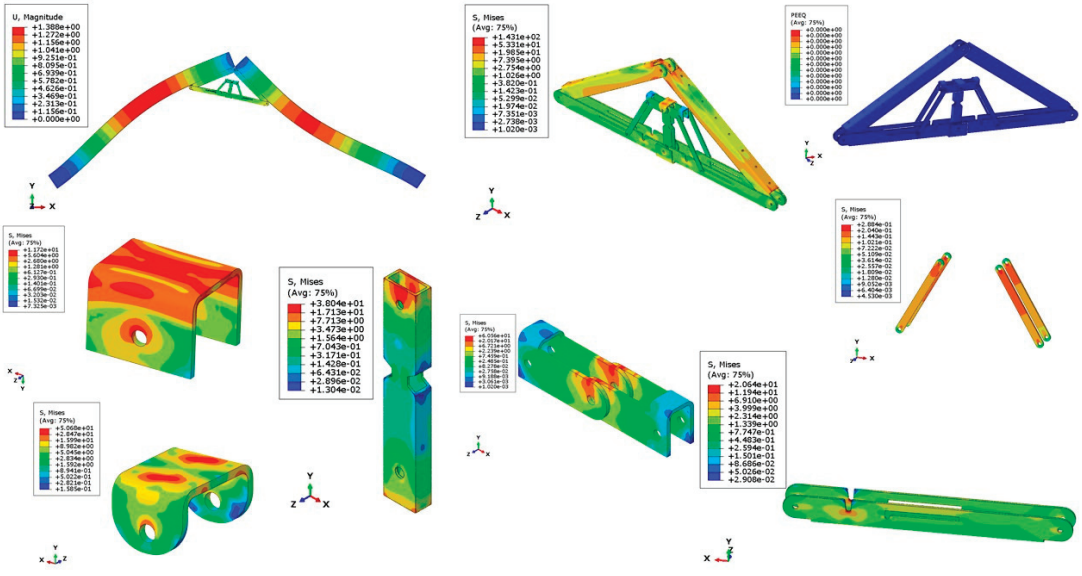

Figure 33. Stress (MPa) for partial wind load case uplift (hourly wind pressure= 0.85 kPa).

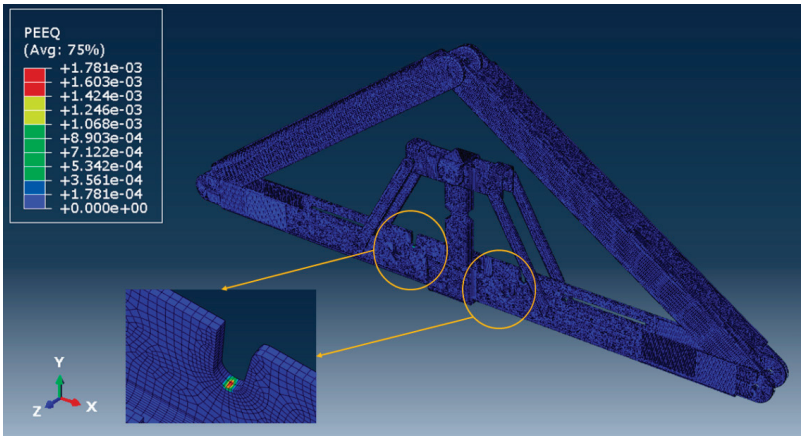

Figure 34. PEEQ value for the link assembly for a factored gravity loading of 4 kPa.

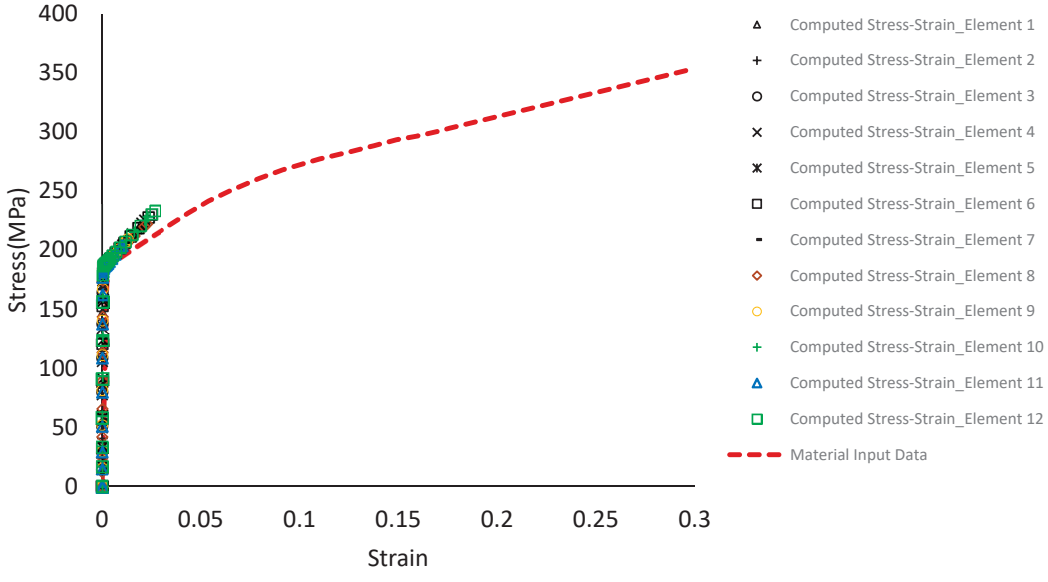

Figure 35. Stress-Strain near the U-slot of primary folding link bar.

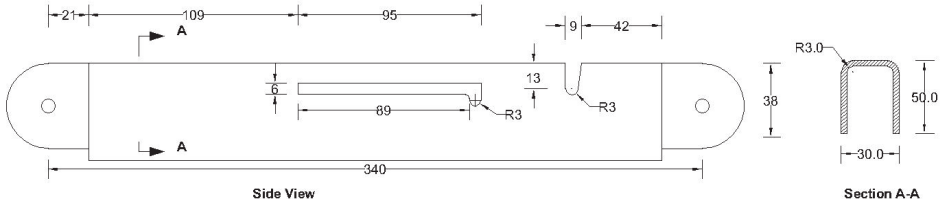

Figure 36. Revised primary folding link bar cross-section.

To observe the load-deflection behaviour of the apex connection assembly, a gravity load up to 12.7 kPa was applied since the load case-a is the governing case. Figure 37 illustrates the mid-point deflection vs. load plot of the primary folding link bars assembly, which ensures reasonably low deflection of the overall assembly at the factored gravity load of 4 kPa.

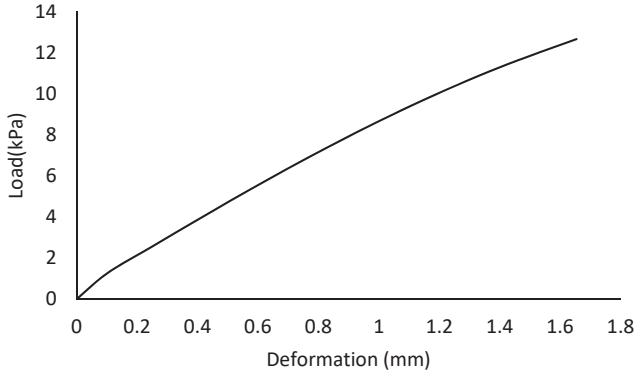

Figure 37. Deflection at the midpoint of the primary folding link bar assembly.

The design of the connection also requires checking the pin shear and bearing capacity of the steel sheet near the hole. Thus, another numerical model was developed to simulate a uniaxial tension test on the pin joint in the middle of the main link bar to observe the localized effect due to the interaction of the pin and the holes of the main link bar (Figure 38). In this case, the pin was modelled using a 3D solid element (C3D8I). Hard contact was defined between the pinhole of the folding bars and the pin. Figure 39 illustrates the von Mises stress distribution and PEEQ value due to the maximum applied load of 15 kN in this case. Using EN 1993-1-8 [13] (Equation (5)) the predicted pin shear capacity was 8919 N, whereas the numerical model shows the shear capacity to be 8070 N, considering no plastic strain at any location of the pin (PEEQ = 0) (Figure 40). However, the literature review has shown that, in experimental investigation, connection capacity is defined based on certain deformation levels [29–34]. In the absence of the experimental test, it is a conservative design approach to adopt the PEEQ value equal to zero as the capacity benchmark for the pin. The maximum stress in the pin was 366.8 MPa (for PEEQ = 0 condition) and the ultimate stress for A-36 steel is 586.7 Mpa. However, for a factored gravity load of 4 kPa (governing load for axial force), the axial force value in the main folding link bar was 5898 N. The maximum stress of the pin for this axial force was 286.9 Mpa. Therefore, the pin section is safe in the case of the factored gravity load of 4 kPa and hourly wind pressure of 0.85 kPa.

For the pin connection, another important mode of failure is bearing for the steel plate and pin. It is required to have a benchmark to understand the bearing failure mechanism. Details of the bearing failure mechanism can be found in single-lap bolt connection studies. Ideally, bolts in a single-lap connection and the pin connection have similar structural behaviour such as shear failure, bearing failure and net section failure, the only difference is that the bolt connection has resistance due to clamping friction, whereas the pin provides free rotation. As the load is gradually applied to the bolted connection, the major force transfer would be friction between the contact surfaces. Once the applied force exceeds the friction capacity of the connected members slip relative to each other until they bear on the bolts, contact with the hole interaction dominates the connection performance similar to the pin connection. Thus, the bearing failure benchmark can be obtained from the bolted connection bearing stress review. The literature review has shown that, in the case of bearing failure, a 3 mm hole elongation level is considered to be the ultimate capacity of the connection, thereby ensuring 1 mm deformation at the serviceability limit state [33]. Using EN 1993-1-8 (Equation (8)) [13], the bearing resistance capacity for the plate and pin was calculated to be 12,527 N, however, at this load level, the numerical model shows hole elongation of 0.56 mm which Is below the threshold limit for bearing failure criterion for serviceability limit state set by Eurocode. Additionally, the maximum design axial force (5898 N) for a factored gravity load of 4 kPa is less than the pin shear capacity (8070 N). Maximum bearing stress in the pinhole was 180.7 Mpa (for PEEQ = 0) and the ultimate strength of ASIS 1008 steel was 353.4 Mpa. Therefore, the assembly is safe in case of the factored gravity load of 4 kPa and wind pressure of 0.85 kPa in bearing. Thus, it can be concluded that the design capacity of the connection assembly is governed by the strain level near the U-slot of the main link bar.

$$\text{Bearing resistance of the plate and the pin, } F_b = \frac{1.5\, t\, d\, f_y}{\gamma_{M0}}, \tag{14}$$

where d is the diameter of the pin, f_y the lower the yield strengths of the pin and the connected part, t is the thickness of the plate, and γ_{M0} is the safety factor.

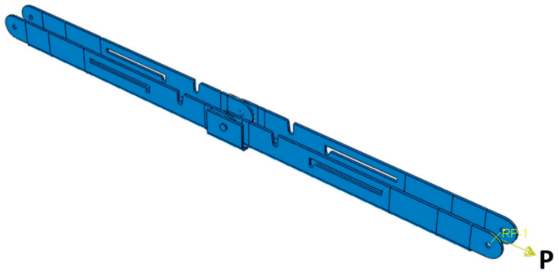

Figure 38. Uniaxial tension simulation of primary folding link bars for bearing and pin shear capacity.

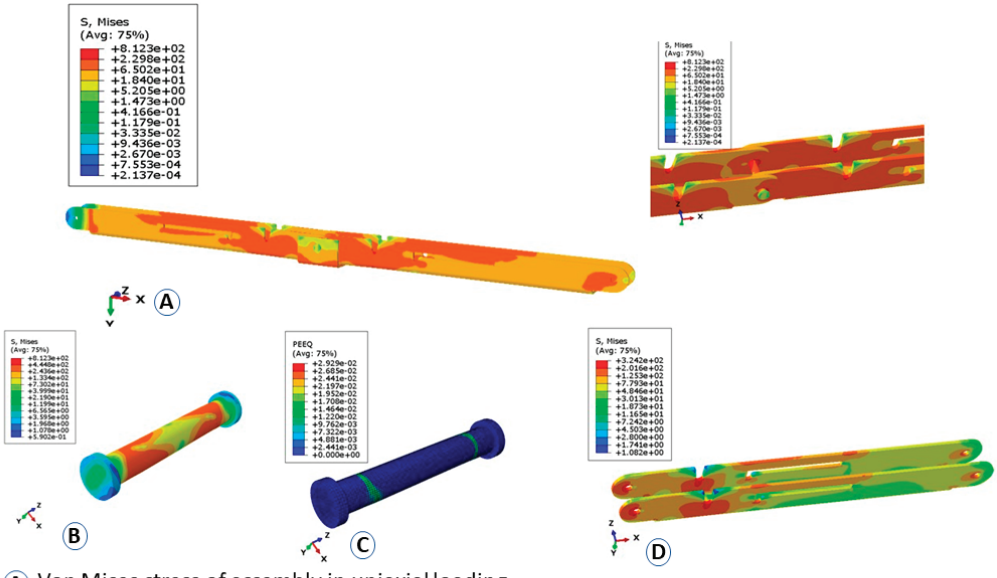

A Von Mises stress of assembly in uniaxial loading
B Von Mises stress of pin connecting two primary folding bars in uniaxial loading
C PEEQ of pin connecting two primary folding bars in uniaxial loading
D Von Mises stress of primary folding bar in uniaxial loading

Figure 39. Von Mises stress (Mpa) and PEEQ plot of uniaxial loading of primary folding link bar and pin (P = 15,000 N).

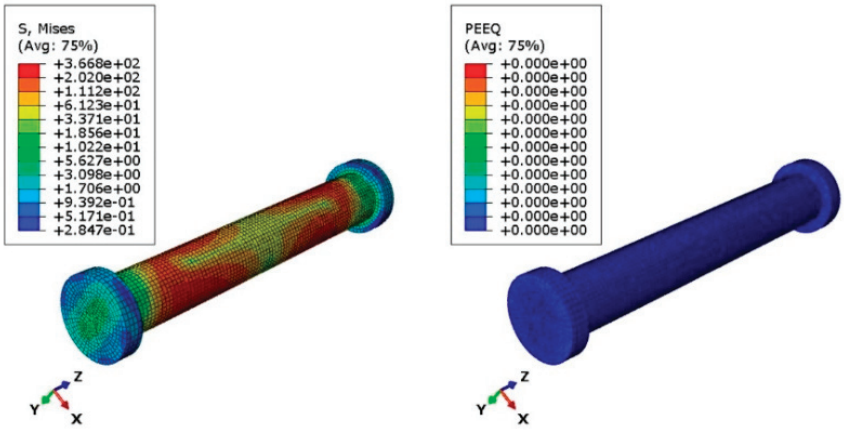

Figure 40. Von Mises stress (Mpa) and PEEQ plot of the pin at the predicted design capacity using the EN 1993-1-8 equation (P = 8070 N).

7. Conclusions

A novel apex connection concept was presented in this paper. The 3D printout of the assembly demonstrates connection effectiveness in providing the folding, unfolding and self-locking mechanism. The folding mechanism of the connection provides easy transportation of the roof panel assembly, and the self-locking mechanism reduces the onsite workload. The connection can be installed at the offsite facility. In order to reduce the onsite workload and enhance productivity, easy installation of the intercomponent connections is required. In this respect, the folding design of the apex connection will facilitate the erection of two panels simultaneously and reduces the crane lifting number. Furthermore, the self-locking mechanism removes the onsite installation activity of the apex connection. Consequently, this novel apex connection is expected to improve onsite productivity. However, the comparison with current truss base roof fabrication requires future time study for this panelized roof system with this folding apex connection.

The validation of 2D FEM with the analytical solution confirms the adequacy of the model for the connection force analysis. The 3D FEM results of PEEQ show that two different C-sections (30 mm × 38 mm and 30 mm × 50 mm) of the main folding bar are required for specified gravity loads of 2.6 kPa and 4 kPa, respectively. The shear capacity of the pin (d = 6.35 mm) obtained from the analytical model was higher than the predicted capacity of FEM since the former procedure is developed based on certain deformation levels in the experimental investigation. To obtain the ultimate strength of a steel connection, validation of the numerical model with an experimental test is necessary. This study was limited by the lack of material coupon tests and actual assembly tests. The benchmark of the PEEQ value equal to zero in determining the design capacity of the assembly is a conservative approach. Therefore, to establish the proper ultimate capacity and serviceability limit of the present connection, actual testing of the connection is recommended. However, the obtained cross-section from this study provides the basis for the fabrication and testing of the assembly in future.

As part of a future study, long-term performance, such as fatigue and durability of this connection, must be investigated. Following the industry practice of light frame connectors such as wood I-Joist hangers, the fabrication of components of the apex connection must use galvanized sheet metal to enhance weatherability.

Supplementary Materials: The following supporting information can be downloaded at: https://www.mdpi.com/article/10.3390/ma15217457/s1, Video S1: Folding mechanism of apex connection.

Author Contributions: Conceptualization, M.S.I. and Y.H.C.; data curation, M.S.I.; formal analysis, M.S.I.; funding acquisition, Y.H.C.; investigation, M.S.I.; methodology, M.S.I. and Y.H.C.; resources, Y.H.C.; supervision, Y.H.C.; validation, M.S.I. and Y.H.C.; visualization, M.S.I.; writing—original draft, M.S.I.; writing—review and editing, Y.H.C. and Z.C. All authors have read and agreed to the published version of the manuscript.

Funding: This work was supported by a grant from the Natural Sciences and Engineering Research Council (NSERC) of Canada through the Engage Grant and Industrial Research Chair programs.

Informed Consent Statement: Not applicable.

Data Availability Statement: Not applicable.

Acknowledgments: The authors would like to thank ACQBUILT Inc., Edmonton, Canada for data sharing and in-kind supports.

Conflicts of Interest: The authors declare no conflict of interest.

Appendix A

SD screw connection analysis:

According to the manufacturer's technical data sheet [16] SD Connector screw is specifically designed to replace nails and the screw used in this study is equivalent to 10d common nails. Hence, the analytical model of timber connection using nails and spikes in CSA86-19 is applicable for the connection analysis.

The factored lateral strength resistance of a connection with nails or spikes, Nr, shall be greater than or equal to the effect of the factored loads, and shall be calculated using Equation (6) of main text.

The unit lateral resistance of steel to timber screw connection per share plane is the smallest value calculated in accordance with failure mode (a) to (f) of Equations (7)–(12) of main text.

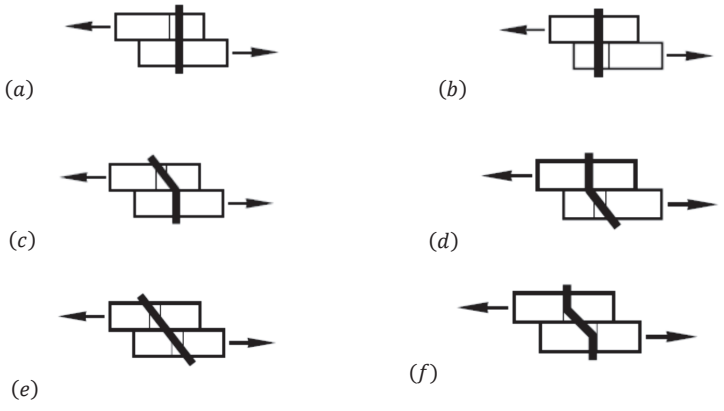

Figure A1. Different failure modes of the screw connection.

Table A1 explains all the parameters values used in the calculating the screw connection capacity and Table A2 presents the results of the connection analysis. As can be observed from Table A2 the failure mode has the lowest connection capacity, so the connection is governed by this failure mode.

Table A1. Input parameters of the connection analysis.

Mean relative density, G (LSL)	0.5
Screw diameter, d_f (mm)	4.5
Factor for light gauge steel, K_{sp}	2.7
Resistance factor for light gauge steel, ϕ_{steel}	0.4
Resistance factor for wood member, ϕ_{wood}	0.8
Ultimate tensile strength of steel fu (MPa)	310
Embedment strength of steel side plate, f_1 (MPa)	418.50
Embedment strength of LSL, f_2 (MPa)	23.88
Embedment strength of main member where failure is screw yielding, f_3 (MPa)	30.17
Screw yield strength, f_y (MPa)	575
Head side member thickness, t_1 (mm)	3.04
Length of screw penetration, t_2 (mm)	35.06
Resistance factor for the lateral resistance of the connection, ϕ	0.8
Number of fasteners, n	7

Table A2. Strength in different failure mode.

Failure Mode	**Strength**
(a)	5725.08 N
(b)	3766.759 N
(c)	2196.59 N
(d)	14,256.92 N
(e)	1898.37 N
(f)	2103.15
Governing failure mode	(e)
Unit lateral strength resistance, n_u	1898.37 N
The factored lateral strength resistance, N_u	10,630.86 N

References

1. Asiz, A.; Chui, Y.H.; Doudak, G.; Ni, C.; Mohammad, M. Contribution of Plasterboard Finishes to Structural Performance of Multi-Storey Light Wood Frame Buildings. *Procedia Eng.* **2011**, *14*, 1572–1581. [CrossRef]
2. Ellingwood, B.R.; Rosowsky, D.V.; Li, Y.; Kim, J.H. Fragility Assessment of Light-Frame Wood Construction Subjected to Wind and Earthquake Hazards. *J. Struct. Eng.* **2004**, *130*, 1921–1930. [CrossRef]
3. naturally:wood. What Is Light-Frame Construction? Available online: https://www.naturallywood.com/topics/light-frame-construction/ (accessed on 1 January 2022).
4. *U.S. Department of Housing and Urban Development Residential Structural Design Guide*; Second Edition In; October 2017. Available online: https://www.huduser.gov/publications/pdf/residential.pdf (accessed on 1 January 2022).
5. Jellen, A.C.; Memari, A.M. Structural Design of a Typical American Wood-Framed Single-Family Home. In *Timber Buildings and Sustainability*; Concu, G., Ed.; IntechOpen: Rijeka, Croatia, 2019.
6. ACQBUILT Inc. Company Database and Personal Visits for Images. Available online: http://www.acqbuilt.com/ (accessed on 3 November 2019).
7. Altaf, M.S.; Bouferguene, A.; Liu, H.; Al-Hussein, M.; Yu, H. Integrated Production Planning and Control System for a Panelized Home Prefabrication Facility Using Simulation and RFID. *Autom. Constr.* **2018**, *85*, 369–383. [CrossRef]
8. Wang, M.; Altaf, M.S.; Al-Hussein, M.; Ma, Y. Framework for an IoT-Based Shop Floor Material Management System for Panelized Homebuilding. *Int. J. Constr. Manag.* **2020**, *20*, 130–145. [CrossRef]
9. Altaf, M.S.; Han, S.H.; Lei, Z.; Demirer, S.; Al-Hussein, M. A Case Study: Prefabricated Wood Framed Panelized Roof System for Single Family Home. In Proceedings of the WCTE 2018—World Conference on Timber Engineering, Seoul, Korea, 20–23 August 2018; pp. 1–6.

10. Islam, M.S.; Chui, Y.H.; Altaf, M.S. A Holistic Design Approach for Innovative Panelized Light-Wood Frame Roof Construction. In Proceedings of the WCTE 2021—World Conference on Timber Engineering, Santiago, Chile, 9–12 August 2021.
11. Islam, M.S.; Chui, Y.H.; Altaf, M.S. Design and Experimental Analysis of Connections for a Panelized Wood Frame Roof System. *Buildings* **2022**, *12*, 847. [CrossRef]
12. Islam, M.S.; Chui, Y.H.; Al-Hussein, M.; Altaf, M. A New Panelized Roof Design Approach for Offsite Fabrication of Light-Frame Wood Residential Construction Projects. In Proceedings of the Canadian Society of Civil Engineering Annual Conference, Calgary, AB, Canada, 26–29 May 2021.
13. *EN 1993-1-8*; Eurocode 3: Design of Steel Structures, Part 1–8: Design of Joints. European Union: Brussels, Belgium, 2006.
14. Schmidt, R.J.; Miller, J.F. Considerations for Design of Rafters in Timber Buildings. *Pract. Period. Struct. Des. Constr.* **2012**, *17*, 127–132. [CrossRef]
15. *CSA O86-19*; Engineering Design in Wood. CSA Group: Mississauga, ON, Canada, 2019.
16. Simpson Strong-Tie ICC-ES Evaluation Report. Available online: https://ssttoolbox.widen.net/view/pdf/lo69jw45jn/ICCES_ESR3046.pdf?t.download=true&u=cjmyin (accessed on 3 November 2021).
17. Liu, X.C.; Pu, S.H.; Zhang, A.L.; Zhan, X.X. Performance Analysis and Design of Bolted Connections in Modularized Prefabricated Steel Structures. *J. Constr. Steel Res.* **2017**, *133*, 360–373. [CrossRef]
18. Zhao, J.; Peng, Y.; Su, W.; Dong, J. Finite Element Analysis of the Shear Capacity of Stainless-Steel Blind-Rivet Connections. *J. Constr. Steel Res.* **2021**, *179*, 106558. [CrossRef]
19. Daneshvar, H.; Driver, R.G. Modelling Benchmarks for Steel Shear Connections in Column Removal Scenario. *J. Build. Eng.* **2018**, *16*, 199–212. [CrossRef]
20. Dassault Systèmes ABAQUS Abaqus Analysis User's Manual, Dassault Systèmes Simulia Corp 2019. Available online: https://help.3ds.com/2019/English/DSSIMULIA_Established/SIMACAECAERefMap/simacae-m-Hlp-sb.htm?contextscope=all&redirect_lang=English (accessed on 3 November 2021).
21. Mohamadi-shooreh, M.R.; Mofid, M. Parametric Analyses on the Initial Stiffness of Flush End-Plate Splice Connections Using FEM. *J. Constr. Steel Res.* **2008**, *64*, 1129–1141. [CrossRef]
22. Fan, L.; Rondal, J.; Cescotto, S. Finite Element Modelling of Single Lap Screw Connections in Steel Sheeting under Static Shear. *Thin-Walled Struct.* **1997**, *27*, 165–185. [CrossRef]
23. Huynh, M.T.; Pham, C.H.; Hancock, G.J. Experimental Behaviour and Modelling of Screwed Connections of High Strength Sheet Steels in Shear. *Thin-Walled Struct.* **2020**, *146*, 106357. [CrossRef]
24. Daneshvar, H. One-Sided Steel Shear Connections in Column Removal Scenario. Ph.D. Thesis, University of Alberta, Edmonton, AB, Canada, 2013.
25. *A1008/A1008M-20*; ASTM Standard Specification for Low-Alloy, High-Strength Low-Alloy with Improved Formability, Solution Hardened, and Bake Hardenable Designation. ASTM: West Conshohocken, PA, USA, 2014.
26. Lenard, J.G. (Ed.) *Primer on Flat Rolling*, 2nd ed.; Elsevier: Amsterdam, The Netherlands, 2014.
27. Li, Z.X.; Zhou, T.Q.; Chan, T.H.T.; Yu, Y. Multi-Scale Numerical Analysis on Dynamic Response and Local Damage in Long-Span Bridges. *Eng. Struct.* **2007**, *29*, 1507–1524. [CrossRef]
28. Verwaerde, R.; Guidault, P.A.; Boucard, P.A. A Non-Linear Finite Element Connector Model with Friction and Plasticity for the Simulation of Bolted Assemblies. *Finite Elem. Anal. Des.* **2021**, *195*, 103586. [CrossRef]
29. Rogers, C.A.; Masc, B.; Hancock, G.J. *New Bolted Connection Design Formulae for G550 and G300 Sheet Steels Less Than 1.0 mm Thick*; School of Civil Engineering, The University of Sydney: Sydney, Australia, 1998.
30. Errera, S.J.; Popowich, D.W.; Winter, G. Bolted and Welded Stainless Steel Connections. *ASCE J. Struct. Div.* **1974**, *100*, 1279–1296. [CrossRef]
31. Winter, G. Tests on Bolted Connections in Light Gage Steel. *J. Struct. Div.* **1956**, *82*, 920–921. [CrossRef]
32. Puthli, R.; Fleischer, O. Investigations on Bolted Connections for High Strength Steel Members. *J. Constr. Steel Res.* **2001**, *57*, 313–326. [CrossRef]
33. Salih, E.L.; Gardner, L.; Nethercot, D.A. Bearing Failure in Stainless Steel Bolted Connections. *Eng. Struct.* **2011**, *33*, 549–562. [CrossRef]
34. Chung, K.F.; Ip, K.H. Finite Element Modeling of Bolted Connections between Cold-Formed Steel Strips and Hot Rolled Steel Plates under Static Shear Loading. *Eng. Struct.* **2000**, *22*, 1271–1284. [CrossRef]
35. Peng, H.; Ou, J.; Mahin, S. Design and Numerical Analysis of a Damage-Controllable Mechanical Hinge Beam-to-Column Connection. *Soil Dyn. Earthq. Eng.* **2020**, *133*, 106149. [CrossRef]

materials

MDPI

Article

The Influence of the Accelerated Aging Process on the Compressive Strength of Wood Treated with Components of a Salt Fire Retardant

Wojciech Łukasz Grześkowiak [1,*], Marta Molińska-Glura [2] and Marcelina Przybylska [1]

[1] Department of Mechanical Wood Technology, Faculty of Forestry and Wood Technology, Poznan University of Life Sciences, Wojska Polskiego 28, 60-637 Poznan, Poland; marcelina.k.przybylska@gmail.com
[2] Department of Economics and Forest Technology, Faculty of Forestry and Wood Technology, Poznan University of Life Sciences, Wojska Polskiego 28, 60-637 Poznan, Poland; marta.glura@up.poznan.pl
* Correspondence: wojciech.grzeskowiak@up.poznan.pl

Abstract: This paper presents the results of research on the influence of the components of salt flame retardants on the compressive strength of wood depending on the time of accelerated aging. The effect of the agent was assessed on the basis of the change in the strength of treated wood compared to that of untreated wood. In addition, a statistical analysis of the obtained results was used to determine which of the components most significantly affect the changes in the compressive strength of wood along the fibers, and to what extent. It was found that extending the aging process time in the case of control and boric acid-protected samples did not significantly change the strength properties. It has also been found that some compounds contained in fire retardant have an antagonistic effect related to the compressive strength of wood.

Keywords: wood; fire retardants; artificial ageing; compression strength

Citation: Grześkowiak, W.Ł.; Molińska-Glura, M.; Przybylska, M. The Influence of the Accelerated Aging Process on the Compressive Strength of Wood Treated with Components of a Salt Fire Retardant. *Materials* **2022**, *15*, 4931. https://doi.org/10.3390/ma15144931

Academic Editor: Marco Corradi

Received: 3 June 2022
Accepted: 13 July 2022
Published: 15 July 2022

Publisher's Note: MDPI stays neutral with regard to jurisdictional claims in published maps and institutional affiliations.

1. Introduction

Fire is the fastest destructive factor for wood, but it is impossible to eliminate it in everyday life. Various measures to reduce the flammability of wood material have been used for centuries, but they are still incapable of completely preventing the burning of this material. They allow for a significant reduction of parameters, such as the spread of flames over the surface, weight loss, or the rate of heat release. Among the fire retardants, salt compounds and mixtures thereof are most commonly used. They include: phosphates, ammonium sulphates and their derivatives, boric acid, borax, urea, and potassium carbonate [1,2]. Undoubted advantages of fire-retardant treatment, after years of use, may have negative consequences for the structural strength of the protected wood. The strength properties are influenced, among others, by the type of flame retardant, its pH, impregnation technology and wood humidity, and the conditions in which the wooden elements are used. Publications presenting research on the fire retardants effectiveness of preparations clearly confirm the deterioration of wood strength on the basis of parameters such as: modulus of elasticity (E) and compressive strength (Rm) [1,3,4]. In the research by Grześkowiak et al. [5] on the fire-retardant use of potassium carbonate, it was found that the strength of pine wood, treated with a 20% solution, was decreased by 20% compared to unprotected wood. Moreover, aspen wood impregnated with the same solution showed a decrease in compressive strength by about 15% when impregnated with the vacuum-pressure method using. The research by Surmiński and Lutomski [6] on the effect of treatment of pine wood with fire retardant preparations also showed that wood treated with the vacuum-pressure method with 25% K_2CO_3 showed a decrease in compressive strength by 11.78%. When impregnating the wood with 25% $NH_4H_2PO_4$, $(NH_4)_2SO_4$ mixture using the vacuum method, an improvement in wood strength of 2% was found compared to unprotected

wood. The same authors using 30% vacuum treatment with the $NH_4H_2PO_4$, $(NH_4)_2SO_4$, H_3BO_3, Na_2B_4O mixture achieved an improvement in compressive strength of 13.19%. The product [7], using a 10% mixture of phosphates, sulphates, boron compounds, and salts of benzoic acid, achieved a strength improvement of 7.1% compared to unprotected wood. The conducted research on long-term heating of wood protected with, among others: phosphoric acid (PA), ammonium dihydrogen phosphate (MAP) or a mixture of borax and boric acid (BBA) showed that phosphoric acid had the greatest impact on the decrease in strength. The mixture of borax and boric acid deteriorated the strength of the wood the least [8,9]. In tests made by Sweet et al. [9], three variants of temperature and humidity were used, imitating: the temperature in a dry room (27 °C), the temperature to which the roof sheathing may be exposed (54 °C), and finally 80 °C. Both during and after the exposure, measurements were made of the modulus of elasticity, moisture, modulus of breaking, and maximum load. It was found that the factor determining the strength drop was the nature of the chemical compound used, followed by the exposure conditions and the method of saturation. In research on the influence of the conditions of use on the properties of protected wood, simulations of these conditions are used, known as accelerated aging. Changes in wood resulting from accelerated, artificial aging should correspond to the changes that would be caused by exposure to weather conditions, with particular emphasis on the effects of humidity and temperature. Wood heated in the atmosphere of water vapor requires lower decomposition activation energy than raw material at elevated temperature, but in a dry environment [10–13]. There are many methods based on the simulation of natural conditions in the laboratory, differing in cycle duration, annealing and freezing temperatures. For example, the ASTM D 1037 method [14] provides a 60-h cycle consisting in soaking the wood, steam, freezing, steam and heating in dry air. Kajita et al. [15] give an accelerated aging method based on BS 5669-1:1989 [16] and consisting in immersion in water at 20 °C for 36 h, freezing at −12 °C for 24 h, and heating in dry air at 70 °C for 36 h. On the other hand, Riwier [17] provides two methods of accelerated aging of the wood used: Cyclic-boil dry method, which consists in repeatedly submerging the material in hot water and heating with dry air, and the vacuum-pressure-dry cycle method, which consists in immersing the wood in water under negative pressure, reducing vacuum, pressure and heating with dry air. As can be seen from the above description, the applied conditions of artificial aging differ in terms of values and duration of action, etc. Accelerated aging is purely theoretical, because it is impossible to transfer this long-term process to laboratory conditions, so as to accurately reproduce the changes taking place in the structure of the tested materials.

In this study, it was decided to focus on determining the effect of fire-retardant treatment of wood and accelerated aging time on the strength parameters of the protected wood. It was decided to protect the wood with chemical compounds included in the fire-retardant preparation, as well as with the fire-retardant preparation itself, in order to determine which of the compounds most significantly influences the changes in the compressive strength of the wood along the fibers, and to what extent. Flammability properties of the tested commercial fire retardant were included in publications [18,19], where the effectiveness of fire retardants was between 75% and 88% measured with the MFT method [20]. Moreover, the effectiveness of chemical compounds is known and described in literature [21].

2. Materials and Methods

Samples with dimensions of 2 cm × 2 cm × 3 ± 0.2 cm were cut from Scots pine (*Pinus sylvestris* L.) sapwood boards. A total of 10 samples for each test variant were selected for the tests. The samples were selected according to sequence of occurrence in a given lath, without defects and visible changes caused by blue stain fungi [22,23]. The research variant consisted of a given chemical compound and the number of accelerated aging cycles. Each of the variants was tested separately. The test specimens were treated in vacuum dryers by the full-cell vacuum method using a vacuum of 0.1 MPa maintained

for 20 min, and then the vacuum was gently reduced to atmospheric pressure and kept in solutions for another 2 h. After impregnation, the samples were air-conditioned for 14 days at the temperature of 23 ± 2 °C and humidity of 65 ± 5%, in a heated room with forced air circulation, until the wood moisture content was 10 ± 2%. The control samples had the same humidity throughout the test. The humidity of the samples was determined by the dryer-weight method [20]. The wood was treated with 6 solutions of chemical compounds with wood impregnation average gain (dry mass of chemical compound) (kg/m^3): monoammonium phosphate (MAP) 62.85 kg/m^3, boric acid (BA) 17.25 kg/m^3, sodium tetraborate (borax) (Bx) 18.6 kg/m^3, urea (U) 64.48 kg/m^3, monoammonium sulphate (MAS) 66.51 kg/m^3 and diammonium phosphate (DAP) 61.57 kg/m^3, and a commercial preparation (FR) 59.98 kg/m^3 at a concentration of 10%, except for borax and boric acid where the concentration was 4%. Tests were also carried out on wood not subjected to impregnation, i.e., control (C). Based on the literature, it was decided to develop a proprietary accelerated aging cycle simulating conditions in a temperate climate. An accelerated aging process was performed to determine progressive changes in the wood. The complete course of the aging process was 0, 8, and 16 cycles. Each cycle consisted of the following phases:

1. Heating (130 °C for 24 h)
2. Freezing (−15 °C for 24 h)
3. Heating (130 °C for 24 h)
4. Maintaining over a supersaturated solution of KNO_3 giving approx. 90% (temp. 40–45 °C for 24 h)
5. Freezing (−15 °C for 24 h)

After the accelerated aging process, the samples were tested for physical changes and strength decline. Before the compression tests, samples were conditioned (until equilibrium moisture content (constant mass) was achieved) in the same conditions and mass as before the aging process, and their dimensions were measured using an analytical balance accurate to 0.001 g (Sartorius GmbH, Göttingen, Germany) and a digital caliper with accuracy to 0.01 mm [23]. Then, the beams were subjected on compressive strength test according to the ISO 13061-1:2014 [24], ISO 13061-5:2020 [25] and ISO 13061-17:2017 [26] standard on the Zwick Z100 testing machine (Zwick GmbH, Ulm, Germany) [23,27]. During the tests, the value of the compressive strength and Young's modulus were recorded [28].

A statistical analysis of the obtained results was performed, starting with the determination of appropriate measures of central tendency (mean) and standard deviation (SD) [28]. The Kolmogorov–Smirnov test was used to verify the compliance with the theoretical normal distribution, and the homogeneity of variance was tested based on the Bartlett test. In order to determine the significance of the analyzed impregnation types and the number of aging cycles, a two-factor analysis of variance was used. Tukey's HSD test was used to determine statistically homogeneous groups. The statistically significant results were those with $p < 0.05$. All calculations were performed in Statistica 13.3 software (StatSoft Polska Sp. z oo, Kraków, Poland).

3. Results

The research results presented below reflect the average values of the analyzed features obtained for individual research variants. Analyzing the basic strength parameters, Rm (compressive strength) and E (Young's modulus), it can be concluded that the highest value of compressive strength was obtained for samples protected with urea and subjected to the aging process for 16 cycles. In this case, Rm was 62 MPa. Samples protected with FR and aged for eight cycles were characterized by a slightly lower value (61 MPa). The lowest Rm values were observed for samples not aged, but protected with MAP, where the value was 38.7 MPa. Slightly higher values were obtained for samples protected with Bx and U, not subjected to aging. These values were 39.3 and 39.8 MPa, respectively. All the non-aged samples had lower Rm values compared to the samples protected with the same aged compounds (Figures 1 and 2).

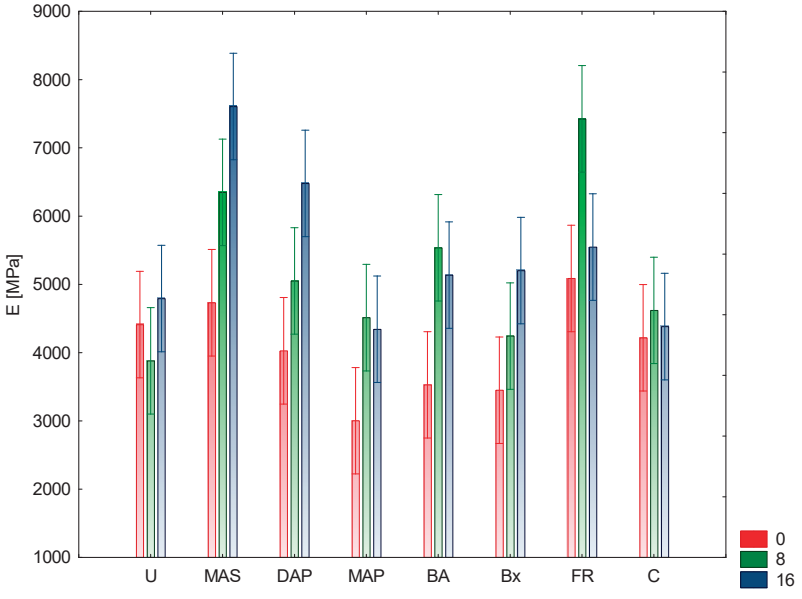

Figure 1. Illustration of the E relationship of aging cycles and chemical compounds. Whiskers represented 95% confidence interval.

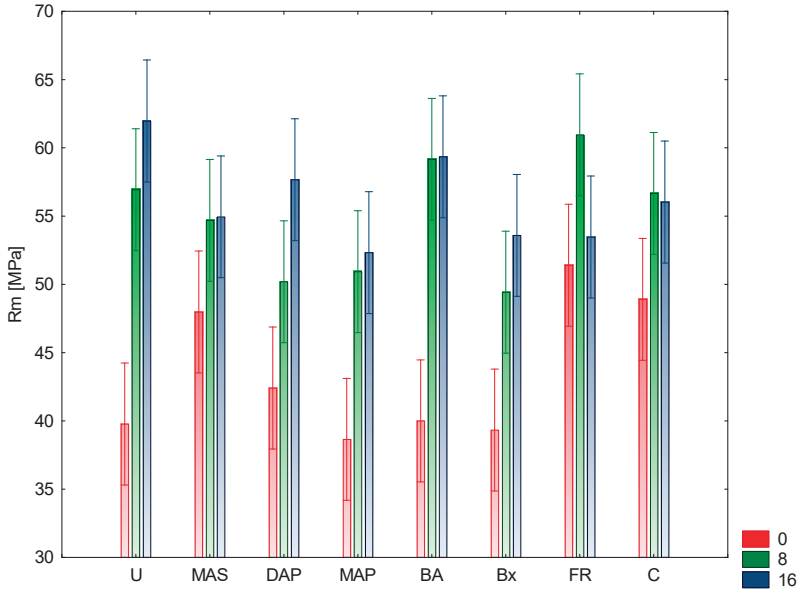

Figure 2. Illustration of the Rm relationship of aging cycles and chemical compounds. Whiskers represented 95% confidence interval.

The absorption of the preparation and individual components was similar for the concentrations used. The obtained data show that the degree of absorption did not affect the strength properties of the protected wood.

Analyzing changes in wood saturated with individual compounds, an increase in strength with aging time was found in the case of U, Bx, MAP, DAP, and MAS. For the above compounds, the increase in Rm over time from 0 to 16 cycles (assuming the values for the 0 aging cycle as reference) was, respectively, for the samples protected: with urea after eight cycles by 42.96% and after 16 cycles by 55.78%, with borax 25.7 and 36.39%, MAP 31.52 and 35.14%, DAP 18.39 and 36.08%, and MAS by 13.95 and 14.58%. For the remaining test variants, the increase in the strength value took place until the 8th aging cycle, while in the 16th cycle it was lower, however, the values did not reach the level for the 0 cycle. These values were respectively 15.95% and 14.52% for the control samples, 48.0% and 47.5% for the samples protected with boric acid, and 18.67% and 3.11% for the FR protected samples. Analyzing the above changes, it can be concluded that extending the aging process in the case of control samples and samples protected with boric acid does not significantly affect the changes in strength between the 8th and 16th cycle. The observed decrease in strength took place in the case of wood protected with FR, where the change amounted to 15.5%. This means that the compounds included in the composition of the preparation may act in an antagonistic manner, considering the influence on the compressive strength. The modulus of elasticity E showed similar dependencies in most of the analyzed research variants. A deviation from this relationship were the samples protected with urea, where the lowest mean value was obtained for samples aged for 8 cycles (Table 1). Significant increases in the value of E were observed after the 16th cycle of aging compared to the 0 and 8 cycles for compounds such as: Bx, MAS, and DAP. For wood treated with Bx, the increase in the value of E after the 8th cycle was 22.98% and after 16th cycle, 50.81% in relation to the 0th cycle as the reference aging. Similar values were obtained for MAS and DAP protected wood, respectively: 34.18% and 60.77% as well as 25.43% and 60.89%. In the case of control samples, the differences between the E values for the unaged and aged samples for 8 and 16 cycles were not that significant and amounted to 9.51% after the eighth cycle and 3.89% after the 16th cycle, respectively. For samples protected with BA and MAP, the drops in E values after the 16th cycle as compared to the 8 aging cycles were not that significant and amounted to 11.33% and 5.66%, respectively. The greatest changes in the values of Young's modulus were observed for wood protected with FR, where after the 8th cycle of aging there was an increase by 45.96%, while after 16 cycles of aging only by 9.04% (the difference between the 8th and 16th cycles were 36.92%. Considering the composition of the FR preparation, it can be concluded that it does not adversely affect the strength properties of wood. Considering the obtained results concerning the basic strength parameters of the tested variants, it can be concluded that urea does not affect the values of the elasticity modulus E, regardless of the aging variant, as compared to the control samples. The highest positive effect on E values was demonstrated by MAS, which obtained higher E coefficient values with increasing time and number of aging phases. Moreover, samples protected with FR showed an increase in the E coefficient value during aging up to eight cycles. After 16 process cycles, the E value for FR dropped to a value similar to that of the unaged samples. In the case of the other variants, the E coefficient was lower than E for the control samples. In the case of DAP and Bx, the values of this coefficient after 16 aging cycles are higher than after eight and 0 cycles, while for samples protected with MAP and BA, after 16 aging cycles, the value of the E coefficient is lower than after eight. Such changes in the values of compressive strength and Young's modulus compared to control wood, especially along with the elongation of the aging time, are caused by the chemical nature of individual components. The pH of the solutions of individual components was of the greatest importance with regard to the decrease in strength. The greatest changes were observed for the components whose pH was acidic (pH near 4–5): U, MAP, MAS, BA. The remaining compounds and the FRs had a pH close to neutral. Control samples without the aging process had a 5.3 pH value, measured using indirect cold water extraction method. Compounds with acidic pH cause, along with the prolongation of the action time, the hydrolysis of cellulose and hemicelluloses, thus lowering the strength properties of wood. Acidic fire retardants have the ability to catalyze the glucose dehydration process, resulting

in cellulose depolymerization. This degrades the fibers, reducing their strength [29]. During the tests, no visual changes of the samples (cracks, twists, etc.) were found after the aging process. It was found that after the aging process, with the increase in the number of aging cycles, the weight loss of the protected samples increased. The highest weight loss was recorded for FR after 16 aging cycles and it amounted to 5.41% and 4.45% after eight cycles, and for MAS (4.18% and 2.95%, respectively). The lowest weight loss after aging was recorded for samples protected with Bx (2.1% and 1.28%, respectively) and BA (2.93% and 1.9%, respectively). The other variants showed weight loss in the range of 3.05–3.75% after 16 cycles and 1.7–2.21% after eight aging cycles. The control variants showed a weight loss after aging, regardless of the number of cycles, at the level of 0.75%. These results may indicate the hydrolytic activity of individual components of the preparation.

Table 1. Summary of statistically homogeneous groups determined on the basis of the HSD Tukey test for E and Rm. The symbol * meaning that results are not statistically different.

Solution	E-Mean	1	2	3	4	Rm [MPa] Mean	1	2
MAP	3953.00	*				47.30	*	
Bx	4298.67	*	*			47.45	*	
U	4361.33	*	*			50.09	*	*
C	4406.33	*	*			52.54	*	*
BA	4733.33	*	*			52.84	*	*
DAP	5185.67		*	*		52.89	*	*
FR	6019.67			*	*	53.86		*
MAS	6228.33				*	55.28		*

In the case of the feature of the Young's coefficient (E), both the relationship ($p = 0.000$) and the number of aging cycles ($p = 0.000$), as well as their interaction ($p = 0.000$), show a statistically significant influence on the difference in its mean values for individual research variants [30]. Based on the results of Tukey's post-hoc test, it can be concluded that the eight and 16 cycle variants show statistically similar results, while the 0 cycle aging variant differs from the other variants. In the case of chemical compounds, due to the values of the E factor, four homogeneous groups can be distinguished (Table 1).

For all non-aging variants except FR, the Rm values are lower than for the control variant. Moreover, the variants aged for eight cycles show Rm values lower than those of the control variant. The exceptions are variants protected with boric acid, FR and urea. For the variants aged for 16 cycles, the Rm values for the samples protected with boric acid and urea were also higher than for the control variant.

Inference similar to the E feature was carried out for the Rm feature. Again, the aging ($p = 0.000$) and the relationship ($p = 0.000$) as well as their interaction ($p = 0.001$) turned out to be statistically significant. As for the aging effect, again, eight and 16 cycles give similar results, and the aging variant 0 differs from them. In the case of Rm values, the homogeneous groups are arranged differently than for E due to the compounds (Table 1).

Figure 3 shows the simultaneous levels of two features (E and Rm) depending on the combination compound × aging. This represents an illustration of the interaction of both factors on the two considered strength characteristics.

Analyzing the relationship between the chemical compounds, aging cycles, and their influence on the strength parameters (E and Rm), it can be stated that the compounds in the Section III of the graph have a positive effect on these parameters (in the studied period), and the negative ones in the Section II. Variants close to the center can be considered the most neutral in terms of strength changes in relation to the controls without aging process.

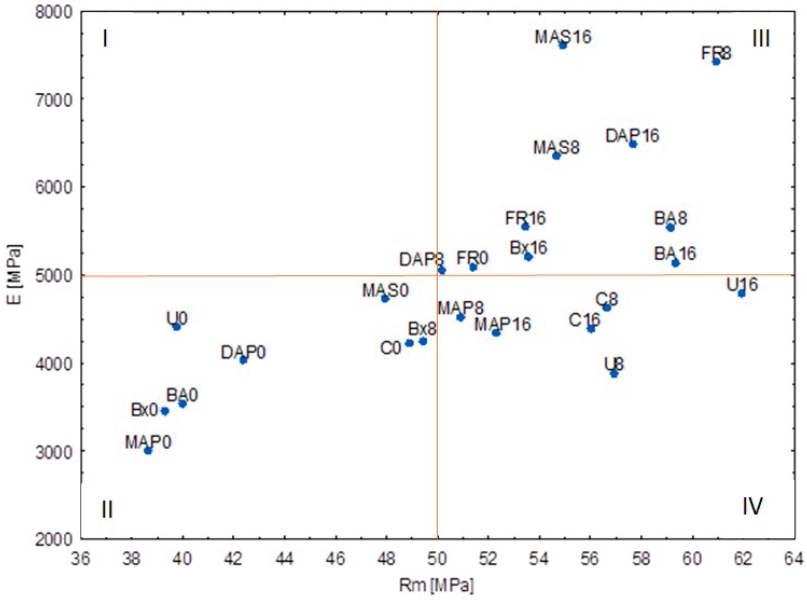

Figure 3. Illustration of the Rm and E relationship of aging cycles and chemical compounds. I–IV are sections of graph.

Applying the analysis of variants, considering at the same time the average values of the observed properties (E and Rm), it can be concluded that the best strength properties were shown by such compounds with aging cycles as FR 8, MAS 8 and 16, and DAP 16. This is confirmation supporting a positive effect on the strength properties of wood in an aging time context. The worst effects were demonstrated for the variants not subjected to aging, i.e., those protected with MAP, DAP, Bx, BA, and U. Moreover, these compounds, in the variant without aging, showed the most negative impact on the strength properties of wood.

4. Conclusions

Extending the aging process in the case of control and boric acid-protected samples does not significantly change the strength between the eight and 16th cycles. The greatest changes in strength were shown by FR.

Some of the compounds contained in FR have an antagonistic effect related to the compressive strength of wood. The greatest influence on this phenomenon is probably the content of boric acid and MAP. Due to the lack of detailed data on the chemical composition of the preparation, it is not possible to clearly determine which of these compounds causes the greatest changes. This is indicated by the results obtained during laboratory tests and their statistical analysis. Changes in the compressive strength and Young's modulus compared to control wood, especially along with the elongation of the aging time, are caused by the chemical nature of individual components. The pH of the solutions of individual components was 321, which is of the greatest importance with regard to the decrease in strength. Acidic FRs can lead to the glucose dehydration process, resulting in cellulose depolymerization and reducing strength of wood fibers.

Author Contributions: Conceptualization, M.P. and W.Ł.G.; methodology, M.P. and M.M.-G.; validation, W.Ł.G., M.M.-G. and M.P.; investigation, M.P.; formal analysis, M.M.-G.; writing—original draft preparation, W.Ł.G., M.P. and M.M.-G.; writing—review and editing, W.Ł.G. and M.M.-G.; visualization, W.Ł.G. and M.M.-G.; supervision, W.Ł.G. All authors have read and agreed to the published version of the manuscript.

Funding: Publication was financed within the framework of the Polish Ministry of Science and Higher Education's program: "Regional Excellence Initiative" in the years 2019–2022, project no. 005/RID/2018/19, financing amount 1,200,000,000 PLN. Research was financially supported by the Ministry of Science and Higher Education as the Project No. 506.224.02.00.

Informed Consent Statement: Not applicable.

Data Availability Statement: Datasets are available in corresponding author archive.

Acknowledgments: The authors wish to thank Krzysztof Moliński for invaluable help, advice and support. We also wish to thank Anna Szulc and Przemysław Mania for their undivided attention and technical support.

Conflicts of Interest: The authors declare no conflict of interest.

References

1. Kučerová, I.; Ohlídalová, M.; Frankl, J.; Kloiber, M.; Michalcova, A. Defibring of historical roof beam caused by ammonium sulphate and ammonium phosphates based fire retardants. In Proceedings of the International Conference on Wood Science for Preservation of Cultural Heritage: Mechanical and Biological Factors, Braga, Portugal, 5–7 November 2008.
2. Le Van, S.L.; Ross, R.J.; Winandy, J.E. *Effects of Fire Retardant Chemicals on the Bending Properties of Wood at Elevated Temperatures*; USDA Service, Forest Products Laboratory: Madison, WI, USA, 1990.
3. Drdácký, M.; Beran, P.; Slížková, Z.; Kucerová, I. Man made hazards in conservation practice-case studies. *Conserv. News* **2009**, *26*, 224–233.
4. Winandy, J.E.; Lebow, P.K. Modelling strength loss in wood by chemical composition. Part I. An individual component model for southern pine. *Wood Fiber Sci.* **2001**, *33*, 239–254.
5. Grześkowiak, W.; Mazela, B.; Cofta, G. The Influence of Salt Agents on the Strength Properties of Wood. GENERAL CONSTRUCTION-Construction, Material and Thermal-Humidity Issues in Construction. In *Chapter I "Building Materials, Material Technologies*; University Publishers of the University of Technology and Agriculture: Bydgoszcz, Poland, 2003; pp. 16–21.
6. Lutomski, K.; Surmiński, J. *Research on the Preparation of Fire Retardants for Wood*; Poznań Society of Friends of Sciences, Faculty of Technical Sciences, Works of the Wood Technology Commission: Poznań, Poland, 1978; Volume VII.
7. Wytwer, T. Fungitox NP.-wood flame retardant and bioprotective agent. In *International Symposium "Advances in Fire Protection and Flammability Test Methods"*; Institute of Natural Fibers: Poznań, Poland, 1995.
8. Le Van, S.L.; Winandy, J.E. Effects of fire retardant treatments on wood strength: A review. *Wood Fiber Sci.* **1990**, *22*, 113–131.
9. Sweet, M.S.; Winandy, J.E. Influence of Degree of Polymerization of Cellulose and Hemicellulose on Strength Loss in Fire-Retardant-Treated Southern Pine. *Holzforschung* **1999**, *53*, 311–317. [CrossRef]
10. Kloiber, M.; Frankl, J.; Drdácký, M.; Bryscejn, J.; Tippner, J.; Kucerová, I. Change of mechanical properties of norway spruce wood due to degradation caused by fire retardants. *Wood Res.* **2010**, *55*, 23–38.
11. Kojima, Y.; Suzuki, S. Evaluating the durability of wood-based panels using internal bond strength results from accelerated aging treatments. *J. Wood Sci.* **2011**, *57*, 7–13. [CrossRef]
12. Follrich, J.; Teischinger, A.; Müller, U. Artificial ageing of softwood joints and its effect on internal bond strength with special consideration of flat-to-end grain joints. *Eur. J. Wood Wood Prod.* **2011**, *69*, 564–597. [CrossRef]
13. Matsuo, M.; Yokoyama, M.; Umemura, K.; Gril, J.; Yano, K.; Kawai, S. Color changes in wood during heating: Kinetic analysis by applying a time temperature superposition method. *Appl. Phys. A Mater. Sci. Processing* **2010**, *99*, 47–52. [CrossRef]
14. *ASTM D 1037*; Standard Test Methods for Evaluating Properties of Wood-Base Fiber and Particle Panel Materials. ASTM: West Conshohocken, PA, USA, 2020.
15. Kajita, H.; Mukudai, J.; Yano, H. Durability evaluation of particleboards by accelerated aging tests. *Wood Sci. Technol.* **1991**, *25*, 239–249. [CrossRef]
16. *BS 5669-1:1989*; Particleboard. Methods of Sampling, Conditioning and Test. British Standards Institution: London, UK, 1989.
17. River, B.H. Outdoor aging of wood-based materials and correlation with laboratory aging. *For. Prod. J.* **1994**, *44*, 55–65.
18. Grześkowiak, W.Ł.; Moliński, K.; Molińska-Glura, M.; Cofta, G. Assessment of the impact of the storage time of fire retardant and heating of the protected wood on the effectiveness of fireproofing. *Drewno* **2021**, *64*, 207. [CrossRef]
19. Grześkowiak, W.Ł.; Moliński, K. Methodological improvement of testing of selected parameters for fire resistance of wood and wood-based materials using the MFT. *Biom. Lett.* **2020**, *57*, 53–62. [CrossRef]
20. Zeinali, D.; Koalitis, D.; Schmid, J. (Eds.) *Guide for Obtaining Data from Reaction to Fire Tests*; ETH: Zürich, Switzerland, 2018. [CrossRef]

21. Grześkowiak, W.; Cofta, G.; Mazela, B. Fire retardant efficacy of selected chemical compounds. *Ann. Wars. Univ. Life Sci.–SGGW For. Wood Technol.* **2008**, *65*, 98–102.
22. Crespo, J.; Majano-Majano, A.; Lara-Bocanegra, A.J.; Guaita, M. Mechanical Properties of Small Clear Specimens of Eucalyptus globulus Labill. *Materials* **2020**, *13*, 906. [CrossRef] [PubMed]
23. Roszyk, E.; Stachowska, E.; Majka, J.; Mania, P.; Broda, M. Moisture-Dependent Strength Properties of Thermally-Modified Fraxinus excelsior Wood in Compression. *Materials* **2020**, *13*, 1647. [CrossRef] [PubMed]
24. *ISO 13061-1:2014*; Physical and Mechanical Properties of Wood—Test Methods for Small Clear Wood Specimens—Part 1: Determination of Moisture Content for Physical and Mechanical Tests. International Organization for Standardization: Geneva, Switzerland, 2014.
25. *ISO 13061-5:2020*; Physical and Mechanical Properties of Wood—Test Methods for Small Clear Wood Specimens—Part 5: Determination of Strength in Compression Perpendicular to Grain. International Organization for Standardization: Geneva, Switzerland, 2020.
26. *ISO 13061-17:2017*; Physical and Mechanical Properties of Wood—Test Methods for Small Clear Wood Specimens—Part 17: Determination of Ultimate Stress in Compression Parallel to Grain. International Organization for Standardization: Geneva, Switzerland, 2017.
27. Roszyk, E.; Mania, P.; Iwańska, E.; Kusiak, W.; Broda, M. Mechanical performance of Scots pine wood from northwestern Poland–A case study. *BioResources* **2020**, *15*, 6781–6794. [CrossRef]
28. Słonina, M.; Dziurka, D.; Molińska-Glura, M.; Smardzewski, J. Influence of Impregnation with Modified Starch of a Paper Core on Bending of Wood-Based Honeycomb Panels in Changing Climatic Conditions. *Materials* **2022**, *15*, 395. [CrossRef] [PubMed]
29. Ozcifci, A.; Okcu, O. The influence of the impregnating chemicals on the bonding strength of impregnated wood materials. *J. Appl. Polym. Sci.* **2008**, *107*, 2871–2876. [CrossRef]
30. Larson, M.G. Analysis of Variance. *Circulation* **2008**, *117*, 115–121. [CrossRef] [PubMed]

materials

MDPI

Article

The Possibility of Using Pine Bark Particles in the Chipboard Manufacturing Process

Radosław Mirski, Adam Derkowski *, Jakub Kawalerczyk *, Dorota Dziurka and Joanna Walkiewicz

Department of Mechanical Wood Technology, Faculty of Forestry and Wood Technology, Poznan University of Life Sciences, 60-627 Poznan, Poland

* Correspondence: adam.derkowski@up.poznan.pl (A.D.); jakub.kawalerczyk@up.poznan.pl (J.K.)

Abstract: This research evaluated the possibility of using sawmill by-products from the roundwood-processing line in the production of wood-based panels. Due to its number of favorable properties, interesting chemical composition and large reserves resulting from the lack of industrial applications, the research focused particularly on the use of bark. Manufactured variants of boards differed in the proportions of wood chips to bark (70:30, 60:40, 50:50). Moreover, the boards containing only wood chips and a mixture of chips and sawdust were used as references. Urea-formaldehyde adhesive mixed with ammonium nitrate as a hardener was applied as a binding agent for the boards. Based on the mechanical properties (modulus of elasticity, modulus of rupture, internal bonding), physical properties (density, thickness swelling, water absorption) and content and emission of formaldehyde, it was found that it is possible to produce boards characterized by good properties from sawmill by-products without advanced processing. Moreover, the use of bark instead of sawdust in order to increase the homogeneity of the cross-section allows one to obtain panels with significantly lower formaldehyde emission and water uptake.

Keywords: bark; chipboard; sawdust; wood-based material; wood chips

Citation: Mirski, R.; Derkowski, A.; Kawalerczyk, J.; Dziurka, D.; Walkiewicz, J. The Possibility of Using Pine Bark Particles in the Chipboard Manufacturing Process. *Materials* **2022**, *15*, 5731. https://doi.org/10.3390/ma15165731

Academic Editor: Tomasz Sadowski

Received: 29 July 2022
Accepted: 17 August 2022
Published: 19 August 2022

1. Introduction

In the production of sawn timber in the sawmill industry, up to 50% of the wood raw material initially intended for the production is so-called material loss [1]. In addition to losses resulting from the desorption changes, very large amounts of residues, such as wood chips, sawdust and bark, are generated in the production process [2,3]. Management of these by-products poses a great challenge [4]. Both the growing issue of shortages of available wood and the appearing trend of maximized use of renewable resources are leading to a constant increase in the application of wood processing residues, e.g., in the production of wood-based materials [5–7].

This paper is a continuation of research aimed at improvements in manufacturing boards characterized by high thickness and made of wood chips produced in the sawmill industry without processing them into particles. Mirski et al. [1] investigated the possibility of using wood chips and sawdust from primary wood processing lines as a raw material for the production of boards. Research has shown that the single-layer boards must have a density of 50–100 kg/m^3 higher in order to reach appropriate mechanical properties required by the standards designed for particleboards as a result of using larger parties and obtaining an inhomogeneous cross-section. However, it was also found that the presence of outer layers (OL) made of microparticles resulted in a major improvement in the strength of the boards. The three-layer boards manufactured this way achieved properties roughly characteristic of P2-type boards. On the other hand, if the core layer (CL) was made of the mixture of chips and sawdust in a mass ratio of 70:30, the boards showed better properties compared to those produced only from the chips. According to the authors, sawdust filled the void spaces in the structure of the board and made it

more homogeneous. Furthermore, it was also found that the chipboards in general are characterized by higher thickness swelling compared to both unfinished and laminated commercially available particleboards. The reason may be the incorporation of various additives, such as paraffin emulsion, in the industrial wood-based materials production process, which are not introduced to chipboard [8]. Moreover, it was also found that the properties of chip-sawdust boards depend also on the structure of the cross-section: the mass ratio of the core layer to outer layers, the dimensional fraction of the microparticles in the outer layers and the share of sawdust in the inner layer. The highest result of bending strength and the lowest value of thickness swelling was obtained for boards with the mass ratio of 60:40 (CL:OL), and the strongest internal bonding was noted for a variant characterized by the mass ratio of 70:30 [9]. In addition, research conducted by Mirski et al. [10] also showed that the application of pMDI (polymeric methylenediphenyl-4,4′-diisocyanate) as a binding agent allows for the use of sawmill by-products with high moisture content: 21% in the case of wood chips and 18% in the case of sawdust.

The incorporation of bark particles in order to increase the homogeneity of the boards is an interesting concept. According to a paper published in 2017, the annual global amount of bark generated is estimated to be approximately 359,111,200 m^3 [11], and a major industrial use has still not been found. It is mainly used as a source of energy in the combustion process and in horticulture (it maintains the moisture and lowers the pH of the soil) [12,13]. According to Sahin and Arslan [14], however, the continuing research on using bark in wood-based materials' production can mitigate wood shortages. Bark particles were previously investigated for use as a filler for adhesives [15–18], as a substitute of wood particles in particleboard production [19–22], as a substitute for wood fibers [23] and as a basic material for decorative [24], sound-absorbing [25] and thermally insulating [11] panels. Research has shown that materials produced with the use of bark are characterized by good physical and mechanical properties. In this case, good properties mean the properties that they are comparable to those of panels made from raw materials usually intended for this purpose in industrial conditions (e.g., technical flour as a filler for adhesives or wood particles for the production of particleboards). Moreover, it was also found that they showed decreased formaldehyde emission. The reasons for the observed improvement include increased reactivity of adhesives due to the lowered pH, high content of phenolic substances that react with formaldehyde, etc.

Therefore, the aim of the study was to investigate the possibility of incorporating ground bark particles characterized by an interesting chemical composition and great availability in the production of boards made of pine wood chips.

2. Materials and Methods

2.1. Materials

Raw materials such as chips, sawdust and bark (Figure 1) were provided from the pine (*Pinus sylvestris* L.) roundwood processing line in the sawmill Koszalińskie Przedsiębiorstwo Przemysłu Drzewnego (KPPD) Szczecinek S.A (Kalisz Pomorski, Poland), one of the largest producers of sawn wood in Poland. Chips were sieved through the sieve with the dimensions of 50 mm × 50 mm. Bark obtained during debarking of logs was ground three times in a disc chipper to obtain smaller particles. Urea formaldehyde (UF) adhesive was applied as a binding agent. It was provided by the industrial manufacturer of wood-based boards, and it was characterized by the following properties: viscosity of 470 mPa × s, gel time at 100 °C of 88 s, solid content of 58% and pH of 8.11.

Figure 1. Materials used for the production of boards: (**a**) bark particles before grinding; (**b**) bark particles after grinding; (**c**) wood chips; (**d**) sawdust.

2.2. Characterization of the Materials

In order to characterize the dimensions of the chips, 250 of them were measured using a caliper with an accuracy of 0.1 mm to determine length, width and thickness (Table 1). The fractional compositions of ground bark particles and sawdust were determined on the basis of sieve analysis with flat sieves made of mesh with the square perforations of: 6.3, 5.0, 4.0, 2.5, 2.0, 1.4, 0.315 mm. The results of conducted analysis are presented in Figure 2.

Table 1. Dimensions of wood chips.

Material	Length (mm)			Width (mm)			Thickness (mm)		
	Mean	Min.	Max.	Mean	Min.	Max.	Mean	Min.	Max.
Wood chips	33.9 (6.3)	18.4	54.7	14.5 (4.2)	7.3	28.7	5.1 (1.3)	1.9	9.9

Note: values in parentheses mean standard deviations; min. means minimum value; max. means maximum value.

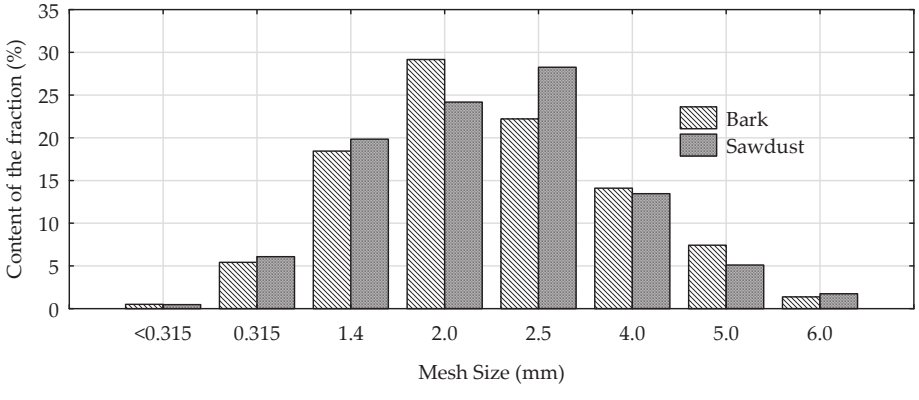

Figure 2. Fractional compositions of sawdust and bark.

Sawdust and bark (small particles) were characterized by very similar fractional compositions. The majority of the particles were in the range of 1.4 to 4.0 mm.

2.3. Materials' Preparation and Board Manufacturing

The steps of the board manufacturing process are presented in Figure 3. Materials were dried at 120 °C to reach a moisture content of 2 ± 2%. The gluing degree, which is a ratio of dry mass of the adhesive to the dry mass of lignocellulosic material, was 8% in the case of chips and 10% for sawdust and bark. An ammonium nitrate solution (20%) was introduced as a hardener to the gluing mixture to constitute 2% of the dry mass of the UF adhesive. The mat was formed manually. The hot pressing was conducted at 190 °C, with the unit pressure of 2.5 N/mm^2 for 20 s/mm of the final board thickness.

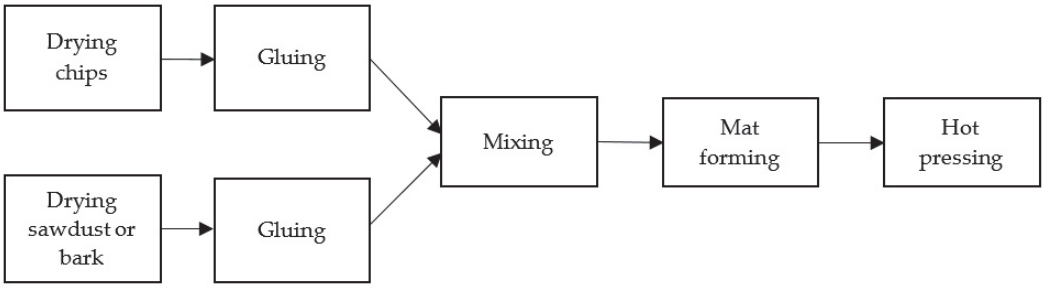

Figure 3. Schematic presentation of the board production process.

The compositions of variants of the manufactured boards with the assumed thickness of 20 mm and a density of 550 kg/m^3 are shown in Table 2.

Table 2. Variants of manufactured boards.

Variant Label	Share of Components in Boards (%)		
	Chips	Bark	Sawdust
A	70	30	0
B	60	40	0
C	50	50	0
D	70	0	30
E	100	0	0

2.4. Determination of Boards Properties

Both the physical and mechanical properties of boards were tested in accordance with the relevant standards. Density was evaluated according to EN 323 [26]. The modulus of elasticity (MOE) and modulus of rupture (MOR) were investigated according to EN 310 [27]. Internal bonding (IB) was determined following the assumptions of EN 319 [28]. Moreover, thickness swelling (TS) in accordance with EN 317 [29] and water absorption (WA) were investigated after 2 or 24 h of soaking in water. WA was calculated based on Equation (1):

$$WA = \frac{m_2 - m_1}{m_1} \times 100\% \quad (1)$$

where: m_1 and m_2 are the weights of sample before and after soaking, respectively.

The investigations of physical and mechanical properties of the board were performed on 12 samples from each variant. The formaldehyde content (CF) was determined using the perforator method according to EN 120 [30]. Furthermore, the formaldehyde emission (EF) was investigated with the use of gas chamber analysis in accordance with EN ISO 12460-3 [31] using a GreCon GA 6000 analyzer (Fagus-GreCon Greten GmbH & Co. KG., Alfeld, Germany) content of formaldehyde in an aqueous solution was determined by

spectrophotometry using the ammonium acetate and acetylacetone method. Absorbance of the samples was measured on a Biosens UV-5600 spectrophotometer (Biosens, Warsaw, Poland) at 412 nm. The results are expressed as the mean values of three replicates.

2.5. Statistical Analysis

The statistical analysis was performed with the use of STATISTICA 13.0 software. The differences between the variants were evaluated by one-way analysis of variance ANOVA followed by post hoc Tukey test with a significance level of $\alpha = 0.05$.

3. Results and Discussion

The density of the board is one of the main factors determining its properties. It is well known that usually as the density increases, the mechanical properties also improve. The results of the investigations are shown in Table 3.

Table 3. Density of manufactured boards.

Variant Label	Density of Boards (kg/m^3)		
	Mean	Min.	Max.
A	551 (12.6) b	538	565
B	548 (11.4) b	537	561
C	549 (10.6) b	538	560
D	552 (11.1) b	541	563
E	531 (10.3) a	516	551

Note: Values in parentheses mean standard deviations; min. means minimum value; max. means maximum value; letters a,b indicate the homogeneous groups.

The outcomes of statistical analysis show that there was a significant difference between the variants consisting of both wood chips and smaller particles and the variant made of only wood chips. Without the addition of bark or sawdust, boards were characterized by a density lower by approximately 20 kg/m^3 (4%) than initially assumed. This was probably due to the void spaces in the board structure that were created between the chips. Their occurrence can be observed in Figure 4. However, both the amount of small particles and their type did not influence the results of density in a statistically significant way. The obtained values are very close to the assumed ones. In addition to affecting the density results, the presence of voids is disadvantageous because it can adversely affect the mechanical properties and water uptake of boards, and their degradation by microorganisms.

(**a**) (**b**) (**c**)

Figure 4. Cross-sections of the boards: (**a**) with bark particles (variant A); (**b**) with sawdust (variant D); (**c**) only with wood chips (variant E) (dashed circles indicate filled spaces; solid circles indicate void spaces).

Results of the modulus of elasticity investigations are presented in Figure 5. Based on the outcomes, it was found that the highest MOE values were obtained for variants containing 30% small particles. In this case, the type of particles, whether they were bark or sawdust, did not have any statistically significant effect. The values were higher by approximately 17% in comparison with the boards consisting of only wood chips. A further increase in the amount of added small particles to 40% also resulted in the results of

MOE being improved by 10% when compared with the chipboard. However, the poorest properties were observed when the share of bark increased to 50%. In this case, the MOE was 14% lower than in the case of the reference variant. Statistical analysis of the modulus of rupture results (Figure 6) showed exactly the same tendency as described for MOE. The best results were obtained for variants labeled as A and D with 30% filling particles incorporated to the manufacturing process. On the other hand, the lowest MOR was noted for boards containing a mixture of bark and wood chips at a weight ratio of 50:50. For the most advantageous variants, the results were higher by up to 35% than in the case of boards made of only wood chips. The worst variant, on the other hand, reached average values that were lower by 23%. The results of internal bonding were also in agreement with the previously described tendencies. The most favorable values noted were 38% higher than those of the reference boards with an inhomogeneous cross-section. When the share of bark was 50%, the results decreased significantly, by 18% (Figure 7).

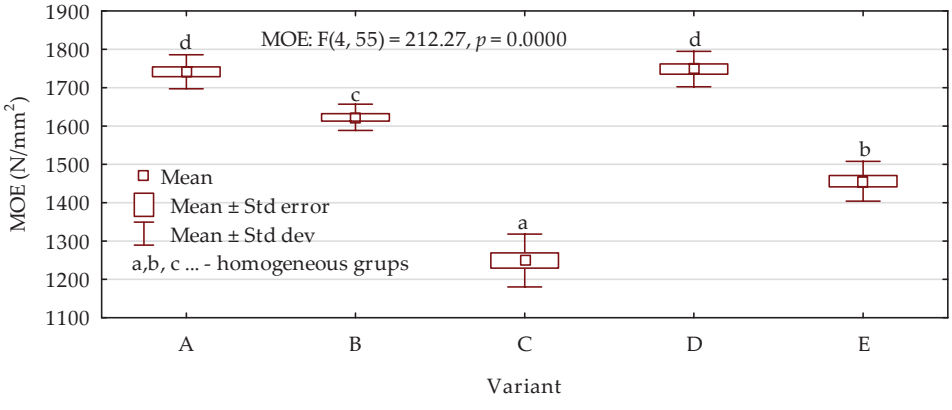

Figure 5. Modulus of elasticity results depending on the board variant (letters A–E mark variants of the boards).

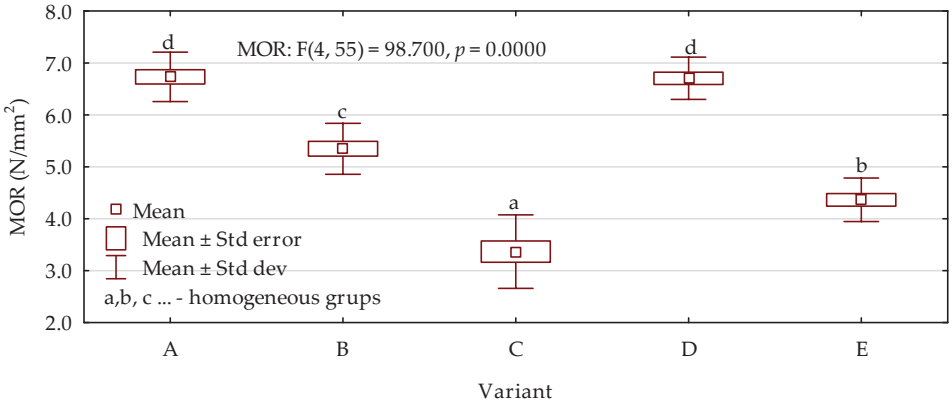

Figure 6. Modulus of rupture results depending on the board variant (letters A–E mark variants of the boards).

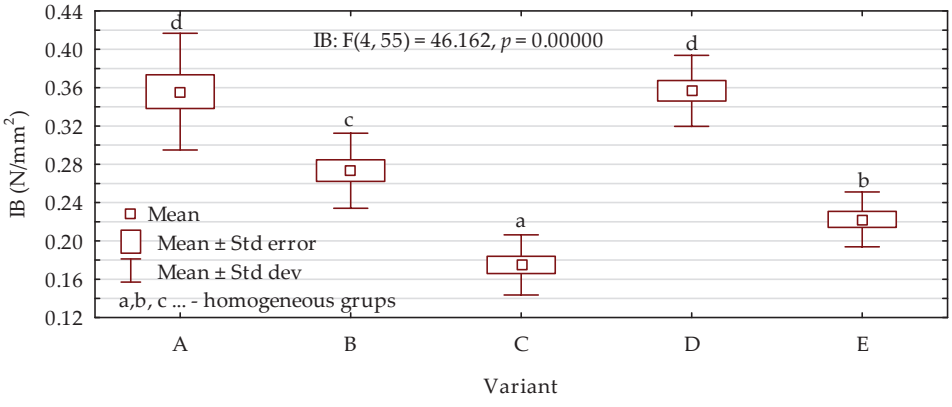

Figure 7. Internal bonding results depending on the board variant (letters A–E mark variants of the boards).

Based on the outcomes of mechanical properties, it was found that mixing the wood chips with bark or sawdust in a weight ratio of 70:30 led to the production of boards with the best properties. This confirms the previous observations that the homogeneity of the cross-section considerably affects the strength parameters of boards [9]. The elimination of void spaces contributes to a more favorable distribution of stresses [32]. Moreover, the deterioration in mechanical properties of boards, which occurred in the variant assuming a 50% share of bark, could have result from its chemical composition. It is characterized by a significantly lower cellulose content than wood [33]. According to Baharoglu et al. [34], the use of lignocellulosic materials with lower cellulose contents can result in the manufacturing of boards characterized by lower strength parameters. Moreover, bark also contains a large amount of extractives. According to literature, it can also negatively affect the strength of glue bonds, which consequently could also influence the mechanical properties of the resultant boards [35,36].

Based on parameters such as thickness swelling and water absorption, the water resistance of boards was determined. The results are presented in Table 4.

Table 4. Thickness swelling and water absorption of boards depending on the variant.

Variant Label	Thickness Swelling (%)		Water Absorption (%)	
	2 h	24 h	2 h	24 h
A	16.3 (0.6) b	18.9 (0.4) b	92.9 (0.8) b	93.7 (0.6) b
B	15.7 (0.9) ab	18.5 (0.7) ab	91.7 (0.9) ab	92.9 (0.7) ab
C	15.9 (1.1) ab	18.4 (0.9) ab	91.3 (1.3) ab	93.2 (1.1) ab
D	17.2 (0.4) c	19.8 (0.6) c	94.6 (0.6) c	95.9 (1.0) c
E	15.2 (0.7) a	17.6 (0.6) a	87.5 (2.4) a	91.2 (1.3) a

Note: Values in parentheses mean standard deviations; letters a,b,c indicate the homogeneous groups.

The highest resistance was observed in the case of the chipboard manufactured without the addition of any smaller particles, and this was probably a result of lower density. However, the statistical analysis showed that the boards containing 40% and 50% bark were characterized by the same level of resistance. The reason for no statistically significant changes was probably the increase in the share of glue in the board (small particles had a higher gluing degree), which could have decreased the water uptake. The statistical analysis also showed that in the case of variants containing the same amounts of smaller particles (30%), boards produced with the use of bark were more resistant to water than sawdust-containing ones. This was probably the chemical composition of the material. Wood contains much a greater amount of holocellulose when compared to bark [33].

According to Baharoglu et al. [34], an increase in the share of hydrophilic components leads to increases in thickness swelling and water absorption of the boards. Moreover, the observed values were higher than the ones observed in previous studies regarding chipboard manufacturing [9]. Considering that the strength of the glue joints is one of the crucial factors affecting the water resistance of boards, the reason could be the binding agent used [37]. UF resin is characterized by a significantly lower resistance to water in comparison with the previously applied melamine-urea-formaldehyde (MUF) resin [38].

The emission of formaldehyde from UF resin-bonded wood-based materials has become a widely investigated problem. It is a highly reactive, colorless gas which can be responsible for serious human harm, especially in indoor environments. Formaldehyde has been classified by the International Agency for Research on Cancer as a "known human carcinogen," and since then, the level of permissible emission has been gradually lowered [39,40]. Therefore, there are many ongoing studies focused on the reduction or even elimination of formaldehyde use in adhesives [41]. The results of investigations performed with the use of the perforator method and gas chamber analysis are presented in Table 5.

Table 5. Formaldehyde emission and content depending on the variant.

Variant Label	Formaldehyde Content (mg/100 g)	Formaldehyde Emission (mg/m^2 h)
A	3.3 (0.3) a	2.1 (0.3) a
B	5.1 (0.2) c	4.6 (0.3) c
C	5.4 (0.3) c	4.4 (0.2) c
D	4.3 (0.2) b	3.1 (0.3) b
E	3.1 (0.4) a	2.3 (0.2) a

Note: Values in parentheses mean standard deviations; letters a,b,c indicate the homogeneous groups.

Regardless of the method by which the analysis was carried out, the results showed the same trend. The lowest CF and EF were observed for variants made of only wood chips and chips mixed with bark in the ratio 70:30. Between them, no statistically significant difference was noted. However, it seems that the type of small particles affected the results. When comparing the boards containing the same amounts of wood (D) and bark (A), it was found that the use of bark reduced both the emission and content of formaldehyde. The reason was probably its chemical composition, especially the contents of tannins and phenolic compounds [20]. The majority of these substances are characterized by the ability to react with formaldehyde [42,43]. A similar effect was observed in the experiments regarding the use of bark as a filler for adhesives [15,17,18,33] and as a substitute for wood particles in boards [20,24]. Moreover, it was also found that bark has the ability to absorb formaldehyde from an aqueous solution [16] and from contaminated air [44]. However, a further increase in the share of bark particles to 40 or 50% resulted in a statistically significant increase in the formaldehyde emission. The reason was probably the higher gluing degree of smaller particles, and consequently, the higher amount of UF adhesive, which still remained the main source of formaldehyde in the boards.

4. Conclusions

The wastes from the sawmill industry, such as chips, sawdust and bark, can be used as the materials for the production of boards characterized by good mechanical and physical properties. However, the application of UF resin instead of MUF resin for boards made of sawmill by-products results in significant increases in their thickness swelling and water absorption. Furthermore, their properties strongly depend on the proportions of individual components. The most advantageous properties were observed for variants consisting of a mixture of wood chips and smaller particles (sawdust or bark) in a weight ratio of 70:30 due to the homogeneous structure of boards. Moreover, the replacement of sawdust with bark allows one to produce materials with equally good mechanical properties, lower water uptake and decreased formaldehyde content and emission. A potential limitation

that will be the subject of further research is the variability of the chemical composition of the bark. The variability of the results depending on the species, habitat, age, size and quality of the barked log will be examined.

Author Contributions: Conceptualization, J.K., A.D. and D.D.; methodology, J.K. and R.M.; software, R.M., A.D. and J.W.; validation, R.M., J.W. and A.D.; formal analysis, A.D., R.M. and D.D.; investigation, J.K., A.D. and D.D.; resources, R.M. and D.D.; data curation, A.D., R.M. and J.K.; writing—original draft preparation, J.K. and A.D.; writing—review and editing, J.K. and D.D.; visualization, R.M. and J.W.; supervision, R.M. and D.D.; project administration, R.M.; funding acquisition, R.M. All authors have read and agreed to the published version of the manuscript.

Funding: This research was funded by the National Centre for Research and Development, BIOSTRATEG3/344303/14/NCBR/2018. The study was also supported by funding for statutory R&D activities as research task number 506.224.02.00 of the Faculty of Forestry and Wood Technology, Poznan University of Life Sciences. The article was co-financed within the Ministry of Science and Higher Education Programme—"Regional Initiative Excellence" 2019–2022, project number 005/RID/2018/19.

Institutional Review Board Statement: Not applicable.

Informed Consent Statement: Not applicable.

Data Availability Statement: The data presented in this study are available on request from the corresponding author.

Acknowledgments: Authors would like to thank Jakub Guziak for his help in preparing the materials.

Conflicts of Interest: The authors declare no conflict of interest.

References

1. Mirski, R.; Derkowski, A.; Dziurka, D.; Dukarska, D.; Czarnecki, R. Effects of a Chipboard Structure on Its Physical and Mechanical Properties. *Materials* **2019**, *12*, 3777. [CrossRef]
2. Ratajczak, E.; Szostak, A.; Bidzinska, G.; Leszczyszyn, E. Market in Wood By-Products in Poland and Their Flows in the Wood Sector. *Drewno Prace Naukowe Doniesienia Komunikaty* **2018**, *61*. [CrossRef]
3. Wieruszewski, M.; Mikołajczak, E. The Influence of Selected Factors on the Share of By-Products in Sawmill Processing. *Ann. Wars. Univ. Life Sci. SGGW. For. Wood Technol.* **2018**, *104*, 540–548.
4. Fregoso-Madueño, J.N.; Goche-Télles, J.R.; Rutiaga-Quiñones, J.G.; González-Laredo, R.F.; Bocanegra-Salazar, M.; Chávez-Simental, J.A. Alternative Uses of Sawmill Industry Waste. *Revista Chapingo Serie Ciencias Forestales y del Ambiente* **2017**, *23*, 243–260. [CrossRef]
5. Wieruszewski, M.; Górna, A.; Mydlarz, K.; Adamowicz, K. Wood Biomass Resources in Poland Depending on Forest Structure and Industrial Processing of Wood Raw Material. *Energies* **2022**, *15*, 4897. [CrossRef]
6. Simal Alves, L.; da Silva, S.A.M.; dos Anjos Azambuja, M.; Varanda, L.D.; Christóforo, A.L.; Lahr, F.A.R. Particleboard Produced with Sawmill Waste of Different Wood Species. In *Advanced Materials Research*; Trans Tech Publications Ltd.: Stäfa, Switzerland, 2014; Volume 884, pp. 689–693.
7. Saal, U.; Weimar, H.; Mantau, U. Wood Processing Residues. *Biorefineries* **2017**, *166*, 27–41.
8. Mirski, R.; Kawalerczyk, J.; Dziurka, D. Properties of particleboards intended for the production of countertops. In Proceedings of the Network for Wood Science and Engineering, Tallin, Estonia, 2–3 October 2018.
9. Mirski, R.; Dukarska, D.; Derkowski, A.; Czarnecki, R.; Dziurka, D. By-Products of Sawmill Industry as Raw Materials for Manufacture of Chip-Sawdust Boards. *J. Build. Eng.* **2020**, *32*, 101460. [CrossRef]
10. Mirski, R.; Derkowski, A.; Dziurka, D.; Wieruszewski, M.; Dukarska, D. Effects of Chip Type on the Properties of Chip–Sawdust Boards Glued with Polymeric Diphenyl Methane Diisocyanate. *Materials* **2020**, *13*, 1329. [CrossRef]
11. Pásztory, Z.; Mohácsiné, I.R.; Börcsök, Z. Investigation of Thermal Insulation Panels Made of Black Locust Tree Bark. *Constr. Build. Mater.* **2017**, *147*, 733–735. [CrossRef]
12. Szwajkowska-Michalek, L.; Rogozinski, T.; Stuper-Szablewska, K. Zawartość Steroli w Korze Po Procesie Wysokotemperaturowego Suszenia Tarcicy w Komorowych Suszarkach Konwekcyjnych. *Sylwan* **2019**, *163*, 610–616. [CrossRef]
13. Kawalerczyk, J.; Siuda, J.; Kuliński, M.; Dziurka, D.; Mirski, R. Wykorzystanie Kory Jako Wypełniacza Żywic w Produkcji Sklejki. *Biuletyn Informacyjny Ośrodka Badawczo-Rozwojowego Przemysłu Płyt Drewnopochodnych w Czarnej Wodzie* **2020**, *61*, 188–197. [CrossRef]
14. Turgut Sahin, H.; Burak Arslan, M. Weathering Performance of Particleboards Manufactured from Blends of Forest Residues with Red Pine (*Pinus brutia*) Wood. *Maderas Ciencia y Tecnología* **2011**, *13*, 337–346. [CrossRef]

15. Mirski, R.; Kawalerczyk, J.; Dziurka, D.; Wieruszewski, M.; Trociński, A. Effects of Using Bark Particles with Various Dimensions as a Filler for Urea-Formaldehyde Resin in Plywood. *BioResources* **2020**, *15*, 1692–1701.
16. Bekhta, P.; Sedliačik, J.; Noshchenko, G.; Kačík, F.; Bekhta, N. Characteristics of Beech Bark and Its Effect on Properties of UF Adhesive and on Bonding Strength and Formaldehyde Emission of Plywood Panels. *Eur. J. Wood Wood Prod.* **2021**, *79*, 423–433. [CrossRef]
17. Réh, R.; Krišťák, Ľ.; Sedliačik, J.; Bekhta, P.; Božiková, M.; Kunecová, D.; Vozárová, V.; Tudor, E.M.; Antov, P.; Savov, V. Utilization of Birch Bark as an Eco-Friendly Filler in Urea-Formaldehyde Adhesives for Plywood Manufacturing. *Polymers* **2021**, *13*, 511. [CrossRef]
18. Réh, R.; Igaz, R.; Krišťák, Ľ.; Ružiak, I.; Gajtanska, M.; Božíková, M.; Kučerka, M. Functionality of Beech Bark in Adhesive Mixtures Used in Plywood and Its Effect on the Stability Associated with Material Systems. *Materials* **2019**, *12*, 1298. [CrossRef]
19. Blanchet, P.; Cloutier, A.; Riedl, B. Particleboard Made from Hammer Milled Black Spruce Bark Residues. *Wood Sci. Technol.* **2000**, *34*, 11–19. [CrossRef]
20. Medved, S.; Gajsek, U.; Tudor, E.M.; Barbu, M.C.; Antonovic, A. Efficiency of Bark for Reduction of Formaldehyde Emission from Particleboards. *Wood Res.* **2019**, *64*, 307–315.
21. Mahieu, A.; Alix, S.; Leblanc, N. Properties of Particleboards Made of Agricultural By-Products with a Classical Binder or Self-Bound. *Ind. Crops Prod.* **2019**, *130*, 371–379. [CrossRef]
22. Pasztory, Z.; Mohácsiné, I.R.; Gorbacheva, G.; Börcsök, Z. The Utilization of Tree Bark. *BioResources* **2016**, *11*, 7859–7888. [CrossRef]
23. Pedieu, R.; Riedl, B.; Pichette, A. Properties of Mixed Particleboards Based on White Birch (Betula Papyrifera) Inner Bark Particles and Reinforced with Wood Fibres. *Eur. J. Wood Wood Prod.* **2009**, *67*, 95–101. [CrossRef]
24. Tudor, E.M.; Barbu, M.C.; Petutschnigg, A.; Réh, R.; Krišťák, Ľ. Analysis of Larch-Bark Capacity for Formaldehyde Removal in Wood Adhesives. *Int. J. Environ. Res. Public Health* **2020**, *17*, 764. [CrossRef]
25. Tudor, E.M.; Dettendorfer, A.; Kain, G.; Barbu, M.C.; Réh, R.; Krišťák, Ľ. Sound-Absorption Coefficient of Bark-Based Insulation Panels. *Polymers* **2020**, *12*, 1012. [CrossRef]
26. *EN 323*; Wood-Based Panels-Determination of Density. European Committee for Standardization: Brussels, Belgium, 2001.
27. *EN 310*; Wood-Based Panels-Determination of Modulus of Elasticity in Bending and of Bending Strength. European Committee for Standardization: Brussels, Belgium, 1999.
28. *EN 319*; Particleboards and Fibreboards—Determination of Tensile Strength Perpendicular to the Plane of the Board. European Committee for Standardization: Brussels, Belgium, 1993.
29. *EN 317*; Particleboards and Fibreboards–Determination of Swelling in Thickness after Immersion in Water. European Committee for Standardization: Brussels, Belgium, 1998.
30. *EN 120*; Wood-Based Panels-Determination of Formaldehyde Release-Extraction Method (Called Perforator Method). CEN, European Committee for Standardization: Brusseles, Belgium, 2011.
31. *ISO 12460-3*; Wood-Based Panels—Determination of Formaldehyde Release—Part 3: Gas Analysis Method. International Organization for Standardization: Geneva, Switzerland, 2020.
32. Medved, S.; Resnik, J. Influence of Beech Particle Size Used in Surface Layer on Bending Strength of Three-Layer Particleboard. *Zbornik Gozdarstva in Lesarstva* **2003**, *72*, 197–207.
33. Mirski, R.; Kawalerczyk, J.; Dziurka, D.; Siuda, J.; Wieruszewski, M. The Application of Oak Bark Powder as a Filler for Melamine-Urea-Formaldehyde Adhesive in Plywood Manufacturing. *Forests* **2020**, *11*, 1249. [CrossRef]
34. Baharoğlu, M.; Nemli, G.; Sarı, B.; Birtürk, T.; Bardak, S. Effects of Anatomical and Chemical Properties of Wood on the Quality of Particleboard. *Compos. Part B Eng.* **2013**, *52*, 282–285. [CrossRef]
35. Hänsel, A.; Sandak, J.; Sandak, A.; Mai, J.; Niemz, P. Selected Previous Findings on the Factors Influencing the Gluing Quality of Solid Wood Products in Timber Construction and Possible Developments: A Review. *Wood Mater. Sci. Eng.* **2022**, *17*, 230–241. [CrossRef]
36. Hse, C.-Y.; Kuo, M. Influence of Extractives on Wood Gluing and Finishing-a Review. *For. Prod. J.* **1988**, *381*, 52–56.
37. Medved, S.; Antonović, A.; Jambreković, V. Impact of Resin Content on Swelling Pressure of Three Layer Particleboard Bonded with Urea-Formaldehyde Adhesive. *Drvna Industrija* **2011**, *62*, 37–42. [CrossRef]
38. Prestifilippo, M.; Pizzi, A.; Norback, H.; Lavisci, P. Low Addition of Melamine Salts for Improved UF Adhesives Water Resistance. *Holz als Roh- und Werkstoff* **1996**, *54*, 393–398. [CrossRef]
39. Antov, P.; Savov, V.; Neykov, N. Reduction of Formaldehyde Emission from Engineered Wood Panels by Formaldehyde Scavengers—A Review. In Proceedings of the 13th International Scientific Conference Wood EMA 2020 and 31st International Scientific Conference ICWST, Vinkovci, Croatia, 28–30 September 2020.
40. Kristak, L.; Antov, P.; Bekhta, P.; Lubis, M.A.R.; Iswanto, A.H.; Reh, R.; Sedliacik, J.; Savov, V.; Taghiyari, H.R.; Papadopoulos, A.N. Recent Progress in Ultra-Low Formaldehyde Emitting Adhesive Systems and Formaldehyde Scavengers in Wood-Based Panels: A Review. *Wood Mater. Sci. Eng.* **2022**, 1–20. [CrossRef]
41. Gumowska, A.; Kowaluk, G.; Labidi, J.; Robles, E. Barrier Properties of Cellulose Nanofiber Film as an External Layer of Particleboard. *Clean Technol. Environ. Policy* **2019**, *21*, 2073–2079. [CrossRef]
42. Jahanshaei, S.; Tabarsa, T.; Asghari, J. Eco-friendly Tannin-phenol Formaldehyde Resin for Producing Wood Composites. *Pigment Resin Technol.* **2012**, *41*, 296–301. [CrossRef]

43. Tanase, C.; Mocan, A.; Coșarcă, S.; Gavan, A.; Nicolescu, A.; Gheldiu, A.-M.; Vodnar, D.C.; Muntean, D.-L.; Crișan, O. Biological and Chemical Insights of Beech (*Fagus Sylvatica* L.) Bark: A Source of Bioactive Compounds with Functional Properties. *Antioxidants* **2019**, *8*, 417. [CrossRef]
44. Pásztory, Z.; Halász, K.; Börcsök, Z. Formaldehyde Adsorption–Desorption of Poplar Bark. *Bull. Environ. Contam. Toxicol.* **2019**, *103*, 745–749. [CrossRef]

materials

MDPI

Article

The Application of Various Bark Species as a Fillers for UF Resin in Plywood Manufacturing

Joanna Walkiewicz *, Jakub Kawalerczyk, Radosław Mirski, Dorota Dziurka and Marek Wieruszewski

Department of Mechanical Wood Technology, Faculty of Forestry and Wood Technology, Poznań University of Life Sciences, Wojska Polskiego 38/42, 60-627 Poznań, Poland
* Correspondence: joanna.walkiewicz@up.poznan.pl

Abstract: The aim of the presented study was to apply various bark species (birch, beech, maple, pine and spruce) as fillers for urea-formaldehyde (UF) resin in three-layer plywood manufacturing. For this purpose, all types of bark were ground and added to the adhesive mixture. The resultant plywood was subjected to investigations of the following: tensile strength, modulus of elasticity (MOE), bending strength (MOR) and formaldehyde emission. The results indicate a reduction in the tensile strength. Moreover, the lack of significant improvement in strength parameters can be explained by too high a load of the filler (20 wt%). In the case of formaldehyde emissions, a reduction was observed for birch (B-1), beech (B-2), maple (B-3) and pine bark (B-4). In addition, an increase in the emission of formaldehyde was recorded only for spruce bark.

Keywords: bark; filler; formaldehyde emission; mechanical properties; UF resin; plywood; wood-base materials

Citation: Walkiewicz, J.; Kawalerczyk, J.; Mirski, R.; Dziurka, D.; Wieruszewski, M. The Application of Various Bark Species as a Fillers for UF Resin in Plywood Manufacturing. *Materials* **2022**, *15*, 7201. https://doi.org/10.3390/ma15207201

Academic Editor: Federica Bondioli

Received: 24 August 2022
Accepted: 12 October 2022
Published: 15 October 2022

Publisher's Note: MDPI stays neutral with regard to jurisdictional claims in published maps and institutional affiliations.

1. Introduction

The adhesive mixtures used for the production of plywood usually contain some additives called fillers [1]. Their role is usually to adjust the rheological properties of the resin in order to reduce the cost of the raw material and improve the properties of the resultant panels, for example, by causing a reduction in formaldehyde emission [2–4].

Current trends focus on the use of most industry by-products. Following this tendency, it is worth emphasizing that the wood industry generates huge amounts of by-products, such as bark, sawdust and dust [5]. Annual global bark production is estimated to be 359,111,200 m^3 [6], which makes it an excellent raw material that can be used in several ways. Generally, bark is used in horticulture as a mulch [7] or is considered a natural source of chemicals [8].

Due to the chemical composition of bark and the presence of numerous organic compounds, such as tannins, catechins, galocatechins, falwonoids, proanthocyaninidins, it can be used as a potential formaldehyde-scavenging filler in the production of plywood. The chemical compounds of bark, such as lignin or tannins, seem to be able to react with formaldehyde. This phenomenon may reduce the toxic effects of formaldehyde on humans by reducing hazardous emissions occurring in the indoor environments [9–12].

Formaldehyde is the simplest aldehyde, and it is widely used in the synthesis of the resins. Unfortunately, it is a harmful compound with a known carcinogenic effect. Studies on the reduction in formaldehyde emissions through the use of various types of fillers are continuously being conducted globally [1,13–19].

Therefore, it is worth looking at bark as a natural filler with a formaldehyde bonding ability. The use of bark can therefore contribute to a reduction in formaldehyde emissions from wood-based materials such as plywood. Currently, a lot of scientific research is focusing on the possibility of producing environmentally friendly materials. There are already existing scientific references from the literature regarding the use of larch bark to reduce formaldehyde emissions from decorative boards [20]. Moreover, Medved et al. [21]

conducted studies showing that the bark of spruce and pine can be used as a substitute for wooden particles in the production of particleboard. Research on the use of the bark was also conducted by Sahin and Arslan [22], Réh et al. [23], Ružiak et al. [24]. The results of these studies also indicate that the bark species could have a significant impact on the effectiveness of reducing formaldehyde emissions.

There are many issues associated with the production of plywood that are constantly being researched. Formaldehyde emissions are a very important aspect; however, mechanical properties should also be considered as crucial for potential applications. Aydin et al. [25] reported that an amount of bark higher than 12.25% has a negative influence on formaldehyde release, thickness swelling, and mechanical strength, whereas research conducted by Mirski et al. [14] showed that the addition of oak bark at a concentration of 15% made it possible to produce plywood panels characterized by reduced formaldehyde release and improved bonding quality, which is the main goal when establishing the potential industrial application. Another important aspect is the influence of the particle size on the parameters of the produced plywood. Different sizes of particles were previously tested, and it was found that the dimensional fraction of 0.315 mm showed the best result [26]. Furthermore, the increase in bending strength and Young's modules of elasticity was observed when 15% of beech bark was added to a urea–formaldehyde adhesive [24].

The aim of the study was to use the selected, various bark species commonly processed in Polish sawmills that were not studied before as fillers for UF resin in plywood manufacturing.

2. Materials and Methods

2.1. Materials

Plywood was produced using rotary cut birch veneer sheets with dimensions of 320 × 320 mm, moisture content of 6% ± 1%, and average thickness of 1.5 mm. An industrial UF resin with the following characteristics was used: pH 9.5 to 10.7, solids content of 64 to 69%, and gel time at 100 °C of 63 s. Ammonium nitrate (20 wt%) was introduced to the adhesive mixture as a hardener. The rye flour and bark powders differing in species were used as a fillers. For this purpose, birch (*Betula* L.), beech (*Fagus* L.), maple (*Acer* L.) pine (*Pinus* L.) and spruce (*Picea* A. Dietr.) bark particles were ground to obtain a fraction of 0.315–0.4 mm. Moisture content of added bark was ~9.0 %. The compositions and pH of adhesive mixtures are presented in Table 1.

Table 1. Compositions of adhesive mixtures with various type of bark particle.

Variant Label	Type of Filler	Quantity (pwb Per 100 pwb of Solid Resin)		pH
		Filler	Hardener Solution	
REF	Rye flour	20	2	6.88
B-1	Birch bark	20	2	6.57
B-2	Beech bark	20	2	6.50
B-3	Maple bark	20	2	6.89
B-4	Pine bark	20	2	6.21
B-5	Spruce bark	20	2	6.26

Note: pbw means parts by weight.

2.2. Methods

The plywood panels were manufactured in the three-layer system. The adhesives mixtures were spread on the surface of veneer sheets in the amount of 170 g/m^2. The pressing parameters, such as temperature, unit pressure and time were 120 °C, 1.4 MPa and 4 min, respectively. The moisture content of manufactured plywood was determined according to EN 322 [27]. The thickness, density and moisture content of produced plywood are given in Table 2.

The manufactured plywood were subjected to an evaluation in terms of mechanical properties, including bonding quality according to EN 314-1 (2004) [28] after soaking (10 repetitions) and modulus of elasticity (MOE) and bending strength (MOR) in a per-

pendicular and parallel direction to the grains of the face veneer layer (12 repetitions), according to EN 310 [29]. The results were subjected to a statistical analysis using HSD Tukey test on the significance level of $\alpha = 0.05$ with Statistica 13.0 software (StatSoft Inc., Tulsa, OK, USA).

Table 2. Parameters of manufactured plywood.

Variant Label	Density [kg/m^3]	Moisture Content [%]	Thickness [mm]
REF	626	5.0	3.98
B-1	689	5.1	4.04
B-2	679	5.2	4.16
B-3	698	4.8	3.95
B-4	643	4.6	3.94
B-5	602	5.2	3.92

Moreover, formaldehyde emissions were also determined. For this purpose, plywood samples were tested using a flask method in accordance with PN EN 717-3 [30] (2 repetitions).

SEM pictures were taken with a Hitachi SU 3500 Electron Microscope (Hitachi, Japan) under high-vacuum conditions. The plywood samples were covered with gold. Au sputtering was performed with a Cressington Sputter Coater 108 auto sputtering machine (Ted Pella, Redding, CA, USA).

3. Results

3.1. Tensile Strength

The changes in tensile strength depending on the resin formulation are presented in Figure 1. As can be seen, all variants (control and plywood with bark particles) fulfilled the standard requirements for tensile strength (values exceeded 1 N/mm^2). Moreover, a statistical analysis was carried out and homogeneous groups were distinguished. They are marked with letters above the bars. The highest values were obtained for both the control variant and maple-bark-containing one. Between them, no statistically significant differences were observed. This means that the addition of maple bark to the UF resin gave comparable results with the control variant. The lowest tensile strength value was shown by variant B-5; however, there are no statistical differences between this variant and variants B-1, B-2 and B-4. Similar results, where a reduction in tensile strength was observed due to the addition of the bark, were presented by Aydin et al. [25].

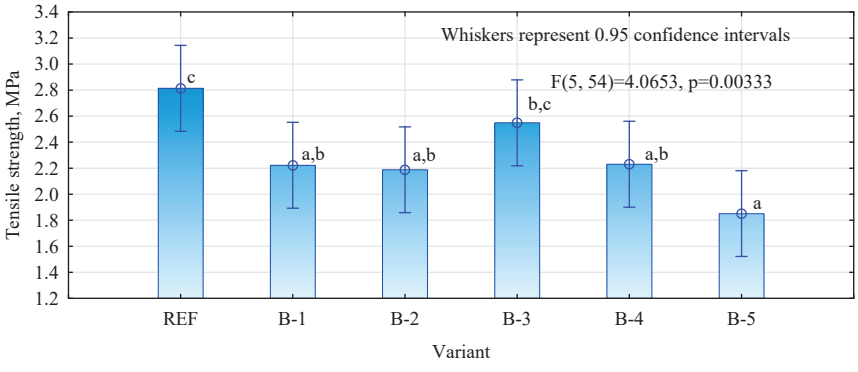

Figure 1. The changes in tensile strength of the produced plywood with bark: (B-1), beech (B-2), maple (B-3) and pine bark (B-4), spruce(B-5) and reference sample (REF). The lowercase letters means homogeneous groups.

This phenomenon can be explained by the pH of the environment and its effect on the adhesive curing process. Elbadawi et al. [31] reported that the curing rates of formaldehyde-

based resins are strongly dependent on the pH of the curing environment. According to Xing et al. [32], when the pH rises above 7 the reactivity of adhesive considerably slows down and it affects bonding strength. On the other hand, if the pH is too low then a pre-curing process may occur. They also observed that as the content of tannins increased (which are included in bark composition), the mechanical properties of the produced panels decreased. Furthermore, the similar results were also observed by Nemli et al. [33]. The phenomenon of lowering tensile strength can be explained by the presence of tannins, which affect the resin curing process. If there is a too major a decrease in the pH, it can lead to the pre-curing of the adhesives before pressing, and thus it can cause a deterioration in the properties of boards [25,31].

3.2. Modulus of Elasticity (MOE) and Bending Strength (MOR)

The MOR and MOE parameters were tested in two directions (longitudinal and perpendicular) (Figures 2 and 3). In the case of the perpendicular direction, the statistically significant differences were observed between the individual variants (Figure 2). The results of the B-1, B-3 and B-4 variants, assuming the use of birch, maple and pine bark as fillers, are similar to the control sample (no statistically significant differences were observed). In the case of the B-5 samples, where spruce bark was applied, a significant decrease in MOR was observed when compared to the flour-filled samples. In the case of MOE, studies showed that, in the case of the variants REF, B-1, B-2, B-3 and B-4, no statistically significant differences were observed. However, as in the case of MOR, variant B-5 showed a significant deterioration.

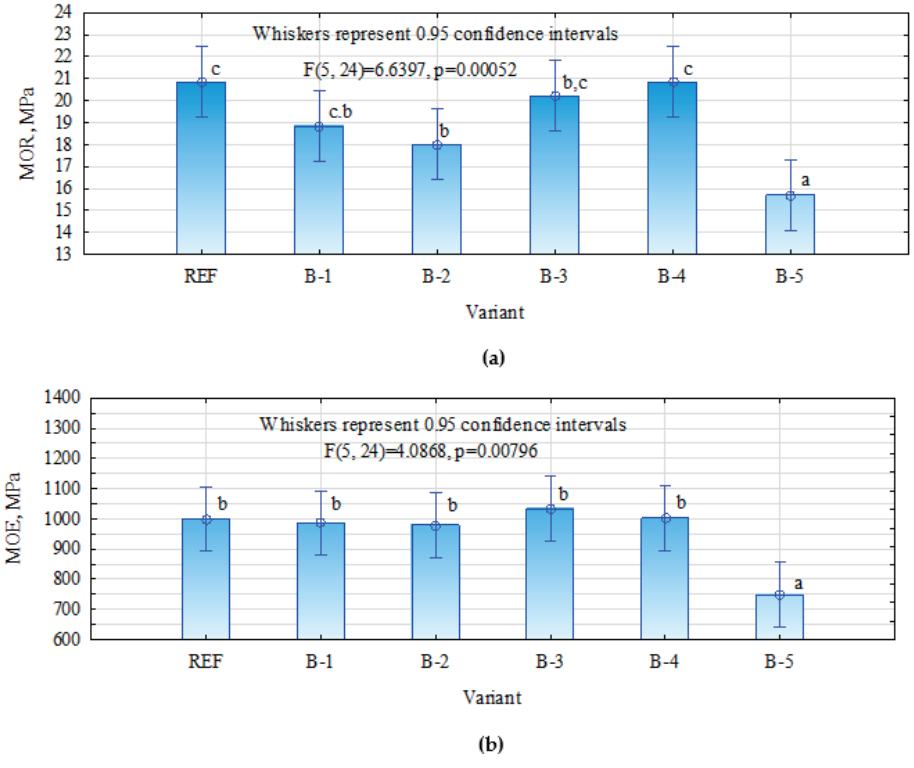

Figure 2. The results of MOR (**a**) and MOE (**b**) tests in perpendicular direction. The lowercase letters means homogeneous groups.

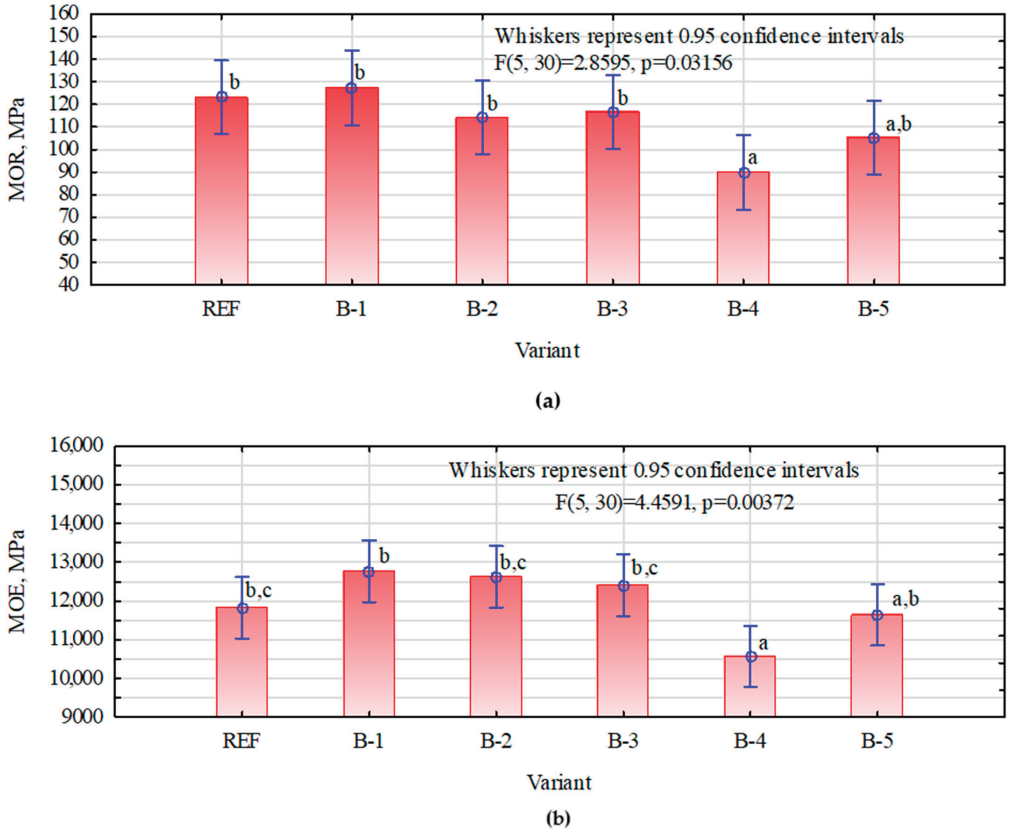

Figure 3. The results of MOR (**a**) and MOE (**b**) tests in longitudinal direction. The lowercase letters means homogeneous groups.

The lack of significant improvement in strength parameters—and in the case of the B-5 variant, their significant reduction—can be explained by too high a proportion of the filler used. According to the literature, an addition of more than 15% significantly increases the viscosity of the resin [23,24,34]. Réh et al. [35] also observed that the addition of 20% (based on the dry weight of the resin) of bark particles increases the viscosity of the resin. This can result in an uneven application of glue.

Another important aspect is the presence of tannins and lignin in the bark, which influences the properties of the resin. Various explanations can be found in the literature, which still remain inconclusive. On the one hand, a high proportion of these compounds can lead to an improvement in mechanical properties [35]. On the other hand, in some cases, a high proportion of these compounds affects their reactivity, which leads to a rapid increase in viscosity, which in turn translates into a short resin pot life and affects intermolecular cross-linking [36,37]. The observations of Nemli et al. [33] confirm that, in this case, the MOE results can be lowered.

Figure 3 presents the results of MOE and MOR in the longitudinal direction. It was observed that MOR parameters for the variants REF, B-1, B-2 and B-3 were at a similar level, and there were no statistically significant differences. Only in the case of B-4 and B-5 variants was there a slight decrease, which may have been observed due to the decreased veneer quality. In the case of MOE, the differences were noticeable, and statistically

significant differences were observed. As in the case of the MOR, the MOE was the lowest for the B-4 variant.

3.3. Formaldehyde Emission

Figure 4 presents the results of the formaldehyde emission of the laboratory-manufactured plywood panels bonded with UF resin and the addition of different wood bark species as fillers. The results of experiment clearly indicate that the replacement of rye flour with birch (B-1), beech (B-2), maple (B-3) and pine (B-4) bark led to a decrease in formaldehyde emissions compared with the reference samples (REF). The reduction in formaldehyde emissions can be explained by the presence of both lignin and tannins in bark. Van Der Klashorst and Strauss [38] reported that lignin is able to react with formaldehyde in an acidic medium. Moreover, tannins are characterized by their phenolic nature, and condensed polyflavonoid tannins are able to react with HCHO [39,40]. Only in the case of spruce bark (B-5), an increase in the emission of formaldehyde was recorded. This can be explained by the weakening of the bonding quality, which was confirmed by the results for the mechanical properties. According to Hogger et al. [41], the hindrance in polymer network formation and a deterioration in bonding quality can result in an increase in formaldehyde emission from UF resin-bonded plywood.

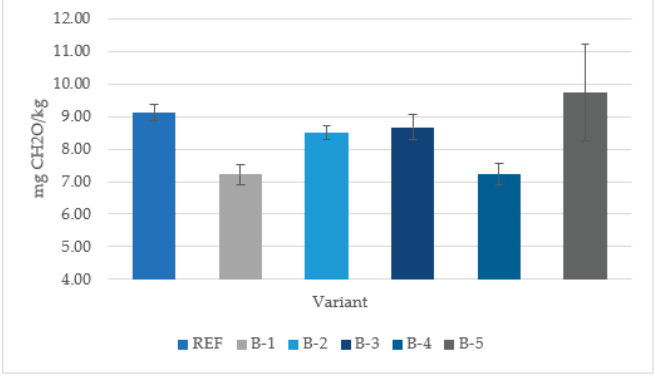

Figure 4. Formaldehyde emission in three-layer plywood panels produced with UF resin.

3.4. SEM Analysis

The cross-sections of plywood characterized with SEM at different magnifications of ×100 and ×1000 are presented at Figure 5. Compared with REF resin plywood (Figure 5a,d), the glue line of B-1 and B-5 adhesive plywood was characterized by larger free spaces (Figure 5b,c,e,f). This could be caused by the fact that bark fillers contained adhesive B-1, and B-5 was characterized by larger particle size. However, these changes affected the mechanical parameters (MOR and MOE in perpendicular direction) and formaldehyde emissions only in the case of the B-5 sample when compared to the REF sample.

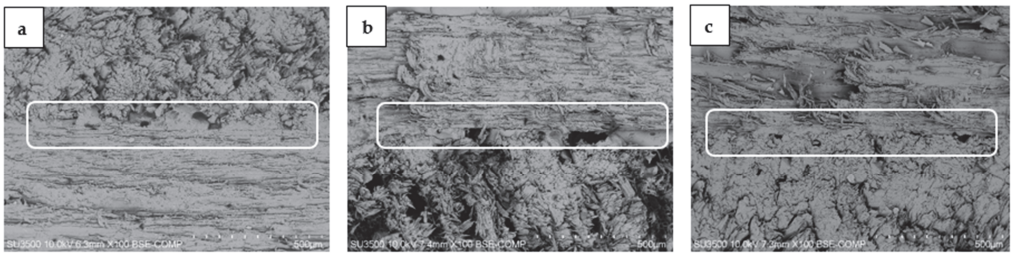

Figure 5. *Cont.*

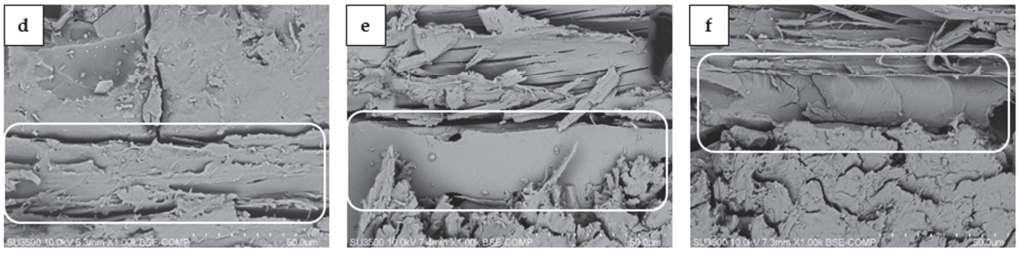

Figure 5. SEM photos of cross-section plywood: (**a**,**d**)—REF; (**b**,**e**)—B-1; (**c**,**f**)—B-5 samples. The bond lines are marked with white frames box.

4. Conclusions

In the case of maple bark, there were no statistically significant differences compared to the reference sample. In other cases, the reduction in the tensile strength was observed after the addition of the bark when compared to the reference variant. The phenomenon of lowering tensile strength can be explained by the chemical composition of bark, which could affect the resin curing process. Moreover, when the pH is considerably lowered, the pre-curing process could occur and consequently affect the bond lines strength.

The lack of significant improvement in strength parameters (MOR, MOE) can likely be explained by too high a proportion of filler (20 wt%).

The results of the experiment clearly indicate that the replacement rye flour with birch (B-1), beech (B-2), maple (B-3) and pine (B-4) bark led to a decrease in formaldehyde emissions. The observed reduction in emissions can be explained by the high lignin and tannins content. Only in the case of spruce bark (B-5), an increase in the emissions of formaldehyde was recorded. These results can be explained by the noted deterioration in the bonding quality, which is in agreement with the results of mechanical properties.

The most important conclusion is that the use of 20% (wt) bark powder is too much, and a lower load of filler should be used in the future studies.

Author Contributions: Conceptualization, J.W. and J.K.; methodology, J.W., J.K. and M.W.; formal analysis, J.W.; investigation, J.W., J.K., R.M. and D.D.; data curation, J.W., J.K. and R.M.; writing—original draft preparation, J.W.; writing—review and editing, J.W. and J.K.; visualization, J.W. and R.M. All authors have read and agreed to the published version of the manuscript.

Funding: This work was supported by Poznań University of Life Sciences (Poland) as the research program "First grant", no. 5/2022. The authors are grateful for the support of Ministry of Science and Higher Education program "Regional Initiative of Excellence" in the years 2019–2022, Project No. 005/RID/2018/19, financing amount 12,000,000.00 PLN.

Institutional Review Board Statement: Not applicable.

Informed Consent Statement: Not applicable.

Data Availability Statement: Not applicable.

Conflicts of Interest: The authors declare no conflict of interest.

References

1. Kawalerczyk, J.; Dziurka, D.; Mirski, R.; Trociński, A. Flour Fillers with Urea-Formaldehyde Resin in Plywood. *BioResources* **2019**, *14*, 6727–6735. [CrossRef]
2. Bekhta, P.; Sedliačik, J.; Kačík, F.; Noshchenko, G.; Kleinová, A. Lignocellulosic Waste Fibers and Their Application as a Component of Urea-Formaldehyde Adhesive Composition in the Manufacture of Plywood. *Eur. J. Wood Wood Prod.* **2019**, *77*, 495–508. [CrossRef]
3. Dukarska, D.; Czarnecki, R. Fumed Silica as a Filler for MUPF Resin in the Process of Manufacturing Water-Resistant Plywood. *Eur. J. Wood Wood Prod.* **2016**, *74*, 5–14. [CrossRef]
4. Sellers, T.; Miller, G.D.; Smith, W. Tool Wear Properties of Five Extender/Fillers in Adhesive Mixes for Plywood. *For. Prod. J.* **2005**, *55*, 27–31.

5. Cichy, W. Combustion of Plywood Waste in a Low-Power Boiler. *Drew. Pr. Nauk. Doniesienia Komun.* **2012**, *55*, 21–36.
6. Pasztory, Z.; Mohácsiné, I.R.; Gorbacheva, G.; Börcsök, Z. The Utilization of Tree Bark. *BioResources* **2016**, *11*, 7859–7888. [CrossRef]
7. Blanco-García, A.; Lindig-Cisneros, R. Incorporating Restoration in Sustainable Forestry Management: Using Pine-Bark Mulch to Improve Native Species Establishment on Tephra Deposits. *Restor. Ecol.* **2005**, *13*, 703–709. [CrossRef]
8. Dou, J. Willow Inner Bark as a Potential Source of Fibres and Chemicals. Master's Thesis, Aalto University School of Chemical Technology, Espoo, Finland, 2015.
9. Scalbert, A.; Monties, B.; Favre, J.-M. Polyphenols of Quercus Robur: Adult Tree and in Vitro Grown Calli and Shoots. *Phytochemistry* **1988**, *27*, 3483–3488. [CrossRef]
10. Fernández de Simón, B.; Cadahía, E.; Conde, E.; García-Vallejo, M.C. Low Molecular Weight Phenolic Compounds in Spanish Oak Woods. *J. Agric. Food Chem.* **1996**, *44*, 1507–1511. [CrossRef]
11. Jordão, A.M.; Ricardo-da-Silva, J.M.; Laureano, O. Ellagitannins from Portuguese Oak Wood (*Quercus Pyrenaica* Willd.) Used in Cooperage: Influence of Geographical Origin, Coarseness of the Grain and Toasting Level. *Wood Res. Technol. Holzforsch.* **2007**, *61*, 155–160. [CrossRef]
12. Skrypnik, L.; Grigorev, N.; Michailov, D.; Antipina, M.; Danilova, M.; Pungin, A. Comparative Study on Radical Scavenging Activity and Phenolic Compounds Content in Water Bark Extracts of Alder (*Alnus Glutinosa* (L.) Gaertn., Oak (*Quercus Robur*, L.) and Pine (*Pinus Sylvestris*, L.). *Eur. J. Wood Wood Prod.* **2019**, *77*, 879–890. [CrossRef]
13. Kawalerczyk, J.; Siuda, J.; Mirski, R.; Dziurka, D. Hemp Flour as a Formaldehyde Scavenger for Melamine-Urea-Formaldehyde Adhesive in Plywood Production. *BioResources* **2020**, *15*, 4052–4064. [CrossRef]
14. Mirski, R.; Kawalerczyk, J.; Dziurka, D.; Siuda, J.; Wieruszewski, M. The Application of Oak Bark Powder as a Filler for Melamine-Urea-Formaldehyde Adhesive in Plywood Manufacturing. *Forests* **2020**, *11*, 1249. [CrossRef]
15. Mari, E.L.; Jimenez, J.; Lapuz, R.B. Spent Tea Leaves as Extender and Scavenger for Urea Formaldehyde-Bonded Plywood. *Philipp. J. Sci.* **2018**, *147*, 285–291.
16. Taghiyari, H.R.; Hosseini, S.B.; Ghahri, S.; Ghofrani, M.; Papadopoulos, A.N. Formaldehyde Emission in Micron-Sized Wollastonite-Treated Plywood Bonded with Soy Flour and Urea-Formaldehyde Resin. *Appl. Sci.* **2020**, *10*, 6709. [CrossRef]
17. Ong, H.R.; Prasad, D.R.; Khan, M.R.; Rao, D.S.; Nitthiyah, J.; Raman, D.K. Effect of Jatropha Seed Oil Meal and Rubber Seed Oil Meal as Melamine Urea Formaldehyde Adhesive Extender on the Bonding Strength of Plywood. *J. Appl. Sci.* **2012**, *12*, 1148–1153. [CrossRef]
18. Ong, H.R.; Prasad, R.; Rahman Khan, M.; Chowdhury, M.; Kabir, N. Effect of Palm Kernel Meal as Melamine Urea Formaldehyde Adhesive Extender for Plywood Application: Using a Fourier Transform Infrared Spectroscopy (FTIR) Study. In Proceedings of the Applied Mechanics and Materials; Trans Tech Publications Ltd: Bach, Switzerland, 2012; Volume 121, pp. 493–498.
19. Ong, H.R.; Khan, M.M.R.; Prasad, D.R.; Yousuf, A.; Chowdhury, M.N.K. Palm Kernel Meal as a Melamine Urea Formaldehyde Adhesive Filler for Plywood Applications. *Int. J. Adhes. Adhes.* **2018**, *85*, 8–14. [CrossRef]
20. Tudor, E.M.; Barbu, M.C.; Petutschnigg, A.; Réh, R.; Krišťák, L. Analysis of Larch-Bark Capacity for Formaldehyde Removal in Wood Adhesives. *Int. J. Environ. Res. Public Health* **2020**, *17*, 764. [CrossRef] [PubMed]
21. Medved, S.; Gajsek, U.; Tudor, E.M.; Barbu, M.C.; Antonovic, A. Efficiency of Bark for Reduction of Formaldehyde Emission from Particleboards. *Wood Res.* **2019**, *64*, 307–315.
22. Turgut Sahin, H.; Burak Arslan, M. Weathering Performance of Particleboards Manufactured from Blends of Forest Residues with Red Pine (Pinus Brutia) Wood. *Maderas. Cienc. Tecnol.* **2011**, *13*, 337–346. [CrossRef]
23. Réh, R.; Igaz, R.; Krišťák, L.; Ružiak, I.; Gajtanska, M.; Božíková, M.; Kučerka, M. Functionality of Beech Bark in Adhesive Mixtures Used in Plywood and Its Effect on the Stability Associated with Material Systems. *Materials* **2019**, *12*, 1298. [CrossRef] [PubMed]
24. Ružiak, I.; Igaz, R.; Krišťák, L.; Réh, R.; Mitterpach, J.; Očkajová, A.; Kučerka, M. Influence of Urea-Formaldehyde Adhesive Modification with Beech Bark on Chosen Properties of Plywood. *BioResources* **2017**, *12*, 3250–3264. [CrossRef]
25. Aydin, I.; Demirkir, C.; Colak, S.; Colakoglu, G. Utilization of Bark Flours as Additive in Plywood Manufacturing. *Eur. J. Wood Wood Prod.* **2017**, *75*, 63–69. [CrossRef]
26. Mirski, R.; Kawalerczyk, J.; Dziurka, D.; Wieruszewski, M.; Trociński, A. Effects of Using Bark Particles with Various Dimensions as a Filler for Urea-Formaldehyde Resin in Plywood. *BioResources* **2020**, *15*, 1692–1701.
27. *EN 322*; Wood-Based Panels-Determination of Moisture Content. European Committee for Standardization: Brussels, Belgium, 1996.
28. *EN 314-1*; Plywood–Bond Quality–Test Methods. European Committee for Standardization: Brussels, Belgium, 2004.
29. *EN 310*; Wood-Based Panels–Determination of Modulus of Elasticity in Bending and of Bending Strength. European Committee for Standardization: Brussels, Belgium, 1994.
30. *EN 717-3*; Wood-Based Panels–Determination of Formaldehyde Release–Part 3: Formaldehyde Release by the Flask Method. European Committee for Standardization: Brussels, Belgium, 1996.
31. Elbadawi, M.; Osman, Z.; Paridah, T.; Nasroun, T.; Kantiner, W. Mechanical and Physical Properties of Particleboards Made from Ailanthus Wood and UF Resin Fortified by Acacias Tannins Blend. *J. Mater. Environ. Sci.* **2015**, *6*, 1016–1021.
32. Xing, C.; Zhang, S.Y.; Deng, J.; Wang, S. Urea–Formaldehyde-Resin Gel Time as Affected by the PH Value, Solid Content, and Catalyst. *J. Appl. Polym. Sci.* **2007**, *103*, 1566–1569. [CrossRef]

33. Nemli, G.; Kırcı, H.; Temiz, A. Influence of Impregnating Wood Particles with Mimosa Bark Extract on Some Properties of Particleboard. *Ind. Crops Prod.* **2004**, *20*, 339–344. [CrossRef]
34. Wang, X.M.; Li, J.Z.; Zhang, J.Z.; Gao, Q. Technics and Properties of Plywood Manufacture with Modified Urea-Formaldehyde Resin. In Proceedings of the Advanced Materials Research; Trans Tech Publications Ltd: Bach, Swizterland, 2013; Volume 602, pp. 743–746.
35. Réh, R.; Krišťák, Ľ.; Sedliačik, J.; Bekhta, P.; Božiková, M.; Kunecová, D.; Vozárová, V.; Tudor, E.M.; Antov, P.; Savov, V. Utilization of Birch Bark as an Eco-Friendly Filler in Urea-Formaldehyde Adhesives for Plywood Manufacturing. *Polymers* **2021**, *13*, 511. [CrossRef]
36. Vázquez, G.; Antorrena, G.; González, J.; Alvarez, J.C. Tannin-Based Adhesives for Bonding High-Moisture Eucalyptus Veneers: Influence of Tannin Extraction and Press Conditions. *Holz Als Roh Und Werkst.* **1996**, *54*, 93–97. [CrossRef]
37. Lubis, M.A.R.; Park, B.-D. Enhancing the Performance of Low Molar Ratio Urea–Formaldehyde Resin Adhesives via in-Situ Modification with Intercalated Nanoclay. *J. Adhes.* **2021**, *97*, 1271–1290. [CrossRef]
38. Van Der Klashorst, G.H.; Strauss, H.F. Polymerization of Lignin Model Compounds with Formaldehyde in Acidic Aqueous Medium. *J. Polym. Sci. Part A Polym. Chem.* **1986**, *24*, 2143–2169. [CrossRef]
39. Jahanshaei, S.; Tabarsa, T.; Asghari, J. Eco-Friendly Tannin-Phenol Formaldehyde Resin for Producing Wood Composites. *Pigment. Resin Technol.* **2012**, *41*, 296–301. [CrossRef]
40. Kunecová, D.; Hlaváč, P. Determination of Activation Energy of the Pellets and Sawdust Using Thermal Analysis. *Agron. Res.* **2019**, *17*, 2306–2316.
41. Hogger, E.M.; Van Herwijnen, H.W.; Moser, J.; Kantner, W.; Konnerth, J. Systematic Assessment of Wheat Extenders in Formaldehyde-Condensation Plywood Resins: Part II–Mechanical Properties of Plywood Panels. *J. Adhes.* **2021**, *97*, 1310–1321. [CrossRef]

materials

MDPI

Article

Properties of Rigid Polyurethane Foam Filled with Sawdust from Primary Wood Processing

Dorota Dukarska *, Joanna Walkiewicz, Adam Derkowski and Radosław Mirski

Department of Mechanical Wood Technology, Faculty of Forestry and Wood Technology, Poznań University of Life Sciences, Wojska Polskiego 38/42, 60-627 Poznań, Poland
* Correspondence: dorota.dukarska@up.poznan.pl

Abstract: In this study, the possibility of using sawdust, a by-product of primary wood processing, as a filler (WF) for rigid polyurethane (PUR) foams was investigated. The effects of the addition of 5, 10, 15 and 20% of WF particles to the polyurethane matrix on the foaming process, cell structure and selected physical-mechanical properties such as density, thermal conductivity, dimensional stability, water absorption, brittleness, compressive and bending strengths were evaluated. Based on the results, it was found that the addition of WF in the amount of up to 10% does not significantly affect the kinetics of the foam foaming process, allowing the reduction of their thermal conductivity, significantly reducing brittleness and maintaining high dimensional stability. On the other hand, such an amount of WF causes a slight decrease in the compressive strength of the foam, a decrease in its bending strength and an increase in water absorption. However, it is important that in spite of the observed decrease in the values of these parameters, the obtained results are satisfactory and consistent with the parameters of insulation materials based on rigid PUR foam, currently available on the market.

Keywords: polyurethane foam; wood by-products; filler; cellular structure; performance properties

Citation: Dukarska, D.; Walkiewicz, J.; Derkowski, A.; Mirski, R. Properties of Rigid Polyurethane Foam Filled with Sawdust from Primary Wood Processing. *Materials* **2022**, *15*, 5361. https://doi.org/10.3390/ma15155361

Academic Editor: Marco Corradi

Received: 6 July 2022
Accepted: 2 August 2022
Published: 4 August 2022

Publisher's Note: MDPI stays neutral with regard to jurisdictional claims in published maps and institutional affiliations.

1. Introduction

In recent years, concern for the environment and sustainable management of renewable resources has become a priority. This trend is clearly visible in the case of the timber industry, for which wood by-products provide an opportunity to expand the resource base but also to produce new materials. Their main source is primary wood processing, but even in highly developed and industrialised countries, the final product in the form of sawn timber placed on the market constitutes only 50% of processed wood. The remaining 50% is material loss, which mainly consists of sawdust and wood chips [1]. The advantage of wood by-products from primary wood processing (sawdust, dust, chips) is that they are free of contaminants that are often found in wood waste harvested from post-consumer wood. These are mainly adhesives, varnishes, paints, metals, glass, plastics, etc. Their presence hinders post-consumer wood recycling processes [2]. Therefore, the use of wood by-products in the manufacturing process of various types of materials is economically and technologically justified. An example of the development of innovative wood-based materials using this type of sorting is chip-sawdust boards or reduced-density cement-chip boards, which can be a substitute for traditional particleboard in the construction industry [3–6]. It should be noted that there has been for years a growing interest in the use of wood by-products not only in the wood industry but also in the paper industry, the energy industry, and the production of wood–polymer composites.

By-products from both the timber and agricultural industries have also become a source of fillers that can be used in the production of polymer-based composites [7,8]. Wood–Polymer composites (WPCs) combine the advantages of both synthetic polymers and lignocellulosic fillers [9]. Numerous studies conducted in this area have shown that

the type, form, shape and particle sizes of the filler significantly affect the properties of WPC composites. In general, it can be stated that the introduction of lignocellulosic filler particles into the polymer matrix reduces the production costs of composites and their weight, provides biodegradability, increases the filling rate, and improves some mechanical properties such as modulus of elasticity or abrasion resistance. Similar results can be obtained in the manufacturing process of composite polyurethane (PUR) foams. Currently, PUR foams account for 2/3 of the world's polyurethane production and due to their wide range of applications in rigid, semi-rigid and flexible forms, they rank high among all foam materials [10]. In addition to the search for alternative raw materials to polyols and isocyanate, research on the chemical and physical recycling of foams, the modification of the properties of foams by introducing various types of fillers into their structure, has now become one of the main research trends in this area [11].

The advantages of rigid PUR foams include low cost, negligible environmental impact, low density, and high insulation properties (0.018–0.025 W/m·K) [12]. However, they are characterised by low mechanical strength, thermal stability and fire resistance, which may limit the scope of their application [12,13]. The introduction of the optimal amount and type of filler into the foam structure usually improves the physical and mechanical parameters of PUR foams, i.e., their compressive strength, brittleness, thermal resistance, as well as thermal and acoustic insulating properties [12–15]. The effectiveness of fillers in reinforcing foam structures depends on the number and size of particles, method of incorporation, compatibility with foam components, and degree of dispersion. For these reasons, the use of various types of nanofillers such as: fume silica [16], cellulose nanocrystals [17], spherical TiO_2, platelet nanoclay, rod-shaped carbon nanofibers [18], montmorillonite [19] and others should be considered as promising solutions in this field. They act as nucleation sites and thus reduce the cell size and, as a result, effectively increase the mechanical properties, fire resistance and thermal stability and reduce the thermal conductivity of PUR foams [13,20]. However, a significant problem with the use of such fillers is their relatively high price and their tendency to agglomerate, which in consequence disturbs the foaming process and deteriorates the properties of the finished foam.

According to Paciorek-Sadowska et al. [21], currently, the modern polyurethane industry is oriented towards environmentally friendly operations. For these reasons, attention has turned to so-called biofillers derived from the processing of natural raw materials. The primary purpose of their use is to improve or maintain the properties of the polyurethane composite while reducing the price of the finished product. The main advantages of biofillers include low acquisition cost, general availability, and an environmentally friendly nature [22]. Moreover, they show the presence of free hydroxyl groups (–OH) capable of reacting with isocyanate groups (–NCO), which gives them sufficient compatibility with polyurethane [23]. The studies carried out so far show that agricultural waste is a material with high application potential in the production of composite PUR foams. It has been shown that waste products such as buckwheat husks [7], walnut shells [12,20], plum stones [22], straw fibre [24], hemp fibre [25], wheat slops [26], rapeseed cake [21], soy and potato protein [27,28], sugar beet pulp [15], egg shell [29], ground coffee [30], keratin chicken feathers [31] and many others have a beneficial effect on the properties of foams. Another source of naturally derived fillers is the timber industry. The suitability of wood waste in the manufacture of PUR composite foams was studied by de Avila Delucis et al. [32], who tested six different forest waste fillers, including wood flour from shavings and sawdust, bark, cones and needles from young pines, kraft lignin and recycled paper sludge from industrial waste. In the course of the study, it was found that the wood floor was the most effective filler among the compositions under study. Rigid PUR foam with its amount of 1 and 5% has the best mechanical and hygroscopic properties, probably due to the higher wood compatibility with the PUR system and the formation of urethane bonds between the filler and isocyanate. Furthermore, according to Yuan and Shi [14], the incorporation of wood flour into the structure of the foam allows it to improve its compressive strength and thermal stability, although it also contributes to a decrease in flexural

and tensile strength. Larger admixtures of wood particles to PUR foam (i.e., 10 and 20%), according to Luo et al. [33], may result in a decrease in compressive strength and an increase in water absorption. Augaitisa et al. [23] demonstrated that biocomposite PUR foam with a 0.7 ratio of PUR to pine sawdust has very good physical and insulating properties and also high strength. It is worth emphasising that the examples cited above mainly concern rigid PUR foams with closed-cell structures. However, the authors of this paper have shown in an earlier study [34] that wood by-products sourced from the primary processing of wood can also be a valuable raw material in the production of composite foams with an open-cell structure. It has been demonstrated that a 10 wt% addition of such a biofiller allows them to increase their compressive strength and improve their thermal insulation.

By continuing the research in this field, the investigations were carried out in order to determine the effect of modification of rigid PUR foam with closed-cell structure by different amounts of sawdust obtained by primary wood processing on the kinetics of the foaming process, its structure and selected performance properties. To the best of our knowledge, no research has been conducted to date on the manufacture of closed-cell rigid PUR foams with this type of wood filler, i.e., with this origin and particle size and shape.

2. Materials and Methods

2.1. Materials

A two-component PUREX WG-2732 closed-cell polyurethane thermal insulation system (Polychem System, Poznań, Poland) was used to produce the experimental foams. A major advantage of the system used in this study is that it can be processed manually and by machine, either by injection moulding or pouring. The system includes component A, which is polyol, and component B, which is polymeric 4,4-diphenylmethane diisocyanate (PMDI). Pine sawdust with the largest fraction between 0.315 and 1.25 mm, bulk density of 182 kg/m^3 and moisture content of about 0.5% were used as foam fillers (WF). This filler, along with its fractional composition and normal distribution, is shown in Figure 1.

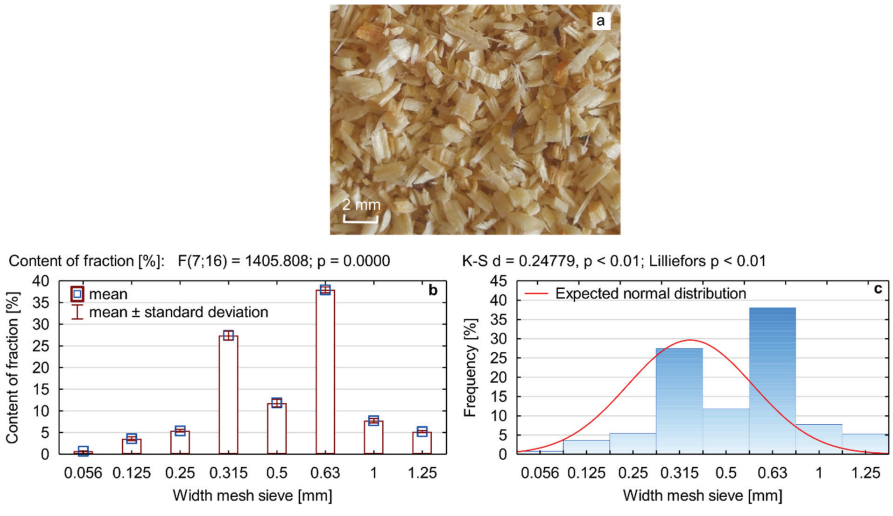

Figure 1. Sawdust used as a filler for PUR foam: (**a**) image, (**b**) fractional composition, (**c**) normal distribution.

These particles were obtained by sorting sawdust generated from primary wood processing. Most of the sawdust from this processing can be successfully used to make chip-sawdust boards; however, the high proportion of fine fractions is always troublesome in the production of this type of panel.

2.2. Preparation of PUR/WF Composite Foams for Testing

According to the PUREX WG system manufacturer's guidelines, the foam components were mixed at a weight ratio of A:B = 100:120. Wood filler was added in amounts of 0, 5, 10, 15 and 20% *w/w* relative to the total weight of the foam components. The entire reaction mixture, including WF, was stirred with a mechanical stirrer at 1200 RPM/min for 10 s at 23 °C and then poured into a metal mould with internal dimensions of 250 × 250 × 130 mm^3. The foams prepared in this way were cut into samples necessary to determine their physical and mechanical properties. In order to determine the effect of wood filler addition on the foam foaming process, mixtures containing 10 g of component A, 12 g of component B, and an appropriate amount of WF particles were prepared in disposable 400 mL plastic containers.

2.3. Characteristics of PUR/WF Composite Foams

The course of foaming of PUR/WF composite foams was characterised on the basis of the duration of successive stages of this process, maximum foaming temperature and measurements of the increase in the height of the foam growth. Thus, creaming times, foam growth start time, gelation and growth time, and tack-free time were measured. The foaming temperature was measured by placing a thermocouple inside the growing foam. Temperature readings were always taken after foam growth was complete, and the readings of the Bench Digital Multimeter (Twintex Electronics Ltd., Shenzhen, China) were stabilised. After the expansion of the foams was completed, the height of the foams was also measured, and the percentage reduction in their growth relative to pure PUR foam was determined on that basis.

The structure of the fabricated foams was visualised using a Hitachi SU3500 (Hitachi, Tokyo, Japan) scanning electron microscope (SEM) at 20× and 60× magnification. A Motic SMZ-168 optical microscope with Motic Images Plus 3.0 software was used to measure cell size and distribution.

The apparent density of foams (ρ), defined as the ratio of the sample mass to its volume, was measured as per EN ISO 845 [35]. Further, 50 × 50 × 50 mm^3 foams were used for this determination.

The insulating properties of PUR/WF foams were determined using a heat flux density sensor type ALMEMO 117 from Ahlborn (Holzkirchen, Germany) with a wafer dimension of 100 × 30 × 3 mm^3. Four specimens with dimensions of 230 × 240 × 50 mm^3 were used for this study. The measured values of heat flux density were used to estimate the average value of thermal conductivity coefficient (λ).

Short-term water absorption (W_p) tests were conducted on four 200 × 200 mm^2 samples as per ISO 29767 [36], method A. The foam samples were placed in containers of water in such a position that they were partially submerged in water and their bottom surfaces were 10 ± 2 mm below the water level. After 24 h of soaking, the samples were removed from the water, and dried on a rack at an angle of 45° for 10 min. After this time, the PUR samples were weighed. The value of short-term water absorption of the tested foams was determined as the ratio of the difference in weight of the PUR samples before and after immersion with respect to their surface area.

The dimensional stability of the manufactured foams was determined in accordance with the requirements of EN 1604 [37]. Eight 200 × 200 mm^2 samples were subjected to conditioning at 23 ± 2 °C and 50 ± 5% relative humidity until equilibrium was reached. The four samples were then placed in a climate chamber at 60 ± 2 °C with a relative humidity of 80 ± 2%. The remaining samples were placed at −20 ± 2 °C. After 24 h of exposure, the percentage changes of their length, width and thickness $\Delta\varepsilon_l$, $\Delta\varepsilon_b$, $\Delta\varepsilon_d$ respectively, were estimated.

Compressive strength tests of the foams ($\sigma_{10\%}$) were conducted 48 h after manufacture and less than 12 h after cutting into specimens. Measurements were performed according to the recommendations of EN 826 [38] using a Tinius Olsen H10KT testing machine (Tinius Olsen Ltd., Salfords, UK). Ten specimens with dimensions of 50 × 50 × 50 mm^3 were used

for this study. The tested foams were compressed at a rate of 5 mm/min in the direction parallel and perpendicular to their growth. The value of the maximum compressive force reached at 10% relative deformation of the foams to their surface was taken as the result.

The three-point bending strength of PUR/WF foams (σ_b) was determined based on the standard as per EN 12089 [39] on specimens of 130 mm × 40 mm × 20 mm [40], using a Tinius Olsen H10KT testing machine (Tinius Olsen Ltd., Salfords, UK) and a loading rate of 10 mm/min. The average flexural strength of each foam variant tested was determined from ten individual measurements.

The brittleness of PUR/WF foams (K) was determined according to the guidelines of ASTM C 421 [41]. Twelve 25 × 25 × 25 mm^3 specimens were used and placed in the apparatus chamber along with twelve oak cubes (19 × 19 × 19 mm^3). The chamber, including samples and oak cubes, was rotated at 60 RPM for 10 min. Brittleness was defined as the percentage weight loss of the test samples. Three trials were performed for each variant.

The yielded test results of composite PUR foams were statistically analysed using STATISTICA software v.13.1 (StatSoft Inc., Tulsa, OK, USA). Mean values of the parameters were compared in a one-factor analysis of variance—post hoc Tukey's test allowed us to distinguish homogeneous groups of mean values for each parameter for $p = 0.05$.

3. Results

3.1. Characteristics of the Processing of PUR/WP Foams

The foaming process is an important step that affects the performance of rigid PUR foams [42]. Table 1 presents the results of the processing times of the tested foams and the maximum temperature that was obtained during foaming. It can be concluded that the addition of wood filler causes an increase in the duration time of all foam stages, especially at a higher proportion of WF particles, i.e., 20%. The addition of this amount of filler primarily increases the gelation time by about 36%, the growth time by 40% and the tack-free time by 15%. The extension of these times is a consequence of the deceleration of the exothermic reaction. This is exhibited by the decrease in the maximum foaming temperature by as much as 25 °C, which was observed together with an increase in WF amount. According to the literature on the subject, such unambiguous shaping of the foaming times and temperatures results from the reduced amount of heat released during the reactions taking place in the latent stage (the time from mixing the components to the start of growth) and the foam growth time. This slows down the crosslinking reaction and consequently increases the tack-free time [10,43]. The increase in viscosity of PUR systems under the influence of the filler is also considered to be the main reason for the increase in these times, which consequently limits proper cell expansion. On the basis of studies conducted so far, it can be concluded that with the increase in the number of various types of fillers introduced into the microstructure of foams, higher viscosity of PUR systems and an increase in their processing times are observed [12,15,31,42,44–49]. Furthermore, the functional groups of fillers can react with isocyanate groups, which can affect the proper stoichiometry of the reaction and limit the release of blowing agents (CO_2) [15,44,50]. A consequence of this is the observed reduction in foam expansion as the amount of WF particles introduced into the PUR polymer matrix increases. Due to its bulk density and relatively large particle size, the filler also places a strain on the foam structure, further inhibiting its growth and contributing to the density increase. It was noted that while the 10% and 15% addition of WF causes a reduction in foam height of about 6% and 8%, respectively, the composition containing the maximum amount of WF showed a reduction in the growth of the reaction mixture of about 15%. It is worth noting that such prolongation of foaming times of composite PUR foams produced with various fillers as well as a decrease in maximum temperature of this process is a phenomenon quite commonly reported by researchers. Similar results were obtained in the case of introducing nanoclay, polyester-glass fibre waste, coir fibres, expandable graphite, potato protein, and kraft lignin into the polyurethane matrix [28,43,44,50–52].

Table 1. Parameters characterising the foaming process of PUR/WF foams.

WF Content [%]	Mean Processing Times [s]					T_{max} [°C]	h [mm]	Δh [%]
	Cream	Start of Growth	Gelling	Growth	Tack-Free			
0	12 ± 1 *	38 ± 1	113 ± 6	180 ± 6	249 ± 11	114 ± 2	155 ± 3	-
5	12 ± 1	33 ± 1	122 ± 2	187 ± 3	260 ± 14	113 ± 1	150 ± 2	3.4
10	12 ± 2	30 ± 2	117 ± 4	201 ± 10	258 ± 5	117 ± 2	146 ± 1	5.8
15	11 ± 1	33 ± 2	136 ± 7	240 ± 3	276 ± 6	114 ± 2	143 ± 2	7.7
20	15 ± 2	30 ± 2	157 ± 4	254 ± 6	288 ± 6	90 ± 3	132 ± 9	15.0

*—standard deviation, T_{max}—maximum foaming temperature of PUR foam, h—height of the PUR foam growth, Δh—percentage reduction of PUR foam growth.

3.2. Structure of PUR/WP Foams

The average cell and pore sizes of composite foams are determined, among other things, by microscopic interactions between the polymer matrix and the filler surface [53]. From the SEM micrographs and cell size distribution plots of the experimental foams presented in Figures 2 and 3, it is evident that the pure PUR foam is characterised by a structure with a high content of closed cells with a relatively uniform size distribution, mainly in the range of 450–600 µm. The average size of the foam cells with the highest frequency is 550 µm. However, while the amount of WF particles introduced into the PUR matrix increases, more and more disruption of the foam structure occurs, accompanied by the production of more defective cells. At 5% WF addition, the changes in PUR structure are still relatively small. Increases in smaller cell size were mainly observed in the range of 350–500 µm but also above 550 µm. Further increase in WF admixture results in greater changes in the morphology of the compositions studied. Foams with 10–20% WF have a much less uniform cell shape and a much wider range of cell size distribution. The formation of a larger number of small-sized cells is mainly visible in the range of 200–500 µm, but also cells with sizes far exceeding the cell size of pure PUR foam, namely in the range of 600–950 µm, are evident as well. Significant reduction of the average cell size and disruption of the structure of the produced composite foams can be observed mainly in the interfacial areas, i.e., where the WF particles are clearly attached to the foam cell walls, weakening the cell structure and leading to cracks (Figure 4). An increase in the number of open cells and defective cells with damaged walls and struts is observed. Furthermore, the use of filler particles with larger sizes also causes cell breakage due to incomplete incorporation into the PUR matrix [20,53].

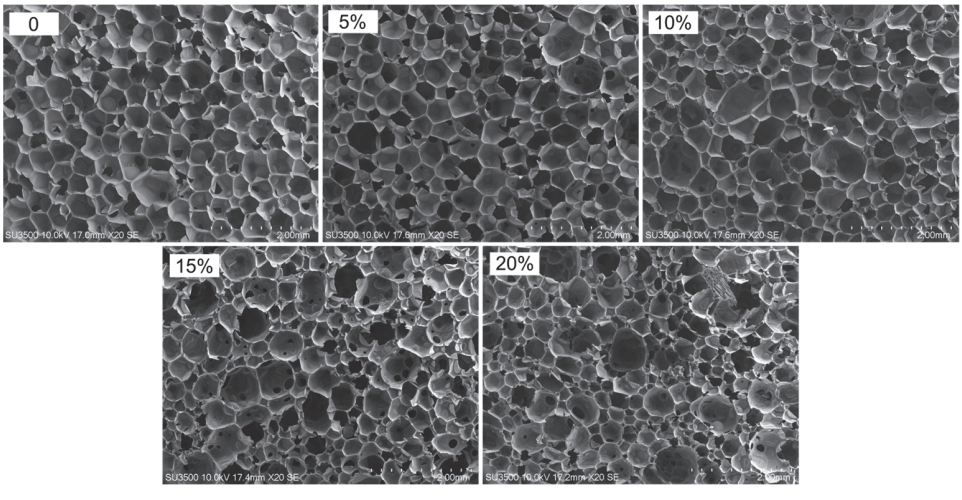

Figure 2. SEM images of PUR foam with different amounts of wood filler.

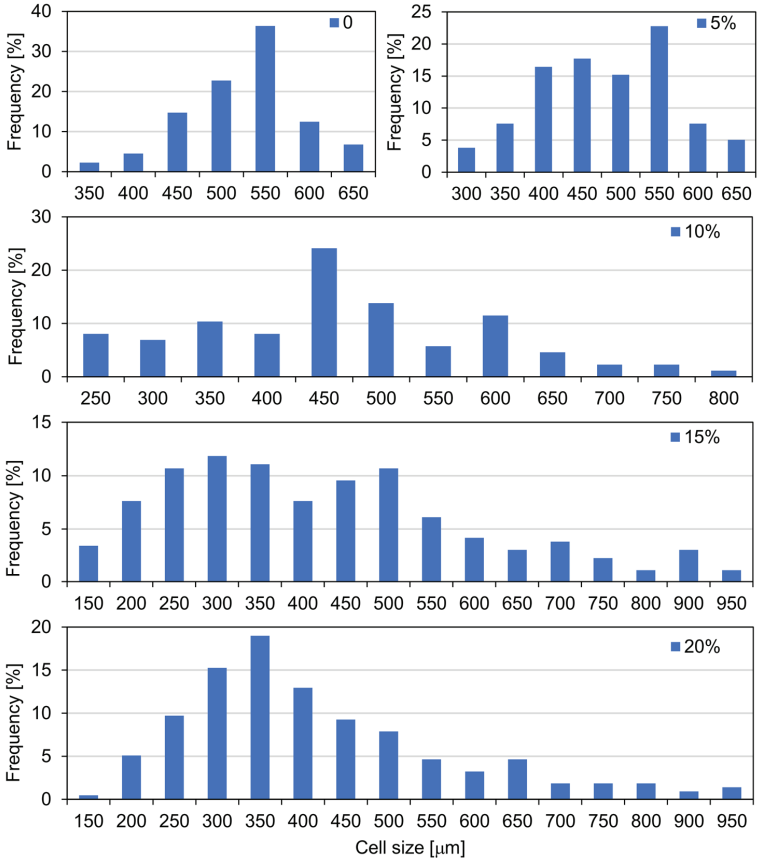

Figure 3. Cell size and cell size distribution of PUR foam depending on wood filler content.

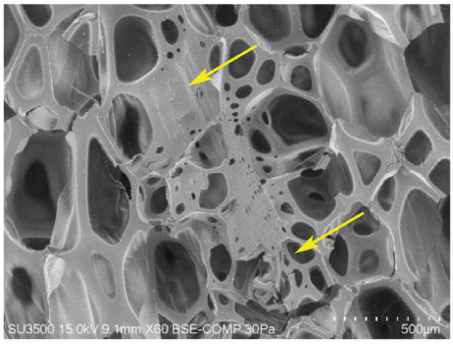

Figure 4. SEM images of PUR foam with addition of wood filler (arrows indicate changes in PUR structure in the presence of wood filler).

From the micrographs shown in Figure 5, it can also be concluded that the addition of WF to the PUR matrix causes a reduction in cell wall thickness, which was reflected in the strength test results of the foams. Such observations are confirmed by the work of other authors. The literature shows that the use of virtually any lignocellulosic filler results in weaker cell structures with a large number of open cells, which significantly

affects the final properties of polyurethane composites [54]. An unfavourable effect of fillers' admixture on the morphology of PUR foams is attributed to changes in viscosity and concentration of the reaction mixture, as a result of which the formation and growth of cells are inhibited, leading to a heterogeneous structure of foams [17,55]. In addition, the filler particles attach to the cell walls of the foam, which consequently weakens its structure and leads to destruction [32]. The filler can also cause the nucleation mode to change from homogeneous to heterogeneous and reduce the nucleation energy. The consequence of this is a reduction in cell size in the microstructure of the foams and thus a deterioration in their physical and mechanical parameters [56,57]. Similar changes in the microstructure of PUR composite foams have also been observed with other types of fillers such as walnut shells, plum stones, egg shell waste, sugar beet pulp, sunflower press cake, oak bark, soy protein isolate, talc, carbon nanotubes, graphite and others [12,13,15,22,27,29,31,45].

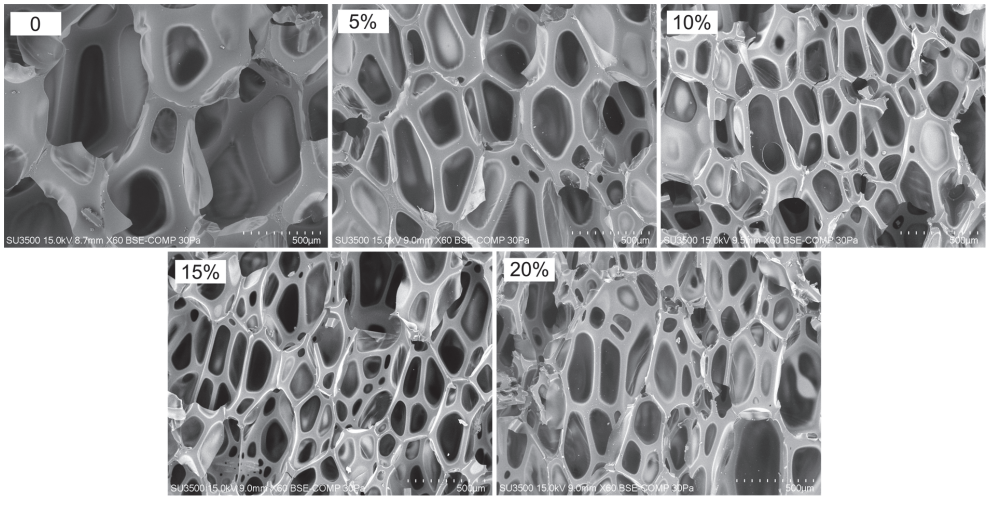

Figure 5. SEM micrographs of PUR showing changes in cell wall structure under the influence of sawdust application.

3.3. Apparent Density, Thermal Conductivity and Water Absorption of PUR/WF Foams

The change in the composition and microstructure of the foams studied was reflected in their physical properties, i.e., density, thermal insulation and surface absorbability determined after short-term immersion. An important characteristic determining the use of foam as an insulating material is its thermal conductivity, the value of which depends, among others, on the apparent density, shape or type of cells (closed or/and open). The data in Figure 6a indicate that the addition of wood filler has a significant effect on the apparent density of the produced foams and on their thermal insulation, which was determined by the thermal conductivity coefficient (λ). This is confirmed by the results of the post hoc test and the different homogeneous groups of mean values of both apparent density and thermal conductivity extracted from it. It is known that the density of composite foams is a function of voids as well as the content and type of filler [31,58]. Since the density of wood filler is greater than that of pure foam, its addition caused a significant increase in the density of PUR/WF foams. This is particularly evident for variants with WF additions above 10%. The apparent density of the pure foam was 35.2 kg/m^3. The maximum apparent density recorded with 20% filler is 48.7 kg/m^3, an increase of approximately 38% over pure PUR foam. Such a significant increase in density of foams (especially above 10% WF addition) is an effect of the presence of sawdust in the composition, but also, as suggested by the study of parameters characterising the foaming process, from a significant reduction in their expansion due to an increase in viscosity of PUR systems [15]. The results

and conclusions obtained in this respect correlate with many works of other authors who also reported an increase in apparent density of PUR foams due to admixture of various types and amounts of fillers [12,15,20,22,23,52,59].

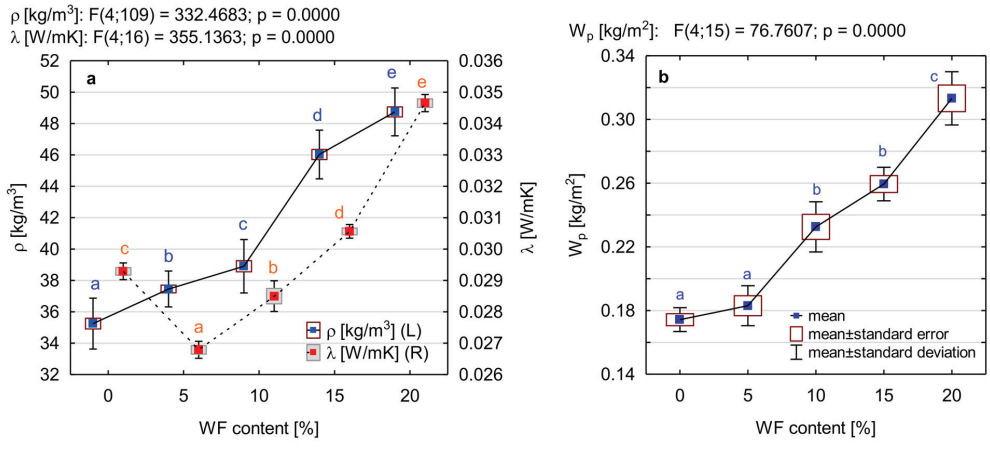

Figure 6. Effect of wood filler addition on: (**a**) apparent density (ρ) and thermal conductivity (λ), (**b**) short-term water absorption by partial immersion (W_p) of PUR composite foams. Different letters in colour indicate homogeneous groups of mean values determined by one-factor ANOVA with Tukey's test.

The consequence of the significant changes in the microstructure and apparent density of the produced composite foams (especially those with higher WF content) are the substitutions of their thermal conductivity. The values of this parameter that were recorded are in the range of 0.0268–0.0347 W/m·K (Figure 6a). Pure PUR foam has a low λ coefficient, i.e., 0.0294 W/m·K. This is close to the values declared by the manufacturers of this type of foam. The introduction of small amounts (5%) of WF into the foam structure resulted in a decrease in thermal conductivity to the level of 0.0267 W/m·K, i.e., by about 10%. According to Kurańska and Prociak [60], the lower value of the thermal conductivity coefficient may be due to an increase in the number of smaller cells and, as a result, cell walls that act as an additional barrier to heat transfer by radiation. A further increase in the WF addition contributes to an increase in thermal conductivity. This is particularly evident in the case of the variant with maximum filler admixture, for which the λ parameter reached values higher than those for pure PUR foam by about 18%. Similar results have been obtained using glass powder, nanoclay, rice straw fibre or walnut shell as PUR foam filler [12,24,51,61]. This is undoubtedly a result of changes in the morphology of the composite foams produced, increased density and increased heat transport by solid parts and thus increased λ_{solid} [19,52]. For closed-cell foams, the increase in thermal conductivity is a consequence of the reduction of closed cells filled with blowing agents, i.e., CO_2 with a lower thermal conductivity than the conductivity of air present in open cells [19,20]. Despite the recorded increase in the λ coefficient, the obtained results seem to be satisfactory due to the fact all the produced composite foams show a lower thermal conductivity than those commonly used thermal insulation materials, such as polystyrene foam or materials made of mineral wool or wood fibres.

The water resistance of the manufactured foams was determined by examining their susceptibility to short-term soaking after 24 h of partial immersion in water (W_p). The susceptibility to water absorption of insulation foams, especially foams with fillers of natural origin, is important because it can affect their mechanical properties, thermal conductivity and biological resistance [23]. The main factors affecting the water absorption of foams are the open and closed cell content and their apparent density. In general, rigid

PU foams have closed cells and hydrophobic nature. The water, therefore, only penetrated into the pores between the foam cells [62]. As shown in Figure 6b, the addition of wood filler results in a gradual increase in absorption. Statistically significant changes were observed with as little as 10% addition of WF. This is confirmed by the post hoc analysis conducted, which has separated individual homogeneous groups (i.e., b and c) for this amount of WF and higher. A 10% admixture of WF increased the water absorption by approximately 34%, while the maximum amount of filler used in the study (i.e., 20%) increased it by 80%. This significant increase in water absorption for foams with a higher proportion of WF is undoubtedly due to two reasons. Firstly, because of disturbances in foam morphology, i.e., an increase in the number of open cells that are able to store more water [15]. In foams with a structure with fewer closed cells, water migrates more easily than in foams with more closed cells [49]. Additionally, this effect is enhanced by the porous structure of the wood and its hydrophilic nature. This is because wood exhibits the ability to bind water molecules through the active hydroxyl groups of cellulose and hemicelluloses [63]. This is confirmed by studies conducted, among others, by Grząbka-Zasadzińska et al. [54], in which cellulose filler was used to produce PUR foam before and after poly(ethylene glycol) modification. Such an increase in water absorption was also observed when PUR foam was modified with cinnamon or coffee [30,64]. However, it should be emphasised that despite a significant increase in the absorbability of foams, the results obtained (even at 20% addition of WF) are satisfactory and consistent with the results for similar products existing on the market [49].

3.4. Dimensional Stability of PUR/WF Foams

The porous structure, especially the number of closed cells, has a significant effect on two of the most important functional properties of PUR foams, i.e., thermal conductivity and dimensional stability [22]. The dimensional stability of the produced foams was determined after conditioning them for 24 h at elevated temperature and humidity and at a temperature below 0 °C. The obtained measurement results are shown in Table 2. They show that regardless of the exposure conditions, pure PUR foam, as well as foams with WF, added up to 10%, do not show significant changes in dimensional stability. On the contrary, the use of higher amounts of WF, i.e., 15% and 20%, results in a significant deterioration of the dimensional stability of the foams under elevated temperature and relative humidity conditions. In fact, about a 4% reduction in length and width of foams with 15% of wood particles and a 7% change of these dimensions in the case of the variant with 20% WF were observed. Advantageously, irrespective of the amount of filler, no significant changes in the linear dimensions of the foams were observed after the ageing test was carried out at temperatures below 0 °C. It should be noted that in the case of the foam with 20% of WF, significant changes in the linear dimensions (shrinkage) were already observed during its preparation for the ageing tests, i.e., in the time of conditioning at 23 °C and 50% relative humidity required by EN 1604 [37] until it reached the equilibrium state. Even then, the variant showed almost 5% shrinkage in the length and width of the foam, with the largest changes in the middle of their length and width, as can be seen in Figure 7.

Table 2. Dimensional stability of PUR foam with different amounts of wood filler acclimated under different conditions.

WF Content [%]	T = 60 °C, RH = 80%			T= −20 °C		
	$\Delta\varepsilon_l$ [%]	$\Delta\varepsilon_b$ [%]	$\Delta\varepsilon_d$ [%]	$\Delta\varepsilon_l$ [%]	$\Delta\varepsilon_b$ [%]	$\Delta\varepsilon_d$ [%]
0	0.32 ± 0.09 *	0.37 ± 0.10	0.29 ± 0.11	0.03 ± 0.03	0.05 ± 0.06	0.05 ± 0.08
5	0.32 ± 0.07	0.42 ± 0.14	0.35 ± 0.14	0.03 ± 0.04	0.03 ± 0.04	0.03 ± 0.05
10	1.31 ± 0.28	1.44 ± 0.47	0.24 ± 0.08	0.14 ± 0.07	0.16 ± 0.05	0.01 ± 0.06
15	3.94 ± 0.55	4.05 ± 0.31	0.20 ± 0.10	0.21 ± 0.08	0.23 ± 0.09	0.05 ± 0.05
20	7.53 ± 1.29	6.92 ± 1.40	−0.57 ± 0.26	0.39 ± 0.15	0.42 ± 0.13	0.05 ± 0.08

*—standard deviation, $\Delta\varepsilon_l$, $\Delta\varepsilon_b$, $\Delta\varepsilon_d$—length, width, thickness changes, respectively.

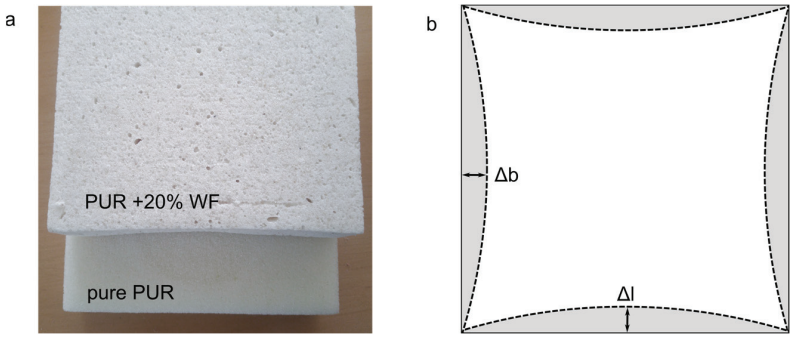

Figure 7. Deformation of pure PUR foam and foam with 20% WF after conditioning: (**a**) images of the tested foams, (**b**) scheme of PUR/WF foam linear dimension changes. Δb, Δl—changes in the width and length of the foams, respectively.

However, no significant changes in foam thickness were observed (<0.5%). By Kairytė et al. [65], the increased shrinkage of the foam means that its structure is not rigid enough to provide equilibrium with the pressure difference between the cellular structure and the surrounding environment. The presence of larger closed cells and thinner cell walls, which were observed for foams with a higher proportion of WF, promotes intense diffusion of CO_2, which increases the shrinkage of the final product [66]. After the ageing tests, this effect is further enhanced by elevated temperature, which accelerates gas diffusion and causes gas expansion, thereby exerting more pressure on the cell walls and consequently changing the volume of the foam [23]. Furthermore, these changes can be attributed to the porous structure and hydrophilic properties of the filler, making it less resistant to wet environments than the hydrophobic polymer matrix. Therefore, the greater its addition, the more negative its effect in this regard on the final product [23].

According to standard EN 13165 [67], for rigid closed-cell foams used as spray insulation, the variation in their length and width after conditioning under elevated temperature and humidity conditions should not exceed 5% and the thickness 10%. By Borkowski [68], in industrial application, polyurethane materials with closed-cell structures should not change their linear dimensions by more than 1–1.5% and geometric volume by more than 3% as a result of ageing. When considering the above requirements, it can be concluded that the foams containing up to 10% wood filler showed a high level of stability. Foams containing higher amounts of WF show significantly lower stability, falling outside the range provided by the above standard.

3.5. Compressive and Flexural Properties of PUR/WF Foams

Figure 8 shows the results of selected mechanical properties of the tested PUR/WF foams, i.e., their compressive strength at 10% relative strain ($\sigma_{10\%}$) and flexural strength (σ_b). Based on them, it was found that despite the increase in apparent density, the introduction of WF particles into the reaction mixture causes a gradual decrease in the compressive strength of the foams, determined both in the direction of growth and perpendicular to it. As expected, higher foam strength values were obtained in the direction parallel to the foam growth, as opposed to the perpendicular direction. These differences are a consequence of the often anisotropic cell structure of PUR foams [69]. For foams with up to 10% WF, the changes in $\sigma_{10\%}$ values are relatively small, at about 10%. A significant decrease in this type of strength was observed at higher amounts of WF, and particularly at 20% addition—the decrease in strength regardless of the direction of foam growth, compared to the reference sample, was 50%. It is well known that increasing the apparent density of foams has a beneficial effect on their mechanical properties, such as flexural strength or compressive strength [70]. The mechanical properties of composite foams are also affected by the type and size of filler particles, surface modification and interaction with the polyurethane

matrix [12,69]. There is no doubt that the decrease in compressive strength of PUR/WF foams is a result of disruption of their morphology due to the incremental introduction of wood filler into the polyurethane matrix. As mentioned above, this resulted in more cells with thinner walls, smaller struts, and pronounced cell damage, which is also presented in Figures 4 and 5. Such cells are not strong enough to withstand the compressive load, and more stress is generated on the cell struts [31]. This lack of strengthening effect of PUR foams when filler particles were introduced into their polymer matrix (especially in larger amounts) was also reported in the works of other researchers. For example, a decrease in compressive strength was also obtained when basalt particles, cellulose filler, biochar, polyester composite waste, ground pedunculate oak shoulder, and wheat slops were used [26,42,45,52,69,71]. According to the literature, improvement in compressive strength can be provided by good interfacial adhesion between the filler particles, which are located in the cell struts, and the polyurethane matrix, which facilitates stress transfer. However, a large amount of filler causes cell defects and cell collapse because its particles can pass through the cells causing damage to the foam structure [72]. In the case of the present work, the relatively large particle size of the WF is also important, with approximately 40% of the particles being of the 0.63 mm fraction. Similar to the study conducted by Augaitis et al. [23] (sawdust was used as PUR filler), it was observed that some of the filler particles were not completely incorporated into the polymer matrix. Some of these particles remained loose, indicating insufficient wetting of their surfaces by the PUR matrix, which in turn leads to the formation of voids and open cells in the foam structure [15,23]. The above corresponds to the results of work by Kurańska and Prociak [60], which showed that the filler fibres of shorter lengths are better embedded into the cells of the polymer matrix and do not cause more damage than longer fibres. As a result, foams with longer fibres show lower compressive strength. This is also confirmed by the results obtained by Sture et al. [59], who introduced sawdust in amounts of 0.5–1.5 wt% into the polymer matrix with a significant degree of fineness, i.e., with sizes mainly in the range up to 0.016 mm. No significant structural defects were observed in the final product obtained.

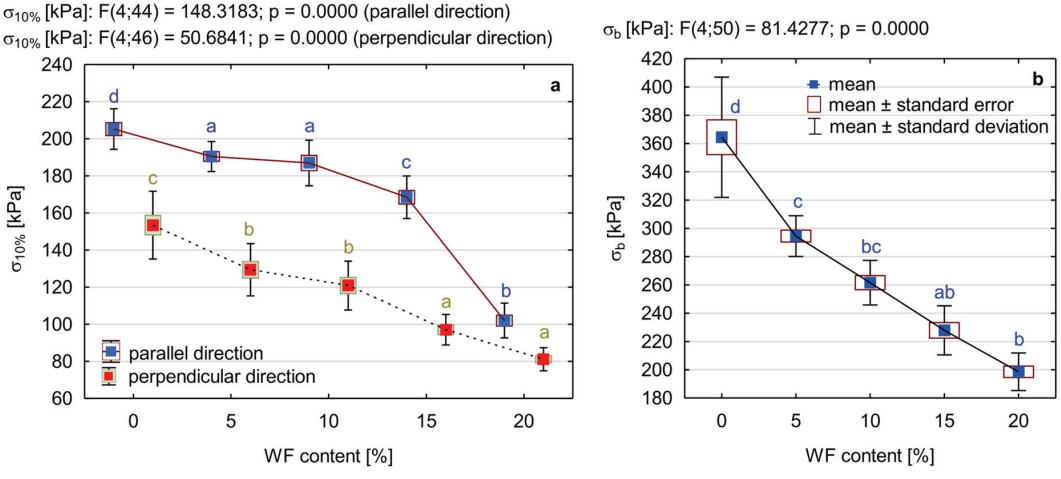

Figure 8. Selected mechanical properties of PUR foam with the addition of different amounts of wood filler: (**a**) compressive strength ($\sigma_{10\%}$), (**b**) flexural strength (σ_b). Different letters in colour indicate homogeneous groups of mean values determined by one-factor ANOVA with Tukey's test.

It should be noted that in spite of the recorded decreases in $\sigma_{10\%}$, the compressive strength of the foams containing up to 15% of WF, exceeds the value of 100 kPa (both in the parallel and perpendicular direction to their growth), which is considered sufficient for rigid PUR foams applications [73]. With a WF content of 10%, the requirements for

insulating materials (≥120 kPa) are still fulfilled [74]. When considering the above, it can be stated that the results obtained in this respect are satisfactory and consistent with the thermal insulation parameters of materials based on rigid PUR foam, currently available on the market [75].

Similar to the compressive strength, there was a decrease in flexural strength (σ_b) of the produced PUR/WF foams as the amount of WF increased. While pure PUR foam showed that type of strength at 364 kPa, the introduction of filler in the amount of 20% caused a decrease in the value of σ_b to the level at 198 kPa, i.e., by as much as 45%. It should be noted that the first 5% of the filler caused the biggest changes—by about 19%. The reasons for such a significant decrease in flexural strength (as in the case of compressive strength) are changes in the morphology of the foam, the amount of filler and its particle size. In general, foams have better mechanical properties when their cells are intact, uniform in size, evenly distributed, and regular in shape [76]. However, as shown in the SEM images, as the proportion of WF particles increases, the produced foams have smaller cells with thinner walls and struts and increasing damage. The number of open cells also increases. For these reasons, the structure of foams becomes increasingly porous and elastic so that not only the compressive strength but also the flexural strength deteriorates despite the increase in density. Saint-Michel et al. [77] found that the addition of filler can lead to the friability of the PUR cell walls, which consequently promotes rupture instead of deformation. However, the literature on the subject shows that the addition of filler in the right amount and particle size can improve the mechanical properties of PUR foams. In this case, the filler particles present in the polyurethane matrix act as reinforcing centres, generating local stresses under the application of the loading force. This means that during a growing crack, the filler particles cause energy dissipation [12]. When excessive amounts of filler are present (or aggregated), the filler particles cause stress concentrations that promote specimen fracture. This is confirmed by previous studies. For example, the introduction of up to 1% ground walnut shells into PUR foam increases its flexural strength and impact strength. A higher admixture of this filler (5 wt%) led to a decrease in the values of these parameters [12]. Analogous relationships were obtained in the work of Ciecierska et al. [13], in which carbon nanotubes (CNTs) were used as PUR foam fillers. These authors further found that poor adhesion between the foam and filler particles and their uneven distribution in the polymer matrix was also the cause of the deterioration in flexural strength. Strąkowska et al. [15] obtained an improvement in flexural strength by introducing POSS-impregnated sugar beet pulp in the foam in the amount of less than 5 wt%. Similar results were also obtained using dolomite and kaolin at up to 3 wt% and plum stones at 1 and 2 wt% [22,78].

3.6. Brittleness of PUR/WF Foams

The brittleness of PUR foams is closely related to their compressive strength and microstructure [69]. It was found that the introduction of wood filler particles into the structure of rigid PUR foam significantly reduces its brittleness (Figure 9a,b). The lowest brittleness of about 5% was characteristic for foams produced with the addition of 20% *w/w* of wood particles. This is almost a 6-fold decrease in the brittleness of this type of foam compared to the reference foam. This is usually the result of reducing the size of the enclosed cells, reinforcing the walls with filler and obtaining a more compact structure [21,45]. According to Liszkowska et al. [64,79], the reduction in brittleness due to foam modification is also due to the opening of foam cells and the increase in flexible bonds in the structure of foams.

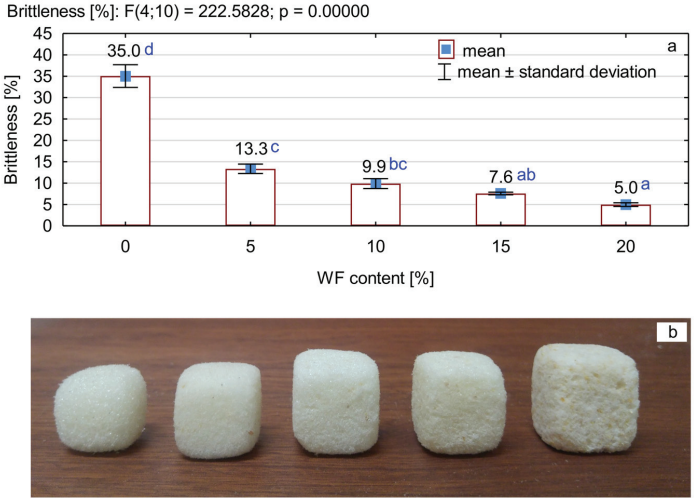

Figure 9. Brittleness of PUR foams with the addition of different amounts of WF: (**a**) average brittleness values of the tested foams, (**b**) image of the foams after the brittleness test (from left to right, an increase in the WF content). Different letters in colour indicate homogeneous groups of mean values determined by one-factor ANOVA with Tukey's test.

4. Conclusions

Our research shows that it is possible to produce rigid PUR foams with high physical and mechanical properties filled with sawdust, which are a by-product of primary wood (WF) processing. However, in order to produce foams with the required parameters, it is necessary to use an optimal amount of this type of filler.

The research demonstrated that with the increase in WF content, the density of the produced foams increases as well and more and more changes take place in their cellular structure, which significantly affects the formation of their physical and mechanical parameters. The use of this type of filler in the amount of up to 10% does not significantly affect the kinetics of the foaming process. Compared to pure PUR foam, this amount of WF allows to minimise its thermal conductivity and significantly reduces brittleness while maintaining high dimensional stability. However, this results in a slight decrease in the compressive strength of the foam, a decrease in its flexural strength and an increase in water absorption. Despite the observed reduction in the above parameters, the results obtained in this respect are satisfactory and consistent with the thermal insulation parameters of materials based on rigid PUR foam, currently available on the market.

Increasing the content of WF particles in the polyurethane matrix to 15 and 20% results in significant defects in the cellular structure of the foam, which in turn leads to an increase in its thermal conductivity to a level significantly exceeding that of pure PUR foam, a significant decrease in compressive and flexural strength, and an increase in short-term partial water absorption. Foams with such a proportion of WF particles also do not show the required dimensional stability, which practically disqualifies them from application prospects.

It seems that rigid PUR foams containing up to 10% of wood sawdust can be used as thermal insulating materials in the building industry (e.g., door insulation), cooling and heating industry (e.g., insulation of cooling furniture or boilers). Due to its considerably reduced friability, it is also used in the production of usable parts, such as ceiling and wall decorations or polyurethane hives.

When taking into account the results obtained, it is advisable to undertake further work in the direction of improving the properties of PUR/WF foams. This can be achieved by optimising the parameters of the wood filler, which includes the selection of the correct

particle size and moisture content. In addition, chemical modification of the surface of the wood filler particles to increase its compatibility with the hydrophobic structure of PUR may be important for improving the properties of foams.

Author Contributions: Conceptualisation, R.M. and D.D.; methodology, R.M., D.D. and J.W.; validation, J.W., A.D. and R.M.; formal analysis, D.D., R.M. and J.W.; investigation, D.D., J.W. and A.D.; resources, D.D.; data curation, D.D. and R.M.; writing—original draft preparation, D.D. and R.M.; writing—review and editing, D.D., J.W. and A.D.; visualisation, D.D. and J.W.; supervision, D.D. and R.M.; project administration, R.M.; funding acquisition, R.M. All authors have read and agreed to the published version of the manuscript.

Funding: This research was funded by the National Centre for Research and Development, grant number BIOSTRATEG3/344303/14/NCBR/2018. The authors are grateful for the support of Ministry of Science and Higher Education program "Regional Initiative of Excellence" in the years 2019–2022, Project No. 005/RID/2018/19.

Institutional Review Board Statement: Not applicable.

Informed Consent Statement: Not applicable.

Data Availability Statement: The data presented in this study are available on request from the corresponding author.

Conflicts of Interest: The authors declare no conflict of interest.

References

1. Mirski, R.; Derkowski, A.; Dziurka, D.; Dukarska, D.; Czarnecki, R. Effects of a Chipboard Structure on Its Physical and Mechanical Properties. *Materials* **2019**, *12*, 3777. [CrossRef]
2. Besserer, A.; Troilo, S.; Girods, P.; Rogaume, Y.; Brosse, N. Cascading Recycling of Wood Waste: A Review. *Polymers* **2021**, *13*, 1752. [CrossRef] [PubMed]
3. Bederina, M.; Marmoret, L.; Mezreb, K.; Khenfer, M.; Bali, A.; Quéneudec, M. Effect of the addition of wood shavings on thermal conductivity of sand concretes: Experimental study and modelling. *Constr. Build. Mater.* **2007**, *21*, 662–668. [CrossRef]
4. Coatanlem, P.; Jauberthie, R.; Rendell, F. Lightweight wood chipping concrete durability. *Constr. Build. Mater.* **2006**, *20*, 776–781. [CrossRef]
5. Mirski, R.; Dukarska, D.; Derkowski, A.; Czarnecki, R.; Dziurka, D. By-products of sawmill industry as raw materials for manufacture of chip-sawdust boards. *J. Build. Eng.* **2020**, *32*, 101460. [CrossRef]
6. Mirski, R.; Derkowski, A.; Dziurka, D.; Wieruszewski, M.; Dukarska, D. Effects of Chip Type on the Properties of Chip–Sawdust Boards Glued with Polymeric Diphenyl Methane Diisocyanate. *Materials* **2020**, *13*, 1329. [CrossRef]
7. Włoch, M.; Landowska, P. Preparation and Properties of Thermoplastic Polyurethane Composites Filled with Powdered Buckwheat Husks. *Materials* **2022**, *15*, 356. [CrossRef] [PubMed]
8. Martins, C.I.; Gil, V.; Rocha, S. Thermal, Mechanical, Morphological and Aesthetical Properties of Rotational Molding PE/Pine Wood Sawdust Composites. *Polymers* **2022**, *14*, 193. [CrossRef]
9. Vitolina, S.; Shulga, G.; Neiberte, B.; Jaunslavietis, J.; Verovkins, A.; Betkers, T. Characteristics of the Waste Wood Biomass and Its Effect on the Properties of Wood Sanding Dust/Recycled PP Composite. *Polymers* **2022**, *14*, 468. [CrossRef]
10. Czech-Polak, J.; Oliwa, R.; Oleksy, M.; Budzik, G. Rigid polyurethane foams with improved flame resistance. *Polimery* **2018**, *63*, 115–124. (In Polish) [CrossRef]
11. Gama, N.V.; Ferreira, A.; Barros-Timmons, A. Polyurethane Foams: Past, Present, and Future. *Materials* **2018**, *11*, 1841. [CrossRef] [PubMed]
12. Członka, S.; Strąkowska, A.; Kairytė, A. Effect of walnut shells and silanized walnut shells on the mechanical and thermal properties of rigid polyurethane foams. *Polym. Test.* **2020**, *87*, 106534. [CrossRef]
13. Ciecierska, E.; Jurczyk-Kowalska, M.; Bazarnik, P.; Gloc, M.; Kulesza, M.; Kowalski, M.; Krauze, S.; Lewandowska, M. Flammability, mechanical properties and structure of rigid polyurethane foams with different types of carbon reinforcing materials. *Compos. Struct.* **2016**, *140*, 67–76. [CrossRef]
14. Yuan, J.; Shi, S.Q. Effect of the addition of wood flours on the properties of rigid polyurethane foam. *J. Appl. Polym. Sci.* **2009**, *113*, 2902–2909. [CrossRef]
15. Strąkowska, A.; Członka, S.; Kairytė, A. Rigid Polyurethane Foams Reinforced with POSS-Impregnated Sugar Beet Pulp Filler. *Materials* **2020**, *13*, 5493. [CrossRef] [PubMed]
16. Marhoon, I. Effect of silica-fume microparticles on rigid polyurethane foam properties. *Int. J. Sci. Technol. Res.* **2016**, *5*, 96–100.
17. Septevani, A.A.; Evans, D.A.C.; Annamalai, P.K.; Martin, D.J. The use of cellulose nanocrystals to enhance the thermal insulation properties and sustainability of rigid polyurethane foam. *Ind. Crops Prod.* **2017**, *107*, 114–121. [CrossRef]

18. Saha, M.C.; Kabir, M.E.; Jeelani, S. Enhancement in thermal and mechanical properties of polyurethane foam infused with nanoparticles. *Mater. Sci. Eng. A* **2008**, *479*, 213–222. [CrossRef]
19. Członka, S.; Kairytė, A.; Miedzińska, K.; Strąkowska, A.; Adamus-Włodarczyk, A. Mechanically Strong Polyurethane Composites Reinforced with Montmorillonite-Modified Sage Filler (*Salvia officinalis* L.). *Int. J. Mol. Sci.* **2021**, *22*, 3744. [CrossRef] [PubMed]
20. Członka, S.; Kairytė, A.; Miedzińska, K.; Strąkowska, A. Polyurethane Composites Reinforced with Walnut Shell Filler Treated with Perlite, Montmorillonite and Halloysite. *Int. J. Mol. Sci.* **2021**, *22*, 7304. [CrossRef]
21. Paciorek-Sadowska, J.; Borowicz, M.; Isbrandt, M.; Czupryński, B.; Apiecionek, Ł. The Use of Waste from the Production of Rapeseed Oil for Obtaining of New Polyurethane Composites. *Polymers* **2019**, *11*, 1431. [CrossRef]
22. Miedzińska, K.; Członka, S.; Strąkowska, A.; Strzelec, K. Biobased Polyurethane Composite Foams Reinforced with Plum Stones and Silanized Plum Stones. *Int. J. Mol. Sci.* **2021**, *22*, 4757. [CrossRef]
23. Augaitis, N.; Vaitkus, S.; Członka, S.; Kairytė, A. Research of Wood Waste as a Potential Filler for Loose-Fill Building Insulation: Appropriate Selection and Incorporation into Polyurethane Biocomposite Foams. *Materials* **2020**, *13*, 5336. [CrossRef]
24. Tao, Y.; Li, P.; Cai, L. Effect of Fiber Content on Sound Absorption, Thermal Conductivity, and Compression Strength of Straw Fiber-Filled Rigid Polyurethane Foams: BioResources. Available online: https://bioresources.cnr.ncsu.edu/ (accessed on 23 May 2022).
25. Sair, S.; Oushabi, A.; Kammouni, A.; Tanane, O.; Abboud, Y.; El Bouari, A. Mechanical and thermal conductivity properties of hemp fiber reinforced polyurethane composites. *Case Stud. Constr. Mater.* **2018**, *8*, 203–212. [CrossRef]
26. Paciorek-Sadowska, J.; Czupryński, B.; Liszkowska, J. Application of waste products from agricultural-food industry for production of rigid polyurethane-polyisocyanurate foams. *J. Porous Mater.* **2011**, *18*, 631–638. [CrossRef]
27. Zhang, S.; Xiang, A.; Tian, H.; Rajulu, A.V. Water-Blown Castor Oil-Based Polyurethane Foams with Soy Protein as a Reactive Reinforcing Filler. *J. Polym. Environ.* **2018**, *26*, 15–22. [CrossRef]
28. Członka, S.; Bertino, M.F.; Strzelec, K. Rigid polyurethane foams reinforced with industrial potato protein. *Polym. Test.* **2018**, *68*, 135–145. [CrossRef]
29. Zieleniewska, M.; Leszczyński, M.K.; Szczepkowski, L.; Bryśkiewicz, A.; Krzyżowska, M.; Bień, K.; Ryszkowska, J. Development and applicational evaluation of the rigid polyurethane foam composites with egg shell waste. *Polym. Degrad. Stab.* **2016**, *132*, 78–86. [CrossRef]
30. Liszkowska, J. The effect of ground coffee on the mechanical and application properties of rigid polyurethane-polyisocyanurate foams. *Polimery* **2018**, *63*, 305–310. [CrossRef]
31. Członka, S.; Sienkiewicz, N.; Strąkowska, A.; Strzelec, K. Keratin feathers as a filler for rigid polyurethane foams on the basis of soybean oil polyol. *Polym. Test.* **2018**, *72*, 32–45. [CrossRef]
32. De Avila Delucis, R.; Magalhães, W.L.E.; Petzhold, C.L.; Amico, S.C. Forest-based resources as fillers in biobased polyurethane foams. *J. Appl. Polym. Sci.* **2018**, *135*, 45684. [CrossRef]
33. Luo, S.; Gao, L.; Guo, W. Influence of Adding Lignin and Wood as Reactive Fillers on the Properties of Lightweight Wood–Polyurethane Composite Foams. *For. Prod. J.* **2021**, *70*, 420–427. [CrossRef]
34. Mirski, R.; Dukarska, D.; Walkiewicz, J.; Derkowski, A. Waste Wood Particles from Primary Wood Processing as a Filler of Insulation PUR Foams. *Materials* **2021**, *14*, 4781. [CrossRef]
35. *EN ISO 845*; Cellular Plastics and Rubbers-Determination of Apparent Density. European Standardization Committee: Brussels, Belgium, 2009.
36. *ISO 29767*; Thermal Insulating Products for Building Applications–Determination of Short-Term Water Absorption by Partial Immersion. European Standardization Committee: Brussels, Belgium, 2019.
37. *EN 1604*; Thermal Insulation Products for Buildings–Determination of Dimensional Stability under Specified Temperature and Humidity Conditions. European Standardization Committee: Brussels, Belgium, 2013.
38. *EN 826*; Thermal Insulating Products for Building Applications–Determination of Compression Behaviour. European Standardization Committee: Brussels, Belgium, 2013.
39. *EN 12089*; Thermal Insulating Products for Building Applications–Determination of Bending Behaviour. European Standardization Committee: Brussels, Belgium, 2013.
40. Barszczewska-Rybarek, I.; Jaszcz, K.; Chladek, G.; Grabowska, P.; Okseniuk, A.; Szpot, M.; Zawadzka, M.; Sokołowska, A.; Tarkiewicz, A. Characterization of changes in structural, physicochemical and mechanical properties of rigid polyurethane building insulation after thermal aging in air and seawater. *Polym. Bull.* **2021**, *79*, 3061–3083. [CrossRef]
41. *ASTM C 421*; Standard Test Method for Tumbling Friability of Preformed Block-Type and Preformed Pipe-Covering-Type Thermal Insulation. ASTM International: West Conshohocken, PA, USA, 1995.
42. Uram, K.; Kurańska, M.; Andrzejewski, J.; Prociak, A. Rigid Polyurethane Foams Modified with Biochar. *Materials* **2021**, *14*, 5616. [CrossRef]
43. Kurańska, M.; Prociak, A.; Cabulis, U.; Kirpluks, M.; Ryszkowska, J.; Auguścik, M. Innovative porous polyurethane-polyisocyanurate foams based on rapeseed oil and modified with expandable graphite. *Ind. Crops Prod.* **2017**, *95*, 316–323. [CrossRef]
44. Gómez-Fernández, S.; Ugarte, L.; Calvo-Correas, T.; Peña-Rodríguez, C.; Corcuera, M.A.; Eceiza, A. Properties of flexible polyurethane foams containing isocyanate functionalized kraft lignin. *Ind. Crops Prod.* **2017**, *100*, 51–64. [CrossRef]

45. Paciorek-Sadowska, J.; Borowicz, M.; Czuprynski, B.; Liszkowska, J. Composites of rigid polyurethane-polyisocyanurate foams with oak bark. *Polimery* **2017**, *62*, 666–672. (In Polish) [CrossRef]
46. Beran, R.; Zarybnicka, L.; Machova, D. Recycling of rigid polyurethane foam: Micro-milled powder used as active filler in polyurethane adhesives. *J. Appl. Polym. Sci.* **2020**, *137*, 49095. [CrossRef]
47. Członka, S.; Strąkowska, A.; Kairytė, A.; Kremensas, A. Nutmeg filler as a natural compound for the production of polyurethane composite foams with antibacterial and anti-aging properties. *Polym. Test.* **2020**, *86*, 106479. [CrossRef]
48. Członka, S.; Strąkowska, A.; Kairytė, A. The Impact of Hemp Shives Impregnated with Selected Plant Oils on Mechanical, Thermal, and Insulating Properties of Polyurethane Composite Foams. *Materials* **2020**, *13*, 4709. [CrossRef]
49. Kairytė, A.; Kremensas, A.; Balčiūnas, G.; Członka, S.; Strąkowska, A. Closed Cell Rigid Polyurethane Foams Based on Low Functionality Polyols: Research of Dimensional Stability and Standardised Performance Properties. *Materials* **2020**, *13*, 1438. [CrossRef]
50. Członka, S.; Strąkowska, A.; Kairytė, A. Coir Fibers Treated with Henna as a Potential Reinforcing Filler in the Synthesis of Polyurethane Composites. *Materials* **2021**, *14*, 1128. [CrossRef]
51. Estravís, S.; Tirado-Mediavilla, J.; Santiago-Calvo, M.; Ruiz-Herrero, J.L.; Villafañe, F.; Rodríguez-Pérez, M. Rigid polyurethane foams with infused nanoclays: Relationship between cellular structure and thermal conductivity. *Eur. Polym. J.* **2016**, *80*, 1–15. [CrossRef]
52. Barczewski, M.; Kurańska, M.; Sałasińska, K.; Michałowski, S.; Prociak, A.; Uram, K.; Lewandowski, K. Rigid polyurethane foams modified with thermoset polyester-glass fiber composite waste. *Polym. Test.* **2019**, *81*, 106190. [CrossRef]
53. Sung, G.; Kim, J.H. Influence of filler surface characteristics on morphological, physical, acoustic properties of polyurethane composite foams filled with inorganic fillers. *Compos. Sci. Technol.* **2017**, *146*, 147–154. [CrossRef]
54. Grząbka-Zasadzińska, A.; Bartczak, P.; Borysiak, S. Highly Insulative PEG-Grafted Cellulose Polyurethane Foams—From Synthesis to Application Properties. *Materials* **2021**, *14*, 6363. [CrossRef] [PubMed]
55. Członka, S.; Bertino, M.F.; Kośny, J.; Strąkowska, A.; Masłowski, M.; Strzelec, K. Linseed oil as a natural modifier of rigid polyurethane foams. *Ind. Crop. Prod.* **2018**, *115*, 40–51. [CrossRef]
56. Silva, N.G.S.; Cortat, L.I.C.O.; Orlando, D.; Mulinari, D.R. Evaluation of rubber powder waste as reinforcement of the polyurethane derived from castor oil. *Waste Manag.* **2020**, *116*, 131–139. [CrossRef]
57. Formela, K.; Hejna, A.; Zedler, Ł.; Przybysz, M.; Ryl, J.; Saeb, M.R.; Piszczyk, Ł. Structural, thermal and physico-mechanical properties of polyurethane/brewers' spent grain composite foams modified with ground tire rubber. *Ind. Crop. Prod.* **2017**, *108*, 844–852. [CrossRef]
58. Stefani, P.M.; Barchi, A.T.; Sabugal, J.; Vazquez, A. Characterization of epoxy foams. *J. Appl. Polym. Sci.* **2003**, *90*, 2992–2996. [CrossRef]
59. Sture, B.; Vevere, L.; Kirpluks, M.; Godina, D.; Fridrihsone, A.; Cabulis, U. Polyurethane Foam Composites Reinforced with Renewable Fillers for Cryogenic Insulation. *Polymers* **2021**, *13*, 4089. [CrossRef]
60. Kuranska, M.; Prociak, A. Porous polyurethane composites with natural fibres. *Compos. Sci. Technol.* **2012**, *72*, 299–304. [CrossRef]
61. Thirumal, M.; Khastgir, D.; Singha, N.K.; Manjunath, B.S.; Naik, Y.P. Mechanical, Morphological and Thermal Properties of Rigid Polyurethane Foam: Effect of the Fillers. *Cell. Polym.* **2007**, *26*, 245–259. [CrossRef]
62. Shalbafan, A.; Choupani, K.; Welling, J. Effect of blowing agent concentration on rigid polyurethane foam and the properties of foam-core particleboard. *Wood Mater. Sci. Eng.* **2021**, *16*, 85–93. [CrossRef]
63. Pouzet, M.; Dubois, M.; Charlet, K.; Béakou, A. From hydrophilic to hydrophobic wood using direct fluorination: A localized treatment. *Comptes Rendus. Chim.* **2018**, *21*, 800–807. [CrossRef]
64. Liszkowska, J.; Moraczewski, K.; Borowicz, M.; Paciorek-Sadowska, J.; Czupryński, B.; Isbrandt, M. The Effect of Accelerated Aging Conditions on the Properties of Rigid Polyurethane-Polyisocyanurate Foams Modified by Cinnamon Extract. *Appl. Sci.* **2019**, *9*, 2663. [CrossRef]
65. Kairytė, A.; Ivdre, A.; Vaitkus, S. Dimensionally stable water-blown polyurethane foam extended with bio-based propylene glycol and modified with paper waste sludge. *Eng. Struct. Technol.* **2017**, *9*, 93–103. [CrossRef]
66. Li, X.; Cao, H.; Zhang, Y. Properties of water blown rigid polyurethane foams with different functionality. *J. Wuhan Univ. Technol. Sci. Ed.* **2008**, *23*, 125–129. [CrossRef]
67. *EN 13165*; Thermal Insulation Products for Buildings–Factory Made Rigid Polyurethane Foam (PU) Products–Specification. European Standardization Committee: Brussels, Belgium, 2016.
68. Borkowski, R. Thermal insulation in industrial applications. *Izolacje* **2014**, *19*, 10. (In Polish)
69. Kurańska, M.; Barczewski, M.; Uram, K.; Lewandowski, K.; Prociak, A.; Michałowski, S. Basalt waste management in the production of highly effective porous polyurethane composites for thermal insulating applications. *Polym. Test.* **2019**, *76*, 90–100. [CrossRef]
70. Voiconi, T.; Linul, E.; Marşavina, L.; Sadowski, T.; Kneć, M. Determination of Flexural Properties of Rigid PUR Foams Using Digital Image Correlation. *Solid State Phenom.* **2014**, *216*, 116–121. [CrossRef]
71. Uram, K.; Leszczyńska, M.; Prociak, A.; Czajka, A.; Gloc, M.; Leszczyński, M.K.; Michałowski, S.; Ryszkowska, J. Polyurethane Composite Foams Synthesized Using Bio-Polyols and Cellulose Filler. *Materials* **2021**, *14*, 3474. [CrossRef] [PubMed]
72. Członka, S.; Strąkowska, A.; Strzelec, K.; Kairytė, A.; Kremensas, A. Melamine, silica, and ionic liquid as a novel flame retardant for rigid polyurethane foams with enhanced flame retardancy and mechanical properties. *Polym. Test.* **2020**, *87*, 106511. [CrossRef]

73. Thermal Insulation Materials Made of Rigid Polyurethane Foam/Thermal-Insulation-Materials-Made-of-Rigid-Polyurethane-Foam.Pdf/PDF4PRO. Available online: https://pdf4pro.com/view/thermal-insulation-materials-made-of-rigid-polyurethane-foam-376aac.html (accessed on 19 May 2022).
74. Jabber, L.J.Y.; Grumo, J.C.; Alguno, A.C.; Lubguban, A.A.; Capangpangan, R.Y. Influence of cellulose fibers extracted from pineapple (Ananas comosus) leaf to the mechanical properties of rigid polyurethane foam. *Mater. Today Proc.* **2021**, *46*, 1735–1739. [CrossRef]
75. High Quality PU PUF PUR PIR Polyurethane Foam Insulation Board Cheap Price-Henan Panels Industry Co., Ltd. Available online: https://www.pnspanels.com/Polyurethane-Foam-insulation-board.html (accessed on 27 May 2022).
76. Guan, J.; Hanna, M.A. Functional properties of extruded foam composites of starch acetate and corn cob fiber. *Ind. Crops Prod.* **2004**, *19*, 255–269. [CrossRef]
77. Saint-Michel, F.; Chazeau, L.; Cavaillé, J.-Y. Mechanical properties of high density polyurethane foams: II Effect of the filler size. *Compos. Sci. Technol.* **2006**, *66*, 2709–2718. [CrossRef]
78. Omotoyinbo, J.A.; Oladele, I.O.; Jabar, J.M.; Borode, J.O.; Alaneme, K.K.; Akinwekomi, A.D.; Oke, S.R.; Omotosho, T.F.; Saliu, L.O. Comparative investigation of the influence of kaolin and dolomite on the properties of polyurethane foam. *Manuf. Rev.* **2021**, *8*, 27. [CrossRef]
79. Liszkowska, J. The use of citric acid in the production of polyols for rigid PUR-PIR foams. *Polym. Bull.* **2017**, *74*, 283–305. [CrossRef]

MDPI
St. Alban-Anlage 66
4052 Basel
Switzerland
Tel. +41 61 683 77 34
Fax +41 61 302 89 18
www.mdpi.com

Materials Editorial Office
E-mail: materials@mdpi.com
www.mdpi.com/journal/materials

Academic Open
Access Publishing

www.mdpi.com

ISBN 978-3-0365-7803-3